AN IMPLICIT FINITE-VOLUME DEPTH-INTEGRATED MODEL FOR COASTAL HYDRODYNAMICS AND MULTIPLE-SIZED SEDIMENT TRANSPORT

A Dissertation

Presented for the

Doctor of Philosophy

Degree

National Center for Computational Hydroscience and Engineering

The University of Mississippi

Alejandro Sánchez

July 2013

ABSTRACT

A two-dimensional depth-integrated model is developed for simulating wave-averaged hydrodynamics and nonuniform sediment transport and morphology change in coastal waters. The hydrodynamic model includes advection, wave-enhanced turbulent mixing and bottom friction; wave-induced volume flux; wind, atmospheric pressure, wave, river, and tidal forcing; and Coriolis-Stokes force. The sediment transport model simulates nonequilibrium total-load transport, and includes flow and sediment transport lags, hiding and exposure, bed material sorting, bed slope effects, nonerodible beds, and avalanching. The flow model is coupled with an existing spectral wave model and a newly developed surface roller model.

The hydrodynamic and sediment transport models use finite-volume methods on a variety of computational grids including nonuniform Cartesian, telescoping Cartesian, quadrilateral, triangular, and hybrid triangular/quadrilateral. Grid cells are numbered in an unstructured one-dimensional array, so that all grid types are implemented under the same framework. The model uses a second-order fully implicit temporal scheme and first- and second-order spatial discretizations including corrections for grid non-orthogonality. The hydrodynamic equations are solved using an iterative pressure-velocity coupling algorithm on a collocated grid with a momentum interpolation for inter-cell fluxes. The multiple-sized sediment transport, bed change, and bed material sorting equations are solved in a coupled manner but are decoupled from the hydrodynamic equations. The spectral wave and roller models are calculated using finite-difference methods on nonuniform Cartesian grids. An efficient inline steering procedure is

developed to couple the flow and wave models.

The model is verified using seven analytical solution cases and validated using ten laboratory and five field test cases which cover a wide range of conditions, time and spatial scales. The hydrodynamic model simulates reasonably well long wave propagation, wetting and drying, recirculation flows near a spur-dike and a sudden channel expansion, and wind- and wave generated currents and water levels. The sediment transport model reproduces channel shoaling, erosion due to a clear-water inflow, downstream sediment sorting, and nearshore morphology change. Calculated longshore sediment transport rates are well simulated except near the shoreline where swash processes, which are not included, become dominant. Model sensitivity to the computation grid and calibration parameters is presented for several test cases.

DEDICATION

This work is dedicated to Sophie Munger.

ACKNOWLEDGEMENTS

This dissertation could not be accomplished without the encouragement, support, and assistance of the people around me especially my wife Sophie Munger. Without her none of this would have been possible. I would like to thank my advisor, Dr. Weiming Wu, for his knowledge, advice and patience. He has provided invaluable insights and precious guidance during my entire Ph.D. study.

I would like to extend gratitude to the members of my dissertation committee, Professor Mustafa S. Altinakar, Yafei Jia, and Cristiane Queiroz Surbeck for their guidance and suggestions. I would like to thank all my colleagues and fellow students at the National Center for Computational Hydroscience and Engineering for their kindness and friendship. In particular, I would like to thank to Ms. Natalie Spenser for their administrative support.

Special thanks to Dr. Julie D. Rosati who supported me throughout my dissertation work. This dissertation would have not been possible if not for encouragement and mentorship of the now passed Dr. Nicholas Kraus. I hope that this work makes him proud.

This research was funded mainly by the Coastal Modeling System work unit of the Coastal Inlets Research Program (CIRP), U.S. Army Corps of Engineers (USACE). The support of the USACE is gratefully acknowledged. I would like to thank everyone in the CIRP program for their support, patience, and helpful suggestions.

Finally, I would like thank my family for their support and encouragement.

TABLE OF CONTENTS

LIST OF FIGURES

LIST OF TABLES

TABLE PAGE

CHAPTER I

INTRODUCTION

1.1 Background

It is well known that two thirds of the world's population lives within 200 km of the coastlines. As population increases, coastal activities are expected to increase. The coastal environment is very dynamic in nature due to time-varying forcing by astronomical tide, wind, waves, and complex interactions between the currents, waves, and morphology change. Natural or anthropogenic-induced morphology changes can interfere with or cause damage to coastal structures. In addition, sea level rise is expected to increase coastal flooding and in turn cause morphological evolution. Many coastal engineering projects often require to some degree the simulation of coastal morphology for planning or design purposes. Examples of coastal engineering problems where a morphologic model is needed are simulation of beach and dune erosion during storms, prediction of beach set-back lines, nourishment studies, design and construction of coastal harbors, entrances, channels, pipelines, outfalls, revetments, etc. There are many types of coastal morphology tools in literature and practice. The proper selection and application of coastal morphology models requires a good understanding of coastal processes and the engineering tools available.

Coastal inlets are vital navigation links and central for exchange of water, sediment, and nutrients between estuaries and the ocean. Because of the multiple interacting forces (waves,

wind, tide, river flows, density currents, etc.) on a wide range of spatial and temporal scales, the complex physical processes of coastal inlets are quantitatively not well understood. Hence prediction of the morphodynamic processes at coastal inlets has been a challenging, but crucial task for coastal sediment management, navigation channel maintenance, and beach erosion protection.

Process-based morphodynamic models capable of simulating short term (hours to days) and long-term (decades) periods have increasingly become popular in engineering studies due to increased computer speeds and user friendly interfaces. Improved physics and experience has increased their reliability especially in the calculation of waves, currents and water levels. However, only partial success has been obtained in the area of sediment transport and morphologic change due to the high level of process aggregation, empiricism, uncertainties in bed characteristics, etc. Combined with a good understanding of coastal processes, morphodynamic models can be a useful tool in making engineering decisions.

1.2 Coastal Morphodynamic Modeling

Coastal morphodynamic models can be classified into six groups (Watanabe 1988, de Vriend et al. 1994, Hanson et al. 2003):

1. Conceptual models
2. Shoreline evolution profiles
3. Beach profile evolution models
4. Coastal area or two-dimensional horizontal (2DH) models
5. Three-dimensional models (3D)

6. Quasi-3D (Q3D) models

Conceptual or behavior models use simple expressions based on reduced physics or empirical knowledge. Conceptual models are intended as qualitative assessment tools of coastal morphology. The complexity of conceptual models can be from simple two variable expressions to several coupled time-varying equations that need to be solved numerically. Examples of conceptual or behavior models include de Vriend et al. (1994), Gravens (1996), Kana et al. (1999), Kraus (2000), and Ruessink and Terwindt (2000).

Shoreline evolution models describe changes in the shoreline horizontal position from longshore sediment transport gradients. Examples of shoreline evolution models are Pelnard-Considere (1956), GENISIS (Hanson and Kraus 1989, 1991), UNIBEST-CL+ (Delft 1999a, van der Salm 2013), SAND94 (Szmytkiewicz et al. 2000), and LITPACK (Foster and Skou 2008).

Beach profile evolution models are generally process-based and compute changes in the cross-shore morphology (bed elevation) using 1D or two-dimensional Vertical (2DV) governing equations. Examples of beach profile evolution models are SBEACH (Larson and Kraus 1989, Larson et al. 1989), UNIBEST-TC (Bosboom et al. 1997, Delft 1999b), CSHORE (Johnson et al. 2012), LITPACK (Hedegaard and Deigaard 1988) and Nairn and Southgate (1993). Although somewhat outdated, Schoonees and Theron (1995) provide a review of 10 cross-shore beach profile evolution models.

2DH, 3D and Q3D morphodynamic models are generally process-based and use basic principles including the conservation of fluid and sediment mass, and the transport of fluid momentum and wave energy. These models are referred to as coastal area models and include

processes such astronomical tidal forcing, atmospheric pressure and wind forcing, wave-current interactions, Coriolis force, bottom and wall friction, river discharge, etc. Inter-comparisons of various morphodynamic models have been presented by de Vriend et al. (1994) and Nicholson et al. (1997).

One key concept in process-based models is that of spatial and temporal scales. Since it is practically impossible to model every grain of sand or wave swashing on the beach on a project scale (several miles), a separation of scales and process aggregation is necessary. The instantaneous fluid velocity is generally split into current, wave, and turbulent components. The current component is by definition the wave-averaged (time averaged over a wave period) fluid velocity. The wave component is due to the oscillatory motion of surface waves. The turbulent component is a fluctuating component with zero mean due to turbulent fluid motions. In morphodynamic models the term hydrodynamics refers to the wave-averaged velocity component. In the case of sediment transport, sediment is usually modeled as a conservative nonreactive constituent. Although some models include the capability to simulating sediment transport in a Lagrangian framework by tracking individual particles or parcels (e.g. MacDonald et al. 2006), they cannot effectively simulate bed change in the current stage and are not a vital component of morphodynamic models; therefore they are not discussed further here.

Coastal morphodynamic models based on the 3D Reynolds-averaged Navier-Stokes equations for incompressible flow are generally too expensive for practical applications. Therefore, 2DH models have found the most use in practical engineering applications. A limitation of 2DH models is that they do not resolve the vertical current velocity structure which leads to dispersion of momentum and sediments. To overcome this limitation several 2D

hydrodynamic models have been proposed which incorporate the vertical velocity structure and dispersion terms (e.g. de Vriend and Stive 1987, Sánchez -Arcilla et al. 1990, Svendsen et al. 2002). However, a simple but still widely used approach is to extend the eddy viscosity and diffusion coefficient in the momentum and scalar transport equations to mixing or general diffusion which includes the effects of molecular diffusion, turbulent diffusion, and dispersion.

Most coastal sediment transport numerical models are based on the assumption that the bed load or the total load (both bed and suspended loads) are instantaneously in equilibrium on each computational node, calculate the transport rate using empirical formulas, and then determine the bed change by solving the sediment balance equation or the Exner (1925) equation (e.g., Struiksma et al. 1985, Chesher et al. 1993, Roelvink and Banning 1994, Ranasinghe et al. 1999, Cayocca 2001, Fortunato and Olveira 2004, Buttolph et al. 2006, Kubatko et al. 2006, Warner et al. 2008). Such models are referred to as equilibrium or saturated transport modeling. However, because of the dynamic nature of currents and waves on the coast, the bed load and especially the suspended load are generally not in an equilibrium state. The assumption of local equilibrium may lead to unrealistic results and instabilities that can mask the morphodynamic bed change and limit long-term simulations. In order to reduce instabilities, filtering procedures and/or diffusive numerical schemes have been commonly implemented in some of these models (e.g., Johnson and Zyserman 2002), but such procedures are without physical basis. In fact, it is well known that analytical solutions of bed evolution using the Exner equation such as a symmetric mound lead to sharp discontinuities (e.g. Leliavsky 1966, Kubatko et al. 2006, Fortunato and Olveira 2007). Johnson and Zyserman (2002) showed that the Exner equations leads to the creation of higher harmonics due to the nonlinear dependence of the bed celerity

with bed elevations, and that these harmonics if not damped numerically, will lead to instabilities. Therefore an Exner model with zero numerical or artificial diffusion is expected to be unstable.

A more realistic modeling approach for bed-load and suspended-load sediment transport is the non-equilibrium formulation, which has been widely used in river sedimentation (e.g., Han 1980, Phillips and Sutherland 1989, and Wu 2004), and is sometimes used for suspended sediments in coastal morphodynamic models. This approach renounces the assumption of local equilibrium and solves the actual transport equations for bed and suspended loads; thus, it describes the temporal and spatial lags between flow and sediment transport. Compared to equilibrium formulations, the non-equilibrium sediment transport model is usually more stable and can more easily describe over- and under-loading as well as hard (nonerodible) bottoms.

The influence of nonuniform or heterogeneous sediment properties on coastal processes is commonly underestimated due to the difficulty in characterizing and quantifying these types of sediments (Holland and Elmore 2008). The tendency of many empirical formulas and numerical models of coastal sediment transport is to assume uniform or homogeneous sediments (e.g. a well-sorted fine sand). Very few studies have concerned nonuniform sediment transport in coastal environments. However, nonuniform sediment transport exists in coastal waters; in particular, sediment size is often coarser in coastal inlets than adjacent beaches and bays. For most beaches, coarser sediment is generally found in the swash zone and the wave breaker line while finer sediment is found in the trough and landward of the breaker line (e.g. Mason and Folk 1958, Ping et al. 1998). Textural changes of the bed can be related to storm events, seasonal climatic changes and long-term depositional and erosional trends due to changes in the amount

or properties of the sediment source(s). For example, Ping et al. (1998) found that storms and the resulting offshore migration of the bar could leave a layer of coarser lag deposit where fine deposits would normally be found.

Nonuniform sediment transport exhibits difference from uniform sediment, even when the mean grain size is the same for both cases. The hiding, exposure, and armoring among different size classes in the nonuniform bed material may significantly affect sediment transport, morphological change, bed roughness, wave dissipation, etc. For example, it is often observed that bed sediment coarsening can affect the navigation channel near a coastal inlet, and a model prediction based on the assumption of single-sized sediment often over predicts the channel depth there. It is necessary to develop multiple-sized sediment transport analysis methods and models for coastal sedimentation.

1.3 Coastal Modeling System (CMS)

The Coastal Modeling System (CMS) is developed under the U.S. Army Corps of Engineers' Coastal Inlets Research Program and recently in collaboration with The University of Mississippi. The CMS is designed for practical applications in navigation channel performance evaluation and sediment management for coastal inlets and adjacent beaches to optimize limited federal channel operation and maintenance funds. CMS has two main components: (1) CMS-Flow which simulates hydrodynamics, salinity and sediment transport, and morphology change; and (2) CMS-Wave which simulates spectral wave transformation. Some examples of CMS-Flow applications are: Batten and Kraus (2006), Zarillo and Brehin (2007), Li et al. (2009), Beck and Kraus (2010), Byrnes et al. (2010), Dabees and Moore (2011), Reed and Lin (2011), Rosati

et al. (2011), Wang et al. (2011), and Beck and Legault (2012). The CMS is intended as a research and engineering tool that can be operated by novice and experienced modelers on desk-top computers and can be also run in parallel using OpenMP (http://openmp.org/wp/). The CMS takes advantage of the Surface-water Modeling System (SMS) interface for grid generation and model setup, as well as for plotting and post-processing (Zundel 2006). Additional details on the CMS are provided in Chapter II. A portion of the model development presented in this dissertation (related to the telescoping Cartesian grid) was funded by the Coastal Modeling System work unit and all of the code development was done within the Coastal Modeling System and SMS framework.

1.4 Objectives of this Study

The goal of this study is to develop comprehensive coastal modeling software, by extending and improving the Coastal Modeling System (CMS). The objectives of this study are:

1. Develop an implicit finite-volume scheme to solve the hydrodynamic and sediment transport equations on Cartesian grids.
2. Develop a multiple-sized nonequilibrium sediment transport model for coastal applications as an add-on to the CMS.
3. Extend the hydrodynamic and sediment transport models to work with general polygonal meshes.
4. Comprehensively verify and validate the developed model system using idealized analytical solutions, laboratory experiments and field measurements.

1.5 Dissertation Outline

A general introduction is presented in Chapter I. The commonly used existing coastal morphodynamic models including the CMS are briefly reviewed in Chapter II. The mathematical formulations used in the present model are described in detail in Chapter III. Chapter IV contains a description of the computational grids, discretization, numerical schemes, and algorithms. Chapters V, VI, and VII present the model verifications and validations using analytical, laboratory, and field test cases, respectively. Finally, the conclusions and recommendations are presented in Chapter VIII.

CHAPTER II

LITERATURE REVIEW

In this chapter, a review is presented of the different approaches used in coastal morphodynamic models for simulating hydrodynamics, waves, sediment transport, and morphology change. Although there are many hydrodynamic models in literature which have been coupled to wave models and applied to the coast, only models which are tightly coupled with waves and simulate sediment transport and morphology change are discussed here.

2.1 Hydrodynamics

The governing equations for hydrodynamics are usually based on the shallow water equations. The equations are derived from the Reynolds-averaged Navier-Stokes equation for incompressible and Newtonian fluids by assuming hydrostatic pressure. In the case of two-dimensional horizontal (2DH) models, the equations are integrated over the flow depth and the vertical velocity profiles are assumed to be uniform (e.g. Zyserman and Ronberg 2001, Roelvink et al. 2010). In quasi-three-dimensional (Q3D) models, the equations are integrated vertically, but the vertical velocity profile is allowed to vary (e.g. Luijendijk et al. 2010). The methods calculating the vertical velocity profile vary significantly in literature but generally reduce to solving a 1DV momentum equation. The nonuniform vertical velocity profile then results in additional current-current and current-wave interaction terms in the depth-integrated momentum

equations. The vertical velocity profile should in principle modify the bed shear stress, although this is not always included.

The governing equations may be written in conservative or nonconservative form. The continuity equation by principle should always be solved in conservative form for local mass conservation. The momentum equations are solved in either the conservative (e.g. Zyserman and Ronberg 2001, Buttolph et al. (2006), Warner et al. 2008) or nonconservative form (e.g. Lesser et al. 2004, Roelvink et al. 2010). Both forms of the equations follow conservation laws; however, their mathematical and numerical behaviors are different. The conservative or integral form has the advantage of allowing discontinuities within a control volume, while the nonconservative form assumes that the flow properties are differentiable and continuous within the control volume (Anderson 1995). The difference between the conservative and nonconservative forms is especially important for the advection term which is nonlinear and a source of numerical instability. Models which use the Finite-Volume Method (FVM) require using conservative form, while models which use the Finite-Element Method (FEM) or Finite-Difference Method (FDM) may use either form. Turbulence closure is generally provided by a two-equation turbulence model such as the k-epsilon model in 3D models. 2DH models may have equivalent depth-averaged formulations, but more often have simpler formulations, such as the subgrid, mixing-length, or energy dissipation-based formulations. Table 2.1 provides a summary of selected hydrodynamic models commonly used in coastal studies.

The Regional Ocean Modeling System (ROMS) is a three-dimensional (3D) finite-difference hydrodynamic model (Warner et al. 2008). ROMS solves the 3D Reynolds-averaged Navier-Stokes equations in conservative flux form using the Finite Difference Method (FDM).

ROMS uses a curvilinear Arakawa C grid (Arakawa and Lamb 1977) in the horizontal and a stretched terrain-following coordinate system in the vertical. For computational efficiency, a split-explicit time stepping algorithm is used. The model has multiple advection schemes from second to forth order. ROMS is coupled with the spectral wave transformation model Simulating Waves in the Nearshore (SWAN) model (Booij et al. 1996). Wave-current interaction includes increased vertical and horizontal mixing, net mass flux due to waves, wave-induced momentum flux, and enhanced bottom friction.

Delft3D solves the 2D or 3D unsteady shallow water hydrodynamic equations in non-conservative form using the finite-difference methods. The model uses an orthogonal curvilinear Arakawa C grid in the horizontal and stretched sigma-coordinate system in the vertical. Several turbulence closure models are available, including simple algebraic, mixing length, and more complicated k-epsilon models. A cut cell approach is available for better representation of boundaries using curvilinear grids. The 2DH model has optional secondary flow model (Q3D) which includes the effects of the centrifugal and Coriolis forces. Recently Luijendijk et al. (2010) implemented a Q3D model in Delft3D which solves the 1DV model for the current velocity by Reniers et al. (2004), which is also used in the profile evolution model UNIBEST-TC (Ruessink et al. 2007). Wave-current interactions include increased vertical and horizontal mixing, net mass flux due to waves, wave-induced momentum flux, and enhanced bottom friction. The wave-induced momentum flux is calculated using the simplified expression of Dingeman et al. (1987) based on the wave breaking dissipation. The effect of enhanced bed shear stress on the flow simulation is accounted for using the parameterizations of Soulsby et al. (1993) and Soulsby (1995). The hydrodynamics are simulated using the Generalized Lagrangian Mean (GLM)

method of Andrews and McIntyre (1978), and adapted by Groeneweg (1999), in which the Stokes drift velocity is added to the Eulerian velocity to obtain the Lagrangian velocity (prognostic model variable). In Delft3D the forcing is included using the formulation of Dingemans et al. (1987) in which wave breaking dissipation is used as a driving force. The original purpose was to avoid spurious flow patterns caused by the full radiation stress gradients as the driving force. However, as pointed out by Roelvink and Reniers (2012), modern wave models such as SWAN now produce accurate and relatively smooth radiation stress gradient fields which no longer cause spurious flow patterns. It is noted that during the preparation of this manuscript a new model called D-Flow FM (flexible mesh) is being developed and beta tested as part of the Delft3D. D-Flow FM uses semi-implicit temporal scheme and finite-difference and finite-volume spatial discretizations on flexible meshes including 1D, 2D, and 3D cells (Kernkamp et al. 2011). However, since the model is still being tested, it is not covered further here.

The Mike suite solves the depth-averaged (Mike 21) and 3D (Mike 3) hydrodynamic equations (Zyserman and Ronberg 2001, Lumborg and Windelin 2003). Mike 21 and Mike 3 also include wave radiation stress forcing, tidal potentials, ice coverage, spatially varying wind and atmospheric pressure forcing, and precipitation and evaporation. 2DH, Q3D, or 3D transport equations are used to simulate water temperature and salinity, which are then used to calculate the water density. Both nonuniform Cartesian and unstructured triangular and/or quadrilateral meshes are supported. The nonuniform Cartesian grid solver uses finite difference methods and a fractional-step Alternating Direct Implicit (ADI) algorithm (Abbott 1979). The momentum equations are in nonconservative form while the continuity equation is in conservative form.

Multiple Cartesian grids may be coupled (dynamically linked). The flexible mesh (unstructured triangular and quadrilateral grids) model uses a cell-centered finite-volume methods based on linear elements. In 2DH a first-order explicit Euler and second-order Runge-Kuttta methods are available. In the 3D flow model all horizontal terms and vertical convective fluxes are treated using a first order explicit Euler or Runge-Kutta method while the vertical diffusive fluxes are treated using a second order implicit trapezoidal rule.. The 3D model uses either sigma combined sigma or z-coordinate system in the vertical. Both Mike 21 and Mike 3 support Cartesian and spherical horizontal coordinate systems. The eddy viscosity is calculated with a Smagorinsky type formulation (Smagorinsky 1963).

XBeach solves the unsteady depth-averaged hydrodynamic equations in non-conservative form on a nonuniform Cartesian grid. The hydrodynamics are calculated using the method of Stelling and Duinmeijer (2003) on a staggered Arakawa C grid. The model uses an adaptive explicit time step based on the Courant condition and mostly first order finite-difference methods. Hydrodynamics are simulated using the GLM method similar to the Delft3D model. Bottom friction due to combined waves and currents is parameterized using the parameterization of Wright and Thompson (1983) and calibrated by Feddersen et al. (2000). Wave forcing is included through the wave and roller radiation stress gradients (Roelvink et al. 2010).

CCHE2D-Coast solves the unsteady shallow water equations in nonconservative form on a non-orthogonal curvilinear grid using the Efficient Element Method (EEM) on a collocated grid system (Wang and Hu 1992, Jia and Wang 1999, Ding and Wang 2008). The solution is advanced with an implicit projection method on a partially staggered grid (Arakawa B grid) (Jia et al. 2002). Velocities are stored at the cell nodes, and water levels at the cell centroids. The

assembled linear system of equations is solved using the Strongly Implicit Procedure of Stone (1968). The mean wave-current bottom shear stress is calculated using the formulation of Tanaka and Thu (1994). Wave forcing is included through wave radiation stresses with an additional term due to the roller following Svendsen (1984). The roller component is calculated based on the local water depth, wave height, and wave length.

The circulation model in the CMS (called CMS-Flow) computes the unsteady water level and current velocity fields by solving the depth-integrated 2DH shallow water flow equations on a non-uniform or Telescoping Cartesian grid with an explicit or implicit finite-volume scheme (Buttolph et al. 2006, Wu et al. 2011). The model can simulate tide, wind and wave driven currents, and includes the Coriolis force, wind forcing, bottom friction, and wave radiation stresses. In the explicit time-stepping scheme, primary variables are defined on a staggered Arakawa C grid. The mean wave-current bottom friction is calculated using the formula of Nishimura (1988). Further details on the explicit flow model can be found in Buttolph et al. (2006). The implicit time-stepping flow model was developed by Wu et al. (2011). The implicit solver uses the SIMPLEC algorithm on a collocated grid to handle the coupling of water level and velocity. Inter-cell fluxes are calculated using a Rhie and Chow (1983) type momentum interpolation method. The model includes wave forcing through spectrally-integrated wave radiation stress gradients. The enhanced bottom friction is calculated using a simple quadratic formula by Wu et al. (2011).

Table 2.1. Summary of hydrodynamic models in several morphodynamic models.

Hydrodynamic Model	**Governing Equations**	**Grid type**	**Solution Techniques**
CMS-Flow	2DH SWE's in conservative form	Nonuniform, and telescoping Cartesian	FVM, first-second order, explicit and fully implicit time stepping
ROMS	3D SWE's conservative form. 3D temperature and salinity transport eq.	Orthogonal curvilinear	FVM/FDM Explicit time-stepping, second-fourth order
MIKE 21 and Mike 3	Nonuniform Cartesian mesh: 2DH, 3D, SWE's in nonconservative form. Flexible mesh: 2DH, Quasi-3D, 3D, SWE's in conservative form. 2DH or 3D, temperature and salinity transport eq. in conservative form	Nonuniform Cartesian and Unstructured hybrid mesh (triangles and quadrilaterals)	First-second order. FDM for Nonuniform Cartesian grid and FVM for flexible mesh. First-and second-orer explicit and semi-implicit methods
Delft3D-Flow	2DH, Q3D, 3D, SWE's in nonconservative form	Curvilinear	FDM, implicit, ADI, second-third order
XBeach Flow model	2DH, Q3D (beta), in nonconservative form	Nonuniform Cartesian	FDM, first order in space and time, explicit time-stepping
CCHE2D-Coast	2DH or Q3D SWE's in conservative form	Non-orthogonal curvilinear	FVM, second-order, fully implicit time-stepping

2.2 Waves

In morphodynamic modeling systems, waves are generally calculated using phase-averaged models due to the prohibitive computational costs of phase-resolving models. Phase-averaged models can be grouped into wave-averaged and short-wave averaged. Shot-wave-averaged models resolve the wave characteristics at the wave group time scale (minutes), while wave-averaged models consider the wave field averaged over both individual waves and wave groups. Examples of coastal wave-averaged models are HISWA (Holthuijsen et al. 1989), SWAN (Booij et al. 1996), STWAVE (Resio 1988, Smith et al. 2001), and CMS-Wave (Lin et al. 2008, 2011a,b). SWAN is commonly used with Delft3D (referred to as Delf3D-Wave) and ROMS, since it supports curvilinear grids. SWAN can run in either stationary or non-stationary mode. Table 2.2 provides a summary of the several spectral wave models.

A fundamental limitation of spectral wave models is that they do not inherently include diffraction (Resio 1988, Booij et al. 1997). Several methods have been proposed to add the effect of diffraction in spectral wave models. STWAVE uses the approach proposed by Resio (1988) in which the wave energy is smoothed using a weighting function. CMS-Wave uses the approach developed by Mase (2001) in which a diffraction term is included in the wave action equation based on a parabolic approximation of the wave equation (see Section 3.2). The wave models SWAN and MIKE 21 SW do not include diffraction.

Most wave models used in morphodynamic models contain some form of a surface roller model. When a wave breaks, part of the momentum and mass are transferred to an aerated region called the surface roller. As the wave continues breaking, momentum and mass from the roller are then transferred below the surface to the current. This process causes a delay in transfer of

momentum and mass from waves to currents and leads to a shoreward movement of the peak alongshore current and set down. In Delft3D and XBeach surface roller is included by solving a 2DH roller energy conservation equation (Roelvink 2003, Roelvink et al. 2010). All of these models use a peak or representative wave frequency. Other models such as CCHE2D-Coast (Ding et al. 2006) include local formulation in which the roller energy is based on the local wave parameters as in Svendsen (2006).

XBeach also includes a finite-difference steady/unsteady wave-action equation solver and a surface roller solver. The surface roller flux is not included in the wave mass transport. The wave energy density and surface roller energy density are calculated using a peak or characteristic wave period. Both the wave and roller equations may be solved in stationary or non-stationary mode. The non-stationary (time-dependent) wave model can be used to simulate the propagation and dissipation of wave groups. The model includes a procedure to obtain infragravity long wave time-varying boundary conditions from short wave energy spectra (van Dongeren et al. 2003). In XBeach the wave radiation stresses are calculated by using linear wave theory and integrating over all directional bins (Roelvink et al. 2010). Delft3D also has the option to use the XBeach wave model.

The CMS-Wave spectral wave transformation solves the steady-state wave-action balance equation on a non-uniform Cartesian grid with a finite difference scheme. It considers wind wave generation and growth, diffraction, reflection, dissipation due to bottom friction, white capping and breaking, wave-wave and wave-current interactions, wave runup, wave setup, and wave transmission through structures. CMS-Wave is a half-plane model based on the assumption that waves propagate from the offshore boundary towards shore. Reflected waves are

calculated with a backward marching routine. Further information on the wave model can be found in Mase et al. (2005) and Lin et al. (2008).

In the Mike suite waves are simulated in the Mike 21 SW model, which has two formulations: fully spectral and directionally decoupled parametric formulation. The fully spectral formulation has source terms similar to those in WAM cycle 4 (Komen et al. 1994). The directionally decoupled parametric formulation solves the zero and first moment of the wave action spectrum following Holthuijsen et al. (1989). The Mike 21 SW models support unstructured triangular and quadrilateral meshes in either Cartesian or spherical coordinate systems. Mike 21 SW uses first-order finite-volume schemes for the spatial discretization.

Table 2.2. Summary of wave models in several morphodynamic models.

Wave Model	**Governing Equations**	**Grid type**	**Solution Techniques**
CMS-Wave	Steady-state wave-action conservation equation. Half-plane.	Nonuniform Cartesian	FDM. Implicit forward and backward marching. First-order upwinding
SWAN	Steady/Unsteady wave action-conservation equation. Half/full plane	Orthogonal Curvilinear	FDM. Implicit first-order Euler. First to third order spatial. Pseudo-time stepping for stationary. Iterative sweeping procedure
Mike 21 NSW	Directionally decoupled parametric wave-action equations. Half-plane	Nonuniform Cartesian	FDM, implicit forward marching
MIKE 21 SW	Full spectrum and directionally decoupled parametric wave-action equations	Unstructured hybrid mesh (triangles and quadrilaterals)	FVM. First order spatial. Fractional-step method for unstationary mode with local time step
XBeach Wave Model	Wave-action equation, half-plane, representative frequency, steady/unsteady. Short-wave-averaged	Nonuniform Cartesian	FDM. First order
CCHE2D-Coast	Half-plane, wave-action equation, steady	Non-orthogonal curvilinear	FDM. First-second order
STWAVE	Half/full plane, wave-action equation, steady	Cartesian grid	FDM. Explicit, parallel

2.3 Sediment Transport

ROMS is coupled with the 3D community sediment transport model NOPP (Warner et al. 2008). The sediment transport model uses the same computational grid as hydrodynamics and is tightly coupled. Suspended sediments are modeled using a 3D advection-diffusion equation with a source/sink term added to bottom computational cell simulating erosion and deposition. The multi-fraction approach is used to simulate multiple sediment size classes represented by their diameter, density, settling velocity, critical stress for erosion, and erodability coefficient. The bed is represented by a user-specified fixed number of layers. Cohesive sediment transport is not modeled, but the erosional flux is modeled using the formulation of Ariathurai and Arulanandan (1978) (almost identical to that of Partheniades 1965) originally intended for cohesive sediments. The depositional flux is modeled using a vertical gradient of the suspended sediment concentration times the fall velocity. A zero-diffusive flux is applied at the water surface and bed boundaries. The effect of sediment on the water-sediment mixture density is included. Bed load transport is calculated using either the Meyer-Peter and Muller (1948) formula for currents only or the Soulsby and Damgaard (2005) formula for waves plus currents. Bed load transport is corrected for the bed slope by multiplying by a correction factor following Lesser et al. (2004). The equilibrium bed load transport rates are computed at cell centers and translated to cell faces using a simple upwind approach. The bed-load flux divergence is then used to calculate the bed change at each computational grid cell. Morphologic scaling factor is available to increase the rate of bed change and can be applied for sediment size class. The bottom friction is represented by either simple drag-coefficient expressions or the wave-current boundary layer formulations of Styles and Glen (2000), Soulsby (1995), and Madsen (1994). The bottom roughness estimates

are based on Grand and Madsen (1982), Nielsen (1986), Li and Amos (2001), Wiberg and Harris (1994), and Harris and Wiberg (2001) depending on the wave-current boundary layer formulation chosen.

In Delft3D the sediment transport module has the option to enter up to five sediment size classes which are labeled as cohesive or noncohesive. Suspended sediments are solved using either 2D or 3D advection-diffusion equation. In 3D a source/sink term is applied at the first cell above a sediment concentration reference height and extrapolated upwards. For noncohesive sediments, the erosion is equal to the vertical mixing flux, and the deposition is equal to the concentration times the fall velocity. In 2D a source sink term is added based on the work of Gallappatti and Vreugdenhil (1985). In the Q3D version of Delft3D, the advective velocity is modified to include the dispersive transport (Luijendijk et al. 2010). Delf3D has 9 equilibrium sediment transport formulas: van Rijn (1993), Bijker (1971), Soulsby-van Rijn (Soulsby 1997), Soulsby (1997), Engelund and Hansen (1967), Meyer-Peter-Muller (1948), van Rijn (1984a,b), Ashida and Michiue (1972), and a general formula similar to the Meyer-Peter-Muller (1948) formula with adjustable coefficients. In 2DH an advection-diffusion equation is solved for the depth-averaged suspended sediment concentration using finite-volume methods. The bed-load is assumed to be in equilibrium and computed at the cell centers. The bed-load related bed change is calculated as the divergence of the bed-load fluxes using an upwinding scheme. The bed layering model uses a constant user specified thickness (Lesser et al. 2004).As the bed surface moves, all of the layer boundaries also move. This produces mixing of buried layers and is also slightly more computationally expensive then only adjusting the thickness of the top two or three surface layers. Sediment fall velocities are calculated using the formula of van Rijn (1993) and

reduced by hindered settling Richardson and Zaki (1954).

The XBeach sediment transport is calculated using a 2D total-load advection-diffusion equation with the source/sink term of Gallappatti and Vreugdenhil (1985) originally intended for suspended sediments only. The advection-diffusion equation is solved using an explicit finite difference method. The equilibrium total-load sediment transport rate is calculated using the Soulsby-van Rijn (Soulsby 1997) formula, with a correction for sheet flow conditions. The root-mean-squared bottom orbital velocity is calculated using the root-mean-squared wave height and the peak wave period. The equilibrium total-load sediment transport is corrected for the bed slope as originally proposed by Soulsby (1997) and adapted from Bailard (1981). The wave skewness and asymmetry are included by adding a correction velocity to the advective transport velocities (Roelvink et al. 2010). The morphology change is evaluated based on the divergence of the total-load sediment transport rates and includes a morphologic acceleration factor. The model uses a constant user-specified bottom roughness. Avalanching is included with different critical bed slope angles for wet and dry cells. The model can simulate multiple-sediment size classes and bed composition evolution. The bed layering model is similar to Delft3D in that all bed layers have a constant user specified thickness. Nonerodible surfaces are included.

The Mike suite (sand transport) is unique in that for the case of combined currents and waves it uses a Q3D approach. A 1DV intrawave hydrodynamic and sediment transport model is used to calculate potential sediment transport rates for a range of conditions and processes and build a table. The table is then used to interpolate the Q3D sediment transport rates during the simulation. Thus, in a 3D hydrodynamic simulation the vertical structure of the current velocity and turbulence are not used directly. Bed load transport is calculated using the instantaneous bed

shear stress and the transport formula of Engelund and Fredsøe (1976). The bed composition is specified through the median grain size and geometric standard deviation. The sediment transport model is called STP and is identical to the sediment transport models included in LITPACK and MIKE 21 ST. The model is described in Fredsøe (1984), Fredsøe et al. (1985), and Deigaard et al. (1986). Elfrink et al. (1996, 2000) provides a description of the Q3D flow and the sediment transport. The bed change is calculated based on the divergence of the equilibrium sediment transport rates. The bed slope effect on the sediment transport is included through an additional diffusion term similar to the approach of Watanabe (1988), except it takes into account both longitudinal and transverse bed slopes (Johnson and Zyserman 2002).

CMS Version 3.0 has two different sediment transport models (Buttolph et al. 2006). The first is a simple Exner equation with additional bed slope terms as originally proposed by Watanabe (1985). The total-load equilibrium model supports the Watanabe (1987), and Lund-CIRP (Camenen and Larson 2005, 2007, 2008) transport formulas. The second method uses a 2DH Advection-Diffusion (A-D) equation for suspended load transport, and assumes equilibrium sediment transport. The divergence of the bed load transport rates are added to the bed change equation, which includes the erosion and deposition terms from the A-D equation. The deposition and erosion terms are based on the near-bed sediment concentration and concentration capacities, respectively. The reference concentration is calculated following van Rijn (1985) or Camenen and Larson (2007, 2008). The near bed sediment concentration is calculated from the depth-averaged concentration and a conversion factor obtained by assuming a vertical concentration profile. For additional details see Buttolph et al. (2006). A summary of the sediment transport models is provided in Table 2.3.

Table 2.3. Summary of sediment transport in several morphodynamic models.

	Total Load		
Sediment Transport Model	**Suspended Load**	**Bed Load**	**Additional Details**
CMS Exner Model	2DH Exner equation. Total load based on Watanabe (1987), van Rijn (1984a,b), and Camenen and Larson (2005, 2007, 2008)		Single size. Hard bottom included
CMS A-D Suspended Equilibrium Bed load	2DH A-D equation. Deposition and erosion based on difference between potential and actual near bed concentrations times the fall velocity. Neared concentration capacity based on van Rijn (1984b) or Camenen and Larson (2007, 2008)	Equilibrium sediment transport based on van Rijn (1984a), and Camenen and Larson (2005, 2007)	Single size. Hard bottom included.
ROMS-Sed	3D A-D equation, with a source/sink term at the bottom cell. Erosional flux specified using Ariathurai and Arulanandan (1978). Multiple sediment sizes.	Equilibrium sediment transport. Meyer-Peter and Muller (1948) formula for currents only or the Soulsby and Damgaard (2005) for currents and waves	Multiple sediment sizes.
Mike STP	Quasi-3D formulation. Intrawave.	Based on instantaneous bed shear stress and transport formula of Engelund and Fredsøe (1976)	Single size. Bed gradation included through geometric standard deviation.
Delft3D	3D or 2DH A-D equation. Source and sink terms calculated assuming a linear concentration gradient between reference concentration height and the first cell above the reference concentration height.	Equilibrium transport. The divergence of the bed load transport is added to the bed change. Correction added for bed slope.	Multiple-grain sizes. Constant bed layer thickness. Hard bottom surfaces included
XBeach	2DH A-D equation with source/sink term of Gallappatti and Vreugdenhil (1985). Total-load transport capacity formula Soulsby-van Rijn (Soulsby 1997).		Multiple-grain sizes in beta. Constant bed layer thickness.
CCHE2D-Sed	2DH Exner equation with bed-slope term. Equilibrium total load transport calculated following Watanabe (1986)		

CHAPTER III

MATHEMATICAL DESCRIPTION

3.1 Hydrodynamics

3.1.1 Governing Equations

Before presenting the depth-integrated and wave-averaged hydrodynamic equations, it is useful to define the coordinate system, and basic variables. A schematic of main variables is provided in Figure 3.1. Variables are defined spatially in a Cartesian coordinate system $x_i = \vec{x} = (x, y, z)$, where x and y are the horizontal coordinates, and z is the vertical coordinate (positive is upwards). The vertical datum is usually the Still Water Level (SWL). The bed elevation z_b is measured from the vertical datum. The instantaneous and wave-averaged water surface elevation (measured from the vertical datum) are η and $\overline{\eta}$, respectively. From herein the overbar is used to denote the time averaging over a wave period of variables. The total water depth is defined as $h = \overline{\eta} - z_b$.

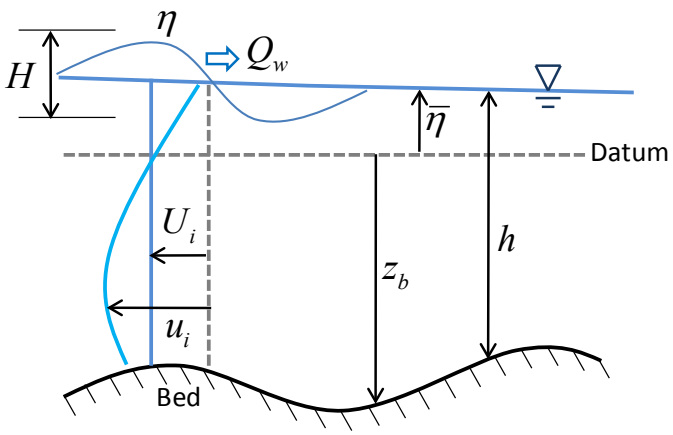

Figure 3.1. Sketch of the vertical coordinate system and variables.

The instantaneous flow velocity, $\hat{u}_i$, is separated into

$$\hat{u}_i = u_i + \tilde{u}_i + u_i' \tag{3.1}$$

in which

u_i = current (wave-averaged) velocity [m/s]

$\tilde{u}_i$ = wave (oscillatory) velocity with $\overline{\tilde{u}_i} = 0$ below the wave trough [m/s]

u_i' = turbulent fluctuation with ensemble average $\langle u_i' \rangle = 0$ [m/s]

[ ] = variable units

The wave-averaged total volume flux in the water column is

$$hV_i = \overline{\int_{z_b}^{\eta} \hat{u}_i dz} \tag{3.2}$$

in which V_i is the total flux velocity representing the total volume flux per unit width and water depth.

The wave-related volume flux is given by

$$Q_{wi} = hU_{wi} = \overline{\int_{z_b}^{\eta} \tilde{u}_i dz} \tag{3.3}$$

in which U_{wi} is a velocity representing the wave volume flux per unit width and water depth.

The current-related volume flux is given by

$$hU_i = \overline{\int_{z_b}^{\eta} u_i dz} = \int_{z_b}^{\bar{\eta}} u_i dz \tag{3.4}$$

in which U_i is by definition the depth-averaged current velocity. For convenience the overbar has been dropped from U_i .

Therefore, the total flux velocity V_i may be written as.

$$V_i = U_i + U_{wi} \tag{3.5}$$

On the basis of the above definitions, and assuming depth-uniform currents (i.e. $u_i(z) = U_i$), the depth-integrated and wave-averaged continuity and momentum equations can be written as (Phillips 1977, Svendsen 2006)

$$\frac{\partial h}{\partial t} + \frac{\partial (hV_j)}{\partial x_j} = 0 \tag{3.6}$$

$$\begin{aligned} &\frac{\partial (hV_i)}{\partial t} + \frac{\partial (hV_iV_j)}{\partial x_j} - \varepsilon_{ij} f_c hV_j = -gh\frac{\partial \bar{\eta}}{\partial x_i} - \frac{h}{\rho}\frac{\partial p_a}{\partial x_i} \\ &+ \frac{\partial}{\partial x_j}\left(\nu_t h \frac{\partial V_i}{\partial x_j}\right) - \frac{1}{\rho}\frac{\partial}{\partial x_j}\left(S_{ij} + R_{ij} - \rho h U_{wi}U_{wj}\right) + \frac{\tau_{si}}{\rho} - m_b\frac{\tau_{bi}}{\rho} \end{aligned} \tag{3.7}$$

where

t = time [s]

f_c = Coriolis parameter [rad/s]. $f_c = 2\Omega \sin\phi$ where Ω= 7.29×10^{-5} rad/s is the earth's angular velocity of rotation and ϕ is the latitude in degrees.

$$\varepsilon_{ij} = \begin{cases} 1 & \text{for } i=1, j=2 \\ -1 & \text{for } i=2, j=1 \\ 0 & \text{otherwise} \end{cases}$$

ρ = sea water density (~1025 kg/m^3)

g = gravitational constant (~9.81 m/s^2)

p_a = atmospheric pressure [Pa]

ν_t = horizontal turbulent eddy viscosity (described in Section 3.1.2) [m^2/s]

τ_{bi} = wave-averaged bed shear stress (described in Section 3.1.3) [Pa]

m_b = bed slope coefficient (described in Section 3.1.3) [-]

τ_{si} = surface shear stress due to wind forcing (described in Section 3.1.4) [Pa]

S_{ij} = wave radiation stress (described in Section 3.2.5) [Pa m]

R_{ij} = roller stress (described in Section 3.3.2) [Pa m]

The first term on the left-hand side of Equation (3.7) represents the local acceleration. The second term is the horizontal advection. The third term is the Coriolis-Stokes force term. The first term on the righ-hand side is the water level gradient forcing. The second term is the atmospheric pressure forcing. The third term on the right-hand side represents the horizontal turbulent mixing. The term $\partial(hU_{wi}U_{wj})/\partial x_j$ represents a wave momentum transport and is often ignored in coastal hydrodynamic models. In some cases such as Phillips (1977) and Svendsen

(2006) it is included in the wave radiation stresses.

The above hydrodynamic equations are similar to those derived by Svendsen (2006), except for the inclusion of the water source/sink term in the continuity equation, as well as the atmospheric pressure and surface roller terms, and bed slope coefficient in the momentum equation. It is also noted that the horizontal mixing term is formulated differently as a function of the total flux velocity, similar to the Generalized Lagrangian Mean (GLM) approach (Andrews and McIntyre 1978, Walstra et al. 2000). Arguably, this approach is physically more meaningful and also simplifies the discretization in the case where the total flux velocity is used as the model prognostic variable.

3.1.2 Eddy Viscosity

The term eddy viscosity arises from the fact that small-scale vortices or eddies on the order of the grid cell size are not resolved and only the large-scale flow (relative to the grid size) is simulated by a numerical model. The eddy viscosity is intended to simulate the dissipation of energy at scales smaller than the model can simulate. In the nearshore environment, intense mixing or turbulence occurs due to waves, wind, bottom shear, and strong horizontal gradients; therefore, the eddy viscosity is an important aspect which can have a large influence on the calculated flow field and resulting sediment transport. The depth-averaged total eddy viscosity, ν_t , is equal to the sum of three parts: (1) a base or background value ν_0, (2) the current-related eddy viscosity ν_c, and (3) the wave-related eddy viscosity ν_w :

$$\nu_t = \nu_0 + \nu_c + \nu_w \tag{3.8}$$

The base value, ν_0, is approximately equal to the kinematic viscosity (~1×10^{-6} m^2/s). The

other two components (ν_c and ν_w) are described below.

3.1.2.1 Current-Related Eddy Viscosity Component

Two algebraic turbulence models are presented to determine the depth-averaged current-related eddy viscosity: (1) subgrid and (2) mixing-length. Unless specified otherwise the default turbulence model is the subgrid model.

3.1.2.1.1 Subgrid Model

The standard subgrid model (Smagorinsky 1963) is modified to include a contribution due to the turbulence produced by the vertical shear (Wu et al. 2004). The modified subgrid turbulence model calculates the current-related eddy viscosity, ν_c, as

$$\nu_c = c_v u_{*c} h + (c_h \Delta)^2 \left|\overline{S}\right| \tag{3.9}$$

in which

c_v = vertical coefficient [-]

u_{*c} = current-related bed shear velocity (Equation 3.13) [m/s]

c_h = horizontal coefficient [-]

Δ = (average) grid size [m]

$\left|\overline{S}\right| = \sqrt{2e_{ij}e_{ij}}$ = magnitude of the deformation (strain rate) tensor e_{ij} [1/s]

$e_{ij} = \frac{1}{2}\left(\frac{\partial V_i}{\partial x_j} + \frac{\partial V_j}{\partial x_i}\right)$ = deformation (strain rate) tensor

The parameter c_v is approximately equal to κ/6 = 0.0667 (default) but may vary from 0.01 to 0.2. The variable c_h is approximately equal to the Smagorinsky coefficient (Smagorinsky 1963) and may vary between 0.1 and 0.3 (default is 0.2).

3.1.2.1.2 Mixing Length Model

The mixing length model implemented for the current-related eddy viscosity includes components due to the vertical and horizontal shear, given by (Wu et al. 2004)

$$\nu_c = \sqrt{\left(c_v u_{*c} h\right)^2 + \left(l_h^2 \left|\overline{S}\right|\right)^2} \tag{3.10}$$

where

l_h = mixing length ($= \kappa \min(c_m h, y')$) [m]

y' = distance to the nearest wall [m]

c_m = coefficient for mixing length [-]

The empirical coefficient c_h is usually between 0.3 and 1.2. The effects of bed shear and horizontal velocity gradients, respectively, are taken into account through the first and second terms on the right-hand side of Equation (3.10). It has been found that the modified mixing length model is better than the depth-averaged parabolic eddy viscosity model that accounts for only the bed shear effect (Wu et al. 2004).

3.1.2.2 Wave-Related Eddy Viscosity

The wave component of the eddy viscosity is separated into two components (Larson and

Kraus 1991):

$$\nu_w = c_{wf} u_{ws} H_s + c_{br} h \left(\frac{D_{br}}{\rho} \right)^{1/3} \tag{3.11}$$

where

c_{wf} = coefficient for the wave bottom friction contribution to the eddy viscosity [-]

c_{br} = coefficient for the wave breaking contribution to the eddy viscosity [-]

D_{br} = wave breaking dissipation [N/m/s]

The first term on the right-hand side of Equation (3.11) represents the component due to wave bottom friction (Larson and Kraus 1991). The second term represents the component due to wave breaking. The coefficient c_{wf} is approximately equal to 0.1 and may vary from 0.05 to 0.2. The coefficient c_{br} is approximately equal to 0.08 and may vary from 0.04 to 0.15.

3.1.3 Bed Shear Stress

The current-related shear stress is calculated using the quadratic law

$$\tau_{ci} = \rho c_b U U_i \tag{3.12}$$

where c_b is the dimensionless bed friction or drag coefficient. The current-related bed shear velocity is given by

$$u_{*c} = \sqrt{\tau_c / \rho} = \sqrt{c_b} U \tag{3.13}$$

where τ_c is the magnitude of the current related bed shear stress.

The bed friction coefficient can either be specified or calculated from the Manning's

roughness coefficient n, or Nikuradse roughness height k_s. It is important to note that the bed roughness parameter for hydrodynamics is assumed constant in time and unchanged according to bed composition and bed forms. This is a common engineering approach which can be justified by the lack of data to initialize the bed composition, and the large error in estimating the bed forms. In addition using a constant bottom roughness simplifies the calibration of hydrodynamics.

The bed friction coefficient, c_b, is related to the Manning's roughness coefficient n by (Graf and Altinakar 1998)

$$c_b = gn^2 h^{-1/3} \tag{3.14}$$

The bed friction coefficient is also calculated by assuming a logarithmic velocity profile as (Soulsby 1997)

$$c_b = \left[\frac{\kappa}{\ln(h / z_0) - 1} \right]^2 \tag{3.15}$$

where $\kappa = 0.4$ is the von Karman constant and z_0 is the bed roughness length which is related to the Nikuradse roughness, k_s, by $z_0 = k_s / 30$ (for hydraulically rough flow).

If waves are not present, then the bed shear stress is equal to current-related bed shear stress (i.e. $\tau_{bi} = \tau_{ci}$). Under combined waves and currents, the mean (wave-averaged) and maximum bed shear stresses are enhanced compared to the case of currents only. This enhancement of the bed shear stress is due to the nonlinear interaction between waves and currents in the bottom boundary layer. There are many formulations for the mean (short-wave averaged) bed shear stress, τ_{bi}. Wu et al. (2010) presented a simple quadratic formula (referred

to as QUAD from herein):

$$\tau_{bi} = \rho c_b U_i \sqrt{U^2 + c_w u_w^2} \tag{3.16}$$

where c_b is the bed friction coefficient from Equations (3.14) or (3.15), c_w is an empirical coefficient, and u_w is a representative bottom wave orbital velocity magnitude. For random waves $u_w = u_{ws}$ where u_{ws} is the bottom wave orbital velocity amplitude calculated based on the significant wave height and peak wave period (see Section 3.2). Wu et al. (2010) originally proposed setting c_w = 0.5 with $u_w = u_{ws}$. Here the coefficient c_w has been calibrated equal to 1.33 for regular waves and 0.65 for random waves to better agree with the two-parameter data-based method of Soulsby (1997). A formula similar to Equation (3.16) was independently proposed by Wright and Thompson (1983) and calibrated using field measurements by Feddersen et al. (2000). The main difference in the two formulations is that Wu et al. (2010) uses the bottom wave orbital velocity based on the significant wave height, while the Wright and Thompson (1983) formulation uses the standard deviation of the bottom orbital velocity.

In the presence of a sloping bed, the bottom friction acts on a larger surface area for the same horizontal area. This increase in bottom friction is included through the coefficient m_b in Equation (3.7) which is given as (Mei 1989, Wu 2007)

$$m_b = |\nabla z_b| = \sqrt{\left(\frac{\partial z_b}{\partial x}\right)^2 + \left(\frac{\partial z_b}{\partial y}\right)^2 + 1} \tag{3.17}$$

where z_b is the bed elevation, and $\nabla = \left(\frac{\partial}{\partial x}, \frac{\partial}{\partial y}, 1\right)$. For bottom slopes of 1/5 and 1/3, the above expression leads to an increase in bottom friction of 2.0% and 5.4%, respectively. In most

morphodynamic models, the bottom slope is assumed to be small and m_b is neglected. However, it is included here for completeness.

3.1.4 Surface Shear Stress

The surface shear stress is calculated as

$$\tau_{si} = \rho_a C_D W W_i \tag{3.18}$$

where

ρ_a = air density at sea level [~1.2 kg/m^3]

C_D = wind drag coefficient [-]

W_i = wind velocity at 10 m above sea level [m/s]

$W_i = W_i^E - \gamma_W U_i$

$$\gamma_W = \begin{cases} 0 \text{ for Eulerian reference frame} \\ 1 \text{ for Lagrangian reference frame} \end{cases}$$

$W = \sqrt{W_i W_i}$ [m/s]

W_i^E = wind velocity measured at 10 m above sea level relative to the solid earth (Eulerian wind velocity) [m/s]

$W_i^L = W_i^E - U_i$ = Lagrangian wind velocity relative to the current velocity [m/s]

Using the Lagrangian reference frame or relative wind speed is more accurate and realistic for field applications (Bye 1985, Pacanowski 1987, Dawe and Thompson 2006), but the option to use the Eulerian wind speed is provided for idealized cases. The difference between the

Lagrangian and Eulerian reference frames is larger for lower wind speeds. As an example, for a current velocity of 1 m/s, with an opposing wind speed of 5 m/s, the Eulerian reference frame will give a surface stress proportional to $(5\ \text{m/s})^2 = 25\ \text{m}^2/\text{s}^2$, while the Lagrangian reference frame will produce a surface stress proportional to $(5\text{-}(-1)\ \text{m/s})^2 = 36\ \text{m}^2/\text{s}^2$, which is an increase of 44%. The same 5-m/s wind with a 1-m/s current in the same direction will produce a Lagrangian surface stress proportional to $(5\text{-}1\ \text{m/s})^2 = 16\ \text{m}^2/\text{s}^2$ which is a 36% decrease with respect to the Eulerian reference frame.

The drag coefficient is calculated using the formula of Hsu (1988) and modified for high wind speeds based on field data by Powell et al. (2003) (see Figure 3.2)

$$C_D = \begin{cases} \left(\dfrac{\kappa}{14.56 - 2\ln W}\right)^2 & \text{for } W \le 30\,\text{m/s} \\ 10^{-3}\max(3.86 - 0.04W, 1.5) & \text{for } W > 30\,\text{m/s} \end{cases} \tag{3.19}$$

Powell et al. (2003) speculate that the reason for the decrease in drag coefficient with higher wind speeds is due to increasing foam coverage leading to the formation of a "slip" surface at the air-sea interface.

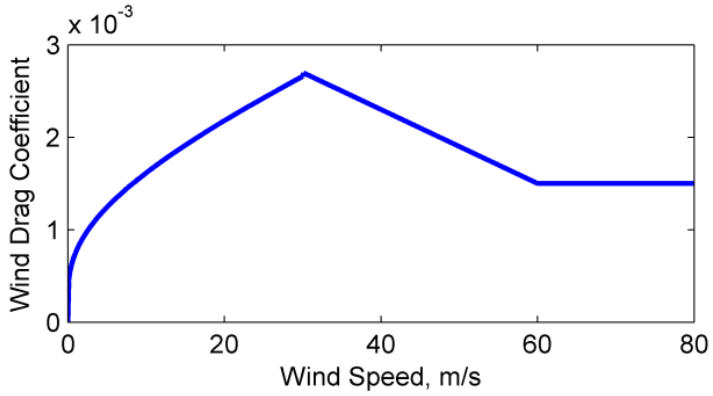

Figure 3.2. Modified Hsu (1988) wind drag coefficient.

Wind measurements taken at heights other than 10 m are converted to 10-m wind speeds using the 1/7 rule (SPM 1984, CEM 2002)

$$W_i = W_i^z \left(\frac{10}{z} \right)^{1/7} \tag{3.20}$$

where z is the elevation above the sea surface of the wind measurement and W_i^z is the wind velocity at height z.

3.1.5 Boundary Conditions

3.1.5.1 Wall Boundary Condition

At wall (closed) boundaries, zero flow is applied in the direction normal to the boundary. Two boundary conditions are available for the tangential flow parallel to the wall boundary. The first one is a free-slip boundary condition in which the tangential shear stress is set to zero, and the second one is a partial-slip boundary condition in which a wall friction term is included in the momentum equation by assuming a log-law for a rough wall:

$$\tau_{wall} = \rho c_{wall} U_{\parallel}^2 \tag{3.21}$$

where $U_{\parallel}$ is the magnitude of the wall parallel current velocity and c_{wall} is the wall friction coefficient equal to

$$c_{wall} = \left[\frac{\kappa}{\ln(y_P / y_0)} \right]^2 \tag{3.22}$$

where y_0 is the roughness length of the wall, and y_P is the distance from the wall to the near-

wall cell center. The cell-face parallel current velocity is calculated as $\vec{U}_{\parallel} = \vec{U} - (\vec{U} \cdot \vec{n})\vec{n}$, where $\vec{n}$ is the unit vector normal to the wall boundary (Ferziger and Peric 1997).

3.1.5.2 Flux Boundary Condition

The flux boundary condition is typically applied to the upstream end of a river or stream and is specified as either a constant or time-series of total water volume flux across the boundary. In a 2DH model, the total volume flux needs to be distributed across the boundary in order to estimate the depth-averaged velocities. This is done using a conveyance approach in which the current velocity is assumed to be a function of the local flow depth $\boldsymbol{h}$ and Manning's n (i.e. $U \propto h^r / n$). Here, r is an empirical coefficient, which is equal to approximately 2/3 based on the Manning equation, but can be adjusted to each case. The smaller the r, value the more uniform the current velocities are across the flux boundary. The current velocity, $\vec{U}_B$, at each boundary cell *i* is calculated as

$$\vec{U}_B = \frac{f_{Ramp} Q}{\left| \sum_B (\hat{e} \cdot \hat{n})_B \frac{h_B^{r+1}}{n_B} \Delta l_B \right|} \frac{h_B^r}{n_B} \hat{e}_B \tag{3.23}$$

where

$\vec{U}_B$ = current velocity at boundary cell *B* [m/s]

Q = total volume flux across the boundary [m^3/s]

$\hat{e}$ = unit vector for inflow direction $= (\sin\varphi, \cos\varphi)$

φ = inflow direction angle measured clockwise from the north [deg]

$\hat{\boldsymbol{n}}$ = boundary face unit vector (positive outward)

n = Manning's coefficient [s/m$^{1/3}$]

r = empirical constant [-]

f_{Ramp} = ramp function (see Section 4.9) [-]

The total volume flux is positive into the computational domain. Since it is not always possible to orient all flux boundaries to be normal to the inflow direction, an option is given to specify an inflow direction angle φ. The angle is specified in degrees clockwise from the true north. If the angle is not specified, then the inflow angle is assumed to be normal to the boundary. The total volume flux is conserved independently of the inflow direction.

3.1.5.3 Water Level Boundary Condition

The general formula for the boundary water surface elevation is given by

$$\overline{\eta}_B = f_{Ramp}(\overline{\eta}_E + \Delta\overline{\eta} + \overline{\eta}_C + \overline{\eta}_G) + (1 - f_{Ramp})\overline{\eta}_0 \tag{3.24}$$

where

$\overline{\eta}_B$ = boundary water surface elevation [m]

$\overline{\eta}_E$ = external boundary water surface elevation [m]

$\Delta\overline{\eta}$ = water surface elevation offset [m]

$\overline{\eta}_0$ = initial boundary water surface elevation [m]

$\overline{\eta}_C$ = correction to the boundary water surface elevation which is a function of the wind and wave forcing [m]

$\overline{\eta}_G$ = water surface elevation component derived from user specified gradients [m]

f_{Ramp} = ramp function (see Section 4.9) [-]

The external water surface elevation $\overline{\eta}_E$ may be specified as a time series, both spatially constant and varying or calculated from tidal constituents. If tidal constituents are specified then $\overline{\eta}_E$ is calculated as

$$\overline{\eta}_E = \sum f_i A_i \cos\left(\omega_i t + V_i^0 + \hat{u}_i - \kappa_i\right) \tag{3.25}$$

where

i = subscript indicating a tidal constituent

A_i = mean tidal amplitude [m]

f_i = node (nodal) factor [-]

ω_i = tidal frequency [deg/hr]

t = elapsed time from midnight of the starting year [hrs]

$V_i^0 + \hat{u}_i$ = equilibrium phase [deg]

κ_i = phase lag or epoch [deg]

The nodal factor is a time-varying correction to the mean amplitude. The equilibrium phase has a uniform component V_i^0 and a relatively smaller periodic component. The zero-superscript of V_i^0 indicates that the constituent phase is at time zero. The tidal amplitudes and phases may be specified as constant or variable along the boundary. Table 3.1 below provides a list of tidal constituents included. More information on U.S. tidal constituent values can be

obtained from U.S. National Oceanographic and Atmospheric Administration (http://tidesonline.nos.noaa.gov) and National Ocean Service (http://co-ops.nos.noaa.gov).

Table 3.1. Tidal Constituents names and speeds in solar hours.

Constituent	**Speed**	**Constituent**	**Speed**	**Constituent**	**Speed**
SA	0.041067	SSA	0.082137	MM	0.54438
MF	1.098	2Q1	12.8543	Q1	13.3987
O1	13.943	M1	14.4967	P1	14.9589
K1	15.0411	J1	15.5854	OO1	16.1391
MU2	27.9682	N2	28.4397	NU2	28.5126
LDA2	29.4556	L2	29.5285	T2	29.9589
R2	30.0411	K2	30.0821	2SM2	31.0159
M3	43.4762	MK3	44.0252	MN4	57.4238
MS4	58.9841	S4	60.0	M6	86.9523
M8	115.9364	2N2	27.8954	M4	57.9682
MSF	1.0159	M2	28.9841	S6	90.0
RHO1	13.4715	S2	30.0		
S1	15.0	2MK	42.9271		

The water surface elevation offset $\Delta\overline{\eta}$ is assumed spatially and temporally constant and may be used to correct the boundary water surface elevation for vertical datums, and sea level rise. The component $\overline{\eta}_G$ is intended to represent regional gradients in the water surface elevation, is assumed to be constant in time, and is only applicable when $\overline{\eta}_E$ is spatially constant. When applying a water level boundary condition to the nearshore, local flow reversals and boundary problems may result if the wave-and wind-induced setup are not included. This problem is avoided by adding a correction $\overline{\eta}_C$ to the local water level to account for the wind and wave

setup by solving for $\overline{\eta}_C$ from

$$\rho g h_B \frac{\partial(\overline{\eta}_E + \Delta\overline{\eta} + \overline{\eta}_G + \overline{\eta}_C)}{\partial x} = \tau_{Wx} + \tau_{sx} - m_b \tau_{bx} \tag{3.26}$$

where h_B is the boundary total water depth, τ_{sx}, τ_{Wx}, and τ_{bx} are the wind, wave, and bottom stresses in the boundary direction *x*. The wave forcing term is equal to

$$\tau_{Wi} = -\frac{\partial}{\partial x_j}\left(S_{ij} + R_{ij} - \rho h U_{wi} U_{wj}\right) \tag{3.27}$$

The water level correction, $\overline{\eta}_C$, is only applicable when $\overline{\eta}_E$ is spatially constant as in the case of a single time-series of water surface elevation.

3.1.5.4 Cross-shore Boundary Condition

In the implicit flow solver, a cross-shore boundary condition is applied by solving the 1-D cross-shore momentum equation including wave and wind forcing (Wu et al. 2010, 2011). Along a cross-shore boundary, it is assumed that a well-developed longshore current exists. Thus, the alongshore (*y*-direction) momentum equation reduces to

$$\frac{\partial}{\partial x}\left(\rho \nu_t h \frac{\partial V_y}{\partial x}\right) = \tau_{Wy} + \tau_{sy} - m_b \tau_{by} \tag{3.28}$$

The equation above is solved iteratively for the longshore current velocity. The cross-shore (*x*) component of the velocity is assigned a zero-gradient boundary condition. The water level due to waves and wind at the cross-shore boundary can be determined by assuming a zero alongshore gradient of flow velocity and negligible cross-shore current velocity. For this case, the cross-shore momentum equation reduces to

$$\rho g h \frac{\partial \overline{\eta}}{\partial x} = \tau_{Wx} + \tau_{sx} - m_b \tau_{bx} \tag{3.29}$$

In the surf zone, the Coriolis and atmospheric pressure gradient terms are relatively small and may be neglected.

3.2 Waves

3.2.1 Spectral Wave Action Balance Equation

As mentioned previously, the spectral wave model used in this study is CMS-Wave (Lin et al. 2008). The wave model is largely based on the work of Mase (2001) and Mase et al. (2005). The governing equation is the steady-state wave-action balance equation (Mase 2001)

$$\frac{\partial (c_x N)}{\partial x} + \frac{\partial (c_y N)}{\partial y} + \frac{\partial (c_\theta N)}{\partial \theta} = \frac{K}{2\sigma}\left[\frac{\partial}{\partial y}\left(cc_g \cos^2\theta \frac{\partial N}{\partial y}\right) - \frac{cc_g}{2}\cos^2\theta \frac{\partial^2 N}{\partial y^2}\right] - \varepsilon_b N - S \tag{3.30}$$

where

$N = \dfrac{E(f,\theta)}{\sigma}$ = wave-action density [N·s/m]

$E(f,\theta)$ = wave energy density [N/m]

θ = wave direction [rad]

$f = 2\pi / \omega$ = wave frequency [1/s]

ω = absolute angular frequency [rad/s]

$\sigma = \omega - \vec{k} \cdot \vec{U}$ = relative angular frequency [rad/s]

$\vec{k} \cdot \vec{U}$ = Doppler-shifting term [rad/s]

$\vec{k} = k\vec{w}$ = wave number vector [rad/m]

$\vec{w} = (\cos\theta, \sin\theta)$ = wave unit vector [-]

c = wave celerity [m/s]

c_g = wave group velocity [m/s]

c_x, c_y, and c_θ = characteristic velocities with respect to x, y, and, θ respectively

K = empirical parameter representing the diffraction intensity

ε_b = wave breaking energy dissipation coefficient

$S = S = S_{in} + S_{ds} + S_{nl}$ = source/sink term

S_{in} = source term due to wind generation

S_{ds} = sink term to due bottom friction, white capping, etc

S_{nl} = nonlinear wave-wave interaction term

In the presence of currents, the wave-action density is conserved, whereas the wave density is not (Whitham 1974). The first term on the right-hand side is the wave diffraction term formulated from a parabolic approximation wave theory (Mase 2001). The characteristic velocities c_x, c_y, and c_θ in Equation (3.30) are expressed as:

$$c_x = c_g \cos\theta + U \tag{3.31}$$

$$c_y = c_g \sin\theta + V \tag{3.32}$$

$$\begin{aligned} c_\theta = {} & \frac{\sigma}{\sinh 2kh}\left(\sin\theta\frac{\partial h}{\partial x} - \cos\theta\frac{\partial h}{\partial y}\right) \\ & + \cos\theta\sin\theta\frac{\partial U}{\partial x} - \cos^2\theta\frac{\partial U}{\partial y} + \sin^2\theta\frac{\partial V}{\partial x} - \sin\theta\cos\theta\frac{\partial V}{\partial y} \end{aligned} \tag{3.33}$$

The wave number is determined using the dispersion relation (Jonsson 1990)

$$\sigma^2 = gk\tanh(kh) \tag{3.34}$$

The dispersion relation is solved using the Newton-Raphson method. For further details on wave model including wave blocking, refection, breaking, whitecapping, and nonlinear interaction terms the reader is referred to Lin et al. (2008).

3.2.2 Spectral Wave Parameters

The significant (zero-moment) wave height, H_s, is related to the wave energy by

$$H_s = 4\sqrt{\frac{E_w}{\rho g}} \tag{3.35}$$

in which E_w is the total wave energy

$$E_w = \iint E(f,\theta)df\,d\theta \tag{3.36}$$

Assuming a Rayleigh distribution for the wave heights, the root-mean-squared wave height is related to the significant wave height by

$$H_{rms} = H_s / \sqrt{2} \tag{3.37}$$

The peak wave period T_p is defined as the wave period of the frequency band where the wave energy is highest. The mean wave direction is defined as

$$\theta_m = \arctan(Y_m, X_m) \tag{3.38}$$

where

$$X_m = \frac{\int \cos\theta \left(\int E(f,\theta)df \right) d\theta}{E_w}, \qquad Y_m = \frac{\int \sin\theta \left(\int E(f,\theta)df \right) d\theta}{E_w}$$

3.2.3 Wave-Related Bed Shear Stresses

The wave-related bed shear stress amplitude is given by (Johnson 1966)

$$\tau_w = \frac{1}{2}\rho f_w u_w^2 \tag{3.39}$$

where f_w is the wave friction factor. The wave-related bed shear velocity is given by

$$u_{*w} = \sqrt{\tau_w / \rho} \tag{3.40}$$

Several formulas have been proposed to estimate the wave friction factor. The formulas used here are:

$$f_w = \exp\left(5.5r^{-0.2} - 6.3\right) \quad \text{(Nielsen 1992)} \tag{3.41}$$

$$f_w = \begin{cases} \exp\left(5.21r^{-0.19} - 6.0\right) & \text{for } r > 1.57 \\ 0.3 & \text{for } r \le 1.57 \end{cases} \quad \text{(Swart 1974)} \tag{3.42}$$

in which

$r = A_w / k_s$ = relative roughness [-]

k_s = Nikuradse roughness [m]

$A_w = u_w T / (2\pi)$ = semi-orbital excursion [m]

u_w = equivalent or representative bottom orbital velocity amplitude [m/s]

3.2.4 Wave Orbital Velocities

The bottom wave orbital velocity amplitude for regular waves, u_w, is calculated based on linear wave theory as

$$u_w = \frac{\pi H}{T \sinh(kh)} \tag{3.43}$$

where H, T, and k are the wave height, period, and number, respectively. Unless specified otherwise, for random waves u_w is set to an equivalent or representative bottom orbital velocity amplitude equal to $u_w = \sqrt{2} u_{rms}$, where u_{rms} is the root-mean-squared bottom wave orbital velocity amplitude defined here following Soulsby (1987, 1997)

$$u_{rms}^2 = \text{var}(\tilde{u}_b) = \int_0^\infty S_u(f) df \tag{3.44}$$

where

var( ) = variance function

$\tilde{u}_b$ = instantaneous bottom orbital velocity [m/s]

S_u = wave orbital velocity spectrum density [s m^2/s^2]

It is noted that the definition of u_{rms} is slightly different from others such as Madsen (1994), Myrhaug et al. (2001), and Wiberg and Sherwood (2008) which include factor of 2 in their definition. Wiberg and Sherwood (2008) reported that u_{rms} estimates based on H_{rms} and T_p agree reasonably well with field measurements (except for T_p < 8.8 s) and produces better estimates than other combinations with H_{rms}, H_s, T_p and the zero-crossing wave period T_z. A better approach is to assume a spectral shape (e.g. JONSWAP, Pierson-Moskowitz, etc.), and obtain an explicit curve for u_{rms} by summing the contributions from each frequency (Soulsby 1987, Wiberg and Sherwood 2008). An explicit expression is provided below based on the

JONSWAP spectrum following the work of Soulsby (1987)

$$u_{rms} = 0.134 \frac{H_s}{T_n} \left[1 + \tanh\left(-7.76 \frac{T_n}{T_P} + 1.34 \right) \right] \tag{3.45}$$

where $T_n = \sqrt{h/g}$. The above expression agrees closely with the curves presented by Soulsby (1987, 1997).

In some cases the bottom wave orbital velocity amplitude is calculated based on the significant wave height and peak wave period, u_{ws}, as

$$u_{ws} = \frac{\pi H_s}{T_p \sinh(kh)} \tag{3.46}$$

in which the wave number is calculated based on the peak wave period.

3.2.5 Wave Radiation Stress

Surface gravity waves produce a depth-integrated and phase-averaged excess momentum flux, which is referred to as radiation stress (in analogy to radiation pressure in electromagnetics) (Longuet-Higgins and Stewart 1961). Spatial gradients of the excess momentum flux (radiation stress) then exert a force on the mean (wave-averaged) flow. The wave radiation stress tensor, S_{ij}, is approximated using linear wave theory as (Phillips 1977, Dean and Dalrymple 1991, Mei 1989, Svendsen 2006)

$$S_{ij} = \iint E(f,\theta) \left[n_g w_i w_j + \delta_{ij} \left(n_g - \frac{1}{2} \right) \right] df\, d\theta \tag{3.47}$$

where

$$\delta_{ij} = \begin{cases} 1 & \text{for } i = j \\ 0 & \text{for } i \neq j \end{cases}$$

$$n_g = \frac{c_g}{c} = \frac{kh}{\sinh 2kh} + \frac{1}{2}$$

Although only accurate to second order, the wave radiation stress based on linear wave theory is a good approximation even in the surf zone (Svendsen 2006).

3.2.6 Wave Flux Velocity

In the presence of waves, the oscillatory wave motion produces a net time-averaged mass (volume) transport referred to as Stokes drift. In the surfzone, the surface roller also provides a contribution to the mean wave mass flux. The wave flux velocity, U_{wi}, is defined as the mean wave volume flux divided by the local water depth and is approximated here as (Phillips 1977, Ruessink et al. 2001, Svendsen 2006)

$$U_{wi} = \frac{Q_{wi}}{h} = \frac{(E_w + 2E_{sr})w_i}{\rho hc} \tag{3.48}$$

where

E_w = total wave energy (Equation 3.36) [N/m]

Q_{wi} = wave volume flux per unit width [m^2/s]

E_{sr} = surface roller energy density (see Section 3.3)[N/m]

$w_i = (\cos\theta_m, \sin\theta_m)$ = wave unit vector for mean direction [-]

θ_m = mean wave direction (Equation 3.38) [rad]

c = wave speed [m/s]

The first component of the wave flux velocity is the Stokes velocity, while the second component is due to the surface roller and is only present in the surfzone. It is noted that because the Stokes velocity is calculated using linear wave theory, it is expected to over predict the wave mass transport in the surf zone (Svendsen 2006). For this reason, the surface roller component is often ignored in order to compensate for the over estimation of the Stokes component (e.g. Roelvink et al. 2010).

3.3 Surface Roller

3.3.1 Surface Roller Energy Equation

As a wave transitions from non-breaking to fully-breaking, some of the energy is converted into momentum that goes into the aerated region of the water column. This phenomenon is known as the surface roller. Under the assumption that the surface roller moves in the mean wave direction, the evolution and dissipation of the surface roller energy is calculated by a steady-state energy balance equation (Stive and de Vriend 1994, Ruessink et al. 2001)

$$\frac{\partial(2E_{sr}cw_j)}{\partial x_j} = -D_{sr} + f_e D_{br} \tag{3.49}$$

where

E_{sr} = surface roller energy density [N/m]

$c = \sqrt{gh}$ = roller propagation speed magnitude [m/s]

$w_j = (\cos\theta_m, \sin\theta_m)$ is the wave unit vector [-]

θ_m = mean wave direction (Equation 3.38) [deg]

D_{sr} = roller energy dissipation (Equation 3.50) [N/m/s]

f_e = efficiency factor for wave breaking energy transfer to roller [-]

D_{br} = wave breaking dissipation (from the wave model) [N/m/s]

The efficiency factor, f_e, is introduced so that only a portion (f_e) of the wave breaking energy is transferred into the roller, while the other portion ($1-f_e$) is transferred directly to the flow. A similar parameter was introduced by Tajima and Madsen (2006). The exact estimation of this parameter is difficult but is expected to be a function of the breaker type. Here it is taken as a calibration parameter with a default value of 1.0. The surface roller dissipation is approximated as

$$D_{sr} = \frac{g 2 E_{sr} \beta_D}{c} \tag{3.50}$$

where β_D is the surface roller dissipation coefficient approximately equal to 0.05-0.1.

3.3.2 Surface Roller Radiation Stresses

The surface roller contribution to the wave stresses, R_{ij}, is given by

$$R_{ij} = 2 E_{sr} w_i w_j \tag{3.51}$$

One effect of surface rollers is to move the peak alongshore current velocity closer to shore. The influence of the surface roller on the mean water surface elevation is usually relatively minor (Sánchez et al. 2011a).

3.4 Sediment Transport

3.4.1 Non-equilibrium Total-Load Transport

The moving sediment (total load) in the water column is traditionally divided to suspended load and bed load according to the transport mode, or bed-material load and wash load according to the sediment source. The bed load moves by rolling, sliding and saltating in a thin layer of a few particle sizes above the bed, whereas the suspended load is transported by the turbulent flow in the water column above the bed-load layer (see Figure 3.3). The wash load is defined as the sediment load which does not contribute appreciably to the bed morphology, whereas the bed-material load appreciably contributes to the bed morphology (Einstein 1950). In the coastal environment, the wash load is usually negligible and the bed-material load may be considered as the total load. The bed-material or total load is the sum of the suspended and bed loads. The sediment transport is also usually separated into current- and wave-related components. The transport due to currents includes the stirring effect of waves; and the wave-related transport includes the transport due to asymmetric oscillatory wave motion as well as contributions by Stokes drift, surface roller, and bottom boundary layer streaming. In this study, the current-related bed-load and suspended-load transports are combined into a single total-load transport equation, thus reducing the computational costs and simplifying the bed change computation.

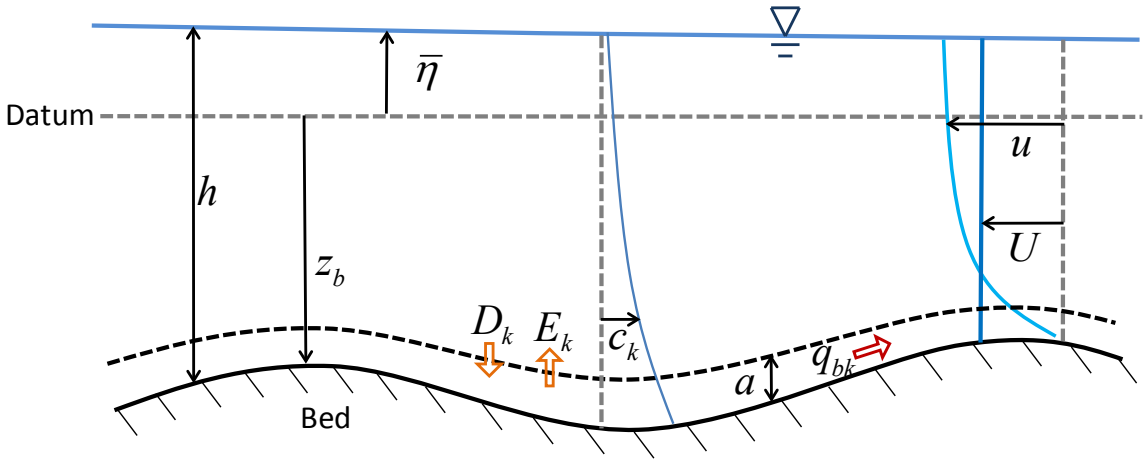

Figure 3.3. Sediment transport configuration.

The derivation of the total-load transport equation begins by first integrating the 3D sediment transport equation over the suspended-load layer and yields the advection-diffusion (A-D) equation for suspended load in tensor notation (Wu et al. 2006):

$$\frac{\partial}{\partial t}\left(\int_{z_b+a}^{\bar{\eta}} c_k dz\right)+\frac{\partial}{\partial x_j}\left(\int_{z_b+a}^{\bar{\eta}} u_j c_k dz\right)=\frac{\partial}{\partial x_j}\left(\nu_s \int_{z_b+a}^{\bar{\eta}} \frac{\partial c_k}{\partial x_j} dz\right)+E_k-D_k \tag{3.52}$$

for $j=1,2;\ k=1,2,...,N$, where N is the number of sediment size classes and

$u_j(z)$ = current velocity [m/s]

$c_k(z)$ = local wave-averaged sediment concentration [kg/m^3]

ν_s = horizontal sediment mixing coefficient [m^2/s]

E_k = entrainment rate [kg/s/m^2]

D_k = deposition rate [kg/s/m^2]

a = thickness of bed-load layer [m]

The depth-averaged sediment concentration for the size class k is commonly defined in either of the following two ways (Wu et al. 2006)

$$\widehat{C}_k = \frac{1}{h}\int_{z_b+a}^{\bar{\eta}} c_k dz \tag{3.53}$$

$$C_k = \frac{q_{sk}}{Uh} \tag{3.54}$$

where

$q_{sk} = \int_{z_b+a}^{\bar{\eta}} uc_k dz$ = suspended sediment transport [kg/m/s]

$U = \frac{1}{h}\int_{z_b}^{\bar{\eta}} udz$ = depth-averaged current velocity magnitude [m/s]

The suspended-load correction factor, β_{sk}, is defined as

$$\beta_{sk} = \frac{C_k}{\widehat{C}_k} = \frac{\int_{z_b+a}^{\bar{\eta}} uc_k dz}{U\int_{z_b+a}^{\bar{\eta}} c_k dz} \tag{3.55}$$

One can define the concentration-weighted depth-averaged velocity of the sediment size class k as

$$U_{sk} = \frac{\int_{z_b+a}^{\bar{\eta}} uc_k dz}{\int_{z_b+a}^{\bar{\eta}} c_k dz} \tag{3.56}$$

Thus, the suspended-load correction factor also denotes the ratio of the depth-averaged suspended sediment and flow velocities and accounts for the time lag (hysteresis) between flow and suspended sediment transport. Since most of the suspended sediment is transported near the bed, β_{sk} usually less than 1.0 and typically about 0.7.

Inserting the above definitions into Equation (3.52) gives (Wu, 2007, Sánchez and Wu 2011a)

$$\frac{\partial}{\partial t}\left(\frac{hC_k}{\beta_{sk}}\right)+\frac{\partial(hU_jC_k)}{\partial x_j}=\frac{\partial}{\partial x_j}\left(\nu_s h\frac{\partial C_k}{\partial x_j}\right)+E_k-D_k \tag{3.57}$$

Formulating the suspended sediment transport equation in terms of C_k rather than $\widehat{C}_k$ has the advantage of simplifying the advection term but introduces the suspended load correction factor, β_{sk}, in the temporal term. It is noted that β_{sk} should also appear in the horizontal mixing term but is lumped here with the horizontal mixing coefficient, ν_s, for simplicity.

The bed-load transport equation is obtained by integrating the 3D sediment transport equation over the bed-load layer as follows (Wu 2007)

$$\frac{\partial}{\partial t}\left(\frac{q_{bk}}{u_{bk}}\right)+\rho_s(1-p'_m)\left(\frac{\partial z_b}{\partial t}\right)_k+\frac{\partial q_{bkj}}{\partial x_j}=D_k-E_k \tag{3.58}$$

where

z_b = bed elevation with respect to the vertical datum [m]

$\left(\frac{\partial z_b}{\partial t}\right)_k$ = bed change due to the k^{th} size class [m/s]

p'_m = bed porosity [-]

ρ_s = sediment density [~2650 kg/m^3 for quartz sediment]

$q_{bk}=\sqrt{q_{bkj}q_{bkj}}$ = bed-load transport magnitude [kg/m/s]

q_{bkj} = bed-load transport components [kg/m/s]

u_{bk} = bed-load transport velocity [m/s]

The sediment density is required in the above equation since the sediment concentrations are in mass per unit volume (kg/m^3). The total bed change is calculated as the sum of the bed change for all size classes

$$\frac{\partial z_b}{\partial t} = \sum_k \left(\frac{\partial z_b}{\partial t} \right)_k \tag{3.59}$$

Summing Equations (3.57) and (3.58) leads to an overall sediment mass balance equation

$$\frac{\partial}{\partial t}\left(\frac{hC_{tk}}{\beta_{tk}} + \frac{q_{bk}}{u_{bk}} \right) + \rho_s (1 - p'_m) \left(\frac{\partial z_b}{\partial t} \right)_k + \frac{\partial q_{bkj}}{\partial x_j} + \frac{\partial (hU_j C_k)}{\partial x_j} = \frac{\partial}{\partial x_j}\left[\nu_s h \frac{\partial C_k}{\partial x_j} \right] \tag{3.60}$$

Temporarily ignoring the bed-slope effects on the bed-load direction and assuming that the bed load moves in the same direction of the current, the total-load depth-averaged sediment concentration may be defined as

$$C_{tk} = C_k + \frac{q_{bk}}{Uh} \tag{3.61}$$

Defining the fraction of suspended sediments for size class *k* as

$$r_{sk} = \frac{C_k}{C_{tk}} \tag{3.62}$$

which follows $q_{bk} = hUC_{tk}(1 - r_{sk})$. The first term in Equation (3.60) may then be rewritten as

$$\frac{\partial}{\partial t}\left(\frac{hC_{tk}}{\beta_{tk}} + \frac{q_{bk}}{u_{bk}} \right) = \frac{\partial}{\partial t}\left[hC_{tk}\left(\frac{r_{sk}}{\beta_{tk}} + \frac{1 - r_{sk}}{u_{bk}/U} \right) \right] = \frac{\partial}{\partial t}\left(\frac{hC_{tk}}{\beta_{tk}} \right) \tag{3.63}$$

where β_{tk} is the total-load correction factor given by (Wu 2007)

$$\beta_{tk} = \frac{1}{r_{sk}/\beta_{sk} + (1 - r_{sk})U/u_{bk}} \tag{3.64}$$

The correction factor, β_{tk}, accounts for the vertical distribution of the suspended sediment concentration and velocity profiles, as well as the fact that bed load usually travels in a velocity slower than the depth-averaged current velocity (see Figure 3.3). By definition, β_{tk} is the ratio of the depth-averaged total-load and flow velocities.

In order to close the sediment transport model, the second (bed change) term is approximated following Wu (2004)

$$\rho_s(1-p'_m)\left(\frac{\partial z_b}{\partial t}\right)_k = \alpha_t \omega_{sk}\left(C_{tk} - C_{tk*}\right) \tag{3.65}$$

where

C_{tk*} = equilibrium concentration of total load [kg/m^3]

α_t = total-load adaptation coefficient [-]

ω_{sk} = sediment fall velocity [m/s]

Using the above definitions the 2DH transport equation for the total load is obtained finally as

$$\frac{\partial}{\partial t}\left(\frac{hC_{tk}}{\beta_{tk}}\right) + \frac{\partial (hU_j C_{tk})}{\partial x_j} = \frac{\partial}{\partial x_j}\left[\nu_s h \frac{\partial (r_{sk} C_{tk})}{\partial x_j}\right] + \alpha_t \omega_{sk}\left(C_{tk*} - C_{tk}\right) \tag{3.66}$$

In the above equations, it is assumed that the wave mass flux is not included in the momentum equations. If the wave mass flux is included, then the total flux velocity should be used instead of the depth-averaged current velocity. The reason for this is because without a wave-induced sediment transport to counter the offshore directed transport due to the undertow, the model would predict excessive movement of sediment offshore.

3.4.1.1 Bed Slope Effect

The effect of the bed slope on the sediment transport is included by adding a diffusion-like term to the bed change equation as.

$$\rho_s \left(1 - p'_m\right)\left(\frac{\partial z_b}{\partial t}\right)_k = \alpha_t \omega_{sk} \left(C_{tk} - C_{tk*}\right) + \frac{\partial}{\partial x_j}\left(D_s q_{bk} \frac{\partial z_b}{\partial x_j}\right) \tag{3.67}$$

where

D_s = empirical bed-slope coefficient (constant) [-]

$q_{bk} = hUC_{tk}(1 - r_{sk})$ = bed load mass transport rate [kg/m/s]

The last term in the above equation is the bed slope term. It was first proposed by Watanabe (1985) and Struiksma et al. (1985) to simulate the effect of the bed slope on the sediment transport magnitude and direction. It has the added benefit of smoothing out spatial oscillations. However, if the bed slope coefficient D_s is set too high, this term can overly smooth the bed morphology.

3.4.1.2 Fraction of Suspended Sediments

In order to close the system of equations for sediment transport, the fraction of suspended sediments must be determined. This is done by assuming

$$r_{sk} = \frac{C_k}{C_{tk}} \approx \frac{C_{k*}}{C_{tk*}} \tag{3.68}$$

where C_k and C_{tk} are the actual suspended- and total-load concentrations and C_{k*} and C_{tk*} are

the equilibrium suspended- and total-load concentrations.

3.4.1.3 Adaptation Coefficient

The total-load adaptation coefficient, α_t, is an important parameter in the sediment transport model. There are many variations of this parameter in literature (e.g. Lin 1984, Gallappatti and Vreugdenhil 1985, Armanini and di Silvio 1986). The total-load adaptation coefficient α_t is related to the total-load adaptation length L_t and time T_t by

$$L_t = \frac{Uh}{\alpha_t \omega_s} = UT_t \tag{3.69}$$

The adaptation length (time) is a characteristic distance (time) for sediment to adjust from non-equilibrium to equilibrium transport. Because the total load is a combination of the bed and suspended loads, the associated adaptation length may be calculated as $L_t = r_s L_s + (1 - r_s) L_b$ or $L_t = \max(L_s, L_b)$, where L_s and L_b are the suspended- and bed-load adaptation lengths. L_s is defined as

$$L_s = \frac{Uh}{\alpha \omega_s} = UT_s \tag{3.70}$$

in which α and T_s are the adaptation coefficient and time for suspended load. The adaptation coefficient α can be calculated either empirically or based on analytical solutions to the pure vertical 2D convection-diffusion equation of suspended sediment (Lin 1984, Gallappatti and Vreugdenhil 1985, Armanini and di Silvio 1986).

The bed-load adaptation length, L_b, is generally related to the dimension of bed forms

such as sand dunes. Large bed forms are generally proportional to the water depth and therefore the bed-load adaptation length can be estimated as $L_b = a_b h$, in which a_b is an empirical coefficient on the order of 5 to 10. Although limited guidance exists on methods to estimate L_b, the determination of L_b is still empirical and in the developmental stage. For a detailed discussion of the adaptation length, the reader is referred to Wu (2007). In general, it is recommended that the adaptation length be calibrated with field data in order to achieve reliable results.

3.4.1.4 Suspended-Load Correction Factor

The suspended-load correction factor can be approximated by assuming a vertical profile for the current and sediment concentration. By assuming logarithmic current velocity and exponential suspended sediment concentration profiles, an explicit expression for the suspended-load correction factor β_{sk} can be obtained as (Sánchez and Wu 2011b)

$$\beta_{sk} = \frac{\int_{z_b+a}^{\bar{\eta}} u c_k dz}{U \int_{z_b+a}^{\bar{\eta}} c_k dz} = \frac{\mathrm{E}_1(\phi_k A) - \mathrm{E}_1(\phi_k) + \ln(A/Z)\mathrm{e}^{-\phi_k A} - \ln(1/Z)\mathrm{e}^{-\phi_k}}{\mathrm{e}^{-\phi_k A}\left[\ln(1/Z) - 1\right]\left[1 - \mathrm{e}^{-\phi_k (1-A)}\right]} \tag{3.71}$$

where

$\phi_k = \omega_{sk} h / \varepsilon$ [-]

$A = a / h$ [-]

$Z = z_a / h$ [-]

ω_{sk} = sediment fall velocity for size class *k* (see Section 3.4.3)[m/s]

ε = vertical mixing (diffusivity) coefficient (Equation 3.90) [m^2/s]

a = reference height for the suspended load equal to the thickness of bed-load layer [m]

z_a = apparent roughness length [m]

$\mathrm{E}_1(x) = \int_x^\infty \frac{e^{-t}}{t} dt$ is the exponential integral

The equation can be further simplified by assuming that the reference height is proportional to the roughness height (e.g. $a = 30 z_a$), so that $\beta_{sk} = \beta_{sk}\left(Z, \phi_k\right)$. Figure 3.4 shows a comparison of the suspended-load correction factor based on the logarithmic velocity with exponential and Rouse suspended sediment concentration profiles.

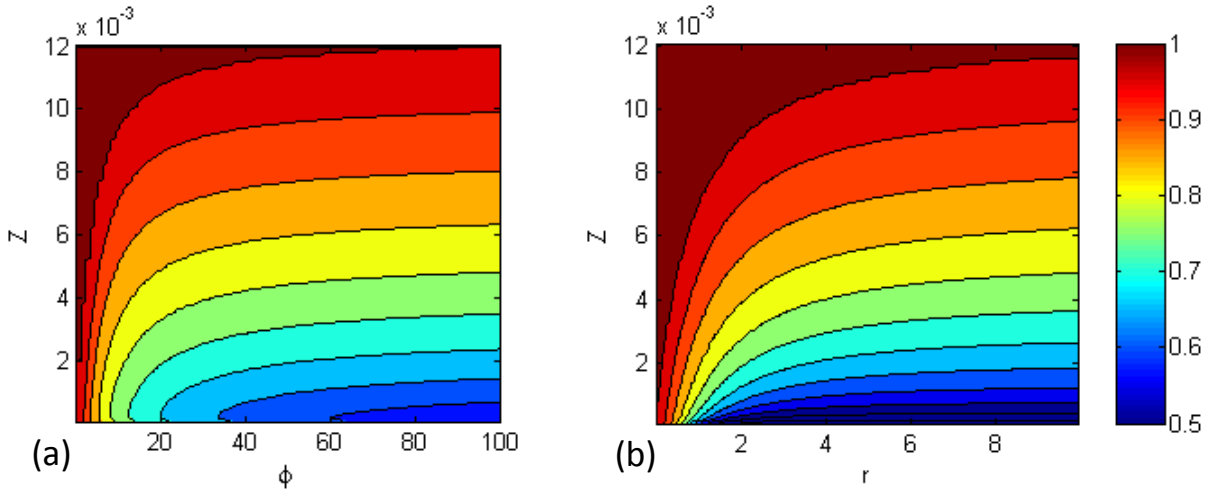

Figure 3.4. Suspended load correction factors based on the logarithmic velocity profile and (a) exponential and (b) Rouse suspended sediment profile. The Rouse number is $r = \omega_s / (\kappa u_*)$.

It is noted that the suspended-load correction factor based on idealized suspended-load and current velocity profiles is only approximate and may be invalid under certain conditions. For example, in the surf zone the undertow velocity does not follow a logarithmic velocity

profile. However, the logarithmic velocity profile is expected to be a reasonable approximation for longshore and tidal currents. In addition, the temporal (storage) term is not expected to be significant in the surf zone since it is usually treated as a quasi-steady problem. Since the present model is 2DH and does not resolve the vertical current and sediment concentration profiles, using the above idealized vertical profiles is considered an improvement over a constant vertical profile and adequate for the purposes of the model. If a more detailed description of the vertical profiles of current velocity and suspended sediment concentration is required, then a Q3D or 3D model should be used.

3.4.1.5 Bed Load Velocity

The bed load velocity, u_{bk}, is calculated using the van Rijn (1984a) formula with re-calibrated coefficients from Wu et al. (2006):

$$u_{bk} = 1.64\left(\frac{\tau_b'}{\tau_{crk}} - 1\right)^{0.5} \sqrt{(s-1)gd_k} \tag{3.72}$$

where s is the specific gravity, τ_b' is the bed shear stress related to the grain roughness and is determined by $\tau_b' = (n'/n)^{3/2}\tau_b$ in which $n' = d_{50}^{1/6}/20$ is the Manning's coefficient corresponding to the grain roughness and τ_{crk} is the critical bed shear stress.

3.4.2 Bed Material Sorting and Layering

Bed material sorting is the process in which the bed material changes size composition. In order to consider the vertical heterogeneity of the bed composition, the bed is discretized into vertical layers. The fraction of each size class is calculated and stored in each layer. The sorting

of sediments is calculated using the mixing or active layer concept (Hirano 1971, Karim and Kennedy 1982, and Wu 1991). The mixing layer is the top layer of the bed which exchanges material directly with the moving sediment.

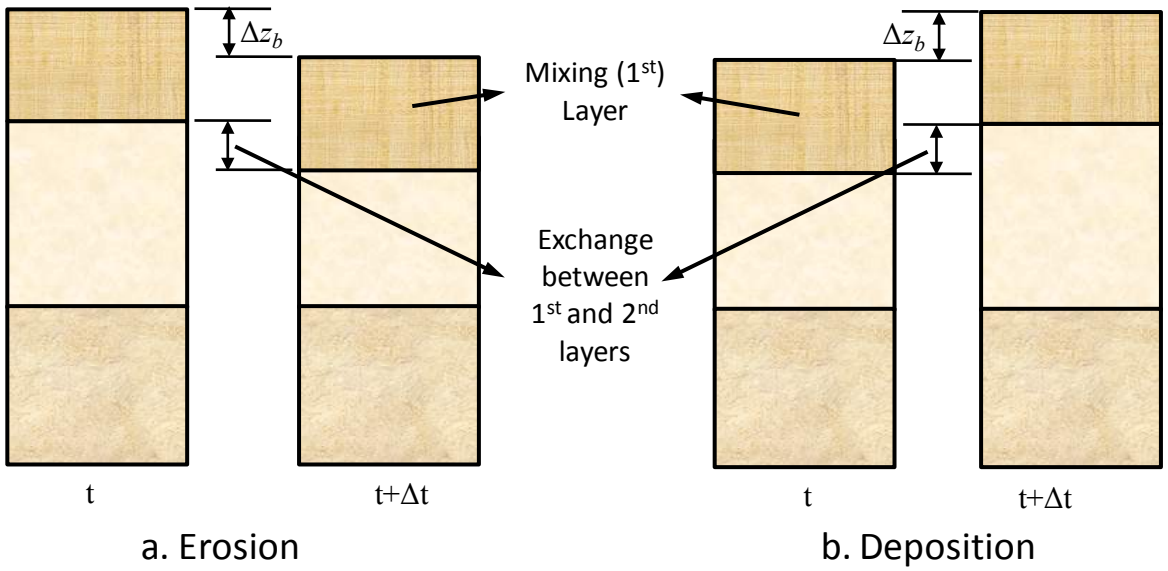

Figure 3.5. Multiple bed layer model of bed material sorting (after Wu 2007).

The temporal variation of the bed-material gradation in the mixing layer is calculated as (Wu and Vieira 2002, Wu 2007)

$$\frac{\partial(\delta_1 p_{1k})}{\partial t} = \left(\frac{\partial z_b}{\partial t}\right)_k + p_{1k}^* \left(\frac{\partial \delta_1}{\partial t} - \frac{\partial z_b}{\partial t}\right) \tag{3.73}$$

where δ_1 is the thickness of the mixing (first) layer. p_{1k}^* is equal to p_{1k} for $\partial z_b / \partial t - \partial \delta_1 / \partial t \geq 0$, and equal to the bed material gradation in the second bed layer for $\partial z_b / \partial t - \partial \delta_1 / \partial t < 0$. The bed-material sorting in the second layer is calculated as

$$\frac{\partial(\delta_2 p_{2k})}{\partial t} = -p_{1k}^* \left(\frac{\partial \delta_1}{\partial t} - \frac{\partial z_b}{\partial t}\right) \tag{3.74}$$

where δ_2 is the thickness of the second layer, and p_{2k} is the fraction of the k^{th} sediment size in the second layer. The mixing layer thickness is calculated as

$$\delta_1 = \max(2d_{50}, 0.5H_r) \tag{3.75}$$

where H_r is the ripple height.

3.4.3 Sediment Fall Velocity

The sediment fall velocity may be user-specified or calculated using the formula by Soulsby (1997)

$$\omega_s = \frac{\nu}{d}\left[\left(10.36^2 + 1.049d_*^3\right)^{1/2} - 10.36\right] \tag{3.76}$$

where ν is the kinematic viscosity [m^2/s], d is the grain size [m], and d_* is the dimensionless grain size given by

$$d_* = d\left[\frac{(s-1)g}{\nu^2}\right]^{1/3} \tag{3.77}$$

3.4.4 Equilibrium Concentration and Transport Rate

In order to close the system of equations describing sediment transport, bed change, and bed sorting, the fractional equilibrium depth-averaged total-load concentration C_{tk*} must be estimated from an empirical formula. The depth-averaged equilibrium concentration is defined as

$$C_{tk*} = \frac{q_{tk*}}{Uh} \tag{3.78}$$

where q_{tk*} is the total-load transport for the k^{th} sediment size class estimated from an empirical

formula. For convenience, C_{tk*} is written in general form as

$$C_{tk*} = p_{1k} C_{tk}^{*} \tag{3.79}$$

where p_{1k} is the fraction of the sediment size k in the first (top) bed layer and C_{tk}^{*} is the potential equilibrium total-load concentration. The potential concentration C_{tk}^{*} can be interpreted as the equilibrium concentration for uniform sediment of size d_k, with a correction factor being considered for hiding and exposure in the bed material. The above equation is essential for the coupling of sediment transport, bed change, and bed sorting equations.

3.4.4.1 Lund-CIRP

Camenen and Larson (2005, 2007, and 2008) developed general sediment transport formulas for bed and suspended loads under combined action of waves and currents. These are referred to as the Lund-CIRP transport formulas. The general transport formulas can be used for both symmetric and asymmetric waves, but for simplicity the waves are assumed to be symmetric. The current-related bed- and suspended-load transport with wave stirring is given by

$$\frac{q_{b*}}{\sqrt{(s-1)gd_{50}^3}} = f_b \rho_s 12 \sqrt{\Theta_c} \Theta_{cw,m} \exp\left(-4.5 \frac{\Theta_{cr}}{\Theta_{cw}}\right) \tag{3.80}$$

$$\frac{q_{s*}}{\sqrt{(s-1)gd_{50}^3}} = f_s \rho_s c_R U \frac{\varepsilon}{\omega_s}\left[1 - \exp\left(-\frac{\omega_s h}{\varepsilon}\right)\right] \tag{3.81}$$

where

q_{b*} = equilibrium bed-load transport rate [kg/m/s]

q_{s*} = equilibrium suspended-load transport rate [kg/m/s]

Θ_c = Shields parameters due to currents [-]

$\Theta_{cw,m}$ = mean Shields parameters due to waves and currents [-]

Θ_{cw} = maximum Shields parameters due to waves and currents [-]

Θ_{cr} = critical Shields parameter [-]

ε = vertical sediment diffusivity [m^2/s]

c_R = reference bed concentration [kg/m^3]

f_b = bed-load scaling factor (default 1.0) [-]

f_s = suspended-load scaling factor (default 1.0) [-]

The critical Shields parameter is calculated using Equation (3.111). The mean and maximum Shields parameters are calculated as

$$\Theta_{cw,m} = \sqrt{\Theta_c^2 + \Theta_{w,m}^2 + 2\Theta_c\Theta_{w,m}\cos\varphi} \tag{3.82}$$

$$\Theta_{cw} = \sqrt{\Theta_c^2 + \Theta_w^2 + 2\Theta_c\Theta_w\cos\varphi} \tag{3.83}$$

in which he mean wave Shields parameter, $\Theta_{w,m}$, is calculated as $\Theta_{w,m} = \Theta_w / 2$ assuming a sinusoidal wave.

The Shields parameters for currents and waves are given by

$$\Theta_{c|w} = \frac{\tau_{c|w}}{g(\rho_s - \rho)d} \tag{3.84}$$

in which the subscript *c|w* indicates either the current- (*c*) or wave-related (*w*) component. The current-related shear stress, τ_c, is calculated with Equation (3.12). The wave-related bed shear

stress is calculated with Equation (3.39) and the wave friction factor, f_w, of Swart (1974) given by Equation (3.42).

The total bed roughness is assumed to be a linear summation of the grain-related roughness k_{sg}, form-drag (ripple) roughness k_{sr}, and sediment-related roughness k_{ss}:

$$k_{s,c|w} = k_{sg} + k_{sr,c|w} + k_{ss,c|w} \tag{3.85}$$

The grain-related roughness is estimated as $k_{sg} = 2d_{50}$. The ripple roughness, k_{sr}, is calculated as (Soulsby 1997)

$$k_{sr,c|w} = 7.5\frac{H_{r,c|w}^2}{L_{r,c|w}} \tag{3.86}$$

where H_r and L_r are the ripple height and length, respectively.

The current- and wave-related sediment roughnesses are estimated as

$$k_{ss,c|w} = 5d_{50}\Theta_{c|w} \tag{3.87}$$

The above equation must be solved simultaneously with the expressions for the bottom shear stress because the roughness depends on the stress.

The reference concentration is given by

$$c_R = A_{cR}\Theta_{cw,m}\exp\left(-4.5\frac{\Theta_{cr}}{\Theta_{cw}}\right) \tag{3.88}$$

where the coefficient A_{cR} is determined by the following relationship

$$A_{cR} = 0.0035\exp\left(-0.3d_*\right) \tag{3.89}$$

The vertical sediment diffusivity is calculated as

$$\varepsilon = h\left(\frac{D_e}{\rho}\right)^{1/3} \tag{3.90}$$

where D_e is the total effective dissipation given by

$$D_e = k_b^3 D_{br} + k_c^3 D_c + k_w^3 D_w \tag{3.91}$$

in which k_b, k_c, and k_w are coefficients, D_{br} is the wave breaking dissipation (from the wave model), and D_c and D_w are the bottom friction dissipation due to currents and waves, respectively, expressed as

$$D_{c|w} = \tau_{c|w} u_{*c|w} \tag{3.92}$$

The coefficient k_b = 0.017 (Camenen and Larson 2008), and the coefficients k_c and k_w are function of the Schmidt number:

$$k_{c|w} = \frac{\kappa}{6}\sigma_{c|w} \tag{3.93}$$

where $\sigma_{c|w}$ is either the current or wave-related Schmidt number calculated from the following relationships (Camenen and Larson 2008):

$$\sigma_{c|w} = \begin{cases} a_{c|w} + b_{c|w}\sin^2\left(\dfrac{\pi}{2}\dfrac{\omega_s}{u_{*c|w}}\right) & \text{for } \dfrac{\omega_s}{u_{*c|w}} \le 1 \\ 1 + (a_{c|w} + b_{c|w} - 1)\sin^2\left(\dfrac{\pi}{2}\dfrac{u_{*c|w}}{\omega_s}\right) & \text{for } \dfrac{\omega_s}{u_{*c|w}} > 1 \end{cases} \tag{3.94}$$

with the coefficients $a_c = 0.4$, $b_c = 3.5$, $a_w = 0.15$, and $b_w = 1.5$.

For multiple-sized (nonuniform) sediments, the fractional equilibrium sediment transport rates are calculated as (Wu and Lin 2011)

$$\frac{q_{bk*}}{\sqrt{(s-1)gd_k^3}} = f_b \xi_k^{-1} p_{1k} \rho_s 12 \sqrt{\Theta_c} \Theta_{cw,m} \exp\left(-4.5 \frac{\Theta_{crk}}{\Theta_{cw}}\right) \tag{3.95}$$

$$\frac{q_{sk*}}{\sqrt{(s-1)gd_k^3}} = f_s \xi_k^{-1} p_{1k} \rho_s c_{Rk} U \frac{\varepsilon_k}{\omega_{sk}} \left[1 - \exp\left(-\frac{\omega_{sk} h}{\varepsilon}\right)\right] \tag{3.96}$$

where the subscript *k* indicates variables which are calculated based only on the sediment size class *k*, and ξ_k is the hiding and exposure coefficient.

3.4.4.2 van Rijn

The van Rijn (1984a,b) equations for bed- and suspended-load transport are used with the recalibrated coefficients of van Rijn (2007a,b), as given by

$$q_{b*} = 0.015 f_b \rho_s U h \left(\frac{U_e - U_{cr}}{\sqrt{(s-1)gd_{50}}}\right)^{1.5} \left(\frac{d_{50}}{h}\right)^{1.2} \tag{3.97}$$

$$q_{s*} = 0.012 f_s \rho_s U d_{50} \left(\frac{U_e - U_{cr}}{\sqrt{(s-1)gd_{50}}}\right)^{2.4} d_*^{-0.6} \tag{3.98}$$

where

U_{cr} = critical depth-averaged velocity for incipient motion [m/s]

U_e = effective depth-averaged velocity [m/s]

The effective depth-averaged velocity is calculated as $U_e = U + \gamma u_w$ with γ = 0.4 for random waves and γ = 0.8 for regular waves. u_w is the bottom wave orbital velocity based on linear wave theory. For random waves, $u_w = u_{ws}$ where u_{ws} is based on the significant wave

height and peak wave period (see Section 3.2.2). The critical depth-averaged velocity is estimated as $U_{cr} = \beta_c U_{crc} + (1-\beta_c) u_{crw}$ in which $\beta_c = U/(U+u_w)$ is a blending factor. U_{crc} is the critical depth-averaged current velocity given by Equation (3.113). u_{crw} is the critical bottom wave orbital velocity amplitude given by Equation (3.114). According to van Rijn (2007a), the bed load transport formula predicts transport rates by a factor of 2 for velocities higher than 0.6 m/s, but under-predicts transport rates by a factor of 2 to 3 for velocities close to the initiation of motion.

The van Rijn formula (1984a,b; 2007a,b) were originally proposed for well-sorted sediments. When applied to multiple-sized sediments the sediment availability is considered by multiplication of transport rates with the fraction of the sediment size class in the upper bed layer. The hiding and exposure is considered by a correction factor which multiples to the critical velocity. The fractional equilibrium transport rates are calculated as

$$q_{bk*} = f_b \rho_s p_{1k} 0.015 U h \left(\frac{U_e - \xi_k^{1/2} U_{crk}}{\sqrt{(s-1) g d_k}} \right)^{1.5} \left(\frac{d_k}{h} \right)^{1.2} \tag{3.99}$$

$$q_{sk*} = f_s \rho_s p_{1k} 0.012 U h \left(\frac{U_e - \xi_k^{1/2} U_{crk}}{\sqrt{(s-1) g d_k}} \right)^{2.4} \left(\frac{d_k}{h} \right) d_{*k}^{-0.6} \tag{3.100}$$

where p_{1k} is the fractional bed composition and ξ_k is the hiding and exposure coefficient. The subscript k indicates values which are calculated based on the k^{th} sediment size class.

3.4.4.3 Soulsby-van Rijn

Soulsby (1997) proposed the following equation for the sediment transport rate under action of combined current and waves,

$$q_{b*} = 0.005 f_b \rho_s U h \left(\frac{U_e - U_{crc}}{\sqrt{(s-1) g d_{50}}} \right)^{2.4} \left(\frac{d_{50}}{h} \right)^{1.2} \tag{3.101}$$

$$q_{s*} = 0.012 f_s \rho_s U h \left(\frac{U_e - U_{crc}}{\sqrt{(s-1) g d_{50}}} \right)^{2.4} \left(\frac{d_{50}}{h} \right) d_*^{-0.6} \tag{3.102}$$

where $U_e = \sqrt{U^2 + \frac{0.018}{c_b} u_{rms}^2}$ is the effective velocity. The critical depth-averaged velocity, U_{crc}, is calculated using Equation (3.113). The bed friction coefficient, c_b, calculated assuming a logarithmic velocity profile using Equation (3.15) in which the bed roughness length, z_0, is set to 0.006 m following Soulsby (1997). The Soulsby-van Rijn formulas are modified for multiple-sized sediments similarly to the van Rijn formulas in the previous section with the equations

$$q_{bk*} = 0.005 f_b \rho_s p_{1k} U h \left(\frac{U_e - \xi_k^{1/2} U_{crk}}{\sqrt{s-1) g d_k}} \right)^{2.4} \left(\frac{d_k}{h} \right)^{1.2} \tag{3.103}$$

$$q_{sk*} = 0.012 f_s \rho_s p_{1k} U h \left(\frac{U_e - \xi_k^{1/2} U_{crk}}{\sqrt{(s-1) g d_k}} \right)^{2.4} \left(\frac{d_k}{h} \right) d_{*k}^{-0.6} \tag{3.104}$$

The availability of sediment fractions is included through p_{1k}, while hiding and exposure of grain sizes is accounted for by modifying the critical velocity. It is noted that the Soulsby-van Rijn (Soulsby 1997) formulas are very similar to the van Rijn's (1984a,b; 2007a,b) except for the definition of the effective velocity and the recalibration of the bed-load formula coefficients in van Rijn (2007a). The proposed changes for multiple-sized sediments should be verified with measurements or numerical simulations for nonuniformly-sized sediment transport.

3.4.4.4 Watanabe

The Watanabe (1987) equilibrium total-load sediment transport rate is given by

$$q_{t*} = \left[f_s r_s + f_b (1 - r_s) \right] \rho_s A_{Wat} U \left(\frac{\tau_{b\max} - \tau_{cr}}{\rho g} \right) \tag{3.105}$$

in which

q_{t*} = potential total-load transport rate [kg/m/s]

r_s = fraction of suspended load defined by Equation (3.68) [-]

$\tau_{b\max}$ = combined wave-current maximum shear stress [Pa]

τ_{cr} = critical shear stress of incipient motion [Pa]

A_{Wat} = empirical coefficient typically ranging from 0.1 to 2.0 [-]

The critical shear stress is determined from Equations (3.111) and (3.112). The combined wave-current maximum shear stress is calculated as (Soulsby 1997)

$$\tau_{b\max} = \sqrt{\left(\tau_b + \tau_w \cos\varphi \right)^2 + \left(\tau_w \sin\varphi \right)^2} \tag{3.106}$$

where φ is the angle between the waves and current. The wave-related shear stress is calculated with Equation (3.39) with the wave friction factor, f_w, by Nielsen (1992) (Equation 3.41).

The fraction of suspended sediment, r_s, is estimated using the van Rijn (2007a,b) transport equations described above. Besides being needed in the total-load transport equation (Equation 3.66), it also allows the application of the bed and suspended load scaling factors in a way similar to all other transport formula. The coefficient A_{Wat} may be viewed as a total-load scaling factor. It is somewhat redundant since separate scaling factors are applied for the bed and

suspended load but is kept to be consistent with the previous versions of the model.

The Watanabe (1987) transport formula is modified for multiple-sized sediments as

$$q_{tk*} = \left[f_s r_{sk} + f_b (1 - r_{sk}) \right] \rho_s p_{1k} A_{Wat} U \left(\frac{\tau_{b\max} - \xi_k \tau_{crk}}{\rho g} \right) \tag{3.107}$$

where τ_{crk} is the critical shear stress of incipient motion for the k^{th} sediment size class.

3.4.5 Hiding and Exposure

When the bed material is composed of multiple grain sizes, larger grains have a greater probability of being exposed to the flow while smaller particles have a greater probability of being hidden from the flow (see Figure 3.6).

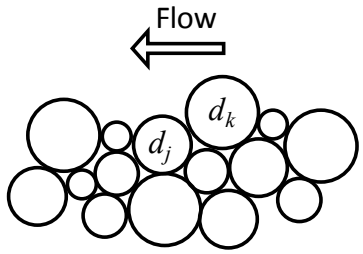

Figure 3.6. Schematic of nonuniform bed sediment grains showing the sediment grain d_j being hidden by d_k.

For the Soulsby-van Rijn (Soulsby 1997), van Rijn (1984a,b; 2007a,b), and Watanabe (1987) transport formulas described above, the hiding and exposure mechanism is considered by correcting the critical shear stress or velocity using a hiding and exposure correction function, ξ_k. For the Lund-CIRP (Camenen and Larson 2005, 2007, 2008) transport formula, an alternate approach is required due to the way in which the Shields number and grain size are included in

the formulation; thus, the hiding and exposure correction function is directly used to multiply the transport rate. Two methods are used to calculate ξ_k, depending on whether the sediment transport model is run with a single sediment size or with multiple sediment sizes, as described in the following subsections.

3.4.5.1 Single-sized Sediment Transport

In some applications, the coastal bed material is dominated by a single sediment size with patches of other sediment sizes or materials (e.g. shell hash) that may not contribute significantly to morphology change in the areas of interest; however, they may modify the sediment transport through hiding and exposure. For example, it is possible for the bed material to consist of mostly uniform sand with patches of shell fragments (bimodal distribution) in some regions. For such regions, sediment transport models often tend to over-estimate erosion since the impacts of hiding effect of the coarser shell material are not represented (e.g. Cayocca 2001). A better and more physical plausible approach is to use the local bed composition along with a correction to account for the hiding and exposure effects of the uniform sand with the patches of coarser shell material. For single-sized sediment transport, the correction function for hiding and exposure is calculated following Parker et al. (1982) as

$$\xi_k = \left(\frac{d_k}{d_{50}} \right)^{-m} \tag{3.108}$$

where m is an empirical coefficient typically between 0.5 to 1.0. The aforementioned sediment transport equations are implemented by using the transport grain size d_k rather than the bed material d_{50}. A single and constant transport size d_k is used, while the bed material d_{50} varies

spatially. The spatial distribution of d_{50} can be obtained from field measurement data and for simplicity is assumed constant during the model simulation time. This is a significant assumption and may not be reasonable for some applications. However, this method provides a simple conceptual mechanism for considering an important process in the proposed single-sized sediment transport model. This approach has been successfully applied to simulate morphology change at Shinnecock Inlet, NY (Sánchez and Wu 2011a). A more accurate and complex approach is to simulate the transport and sorting of multiple-sized sediments.

3.4.5.2 Multiple-sized Sediment Transport

When multiple sediment sizes are considered, the hiding and exposure correction for each sediment size class is based on Wu et al. (2000)

$$\xi_k = \left(\frac{P_{ek}}{P_{hk}} \right)^{-m} \tag{3.109}$$

where m is an empirical coefficient that varies for each transport formula, approximately equal to 0.6 to 1.0. P_{ek} and P_{hk} are the total hiding and exposure probabilities calculated as

$$P_{hk} = \sum_{j=1}^{N} p_{1j} \frac{d_j}{d_k + d_j}, \qquad P_{ek} = \sum_{j=1}^{N} p_{1j} \frac{d_k}{d_k + d_j} \tag{3.110a,b}$$

where N is the number of grain size classes.

3.4.6 Incipient Motion

In the case of the Lund-CIRP (Camenen and Larson 2005, 2007, and 2008) and Watanabe (1987) formula, the incipient motion is based on the critical Shields parameter estimated using the formula proposed by Soulsby (1997)

$$\Theta_{cr} = \frac{0.3}{1+1.2d_*} + 0.055\left[1 - \exp\left(-0.02d_*\right)\right] \tag{3.111}$$

in which the dimensionless grain size, d_*, is defined in Equation (3.77). The critical Shields parameter is related to the critical shear stress, τ_{cr}, by

$$\Theta_{cr} = \frac{\tau_{cr}}{g(\rho_s - \rho)d} \tag{3.112}$$

In the case of the van Rijn (1984a,b; 2007a,b) and Soulsby-van Rijn (Soulsby 1997) transport formulas, the critical depth-averaged velocity for currents alone, U_{crc}, is calculated using the formula proposed by van Rijn (1984c):

$$U_{crc} = \begin{cases} 0.19 d_{50}^{0.1} \log_{10}\left(\dfrac{4h}{d_{90}}\right), & \text{for } 0.1 \le d_{50} \le 0.5\,\text{mm} \\ 8.5 d_{50}^{0.6} \log_{10}\left(\dfrac{4h}{d_{90}}\right), & \text{for } 0.5 \le d_{50} \le 2.0\,\text{mm} \end{cases} \tag{3.113}$$

where d_{50} and d_{90} are the sediment grain size in meters of 50$^{\text{th}}$ and 90$^{\text{th}}$ percentile diameters, respectively.

The critical bottom orbital velocity magnitude for waves alone is calculated using the formula of Komar and Miller (1975):

$$u_{crw} = \begin{cases} 0.24\left[\left(s-1\right)g\right]^{0.66} d_{50}^{0.33} T_p^{0.33}, & \text{for } 0.1 \le d_{50} \le 0.5\,\text{mm} \\ 0.95\left[\left(s-1\right)g\right]^{0.57} d_{50}^{0.43} T_p^{0.14}, & \text{for } 0.5 \le d_{50} \le 2.0\,\text{mm} \end{cases} \tag{3.114}$$

where T_p is the peak wave period.

3.4.7 Ripple Dimensions

The ripple heights due to waves and currents are calculated separately and the representative ripple height is estimated as the maximum of the current- and wave-related ripple heights:

$$H_r = \max(H_{r,c}, H_{r,w}) \tag{3.115}$$

The current-related ripple height and length are calculated as (Soulsby 1997)

$$H_{r,c} = L_{r,c} / 7 \tag{3.116}$$

$$L_{r,c} = 1000 d_{50} \tag{3.117}$$

The wave-related ripple height and length are calculated using the expressions proposed by van Rijn (1984b, 1989)

$$H_{r,w} = \begin{cases} 0.22 A_w & \text{for } \psi_w < 10 \\ 2.8 \times 10^{-13} (250 - \psi_w)^5 A_w & \text{for } 10 \le \psi_w < 250 \\ 0 & \text{for } 250 \le \psi_w \end{cases} \tag{3.118}$$

$$L_{r,w} = \begin{cases} 1.25 A_w & \text{for } \psi_w < 10 \\ 1.4 \times 10^{-6} (250 - \psi_w)^{2.5} A_w & \text{for } 10 \le \psi_w < 250 \\ 0 & \text{for } 250 \le \psi_w \end{cases} \tag{3.119}$$

where

$A_w = \dfrac{u_w T}{2\pi}$ = semi-orbital excursion [m/s]

$\psi_w = \dfrac{u_w^2}{(s-1) g d_{50}}$ = wave mobility parameter [-]

The current- and wave-related ripple height and length are used in calculating the bed form roughness for use in the Lund-CIRP transport formula.

3.4.8 Horizontal Sediment Mixing Coefficient

The horizontal sediment mixing coefficient, ν_s, represents the combined effects of turbulent diffusion and dispersion. The horizontal sediment mixing coefficient is assumed to be proportional to the turbulent eddy viscosity as

$$\nu_s = \nu_t / \sigma_s \tag{3.120}$$

where σ_s is the Schmidt number and ν_t is the turbulent horizontal eddy viscosity described in Section 3.1.2. There are many formulas to estimate the Schmidt number. The Schmidt number is set by default equal to 1.0, but may be modified.

3.4.9 Boundary Conditions

At the interface between wet and dry cells, the sediment flux normal to the interface is set to zero. The inflow boundary condition requires a given sediment concentration at the boundary. However, for most coastal applications, the actual sediment concentration is not available and the model implements the equilibrium concentration capacity. At outflow boundaries, the sediment concentration gradient in the streamwise direction is set to zero.

CHAPTER IV

NUMERICAL METHODS

The hydrodynamic equations are solved using the finite volume method on a variety of grids including regular and telescoping Cartesian grids and unstructured triangular and quadrilateral grids. The model uses the SIMPLEC (Semi-Implicit Method for Pressure Linked Equation Consistent) algorithm (van Doormal and Raithby 1984) on a non-staggered grid to handle the coupling of water level and velocity. Primary variables *u*-, *v*-velocity, and water level are stored on the same set of grid points, and fluxes at cell faces are determined using a Rhie and Chow (1983) type momentum interpolation method (Wu et al. 2011). The sediment transport and morphology change equations are solved using the finite volume method on the same grid as the hydrodynamics. The spectral wave-action and surface roller energy balance equations are solved using finite difference methods on Cartesian grids. The flow and wave models are coupled using a steering procedure. Details of the numerical methods are presented in the following sections.

4.1 Computational Grids and Data Structures

One important aspect of incompressible flow models is the location of primary variables: velocity and water level (pressure). On a staggered grid, the water level is located at the center of cells and the velocities are located along the faces or nodes of cells (Harlow and Welsh 1965, Patankar 1980). On a non-staggered grid, all of the primary variables are located at the cell

centers. Since the water level is calculated by the divergence of the velocity field and the velocities are driven by water level gradients, the staggered grid facilitates the use of central difference type schemes without producing the checkerboard instabilities. The non-staggered grid involves a simpler source code and for an implicit scheme can minimize the number of coefficients that must be computed and stored during a simulation because many of the terms in the equations are equal. In particular, staggered grids require defining additional control volumes (e.g. dual meshes) at cell faces or nodes and the interpolation of variables on the faces of the additional control volumes. Therefore, a non-staggered (collocated) grid approach is adopted in this study with a Rhie and Chow (1983) type momentum interpolation technique used to eliminate the checkerboard oscillations.

The developed model supports general polygonal meshes with cells consisting of convex polygons with any number of faces. An example of a general polygonal mesh is shown in Figure 4.1.

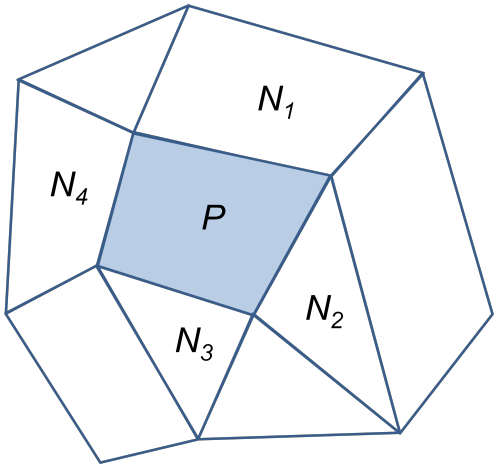

Figure 4.1. Polygonal mesh. Shaded area indicates the control volume *P*. Neighboring cells sharing a cell face are indicated by the letter *N*. The subscripts indicate the neighbor number.

To improve computational efficiency, memory usage, stability, and simplification of grid generation, grids used in the present model are classified as structured or non-telescoping Cartesian, telescoping Cartesian, structured quadrilateral, unstructured triangular, and hybrid triangular/quadrilateral. Depending on the grid topology, simplifications can be made in the discretization and specialized solution techniques used. For example, structured Cartesian and quadrilateral grids result in a penta-diagonal coefficient matrix which can be solved using specialized solvers such as Stone's (1968) Strongly Implicit Procedure (SIP). Additional aspects of the model where simplifications are made depending on the grid topology are the calculation of cell-face interpolations, spatial gradients, slope limiters, and advection schemes. Further details are provided in subsequent sections.

Currently, all of the computational grids are generated in the Surface-water Modeling System (Zundel 2006). Hence, although the model supports general polygonal meshes, it has only been tested for grid types which can be generated in SMS. Examples of different types of computational grids which can be generated in the SMS interface and have been tested are shown in Figure 4.2. Cartesian grids are classified as uniform, nonuniform, or telescoping. Telescoping locally refines the mesh by splitting a cell into subcells. The only requirement imposed by the numerical methods is that the cells must have a rectangular shape. Additional requirements imposed by the user interface limit the variety of types of Cartesian grids to help simplify the grid generation and avoid grid quality issues. The following requirements are applied to telescoping Cartesian grids:

1. Cells can only be subdivided into four subcells.

2. Cells may have a maximum of 6 neighbors.
3. Only two neighboring cells are allowed in the same direction (i.e. north, south, east, and west).
4. Refinement levels must be spaced by at least one cell apart (i.e. cells that share the same corner must be one refinement level apart).

The first requirement simplifies the grid generation process but may be relaxed in future versions. The last three requirements are for grid quality purposes. Requirement 2 avoids having a cell surrounded by refined cells. The last two requirements avoid having excessive cell refinement which can cause numerical instabilities.

For unstructured meshes the model does not have limitations on the number of cell faces, number of cells connected to a single node, grid orthogonality, or any other type. Although grid orthogonality is not a requirement, highly distorted meshes are not recommended since they can cause divergence issues. The only requirement for unstructured meshes is that the cells be convex polygons. A grid is defined as orthogonal if all of the lines connecting the cell centers intersect the cell-face mid points. A grid does not have to be structured to be orthogonal. For example, an unstructured triangular mesh made of equilateral triangles is orthogonal. In general however, it is difficult to enforce orthogonality on unstructured meshes and most unstructured meshes used in practice are non-orthogonal.

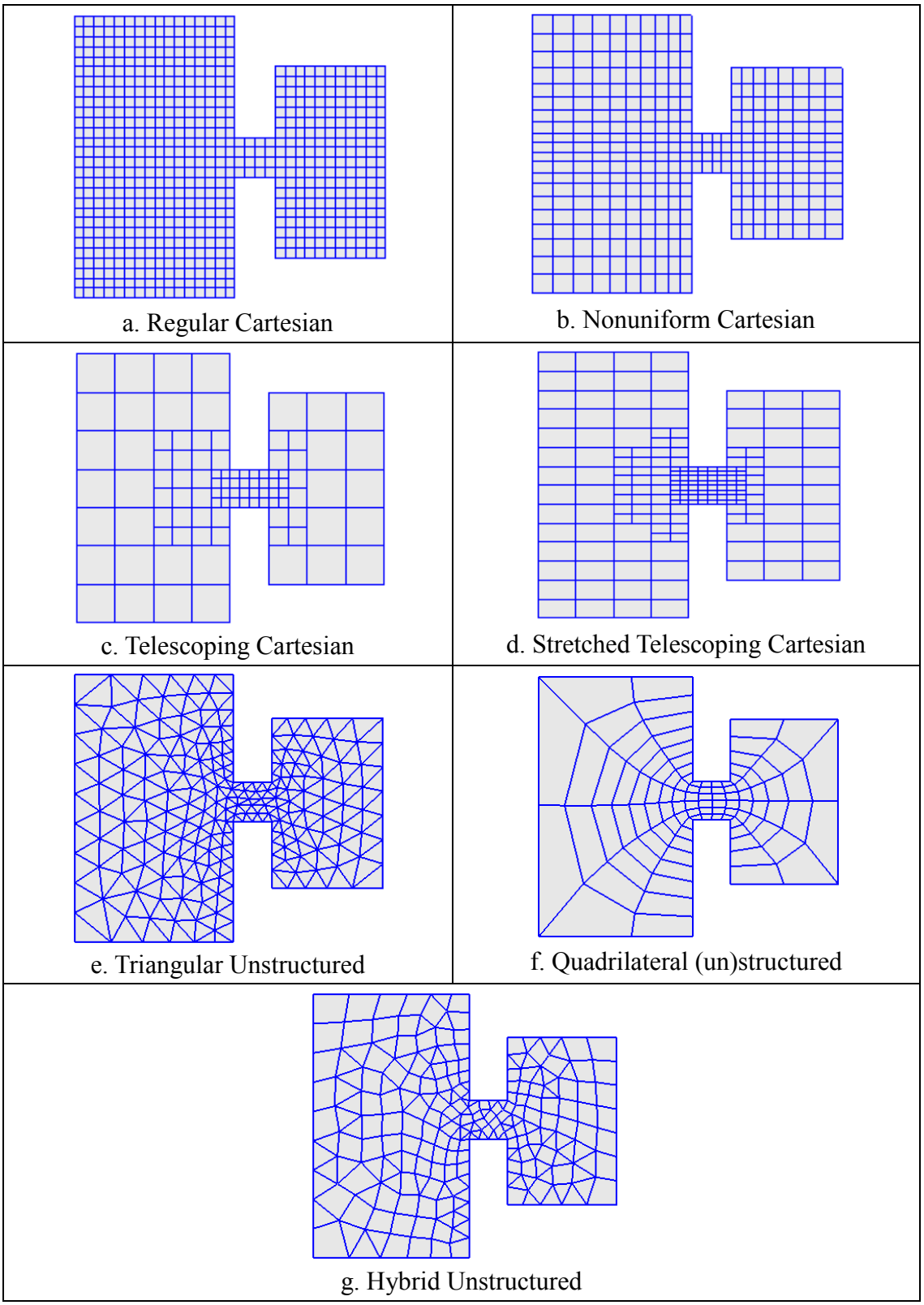

Figure 4.2. Examples of different types of computational grids.

Different types of grids have their own advantages and disadvantages. Regular (uniformly spaced) Cartesian grids have the advantage of being the simplest to generate. However, regular Cartesian grids require a large number of computational cells in order to properly resolve complex geometries. Nonuniform Cartesian grids maintain the same structure as regular Cartesian grids but allow the grid spacing to vary spatially. Telescoping Cartesian grids offer greater flexibility in resolving complex geometries and are relatively simple to generate and also suffer less from grid quality problems compared to unstructured grids. Telescoping Cartesian grids are more difficult to generate than non-telescoping Cartesian grids, but much less difficult than unstructured grids.

A complication of telescoping Cartesian grids compared to non-telescoping Cartesian grids comes from non-orthogonality corrections which are necessary for second-order accuracy. However, since only relatively small fraction of cells have non-orthogonal faces, the increase in computational cost is relatively minor. Another complication from telescoping grids is that for implicit time marching schemes they lead to systems of equations whose matrix coefficients are unbanded and are more difficult to solve compared to the penta-diagonal coefficient matrix of uniform and nonuniform Cartesian grids. Cartesian grids also suffer from the stair-case representation of boundaries unless a boundary fitting method is implemented such as 'cut cells' (e.g. Popinet and Richard 2006) or immersed boundaries (e.g. Wang and Wu 2010). Unstructured grids offer the greatest flexibility for resolving complex geometries, but are the most difficult and time consuming to generate. They are more prone to grid quality issues. Lastly, for problems with wetting and drying the boundary fitting capability of unstructured grids may deteriorate unless the mesh is always aligned with the moving boundary (wetting and drying

front), which is generally difficult to achieve for practical problems.

The data structure for all grid types is treated in an unstructured manner in which all cells are numbered in a one-dimensional array and tables are used to determine the connectivity of neighboring cells. This allows for both structured and unstructured grids to exist under the same framework. For structured grids, this approach also has the disadvantage of having to use the connectivity tables to point to neighboring cells. However, this is a relatively small computational expense. For most practical applications, there are large portions of the grid which are inactive (permanently dry). By using the unstructured data structure, inactive cells can be easily excluded from the computational domain and the efficiencies in memory and computation time far outweigh the cost of having to use tables for the cell connectivity. Lastly it is noted that for convenience in handling boundary conditions, each boundary cell has a neighboring ghost cell outside of the computational domain. Ghost cells are stored at the end of the 1D index array.

4.2 General Transport Equation

The hydrodynamic and sediment transport equations are some form of a general transport equation. Therefore, in order to avoid redundancy, the discretization procedure is presented for the general transport equation below and the same discretization may be applied to hydrodynamic and sediment transport equations. The general transport equation is written in vector notation as

$$\underbrace{\frac{\partial}{\partial t}\left(\frac{h\phi}{\beta}\right)}_{\text{Temporal Term}} + \underbrace{\nabla\cdot(h\vec{V}\phi)}_{\text{Advection Term}} = \underbrace{\nabla\cdot\left(\Gamma h\nabla\phi\right)}_{\text{Diffusion Term}} + \underbrace{S}_{\text{Source Term}} \tag{4.1}$$

where

∇ = gradient operator

ϕ = general scalar

t = time [s]

h = total water depth [m]

β = correction factor [-]

$\vec{V} = V_j$ = is the transport velocity [m/s]

Γ = diffusion coefficient for ϕ

S = source/sink term including all remaining terms

4.2.1 Spatial Discretization

Integration of Equation (4.1) over a control area (see Figure 4.3) yields:

$$\int_A \frac{\partial}{\partial t}\left(\frac{h\phi}{\beta}\right)\mathrm{d}A + \int_A \nabla\cdot\left(h\vec{V}\phi - \Gamma h\nabla\phi\right)\mathrm{d}A = \int_A S\mathrm{d}A \tag{4.2}$$

where A is the control area. Using Gauss's Divergence Theorem to convert the area integral to a boundary integral, the convection term is discretized as

$$\int_A \nabla\cdot(h\vec{V}\phi)\mathrm{d}A = \oint_L h\left(\vec{n}\cdot\vec{V}\right)\phi\mathrm{d}L = \sum_f h_f V_f \phi_f \Delta l_f = \sum_f F_f\phi_f \tag{4.3}$$

where L is boundary of the control area A, $V_f = \vec{n}_f\cdot\vec{V}_f$ is the outward cell face velocity, $\vec{n}_f$ is the outward unit vector normal to cell face f, Δl_f is the length of the cell face f, $F_f = h_f V_f \Delta l_f$ is the convection flux at cell face, and ϕ_f is the advective value of ϕ on cell face f.

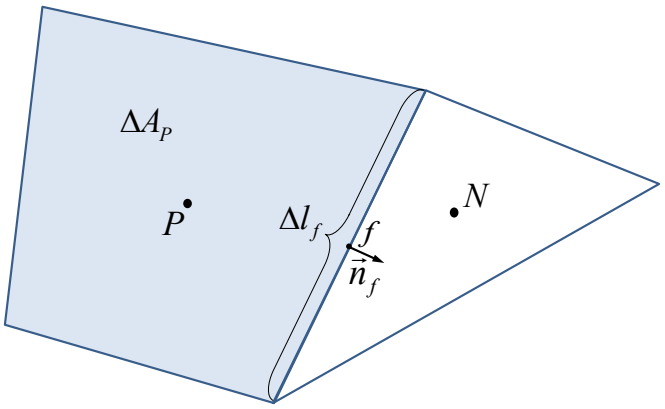

Figure 4.3. Schematic showing a polygonal cell.

The diffusion term is discretized using Gauss's Divergence Theorem as

$$\int_A \nabla \cdot \left(\Gamma h \nabla \phi\right) \mathrm{d}A = \oint_L h\Gamma \left(\vec{n} \cdot \nabla \phi\right) \mathrm{d}L = \sum_f h_f \Gamma_f (\nabla_\perp \phi)_f \Delta l_f \tag{4.4}$$

where $(\nabla_\perp \phi)_f = (\vec{n} \cdot \nabla \phi)_f$ is the outward normal gradient of ϕ at cell face f.

The temporal and source/sink terms are assumed to vary linearly within the cell, and their integrals are approximated using the second-order accurate mid-point rule (Ferziger and Peric 1997)

$$\int_A \frac{\partial}{\partial t}\left(\frac{h\phi}{\beta}\right) \mathrm{d}A = \frac{\partial}{\partial t}\left(\frac{h_P \phi_P}{\beta_P}\right) \Delta A_P \tag{4.5}$$

$$\int_A S \mathrm{d}A = S_P \Delta A_P \tag{4.6}$$

where ΔA_P is the area of cell P.

Thus, Equation (4.2) is converted as

$$\frac{\partial}{\partial t}\left(\frac{h_P \phi_P}{\beta_P}\right) \Delta A_P + \sum_f h_f \left[V_f \phi_f - \Gamma_f \left(\nabla_\perp \phi\right)_f\right] \Delta l_f = S_P \Delta A_P \tag{4.7}$$

In order to derive the final discretized equation, several quantities such as the cell-face values and gradients in the above equation need to be further treated. The cell face velocity, V_f, is calculated using a momentum interpolation method similar to that of Rhie and Chow (1983) (see Section 4.3). ϕ_f in the convection term is determined using one of several upwind schemes, including Hybrid (Spalding 1972), Exponential (Spalding 1972), and HLPA (Zhu 1991) (see Section 4.2.7). The temporal derivative is discretized using an implicit scheme. These schemes are described in detail below.

4.2.2 Temporal Discretization

The general transport equation is rewritten as

$$\frac{\partial}{\partial t}\left(\frac{h\phi}{\beta}\right) = \hat{G} \tag{4.8}$$

where $\hat{G}$ includes all the remaining terms. For stability and efficiency, a fully implicit time-stepping scheme is used to discretize the temporal term as

$$\frac{1}{\Delta t}\left[(1+0.5\hat{\theta})\frac{h^{n+1}\phi^{n+1}}{\beta^{n+1}} - (1+\hat{\theta})\frac{h^{n}\phi^{n}}{\beta^{n}} + 0.5\hat{\theta}\frac{h^{n-1}\phi^{n-1}}{\beta^{n-1}}\right] = \hat{G}^{n+1} \tag{4.9}$$

where $\hat{\theta}$ is a weighting factor between 0 and 1. For $\hat{\theta}$ = 0, the scheme reduces to the first-order backward Euler scheme, and for $\hat{\theta}$ = 1, the scheme reduces to the second-order backward scheme (Ferziger and Peric 1997). The superscripts indicate the time step levels, with *n* + 1 being the current time step and *n* being the previous time step.

4.2.3 Cell-face Interpolation

The general formula for the cell-face interpolation of ϕ is given by (see Figure 4.4)

$$\phi_f = f_\perp \phi_{\perp,N} + (1 - f_\perp)\phi_{\perp,P} \tag{4.10}$$

where

$\phi_{\perp,C} = \phi_C + (\vec{r}_\parallel \cdot \nabla\phi)_C$ = reconstructed value within cell ($C = P, N$) (see Section 4.2.6)

$f_\perp = |\vec{r}_{\perp,P}| / |\delta_\perp|$ = linear interpolation factor

$|\delta_\perp| = |\vec{r}_{\perp,P}| + |\vec{r}_{\perp,N}|$

The subscripts $\parallel$ and $\perp$ indicate variables which are parallel and perpendicular to the face f, respectively. Equation (4.10) is second-order accurate and linearly exact.

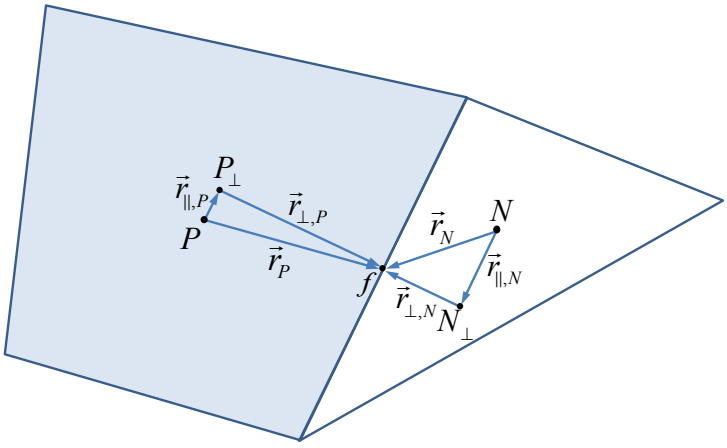

Figure 4.4. Schematic showing a control volume P, neighboring N, and cell-face related geometric variables.

The cell-reconstructions are used to account for grid non-orthogonality and are necessary

for second-order accuracy. For orthogonal grids, such as regular Cartesian grids, $\vec{r}_{\|} = 0$ and no reconstructions are necessary. For telescoping Cartesian grids, reconstructions are only calculated at adjacent cells with different refinement levels. Thus, the underlying Cartesian geometry is taken advantage of by reducing the number of reconstructions and simplifying them as $(\vec{r}_{\|} \cdot \nabla\phi)_C \rightarrow (r_{\|} \nabla_{\|}\phi)_C$.

4.2.4 Cell-face Gradient

The outward normal gradient at cell face *f* is calculated using the central difference scheme and the auxiliary node concept of Ferziger and Peric (1997) as

$$(\vec{n} \cdot \nabla\phi)_f = \nabla_{\perp}\phi_f = \frac{\phi_{\perp,N} - \phi_{\perp,P}}{|\delta_{\perp}|} \tag{4.11}$$

where again $\phi_{\perp,C} = \phi_C + (\vec{r}_{\|} \cdot \nabla\phi)_C$ is reconstructed value within cell (*C* = *P*, *N*) (see Section 4.2.6). Ham et al. (2002) compared the above auxiliary node formulation with the fully-unstructured discretization proposed by Zwart et al. (1998) for the viscous terms and found that the auxiliary node formulation is significantly more stable. The above central difference scheme is linearly exact and second-order accurate for $|\vec{r}_{\perp,P}| = |\vec{r}_{\perp,N}|$ (Ferziger and Peric 1997). The cell-reconstructions are used to account for the grid non-orthogonality.

4.2.5 Cell-centered Gradient

There are two schemes used for determining the cell-centered gradient: (1) Gauss Divergence Theorem and (2) Weighted Least-Squares. The schemes are described below.

4.2.5.1 Divergence Theorem

The integral of the cell-centered gradient operator over the control volume is calculated using Gauss's Divergence Theorem as

$$\int_A \nabla_i \phi \mathrm{d}A = \oint_L (n_i \phi)\mathrm{d}L = \sum_f n_i \phi_f \Delta l_f \tag{4.12}$$

where n_i is the i^{th} component of the unit vector normal to the cell face. Thus, the cell-centered gradient operator is given by

$$\nabla_i \phi_P = \frac{1}{\Delta A_P} \sum_f n_i \phi_f \Delta l_f \tag{4.13}$$

The above equation is conservative, second order, and linearly exact (due to ϕ_f).

4.2.5.2 Weighted Least-Squares

In the weighted least-squares method the solution is assumed to vary linearly so that

$$w_N(\vec{x}_N - \vec{x}_P) \cdot \nabla \phi_P = w_N(\phi_N - \phi_P) \tag{4.14}$$

The above equation leads to an over-determined and linear system of equations which can be solved by decomposing the coefficient matrix using the Gram Schmidt process (Barth 1992). It is noted that the neighboring cells do not need to share a cell face. The system of equations is solved by minimizing the error over the computational stencil in a least-squares sense. The final cell-centered weighted least-squares gradient operator is given by

$$\nabla_i \phi_P = \frac{1}{\Lambda}\left[I_{jj} \sum_N w_N^2 \left(\phi_N - \phi_P\right)\left(x_{i,N} - x_{i,P}\right) - I_{ij} \sum_N w_N^2 \left(\phi_N - \phi_P\right)\left(x_{i,N} - x_{i,P}\right) \right] \tag{4.15}$$

where

$$w_N = \left|\vec{x}_N - \vec{x}_P\right|^{-N_{LS}}$$

$$I_{ii} = \sum_N w_N^2 \left(x_{i,N} - x_{i,P}\right)^2$$

$$I_{ij} = I_{ji} = \sum_N w_N^2 \left(x_{i,N} - x_{i,P}\right)\left(x_{j,N} - x_{j,P}\right)$$

$$\Lambda = I_{ii} I_{jj} - I_{ij} I_{ji} I$$

Here, N_{LS} is an integer value typically between 1 and 3. The geometric weights w_N are used to reduce the relative influence of neighboring points which are further away. This method reduces the gradient operator sensitivity to highly distorted meshes.

4.2.6 Reconstruction, Monotonicity, and Slope Limiters

A linear reconstruction of the variable ϕ within a cell is expressed as

$$\phi = \phi_P + \vec{r} \cdot \nabla \phi_P \tag{4.16}$$

where ϕ_P is the cell-average value specified at the cell centroid, $\vec{r}$ is the distance vector from the cell centroid to any location within the cell, and $\nabla \phi_P$ is the cell-centered gradient. The reconstruction is second order and conservative in the sense that $\phi_P \Delta A_P = \int_A \phi dA$. If the reconstruction satisfies the local maximum principle

$$\min(\phi - \phi_P, 0) \le \vec{r} \cdot \nabla \phi_P \le \max(\phi - \phi_P, 0) \tag{4.17}$$

then no new extrema are created within the cell and the solution is monotonic. Figure 4.5 shows two examples of linear reconstruction with and without slope limiters.

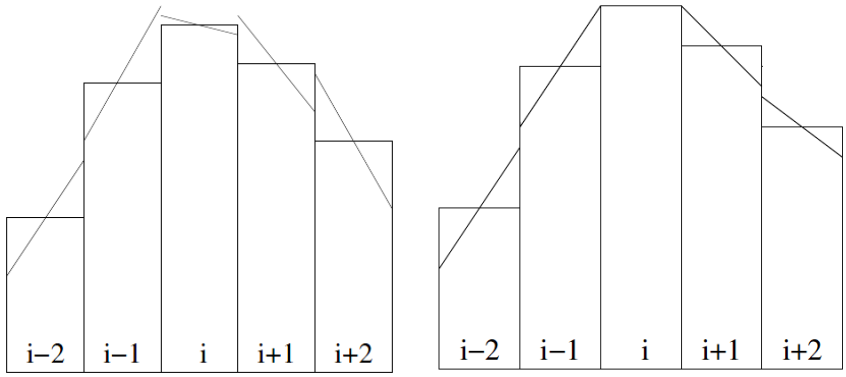

Figure 4.5. Examples of linear reconstructions: (a) non-limited and (b) limited.

For structured grids, the following three slope limiters are implemented (see Figure 4.6):

$$\Phi_i(R) = \begin{cases} \dfrac{4R}{(R+1)^2} & \text{van Leer (1979)} \\ \dfrac{2R}{R^2+1} & \text{van Albada (1982)} \\ \min\left(1, \dfrac{4}{R+1}, \dfrac{4R}{R+1}\right) & \text{MUSCL (van Leer 1979)} \end{cases} \tag{4.18}$$

where R is the ratio between two consecutive slopes

$$R = \frac{(\phi_{i+1} - \phi_i)(x_i - x_{i-1})}{(x_{i+1} - x_i)(\phi_i - \phi_{i-1})} \tag{4.19}$$

Note that the slope limiter is applied in each direction separately. In addition, all of the slope limiters should be set to zero for $R \leq 0$. The second-order van Leer (1979) limiter is used in this study because of its smoothness.

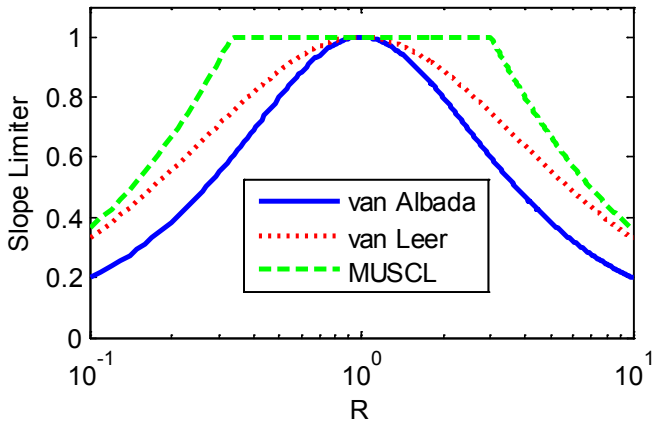

Figure 4.6. Comparison of three different slope limiters.

For unstructured grids the slope limiters described above are difficult to implement because of the complexity in defining forward and backward differences. For unstructured grids the Limited Central Difference (LCD) slope limiting procedure of Hubbard (1999) is applied and is given by

$$\Phi_f = \begin{cases} \dfrac{\max(\phi_N - \phi_P, 0)}{(\vec{r} \cdot \nabla\phi)_P} & \text{for } (\vec{r} \cdot \nabla\phi)_P > \max(\phi_N - \phi_P, 0) \\ \dfrac{\min(\phi_N - \phi_P, 0)}{(\vec{r} \cdot \nabla\phi)_P} & \text{for } (\vec{r} \cdot \nabla\phi)_P < \min(\phi_N - \phi_P, 0) \\ 1 & \text{otherwise} \end{cases} \tag{4.20}$$

where $\vec{r}_P = \vec{x}_f - \vec{x}_P$. In the procedure outlined by Hubbard (1999) a scalar limiter is calculated as $\Phi = \min\left(\Phi_f\right)$. For telescoping grids a directional limiter can be calculated as $\Phi_i = \min_{f \in f \perp i}\left(\Phi_f\right)$, which is less dissipative. Finally, the cell-centered gradient is limited as

$$\nabla_i \phi_P = \Phi_i \nabla_i^* \phi_P \tag{4.21}$$

where $\nabla_i^* \phi_P$ is the unlimited gradient.

4.2.7 Advection Schemes

The advection schemes used include Hybrid (Spalding 1972), Exponential (Spalding 1972), and HLPA (Zhu 1991). These schemes are described in detail below.

4.2.7.1 Hybrid Upwind/Central Scheme

The hybrid scheme is composed of a first-order upwind scheme and a second-order central difference scheme (Spalding 1972):

$$\phi_f = \begin{cases} \left(\phi_D + \phi_C\right)/2 & \text{for } \left|P_f\right| < 2 \\ \phi_C & \text{for } \left|P_f\right| > 2 \end{cases} \tag{4.22}$$

where the subscripts *D* and *C* indicate the first downstream and first upstream nodes. The Peclet number at the cell face is given by $P_f = V_f \left|\delta_\perp\right| / \Gamma_f$. When P_f is larger than 2, the first-order upwind scheme is used; otherwise, the second-order central difference scheme is used.

4.2.7.2 Exponential Scheme

The exponential scheme interpolates the face value using an exact solution of the 1D steady advection-diffusion equation between $P_\perp$ and $N_\perp$ (Spalding 1972):

$$\frac{\phi_f - \phi_{\perp P}}{\phi_{\perp N} - \phi_{\perp P}} = \frac{\exp(P_f f_\perp) - 1}{\exp(P_f) - 1} \tag{4.23}$$

The exponential scheme has automatic upwinding and is stable, but is usually less than second order. For a P_f = 0 (no flow) the exponential scheme is equivalent to a linear interpolation.

4.2.7.3 Hybrid Linear/Parabolic Scheme

The Hybrid Linear/Parabolic Approximation scheme of Zhu (1991) may be written as

$$\phi_f = \begin{cases} \phi_{\perp,C} + \left(\phi_{\perp,D} - \phi_{\perp,C}\right)\hat{\phi}_C & \text{for } 0 < \hat{\phi}_C \le 1 \\ \phi_{\perp,C} & \text{otherwise} \end{cases} \tag{4.24}$$

where the subscripts *D*, *C*, and *U* indicate the first downwind and first and second upwind cells, respectively. For structured grids the normalized variable, $\hat{\phi}_C$, is given by

$$\hat{\phi}_C = \frac{\phi_C - \phi_U}{\phi_D - \phi_U} \tag{4.25}$$

For unstructured grids it is difficult to determine the second upstream value ϕ_U and the above expression is replaced with the formulation of Jasak et al. (1999)

$$\hat{\phi}_C = 1 - \frac{\phi_{\perp,D} - \phi_{\perp,C}}{2\left(\nabla_\perp \phi\right)_C \delta_{\perp,C}} \tag{4.26}$$

where $\vec{\delta}_{\perp,C} = \vec{r}_{\perp,C} - \vec{r}_{\perp,D}$ is the distance vector from $C_\perp$ to $D_\perp$ with the letters indicating the first upwind and downwind nodes.

The Hybrid Linear/Parabolic Approximation scheme is second order. Choi et al. (1995) found that the HLPA scheme has similar accuracy to the third-order SMARTER (Sharp and Monotonic Algorithm for Realistic Transport Efficiently Revised) and LPPA (Linear and Piecewise-Parabolic Approximation) schemes but is simpler and more efficient (Shin and Choi 1992, Choi et al. 1995).

4.2.8 Source/Sink Term

The source/sink term is linearized as (Patankar 1980)

$$S_P = S_P^C + S_P^P \phi_P \tag{4.27}$$

in which the term S_P^P is required to be non-positive for stability.

4.2.9 Assembly of Algebraic Equations

Assembly refers to the process of combining terms to create a system of linear algebraic equations. The derivation begins by writing the combined advection and diffusion as

$$\begin{aligned}\sum_f \left[F_f \phi_f - \Gamma_f h_f \Delta l_f (\nabla_\perp \phi)_f \right] = \sum_f \left\{ \left[D_f \Lambda\left(\left|P_f\right|\right) + F_f^+ \right] \phi_{\perp,P} - \left[D_f \Lambda\left(\left|P_f\right|\right) - F_f^- \right] \phi_{\perp,N} \right\} \\ + \sum_f \left[F_f^+ \gamma_P \hat{\phi}_P (\phi_{\perp,N} - \phi_{\perp,P}) + F_f^- \gamma_N \hat{\phi}_N (\phi_{\perp,P} - \phi_{\perp,N}) \right]\end{aligned} \tag{4.28}$$

where

$\phi_{\perp,C}$ = reconstructed value within cell C with $C = P, N$ (see Section 4.2.6)

$$\phi_{\perp,C} = \phi_C + \begin{cases} (\vec{r}_\parallel \cdot \nabla \phi)_C & \text{for unstructured} \\ (r_\parallel \nabla_\parallel \phi)_C & \text{for telescoping Cartesian} \\ 0 & \text{for nontelescoping} \end{cases} \tag{4.29}$$

$$F_f^\pm = \frac{1}{2}\left(F_f \pm \left| F_f \right| \right) \tag{4.30}$$

$$D_f = \frac{\Gamma_f h_f \Delta l_f}{\delta_\perp} \tag{4.31}$$

$$\Lambda\left(\left|P_f\right|\right)=\begin{cases}\max\left(1-0.5\left|P_f\right|,0\right) & \text{for hybrid scheme}\\ \left|P_f\right|/\left[\exp\left(\left|P_f\right|\right)-1\right] & \text{for exponential scheme}\\ 1 & \text{for HLPA scheme}\end{cases} \tag{4.32}$$

$$\gamma_C=\begin{cases}1 & \text{for HLPA scheme and } 0<\hat{\phi}_C\le 1\\ 0 & \text{otherwise}\end{cases}$$

The subscripts *D*, *C*, and *U* indicate the first downstream and first and second upstream nodes, respectively. In the above equations and elsewhere, variable without a superscript indicating the time step level are assumed to at $n + 1$.

The discretized transport equation may be written as

$$\begin{gathered}\left[(1+0.5\hat{\theta})\frac{h^{n+1}\phi^{n+1}}{\beta^{n+1}}-(1+\hat{\theta})\frac{h^{n}\phi^{n}}{\beta^{n}}+0.5\hat{\theta}\frac{h^{n-1}\phi^{n-1}}{\beta^{n-1}}\right]\frac{\Delta A_P}{\Delta t}+\\ \sum_f\left\{\left[D_f\Lambda\left(\left|P_f\right|\right)+F_f^+\right]\left[\phi_P+\left(\vec{r}_{\parallel}\cdot\nabla\phi\right)_P\right]-\left[D_f\Lambda\left(\left|P_f\right|\right)-F_f^-\right]\left[\phi_N+\left(\vec{r}_{\parallel}\cdot\nabla\phi\right)_N\right]\right\}\\ \sum_f\left\{F_f^+\left[\gamma_P\hat{\phi}_P\left(\phi_N-\left(\vec{r}_{\parallel}\cdot\nabla\phi\right)_N-\phi_P-\left(\vec{r}_{\parallel}\cdot\nabla\phi\right)_P\right)\right]+F_f^-\left[\gamma_N\hat{\phi}_N\left(\phi_P+\left(\vec{r}_{\parallel}\cdot\nabla\phi\right)_P-\phi_N-\left(\vec{r}_{\parallel}\cdot\nabla\phi\right)_N\right)\right]\right\}\\ =\left(S_P^C+S_P^P\phi_P\right)\Delta A_P\end{gathered} \tag{4.33}$$

The cell-reconstruction terms $\vec{r}_{\parallel}\cdot\nabla\phi$, in the equation above are corrections for grid non-orthogonality and are treated explicitly and 'deferred' to the source/sink term. Separating ϕ_P and ϕ_N and summing all other terms together leads to the linear algebraic equation

$$a_P\phi_P^{n+1}=\sum_N a_N\phi_N^{n+1}+b \tag{4.34}$$

in which

$$a_P = \sum_N a_N + \sum_f F_f + (1+0.5\hat{\theta})\frac{h_P^{n+1}}{\beta_P^{n+1}}\frac{\Delta A_P}{\Delta t} - S_P^P \Delta A_P$$

$$b = \left[(1+\hat{\theta})\frac{h_P^n \phi_P^n}{\beta_P^n} - 0.5\hat{\theta}\frac{h_P^{n-1}\phi_P^{n-1}}{\beta_P^{n-1}} \right]\frac{\Delta A_P}{\Delta t} + S_P^C \Delta A_P + \sum_f \left(F_f^{\parallel} + F_f^{\perp} \right) \tag{4.35}$$

$$a_N = D_f \Lambda\left(\left|P_f\right|\right) - F_f^- \tag{4.36}$$

$$F_f^{\perp} = -F_f^+ \gamma_P \hat{\phi}_P (\phi_{\perp,N} - \phi_{\perp,P}) - F_f^- \gamma_N \hat{\phi}_N (\phi_{\perp,P} - \phi_{\perp,N}) \tag{4.37}$$

$$F_f^{\parallel} = a_N \left(\vec{r}_{\parallel} \cdot \nabla\phi\right)_N - \left(a_N + F_f\right)\left(\vec{r}_{\parallel} \cdot \nabla\phi\right)_P \tag{4.38}$$

In the above derivation, the identity $F_f = F_f^- + F_f^+$ is used to replace $D_f \Lambda\left(\left|P_f\right|\right) + F_f^+$ with $a_N + F_f$. The flow divergence $\sum F_f$ in the a_P coefficient can lead to problems if mass is not conserved as is the case during the iteration process before convergence. For stability purposes it is required that $a_P = \sum a_N$ in the absence of temporal and source/sink terms (Patankar 1980). The condition is satisfied by multiplying the discretized continuity equation (Equation 4.43) by ϕ_p^{n+1} and subtracting it from Equation (4.34) resulting in the following modified a_P term:

$$a_P = \sum_N a_N + \left[(1+0.5\hat{\theta})h_P^{n+1}\left(\frac{1}{\beta_P^{n+1}} - 1\right) + (1+\hat{\theta})\frac{h_P^n}{\beta_P^n} - 0.5\hat{\theta}\frac{h_P^{n-1}}{\beta_P^{n-1}} \right]\frac{\Delta A_P}{\Delta t} - S_P^P \Delta A_P \tag{4.39}$$

All other terms remain the same. It is clear that the above equation satisfies $a_P = \sum a_N$ when the temporal and source/sink terms are zero. The explicit deferred corrections $F_f^{\perp}$ and $F_f^{\parallel}$ improve accuracy but may slow the model convergence since they must be estimated using

previous iteration values. Othogonal grids require less deferred corrections (computations) and generally have faster convergence rates. Finally, Equation (4.34) is applied at all of the internal computational cells resulting in a system of linear algebraic equations.

4.2.10 Implicit Relaxation

The above algebraic system of equations is solved using iterative solvers. Because of the non-linearity, and deferred corrections, under-relaxation is applied in the inner loop to each system of equations in order to increase the stability and convergence of the outer non-linear (outer) iteration loop. This under-relaxation, known as implicit relaxation, is applied by introducing a relaxation parameter in the discretized equations (Majumdar 1988) as

$$\frac{a_P}{\alpha_\phi}\phi_P^{n+1} = \sum_N a_N \phi_N^{n+1} + b + \frac{1-\alpha_\phi}{\alpha_\phi} a_P \phi_P^m \tag{4.40}$$

where α_ϕ is an under-relaxation parameter and the superscript m indicates the previous iteration value. An effect of under-relaxation is to make the coefficient matrix more diagonally dominant which improves the solver convergence.

4.3 Hydrodynamics

4.3.1 Discretized Continuity and Momentum Equations

The discretized form of the hydrodynamic equations may be obtained using the methods described in Section 4.2. The resulting discretized momentum equation for cell P is given by Equation (4.34) with $\phi = V_i^*$, $\Gamma = \nu_t$, and $\beta = 1$. The source/sink terms are given by

$$S_P^P = -\left(m_b c_b \sqrt{U^2 + c_w u_w} + \gamma_W \frac{\rho_a}{\rho} C_D W \right)_P \tag{4.41}$$

$$S_P^C = \left[\varepsilon_{ij3} f_c h V_j + \frac{\tau_{Wi}}{\rho} + m_b c_b \sqrt{U^2 + c_w u_w} U_{wi} + \frac{\rho_a}{\rho} C_D W \left(W_i^E + \gamma_W U_{wi} \right) - \frac{h}{\rho} \nabla (p + p_a) \right]_P \tag{4.42}$$

All other terms remain the same. The pressure is discretized using the Gauss Divergence Theorem because it is conservative. In addition it is also least computationally intensive since the water levels (pressure) need to be calculated at the cell faces. The velocity gradients may be calculated with Gauss's Divergence Theorem or the Weighted Least-Squares method (see Section 4.2.5). As noted in Section 4.1 an advantage of using a collocated grid is that the coefficients a_P and a_N, and the sink term S_P^P are the same for both momentum equations thereby reducing the computational cost compared to a staggered grid.

The discretized continuity equation is given by

$$\left[(1 + 0.5\hat{\theta}) h_P^{n+1} - (1 + \hat{\theta}) h_P^n + 0.5\hat{\theta} h_P^{n-1} \right] \frac{\Delta A_P}{\Delta t} + \sum_f F_f^{n+1} = 0 \tag{4.43}$$

where $F_f^{n+1} = h_f^{n+1} V_f^{n+1} \Delta l_f$ is the outward flux at cell face *f*.

4.3.2 Coupling of Velocity and Water Level – SIMPLEC Algorithm

The hydrodynamic equations are solved in a segregated manner in which each equation is linearized and solved separately in a sequential manner within an iteration loop in order to obtain a converged solution. This is referred to as a segregated iterative solver. Coupling between the velocity and water level is achieved with the SIMPLEC algorithm (van Doormal and Raithby 1984). The main difficulty in solving the momentum equations is that the water level is not

known a priori and must be calculated as part of the solution. The solution algorithm procedure is described below.

First, the pressure $p^* = \rho g \overline{\eta}^*$ is assumed based on the previous time step water level (i.e. $\overline{\eta}^* = \overline{\eta}^n$). Then, the momentum equations are solved for the corresponding intermediate or approximate velocity, V_i^*, as

$$\frac{\partial (hV_i^*)}{\partial t} + \frac{\partial (hV_j^* V_i^*)}{\partial x_j} = \frac{\partial}{\partial x_j}\left(\nu_t h \frac{\partial V_i^*}{\partial x_j} \right) - \frac{h}{\rho}\frac{\partial p^*}{\partial x_i} + S_i \tag{4.44}$$

where S_i includes all the remaining terms.

The discretized momentum equations for V_i^{n+1} and V_i^* including implicit relaxation are given by (see Section 4.2.10)

$$\frac{a_P}{\alpha_V} V_{i,P}^{n+1} = \sum_N a_N V_{i,N}^{n+1} - \frac{h_P}{\rho}\nabla_i p_P^{n+1} \Delta A_P + S_P \Delta A_P + \frac{1-\alpha_V}{\alpha_V} a_P V_{i,P}^m \tag{4.45}$$

$$\frac{a_P}{\alpha_V} V_{i,P}^{*} = \sum_N a_N V_{i,N}^{*} - \frac{h_P}{\rho}\nabla_i p_P^{*} \Delta A_P + S_P \Delta A_P + \frac{1-\alpha_V}{\alpha_V} a_P V_{i,P}^m \tag{4.46}$$

where α_V is the implicit relaxation coefficient set here to 0.8 (see Section 4.2.10).

The velocity correction, V', and pressure corrections, p', are defined such that both the momentum and continuity equations are satisfied:

$$V_i^{n+1} = V_i^* + V_i' \ , \ p^{n+1} = p^* + p' \tag{4.47.a.b}$$

The discretized velocity correction equation is obtained by subtracting Equation (4.46) from Equation (4.45) and using Equation (4.47a,b) as

$$\frac{a_P}{\alpha_V} V'_{i,P} = \sum_N a_N V'_{i,N} - \frac{h_P}{\rho} \nabla_i p'_P \Delta A_P \tag{4.48}$$

In the SIMPLEC algorithm, the velocity correction is assumed to vary smoothly so that $\sum a_N V'_{i,N}$ may be approximated as $V'_{i,P} \sum a_N$. This leads to the velocity and pressure correction relation:

$$V'_i = -G \nabla_i p' \tag{4.49}$$

where

$$G = \frac{\alpha_V \frac{h_P \Delta A_P}{\rho a_P}}{1 - \frac{\alpha_V}{a_P} \sum a_N}$$

An equation for the pressure correction, p', is derived as follows. First, the bed elevation is assumed constant so that the temporal term in the continuity equation may be rewritten as $\partial h / \partial t = (\partial p / \partial t) / (\rho g)$. Next, the temporal term $\partial p / \partial t$ is discretized in time using Equation (4.9) and the velocity and pressure definitions $V_i \rightarrow V_i^{n+1} = V_i^* + V'_i$ and $p \rightarrow p^{n+1} = p^* + p'$ are substituted leading to the following semi-discrete pressure correction equation:

$$\frac{(1 + 0.5\hat{\theta})(p^* + p') - (1 + \hat{\theta}) p^n + 0.5\hat{\theta} p^{n-1}}{\rho g \Delta t} = \frac{\partial}{\partial x_j} \left(hG \frac{\partial p'}{\partial x_j} \right) - \frac{\partial \left(h V_j^* \right)}{\partial x_j} \tag{4.50}$$

Note that at convergence, $p' \rightarrow 0$, $V_i^{n+1} = V_i^*$, $p^{n+1} = p^*$, and the above equation reduces to the discretized continuity equation (see Section 4.3.1).

The inter-cell velocities are calculated with a Rhie and Chow (1983) type momentum interpolation method:

$$V_f^* = \overline{\left(n_i H_i^*\right)}_f - \alpha_V \overline{\left(\frac{\Delta A_P}{a_P}\right)}_f \left(\frac{h}{\rho}\nabla_\perp p^*\right)_f \tag{4.51}$$

where

$H_{i,C}^* = V_{i,C}^* + \alpha_V \frac{\Delta A_C}{a_{P,C}} \frac{h_C}{\rho} \nabla_i p_C^*$, with C = (P,N), and $a_{P,C}$ is the coefficient a_P for the momentum equation applied on cell C

$\overline{(\ )}_f$ = denotes interpolation (see Section 4.2.3)

The cell face velocities are also corrected as $V_f^{n+1} = V_f^* + V_f'$. The momentum interpolation equation for the cell-face velocity correction is given by

$$V_f' = \overline{\left(n_i H_i'\right)}_f - \alpha_V \overline{\left(\frac{\Delta A_P}{a_P}\right)}_f \left(\frac{h}{\rho}\nabla_\perp p'\right)_f \tag{4.52}$$

where

$$H_{i,C}' = V_{i,C}' + \alpha_V \frac{\Delta A_C}{a_{P,C}} \frac{h_C}{\rho} \nabla_i p_C' = \frac{\alpha_V}{a_{P,C}} \left(\sum_N a_N V_{i,N}'\right)_C$$

Using again the assumption that the velocity correction varies smoothly so that $\sum_N a_N V_{i,N}'$ may be approximated by $V_{i,N}' \sum_N a_N$ and substituting in the Equation (4.52) leads to the equation for the cell-face velocity correction:

$$V_f' = -G_f \left(\nabla_\perp p'\right)_f \tag{4.53}$$

where

$$G_f = \frac{\alpha_V \dfrac{h_f^*}{\rho}\overline{\left(\dfrac{\Delta A_P}{a_P}\right)}_f}{1-\overline{\left(\dfrac{\alpha_V}{a_P}\sum a_N\right)}_f}$$

The momentum interpolation method avoids the checkerboard oscillations associated with the collocated grid. It is noted that this approach is slightly different from the original Rhie and Chow (1983) method used by similar models such as Lai (2010). The present approach is found to be significantly more stable.

The overall procedure of the SIMPLEC algorithm consists of the following steps:

1. Guess the water level and pressure field p^*
2. Solve the momentum equations (Equation 4.44) to obtain V_i^*
3. Calculate the velocities and fluxes at cell faces
4. Solve the pressure correction equation (Equation 4.50) to obtain p'
5. Use the correction equations to adjust the velocities and water levels
6. Treat the corrected water level and pressure field as a new guess, and repeat this procedure from Step 2 until convergence

4.3.3 Discretized Pressure Correction Equation

The discretized pressure correction equation is given by Equation (4.34) with $\phi = p'$ and the following modifications:

$$a_P = \sum_N a_N - S_P^P \Delta A_P \tag{4.54}$$

$$a_N = \frac{h_f^* G_f \Delta l_f}{\left|\delta_\perp\right|} \tag{4.55}$$

$$S_P^P = -\frac{1+0.5\hat{\theta}}{\rho g \Delta t} \tag{4.56}$$

$$b = -\frac{(1+0.5\hat{\theta})p^* - (1+\hat{\theta})p^n + 0.5\hat{\theta}p^{n-1}}{\rho g}\frac{\Delta A_P}{\Delta t} + \sum_f \left(F_f^{\parallel} - F_f^*\right) \tag{4.57}$$

$$F_f^{\parallel} = a_N\left[\left(\vec{r}_{\parallel}\cdot\nabla p'\right)_N - \left(\vec{r}_{\parallel}\cdot\nabla p'\right)_P\right] \tag{4.58}$$

The terms S_P^C and $F_f^{\perp}$ described in Section 4.2.9 are not used in the case of the pressure correction equation. No implicit relaxation is applied to the pressure correction equation.

4.3.4 Wetting and Drying

During numerical simulations of the surface water flows with sloped beaches, sand bars, and islands, the land-water interface changes with time. This means that it is possible for nodes at the land-water interface to be wet or dry throughout a given simulation. A threshold water depth (i.e. a small value such as 0.02 m for field cases) is used to judge drying and wetting. If the depth at the cell center is larger than the threshold value, then the node is considered to be wet. If the depth at the cell center is smaller than the threshold value, then the node is considered to be dry. For the implicit solver, all of the wet and dry cells are included in the matrix solver. Dry cells are assigned with a zero velocity.

4.4 Spectral Waves

The wave-action balance equation is solved on a nonuniform Cartesian grid. Half-plane spectral waves are propagated from the ocean towards land using an implicit finite difference forward marching scheme. For additional details on the numerical methods the reader is referred to Mase (2001) and Mase et al. (2005).

4.5 Discretized Surface Roller

The surface roller energy equation is solved on the wave grid using a finite difference method. The source terms are calculated at the cell centers. The advective or transport term is approximated using either the first-order or second-order upwind finite difference scheme. The first-order upwind scheme is illustrated in one dimension as

$$\left.\frac{\partial \phi}{\partial x}\right|_i = \begin{cases} \dfrac{\phi_i - \phi_{i-1}}{x_i - x_{i-1}}, & \text{for } w_{x,i} > 0 \\ \dfrac{\phi_{i+1} - \phi_i}{x_{i+1} - x_i}, & \text{for } w_{x,i} < 0 \end{cases} \tag{4.59}$$

where

$\phi = 2E_{sr} c w_x$

i = subscript indicating the position along the x-direction

x_i = cell coordinate at position i

w_x = wave unit vector in the x-direction

A similar equation can be written in the y-direction. The second-order upwind scheme is given by (Ferziger and Peric 1997)

$$\left.\frac{\partial \phi}{\partial x}\right|_i = \begin{cases} \dfrac{-\left[(x_{i-2}-x_i)^2-(x_{i-1}-x_i)^2\right]\phi_i+(x_{i-2}-x_i)^2\phi_{i-1}-(x_{i-1}-x_i)^2\phi_{i-2}}{(x_{i-1}-x_i)(x_{i-1}-x_i)(x_{i-2}-x_{i-1})}, & \text{for } w_{x,i}>0 \\ \dfrac{-\left[(x_{i+2}-x_i)^2-(x_{i+1}-x_i)^2\right]\phi_i+(x_{i+2}-x_i)^2\phi_{i+1}-(x_{i+1}-x_i)^2\phi_{i+2}}{(x_{i+1}-x_i)(x_{i+1}-x_i)(x_{i+2}-x_{i+1})}, & \text{for } w_{x,i}<0 \end{cases} \tag{4.60}$$

For uniformly spaced grids, the above equation reduces to

$$\left.\frac{\partial \phi}{\partial x}\right|_i = \begin{cases} \dfrac{3\phi_i-4\phi_{i-1}+\phi_{i-2}}{2\Delta x}, & \text{for } w_{x,i}>0 \\ \dfrac{-3\phi_i+4\phi_{i+1}-\phi_{i+2}}{2\Delta x}, & \text{for } w_{x,i}<0 \end{cases} \tag{4.61}$$

where Δx is the grid resolution in the *x*-direction.

The surface roller equation involves only the spatial derivate term or advection term, but is solved using a pseudo time marching method, which is equivalent to an iteration method. An Euler scheme is applied in pseudo time as

$$E_{sr}^{n+1} = E_{sr}^{n} + \frac{\Delta t_{sr}}{2}\left(-D_r + f_e D_{br} - \frac{\partial(2E_{sr}cw_j)}{\partial x_j}\right)^n \tag{4.62}$$

where the superscript *n* indicates the pseudo time step, Δt_{sr} is the surface roller time step and is determined as $\Delta t_{sr} = 0.5\min\left(\max(\Delta x, \Delta y)/c\right)$, with Δx and Δy being the cell sizes in the *x* and *y* directions, respectively.

The calculation is performed by setting the initial guessed roller energy and computing the new approximate value using Equation (4.62). For the first wave condition (time step) the initial roller energy is set to zero and subsequently the initial guess roller energy is set to the value of the previous wave condition. The converged solution is usually reached after about 40 to 80 pseudo-time steps for the first wave time step and 10 to 20 iterations for subsequent wave

time steps.

4.6 Sediment Transport

The so-called semi-coupled sediment transport model proposed by Wu (2004) is adopted here, in which the sediment calculations are decoupled from the hydrodynamic calculations but the sediment transport, bed change, and bed material sorting equations are simultaneously solved in a coupled form at each time step.

4.6.1 Discretized Sediment Transport Equation

The sediment transport equation is discretized using the finite volume method described in the previous section for the general transport equation. The resulting discretized equation is given by Equation (4.34) with $\phi = C_{tk}$, $\Gamma = r_{sk}\nu_s$, and $\beta = \beta_{tk}$. The source/sink terms are given by

$$S_P^P = -\left(\alpha_t \omega_{sk}\right)_P, \qquad S_P^C = \left(\alpha_t \omega_{sk}\right)_P C_{tk*,P}^{n+1}$$

4.6.2 Discretized Bed Change Equation

The fractional bed change equation is discretized as

$$\Delta z_{bk} = \frac{\Delta t}{\rho_s (1 - p'_m)} \left[\alpha_t \omega_{sk} \left(C_{tk}^{n+1} - C_{tk*}^{n+1} \right) + S_{bk}^{n+1} \right] \tag{4.63}$$

where

$$S_{bk}^{n+1} = \frac{\partial}{\partial x_j} \left(D_s q_{bk} \frac{\partial z_b}{\partial x_j} \right) = \frac{D_s}{\Delta A_P} \sum_f (q_{bk})_f \left(\nabla_\perp z_b \right)_f \Delta l_f$$

D_s = bed slope coefficient [-]

$(q_{bk})_f$ = magnitude of the fractional bed load at the cell face f [kg/m/s]

$(\nabla_\perp z_b)_f$ = bed slope calculated at the cell face

The bed slope term, S_{bk}^{n+1}, is usually small and can be treated explicitly during the iteration procedure.

The total bed change is equal to

$$\Delta z_b = \sum_k \Delta z_{bk} \tag{4.64}$$

4.6.3 Discretized Bed Material Sorting Equations

The bed material sorting equation (Equation 3.73) is discretized as

$$p_{1k}^{n+1} = \frac{\Delta z_{bk} + \delta_1^n p_{1k}^n - \Delta z_2 p_k^{*n}}{\delta_1^{n+1}} \tag{4.65}$$

where $\Delta z_2 = \Delta z_b - \delta_1^{n+1} + \delta_1^n$ is the change in the top elevation of the second bed layer and

$$p_k^{*n} = \begin{cases} p_{1k}^n \text{ for } \Delta z_2 \geq 0 \\ p_{2k}^n \text{ for } \Delta z_2 < 0 \end{cases} \tag{4.66}$$

At the beginning of each time step, the thickness of the first layer (mixing layer) is calculated as

$$\delta_1 = \min\left[\max(\delta_{1,\min}, 2d_{50}, \Delta/2), \delta_{1,\max}\right] \tag{4.67}$$

where Δ is the bed form height (see Section 3.4.7), and $\delta_{1,\min}$ and $\delta_{1,\max}$ are the user specified minimum and maximum mixing layer thicknesses, respectively.

The thickness of the second layer is $\delta_2^{n+1} = \delta_2^n + \Delta z_2$. The bed material gradation in the second layer is calculated from the following discretized form of Equation (3.74):

$$p_{2k}^{n+1} = \frac{\delta_2^n p_{2k}^n + \Delta z_2 p_k^{*n}}{\delta_2^{n+1}} \tag{4.68}$$

In order to avoid the second layer from becoming extremely thin or thick, a layer merging and splitting algorithm is implemented between layers 2 and 3. If the second layer is too thick, it is divided into two layers; thus, the previous third layer becomes the new fourth layer, and the last two bottom layers are merged into one. If the second layer is too thin, it is merged with the previous third layer to form a new second layer; thus, the previous fourth layer becomes the new third layer. To illustrate the bed layering process, Figure 4.7 shows an example of the temporal evolution of 7 bed layers during erosional and depositional regimes.

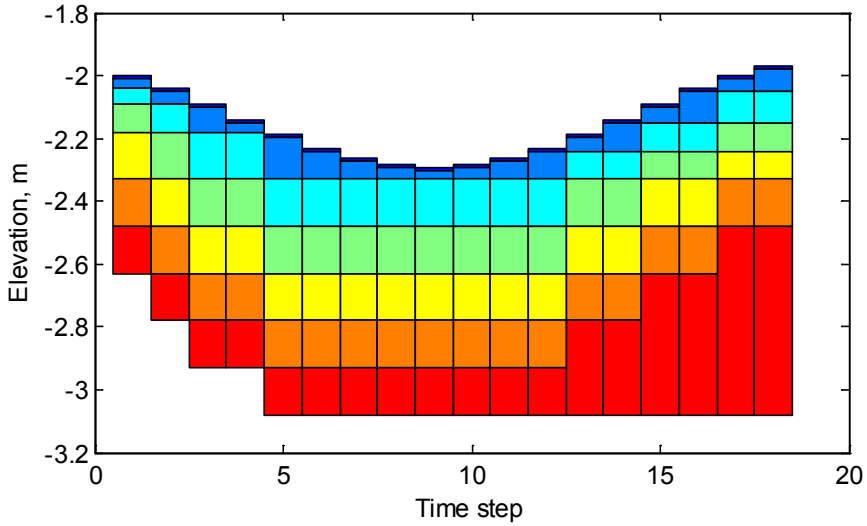

Figure 4.7. Schematic showing an example bed layer evolution. Colors indicate layer number and not bed composition.

4.6.4 Avalanching

When the slope of a non-cohesive bed, ϕ_b, is larger than the angle of repose, ϕ_R, the bed material will slide (avalanche) to form a new slope approximately equal to the angle of repose. The process of avalanching is simulated by enforcing $|\phi_b| \le \phi_R$ while maintaining mass conservation between adjacent cells (Sánchez and Wu 2011a). When the angle of repose is exceeded, the bed change due to avalanching between cell *P* and its adjacent cell *N* is given by (see Figure 4.8)

$$\frac{(z_{b,N} + \Delta z^a_{b,N}) - (z_{b,P} + \Delta z^a_{b,P})}{\delta} = \text{sgn}\,\phi_b \tan\phi_r \tag{4.69}$$

where

Δz^a_b = avalanching bed change [m]

δ = cell center distance between cells *P* and *N,*

$$\text{sgn}(X) = \begin{cases} -1 \text{ for } X \ge 0 \\ 1 \text{ for } X < 0 \end{cases} = \text{sign function}$$

$$\tan\phi_b = (z_{b,N} - z_{b,P}) / \delta$$

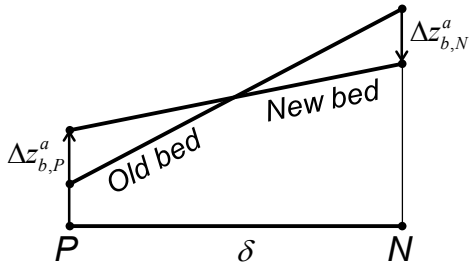

Figure 4.8. Avalanching between two cells.

The sgn(X) function accounts for the fact that the bed slope may have a negative or positive sign. The corresponding mass balance equation is given by

$$\Delta A_N \Delta z^a_{b,N} + \Delta A_p \Delta z^a_{b,P} = 0 \tag{4.70}$$

where ΔA is the cell area. Combining Equations (4.69) and (4.70) leads to

$$\Delta z^a_{b,P} = \frac{\Delta A_N \delta}{\Delta A_P + \Delta A_N} \left(\tan\phi_b - \operatorname{sgn}\phi_b \tan\phi_R\right) \mathrm{H}\left(|\phi_b| - \phi_R\right) \tag{4.71}$$

where H(X) is the Heaviside step-function equal to 1 for $X \geq 0$ and equal to 0 for $X < 0$. H(X) represents the activation of avalanching. The above equation is exact but limited to avalanching between two cells. In actuality avalanching may occur over multiple cells and induce additional avalanching at neighboring cells. A relaxation approach is adopted as follows (see Figure 4.9):

$$\Delta z^a_{b,P} = \alpha_a \sum_N \frac{\Delta A_N \delta}{\Delta A_P + \Delta A_N} \left(\tan\phi_b - \operatorname{sgn}\phi_b \tan\phi_R\right) \mathrm{H}\left(|\phi_b| - \phi_R\right) \tag{4.72}$$

where α_a is the under-relaxation factor (approximately 0.25-0.5). α_a is used to stabilize the avalanching process and avoid overshooting.

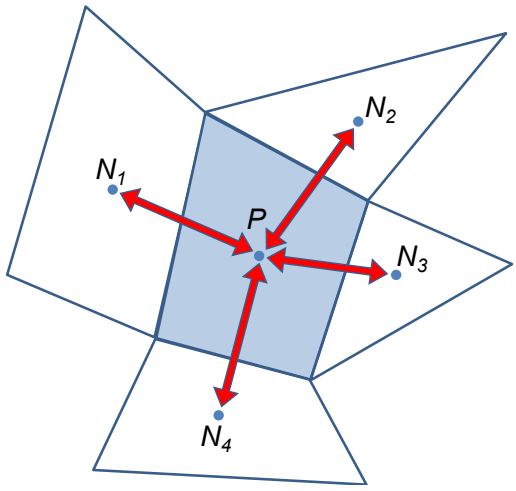

Figure 4.9. Avalanching computational stencil.

Equation (4.72) may be applied to any grid geometry type (i.e. triangle, rectangle, etc.) and for situations in which neighboring cells are joined at corners without sharing a cell face. Equation (4.72) is applied by sweeping through all computational cells to calculate Δz_b^a and then modifying the bathymetry as

$$z_b^{m+1} = z_b^m + \Delta z_b^a \tag{4.73}$$

where the superscript *m* indicates the avalanching iteration. The sweeping process is repeated until avalanching no longer occurs. The above avalanching procedure is relatively simple and is very stable.

4.6.5 Hard Bottom

The sediment transport and bed change equations assume a loose bottom in which the bed material is available for entrainment. However, hard bottoms may be encountered in practical engineering applications where bed materials are non-erodible, such as bare rocks, carbonate reefs, and concrete coastal structures. At hard bottom cells it is required that the bed elevation, z_b, be at or above the hard bottom elevation, z_{hb} (i.e. $z_{hb} \le z_b$). At each time step it is required that

$$z_{hb} \le z_b^{n+1} = z_b^n + \Delta z_b \tag{4.74}$$

The hard bottom limited bed change (lower limit) at each time step is defined as

$$\Delta z_{b,hb} = z_{hb} - z_b^n \tag{4.75}$$

The bed change for each size class is limited according to

$$\Delta z_{bk,hb} = p_{1k}^{m} \Delta z_{b,hb} \tag{4.76}$$

where the superscript *m* indicates the previous iteration value. Inserting the above equation into the bed change equation leads to

$$C_{tk,hb} = C_{tk} + \frac{\rho_s \left(1 - p'_m\right) p_{1k}^{m} (z_b^n - z_{b,hb})}{\alpha_t \omega_{sk} \Delta t} + \frac{D_s}{\alpha_t \omega_{sk} \Delta A_P} \sum_f \left(q_{bk}^{m}\right)_f \left(\nabla_\perp z_b^{m}\right)_f \Delta l_f \tag{4.77}$$

The bed-slope term (last term) is somewhat difficult to deal with because of the spatial gradients. However, it is generally much smaller than the erosion/deposition term. Here, for simplicity, the bed-slope term is limited by simply setting the bed-slope fluxes to zero once the upslope cell has reached the hard bottom. The equilibrium sediment concentration is limited as

$$C'_{t*k} = \min(C_{tk*}, C_{tk,hb}) \tag{4.78}$$

It is noted that when the bed reaches the hard bottom (i.e. $z_b^n = z_{b,hb}$) and the bed-slope term not considered, then the above equation becomes simply

$$C'_{t*k} = \min(C_{tk*}, C_{tk}) \tag{4.79}$$

which is the equation proposed by Wu (2007).

4.6.6 Coupling of Sediment Transport, Bed Change, and Bed Material Sorting

The discretized sediment transport, bed change, and bed material sorting equations are solved in a coupled manner but decoupled from the flow equations during each time step. This is referred to semi-coupling. In order to derive the coupling procedure, the sediment transport capacity in Equation (3.79) is treated implicitly as

$$C_{t*k}^{n+1} = p_{1k}^{n+1} C_{tk}^{*n+1} \tag{4.80}$$

Substituting Equation (4.80) into the bed change (Equation 4.63) and sorting equations (Equation 4.65) and then substituting the bed sorting equation into the bed change equation, one can derive the fractional and total bed change equations as

$$\Delta z_{bk} = \frac{A_k + \Delta z_b G_k}{B_k} \tag{4.81}$$

Summing Equation (4.81) over all sediment size classes and using Equation (4.64) yields the following total bed change equation:

$$\Delta z_b = \frac{\sum_{k=1}^{N} \frac{A_k}{B_k}}{1 - \sum_{k=1}^{N} \frac{G_k}{B_k}} \tag{4.82}$$

where

$$B_k = \rho_s \left(1 - p'_m\right) \delta_1^{n+1} + \Delta t \alpha_t \omega_{sk} C_{tk}^{*n+1}$$

$$A_k = \Delta t \left\{ \alpha_t \omega_{sk} \left[C_{tk}^{n+1} \delta_1^{n+1} - C_{tk}^{*n+1} \left(\delta_1^n p_{1k}^n + (\delta_1^{n+1} - \delta_1^n) p_{1k}^{*n} \right) \right] + S_{bk}^{n+1} \delta_1^{n+1} \right\}$$

$$G_k = \Delta t \alpha_t \omega_{sk} C_{tk}^{*n+1} p_{1k}^{*n}$$

The sediment transport solution procedure is summarized as follows:

1. Calculate bed roughness and shear stresses
2. Calculate the mixing layer thickness δ_1^{n+1}
3. Estimate the potential sediment concentration capacity C_{tk}^{*n+1}
4. Guess the new bed composition as $p_{1k}^{n+1} = p_{1k}^n$
5. Calculate the fractional concentration capacity $C_{t*k}^{n+1} = p_{1k}^{n+1} C_{tk}^{*n+1}$

6. Solve sediment transport equations for each sediment size class for C_{tk}^{n+1}
7. Calculate the total and fractional bed changes Δz_b and Δz_{bk}
8. Determine the bed sorting in the mixing layer p_{1k}^{n+1}
9. Repeat steps 5 through 8 until convergence
10. Update the bed elevation as $z_b^{n+1} = z_b^n + \Delta z_b$
11. Calculate the bed gradation in the bed layers below the mixing layer
12. Calculate avalanching
13. Correct the sediment concentration due to the change in flow depth

The algorithm usually converges within 10 to 20 iterations.

4.7 Iterative Solvers for Discretized Algebraic Equations

The selection of an iterative solver is one of the key issues impacting the overall performance of the model. The developed model has six iterative solvers available: 1) GMRES, 2) BiCGStab, 3) SIP, 4) ICCG, 5) Gauss-Seidel, and 6) Gauss-Seidel with Successive-Over-Relaxation.

The default iterative solver is a variation of the GMRES (Generalized Minimum RESidual) method (Saad 1993). The original GMRES method (Saad and Schultz 1986) utilizes the Arnoldi process to reduce the coefficient matrix to the Hessenburg form and minimizes the norm of the residual vector over a Krylov subspace at each iterative step. The variation of the GMRES method used here allows changes in preconditioning at every iteration (Saad 1993). The Incomplete Lower Upper Factorization ILUT (Saad 1994) is used as the preconditioner to speed-

up convergence. The GMRES solver is applicable to symmetric and non-symmetric matrices and leads to the smallest residual for a fixed number of iterations. However, the memory requirements and computational costs become increasingly expensive for larger systems.

The BiCGStab (BiConjugate Gradient Stabilized) iterative solver is also a Krylov subspace solver and is applicable to symmetric and non-symmetric matrices (Saad 1996). BiCGStab also uses ILUT as a preconditioner (Saad 1994). The BiCGStab method can be viewed as a combination of the standard Biconjugate Gradient solver where each iterative step is followed by a restarted GMRES iterative step.

The SIP (Strongly Implicit Procedure) iterative solver uses an Incomplete Lower Upper decomposition, with an approximation to the exact Lower Upper decomposition (Stone 1968). The method is specifically designed for systems of algebraic equations derived from partial differential equations. The implementation here is for a 5-point stencil and therefore only applies to structured grids.

The ICCG (Incomplete Cholesky preconditioned Conjugate Gradient) iterative solver is applicable to symmetric matrices such as the pressure correction equation (Ferziger and Peric 2002). The implementation here is also for a 5-point stencil and therefore can only be applied to structured grids.

The simplest iterative solvers implemented here are the point-implicit Gauss-Seidel solvers with or without Successive-Over-Relaxation. The Successive-Over-Relaxation may speed-up convergence but can also lead to model divergence (Patankar 1980); thus it is used only for the pressure correction. Even though the Gauss-Seidel method requires more iterations for convergence, the overall efficiency may be higher than the GMRES and BiCGStab because each

iteration is computationally inexpensive and the code is efficiently parallelized. However, based on experience and testing, the GMRES and BiCGStab methods are usually more robust and perform better for large time steps.

4.8 Convergence and Time-Stepping

During the iterative solution process, error is calculated and used to determine if a solution has converged, diverged, or stalled at an error below a predefined tolerance threshold. An estimate of the error in solving the general algebraic equation is given by

$$r_P = \frac{1}{a_P}\left(\sum_N a_N \phi_N^{n+1} - a_P \phi_P^{n+1} + b\right) \tag{4.83}$$

Statistics can be defined based on normalized errors. For example, the l^2-norm is given by

$$\|r\|_2 = \sqrt{\sum_{cells\ P} r_P^2} \tag{4.84}$$

Since this value depends on the total number of cells, the final statistic (referred to as the residual) that is used for estimating the model convergence is obtained by dividing the norm by the number of cells:

$$R^m = \frac{\|r\|_2}{\sqrt{N_c}} \tag{4.85}$$

where R^m is referred to as the "normalized residual error" and the superscript refers to the iteration number. R^m is calculated for each variable that is solved at each iteration step of the solution process. Each equation has default maximum tolerances for determining if the solution has converged, diverged, or stalled. The maximum number of iterations that is imposed is set equal to M. A minimum of 5 iterations are required for the hydrodynamic equations, and a

minimum of M/2 iterations are required for the sediment transport equations. Table 4.1 lists the default criteria to determine whether the iterative solution procedure has converged, diverged, or requires a reduced time step.

Table 4.1. Default criteria to determine whether the iterative solution procedure has converged, diverged, or requires a reduced time step.

Variable	Converged	Diverged	Reduce Time Step
Current velocity [m/s]	*If* $R^m<1\times10^{-7}$ *or* $\lvert R^m-R^{m-2}\rvert<1\text{x}10^{-7}$	*If* $R^M>1.0\times10^{-2}$ or $\lvert V_i\rvert>10$	*If* $R^M>1.0\times10^{-3}$
Pressure-correction/ρ [Pa/ρ]	*If* $R^m<1\times10^{-8}$ *or* $\lvert R^m-R^{m-2}\rvert<1\text{x}10^{-8}$	*If* $R^M>1.0\times10^{-3}$ or $\lvert p/\rho\rvert>50$	*If* $R^M>1.0\times10^{-4}$
Total-load concentration [kg/m^3]	*If* $R^m<1\times10^{-8}$ *or* $\lvert R^m-R^{m-2}\rvert<1\times10^{-8}$	*If* $R^M>1.0\times10^{-3}$ or $C_{tk}<0$	None

The time steps for the flow and sediment transport are the same in order to avoid mass conservation problems and for simplicity. If any of the time step reduction criteria is met, then the time step is reduced by half and a minimum number of 3 time steps are calculated at the newly reduced time step. If the last time step converges properly, then the time step is increased. The maximum time step allowed is equal to the user-specified initial time step.

4.9 Ramp and Spin-up Periods

For most coastal applications, the model is initialized from a “cold start”, which means that the water level and current velocities are initially set to zero. The ramp period is the time period over which the model forcing is relaxed from the initial condition to the actual prescribed values. The ramp period (also known as relaxation period) allows the model to slowly transition from the initial condition without “shocking” the system. The ramp function is defined as

$$f_{Ramp} = \frac{1}{2} - \frac{1}{2}\cos\left[\pi \min\left(t / t_{Ramp}, 1\right)\right] \tag{4.86}$$

where t is the simulation time and t_{Ramp} is the ramp duration. The ramp function provides a smooth function for transitioning from the initial condition and is plotted in Figure 4.10.

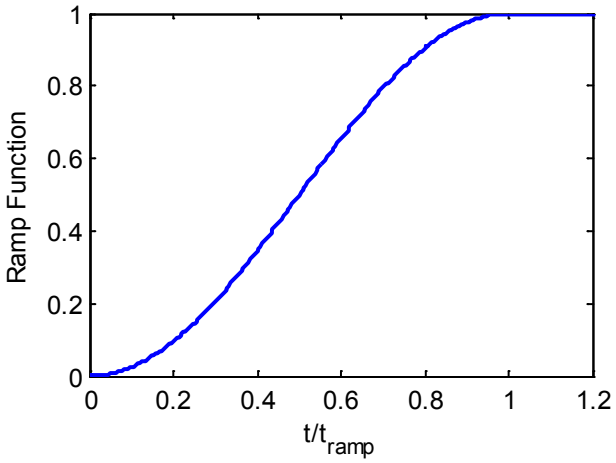

Figure 4.10. Ramp function.

The ramp function is applied to the model forcing conditions, including the wave forcing, surface wind, and significant wave height, by direct multiplication of these parameters by the ramp function at each time step during the ramp period. Boundary conditions are specified without consideration of this ramp period; therefore, the boundary values, such as water levels, current velocities, and fluxes, are also slowly transitioned from the initial conditions by direct multiplication of the boundary values by the ramp function at each time step during the ramp period.

The spin-up period is the time it takes for the effects of the initial condition to disappear from the model solution and has reached either a steady or dynamic equilibrium. The length of

the spin-up period depends on the problem. For simple steady-state problems of nearshore hydrodynamics, the spin-up period is usually slightly larger than the ramp period. For field applications however the spin-up period may be several days, or weeks.

4.10 Coupling Procedure of Flow and Wave Models

The flow and wave models can be run separately or coupled together using a process called steering. The variables passed from the wave model to flow are the significant wave height, peak wave period, wave direction, wave breaking dissipation, and radiation stress gradients. The wave model uses the updated bathymetry (if sediment transport is turned on), water levels, and current velocities from the flow model. The time interval at which the wave model is run is called the steering interval. Currently, the steering interval is constant and the input spectra in the wave model must be at constant intervals without any gaps. The steering process is illustrated in Figure 4.11 in which the simulation time is plotted as a function of the computational time.

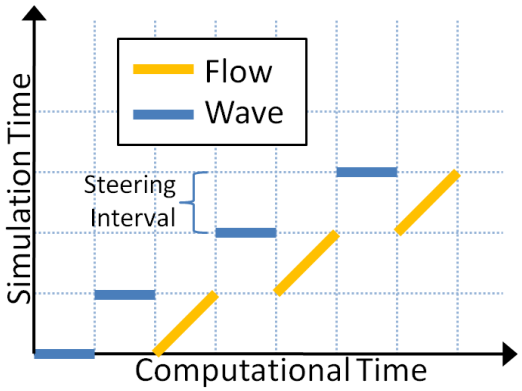

Figure 4.11. Schematic of coupling (steering) process between the flow and wave models.

The flow and wave model steering process is contained within the same code (known as the inline steering). Two main advantages of the inline steering module are: (1) the model runs faster because there is no need to use communication files or reinitialize the models (memory allocation, variable initialization, etc.) and (2) the inline steering makes the improvement and maintenance of the steering module easier for the developers and also makes the code portable for other operating systems. The inline steering process is summarized below:

1. The wave model is run for the first two time steps and the wave information is passed to the flow model (Figure 4.11). If specified, the surface roller model is run on the wave grid and the roller contributions are added to the wave radiation stresses.
2. The wave height, period, dissipation, radiation stress gradients, and wave unit vectors are interpolated spatially from the wave grid to the flow grid.
3. The flow model is run until the next steering interval and wave variables are linearly interpolated throughout time during the specified steering interval. At each flow time step, variables such as wave length and bottom orbital velocities are updated using the new water depths and current velocities.
4. Water levels, current velocities, and bed elevations are estimated for the next wave steering interval and are interpolated from the flow grid to the wave grid.
5. The wave model is then run again for the following wave time step.
6. Step 2-5 are repeated until the end of the simulation.

4.10.1 Spatial Interpolation and Extrapolation

The developed model allows for the flow and wave models to have the same or different grids. If the same grid is used, then no spatial interpolation is carried out. If different grids are used, then spatial interpolation is necessary in order to transfer information from one model grid to another model grid. The interpolation of wave variables from the wave grid to the flow grid is done using a combination of bilinear and linear triangular interpolation methods. Bilinear interpolation is applied at regular Cartesian cells where 4 neighboring points can be identified, and triangular interpolation is applied otherwise. If the extents of the wave and flow grids are different (e.g. if the flow or wave grid is smaller), then the extrapolation of variables is necessary in order to avoid boundary problems with the models. Different extrapolation methods are applied to different variables as described below.

4.10.1.1 Water Levels

Water levels are extrapolated using a nearest neighbor interpolation over the entire domain, but not across land (dry) boundaries. This approach is more physically accurate than extrapolating only to a certain distance since water levels are controlled mainly by tides along the coast and the spatial variation is usually much smaller than the tidal range.

$$\left(\overline{\eta}_P\right)^m_{wave} = \left(\overline{\eta}_N\right)^m_{flow} \tag{4.87}$$

where $\overline{\eta}_P$ is the water level at cell P, $\overline{\eta}_N$ is the water level at the nearest neighbor, and m is the wave time step. The subscripts '*flow*' and '*wave*' indicate the flow and wave grids, respectively. The calculation of the water level at the wave time step on the flow grid is described in a subsequent section.

4.10.1.2 Current Velocities

Current velocities are extrapolated to a certain distance referred to as the extrapolation distance. A nearest neighbor extrapolation is applied to cells within that distance and multiplied by a cosine function to produce a smooth transition from the boundary to a value of zero:

$$\left(U_{i,P}\right)_{wave}^{m} = f_{ext}\left(U_{i,N}\right)_{flow}^{m} \tag{4.88}$$

where $U_{i,P}$ is the current velocity at the extrapolated cell, $U_{i,N}$ is the current velocity at the nearest neighbor, and f_{ext} is an extrapolation function given by

$$f_{ext}\left(r_N, r_{ext}\right) = \frac{1}{2}\left\{1 + \cos\left[\pi \min\left(\frac{r_N}{r_{ext}}, 1\right)\right]\right\} \tag{4.89}$$

where $r_N = \left|\vec{r}_N\right|$ is the distance vector from cell *P* to *N*, r_{ext} is the flow extrapolation distance. The extrapolation function provides a smooth transition from the nearest neighbor to zero.

4.10.1.3 Bed Elevations

Extrapolating bed elevations from a boundary can lead to sharp changes in bathymetry in the wave model and instability problems in both the wave and flow models. Therefore, a plausible approach is to extrapolate the bed change as follows:

$$\left(z_{b,P}\right)_{wave}^{m} = \left(z_{b,P}\right)_{wave}^{m-1} + f_{ext}\left(\Delta z_{b,N}\right)_{flow}^{m} \tag{4.90}$$

where $z_{b,P}$ is the bed elevation at the extrapolated cell, and $z_{b,N}$ is the bed elevation at the nearest neighbor.

4.10.1.4 Significant Wave Height

The significant wave height is extrapolated in the same way as the current velocities to an extrapolation distance as:

$$\left(H_{s,P}\right)_{flow}^{m} = f_{ext}\left(H_{s,N}\right)_{wave}^{m} \tag{4.91}$$

where $H_{s,P}$ is the significant wave height at the extrapolated cell, and $H_{s,N}$ is the significant wave height at the nearest neighbor.

4.10.1.5 Peak Wave Period

The peak wave period is extrapolated in a similar way as the water levels using a nearest neighbor extrapolation over the entire domain, but not across land (dry) boundaries. This approach is more physically plausible than extrapolating to a finite distance.

4.10.1.6 Mean Wave Direction

The mean wave direction is first converted to wave unit vectors which are extrapolated in space. Wave unit vectors are also extrapolated over the entire domain, except across land (dry) boundaries, without consideration of an extrapolation distance.

4.10.2 Temporal Interpolation and Prediction

Because the wave model requires the water surface elevation at times that are ahead of the flow model, the water surface elevation and currents must be predicted for the wave time step. If the steering interval is relatively small (<30 min), then the values from the last flow time step may be used without significant error:

$$\left(U_i\right)_{flow}^{m} = \left(U_i\right)_{flow}^{n}, \quad \left(\overline{\eta}\right)_{flow}^{m} = \left(\overline{\eta}\right)_{flow}^{n}, \quad \left(z_b\right)_{flow}^{m} = \left(z_b\right)_{flow}^{n} \tag{4.92a,b,c}$$

where *m* is the next wave time step, and *n* is the last flow model time step. For many coastal engineering applications, it is desirable and common to use relatively large steering intervals of 2 to 3 hours. In such cases, the change in water depth has the largest influence on the nearshore wave heights. Therefore, when using large steering intervals, it is desirable to make better predictions of water levels and not use water levels of the previous flow time step. In cases where the relative surface gradients at any time are much smaller than the mean tidal elevation, a better approximation of water level may be obtained by decomposing the water level into

$$\left(\overline{\eta}\right)_{flow}^{m} = \left(\overline{\eta}_m\right)_{flow}^{m} + \left(\overline{\eta}_v\right)_{flow}^{m} \tag{4.93}$$

where $\overline{\eta}_m$ is the mean water level and $\overline{\eta}_v$ is a variation around the mean due to tide, wave, and wind generated surface gradients. $\overline{\eta}_m$ can be estimated from water level boundary conditions and is generally much larger, so $\overline{\eta}_v$ may be neglected. The surface gradient term may be approximated as

$$\left(\overline{\eta}_v\right)_{flow}^{m} \approx \left(\overline{\eta}_v\right)_{flow}^{n} = \left(\overline{\eta}\right)_{flow}^{n} - \left(\overline{\eta}_m\right)_{flow}^{n} \tag{4.94}$$

For most coastal inlet applications, the above equation is a better representation of the water surface elevation and is used as the default.

After spatially interpolating the wave height, period, dissipation, and forcing onto the flow model grid, the variables are linearly interpolated in time. The wavelength, bottom orbital velocity, and mean wave-current bottom friction are then updated including current-wave interactions at each time step.

CHAPTER V

VERIFICATION: ANALYTICAL SOLUTIONS

The analytical cases described in this chapter were selected for verification of the model to confirm that the intended numerical algorithms have been correctly implemented. Four goodness-of-fit statistics are used to assess the model performance and are defined in Appendix A. The verification test cases are:

a. 1D scalar transport
b. Wind setup in a flat basin
c. Wind-driven flow in a circular basin
d. Tidal propagation in a quarter annulus
e. Transcritical flow over a bump
f. Long-wave runup over a frictionless slope

5.1 Scalar Transport

The model is applied to a one-dimensional (1D) problem of scalar transport in an idealized rectangular domain to analyze the model performance in simulating the processes of advection and diffusion and assess numerical diffusion in the model as a function of time step and grid resolution. For a 1D rectangular channel, the depth-averaged scalar transport equation is given by

$$\frac{\partial(h\phi)}{\partial t}+\frac{\partial(hU\phi)}{\partial x}=\frac{\partial}{\partial x}\left(\Gamma h\frac{\partial\phi}{\partial x}\right)-kh\phi \tag{5.1}$$

where t is the time, x is the distance along the channel, h is the total water depth, ϕ is a depth-averaged scalar quantity (e.g. sediment concentration, salinity), Γ is the diffusion coefficient, and k is a decay coefficient. Assuming a constant water depth, current velocity and diffusion coefficient, the analytical solution to the above problem for an initial Gaussian shaped scalar field can be derived as (Chapra 1997)

$$\phi(x,t)=\frac{M}{2\sqrt{\pi(\Gamma t+C)}}\exp\left[-\frac{\left(x-x_0-Ut\right)^2}{4(\Gamma t+C)}-kt\right] \tag{5.2}$$

where x_0 is the location of the initial profile center, M is a constant which controls the magnitude of the initial profile, and C is also a constant which controls the width of the initial profile. The analytical solution is compared with the calculated results for advection only, combined advection and diffusion, and combined advection, diffusion and sink.

The test considers a wide rectangular flume 10 km long and 30 m wide. Two grids are set up with constant resolutions of 10 and 50 m, and calculations are made with two different time steps of 1 and 10 min. A summary of the selected model parameters are listed in Table 5.1. The second-order Hybrid Linear/Parabolic Approximation (HLPA) scheme of Zhu (1991) is used for the advection term. Results using the first-order upwind and exponential schemes are also provided for reference. The diffusion term is discretized with the standard second-order central difference scheme. The temporal term is discretized with the first-order backward difference scheme. The same numerical methods employed here are implemented for the momentum, sediment and salinity transport equations.

Table 5.1. Model setup for the scalar transport test cases.

Parameter	**Value**
Simulation duration	24 hr
Ramp period duration	0.0
Grid resolution, Δx	10, 50 m
Time step, Δt	1, 10 min
Advection scheme	HLPA, Upwind, and Exponential
Current velocity	-0.05 m/s
Water depth	2.0 m
Diffusion coefficient	0.0, 3.0 m^2/s
Constant M	1800
Constant *C*	259,200 m^2

5.1.1 Advection Only

For this case, the diffusion and decay coefficients are set to zero. The scalar profile is initially located x_0 = 7.5 m and transported upstream with a velocity of -0.05 m. The calculated and analytical scalar profiles at times 0 and 24 hr are presented in Figure 5.1. The corresponding goodness-of-fit statistics are presented in Table 5.2. The analytical scalar profile at 24 hr is equal to the initial profile displaced by 4.32 km. The first-order upwind produces significantly more numerical dissipation than the second-order HLPA scheme. The HLPA scheme is found to significantly increase the solver convergence rate leading to shorter computational times by about 37% compared to the simpler and less computationally intensive upwind scheme.

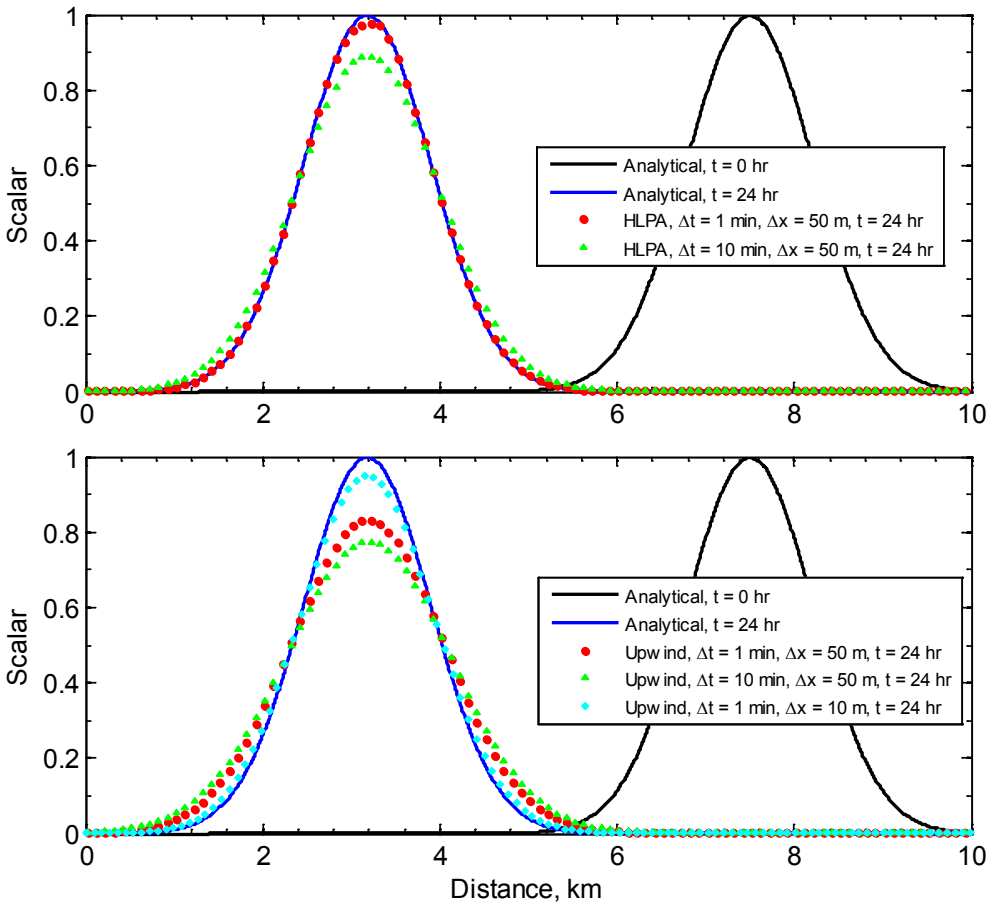

Figure 5.1. Analytical and calculated scalar profiles for the advection only case. Current is from right to left.

Table 5.2. Goodness-of-fit statistics* for the scalar advection test case.

Setting/Statistic	**Run**				
	1	**2**	**3**	**4**	**5**
Advection scheme	HLPA	HLPA	Upwind	Upwind	Upwind
Resolution, m	50	50	50	50	10
Time step, min	1	10	1	10	1
NRMSE, %	0.49	3.39	5.39	7.36	1.58
NMAE, %	0.34	2.05	3.30	4.54	1.00
R^2	0.999	0.993	0.983	0.965	0.999
*defined in Appendix A					

5.1.2 Advection and Diffusion

The scalar profile is initially located x_0 = 7.5 m and transported upstream with a -0.05 m/s velocity. The diffusion coefficient is set to 3 m^2/s, which is representative of sediment and salinity diffusion coefficients for coastal applications. The decay coefficient is set to zero. The initial scalar and the analytical and calculated ones at 24 hr are shown in Figure 5.2 for the HLPA and exponential schemes. Table 5.3 displays the correlation coefficients, RMSEs, and NRMSEs between the analytical solution and the calculations. Comparing to the previous case of advection only, the results show better correlation and smaller errors with both the advection and diffusion terms included. Physical diffusion tends to smooth out the scalar distribution, reducing the horizontal gradients and thus numerical dissipation. In the case of the exponential scheme a small phase lag is noticeable, which decreases with the smaller time step. Similar results were obtained by Chapra (1997). When diffusion is present, the differences between first and second order advection schemes become less significant. For a grid size of 50 m and time step of 1 min, the NMAEs for HLPA and exponential schemes are 0.36 and 0.73%, respectively for the case of advection and diffusion.

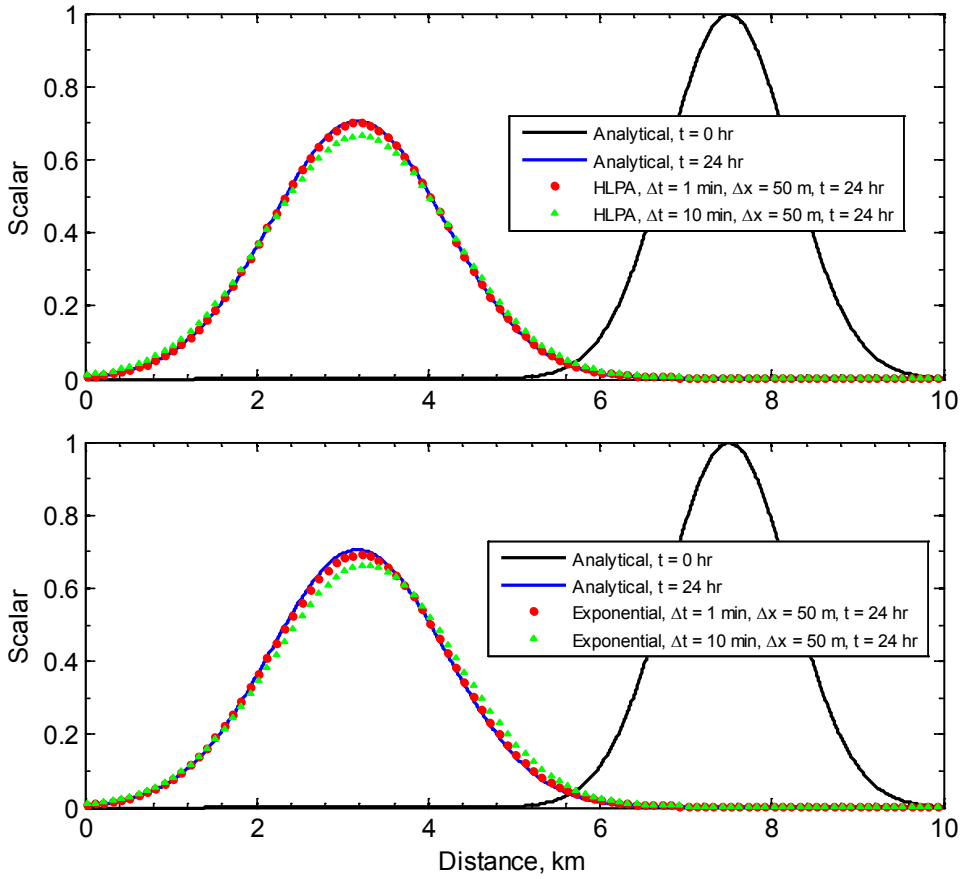

Figure 5.2. Analytical and calculated scalar profiles for the case of advection and diffusion using. Current is from left to right.

Table 5.3. Goodness-of-fit statistics* for the scalar advection-diffusion test case.

Setting/Statistic	**Run**			
	6	**7**	**8**	**9**
Advection scheme	HLPA	HLPA	Exponential	Exponential
Resolution, m	50	50	50	50
Time step, min	1	10	1	10
NRMSE, %	0.40	2.19	0.87	3.15
NMAE, %	0.36	1.64	0.73	2.22
R^2	0.999	0.998	0.999	0.994
*defined in Appendix A				

5.1.3 Advection, Diffusion, and Sink

As in the previous test cases, the initial scalar profile is located at x_0 = 7.5 m, the velocity is -0.05 m/s, and the diffusion coefficient is 3 m^2/s. The magnitude of the decay coefficient is chosen as 0.864 day^{-1} to test the numerical implantation and for illustration purposes. Figure 5.3 shows the initial scalar profile and the analytical and calculated scalar profiles at 24 hr. The corresponding goodness-of-fit statistics are presented in Table 5.4. Results show similar goodness-fit-statistics to the previous advection and diffusion test case. Similarly to the previous case, differences between first- and second order advection schemes are less significant compared to the advection only case due to the fact that physical diffusion tends to smooth out the scalar profile, reducing the horizontal gradients and numerical dissipation.

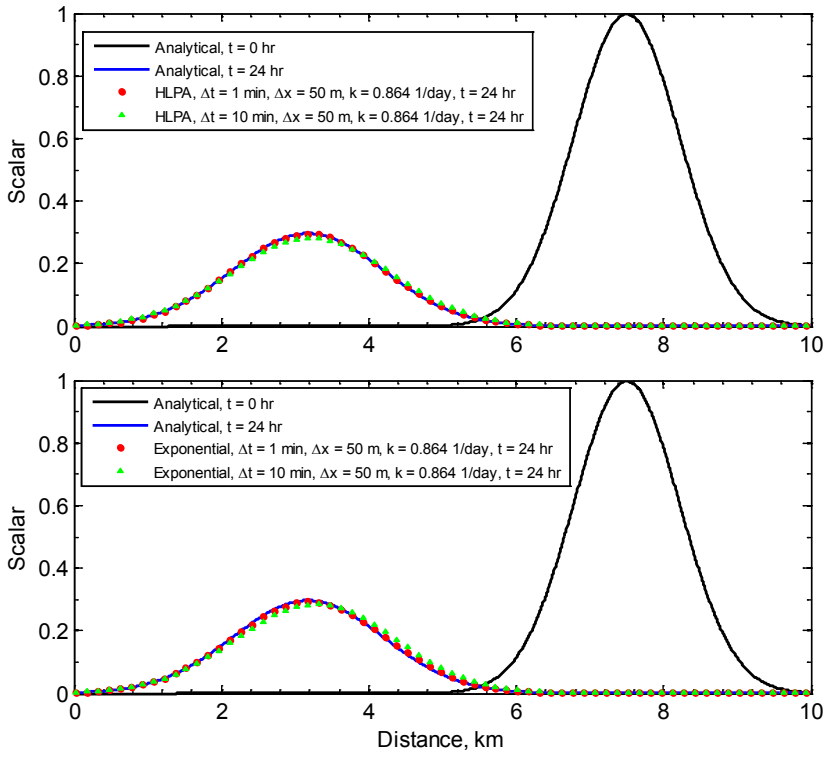

Figure 5.3. Analytical and calculated scalar profiles for the case of advection, diffusion, and decay. Current is from right to left.

Table 5.4. Goodness-of-fit statistics* for the scalar advection-diffusion-decay test case.

Setting/Statistic	**Run**			
	10	**11**	**12**	**13**
Advection scheme	HLPA	HLPA	Exponential	Exponential
Resolution, m	50	50	50	50
Time step, min	1	10	1	10
NRMSE, %	0.40	2.29	0.93	3.45
NMAE, %	0.36	1.71	0.77	2.42
R^2	0.999	0.997	0.999	0.991
*defined in Appendix A				

The above model testing shows that the best model results are obtained with the second-order HLPA advection. Simulations with large time steps and coarse mesh could generate extra numerical dissipation and result in excessive smoothing of the scalar field and thus underestimate of peak scalar values. To solve the transport problems with sharp gradients, a fine grid resolution and small time step are necessary.

5.2 Wind Setup in a Flat Basin

This verification case is designed to test the most basic model capabilities by solving the most reduced or simplified form of the governing equations in which only the water level gradient balances the wind surface drag. The specific model features/aspects to be tested are (1) spatially constant wind fields, (2) water surface gradient implementation, and (3) land-water boundary condition.

Assuming a closed basin with a spatially constant, steady state wind in one direction, no

advection, diffusion, bottom friction, waves or Coriolis force, the momentum equations reduce to

$$\rho g h \frac{\partial \eta}{\partial y} = \rho_a C_D |W| W \tag{5.3}$$

where $h = \zeta + \eta$ is the total water depth, ζ is the still water depth, η is the water surface elevation (water level) with respect to the still water level, C_D is the wind drag coefficient, y is the coordinate in the direction of the wind, g is the gravitational acceleration, ρ is the water density, ρ_a is the air density, and W is the wind speed. Assuming a constant wind drag coefficient, the following analytical expression for the water level may be obtained by integrating the above equation (Dean and Dalrymple 1984)

$$\eta = \sqrt{\frac{2\rho_a C_D |W| W}{\rho g}(y + C) + \zeta^2} - \zeta \tag{5.4}$$

where C is a constant of integration.

A computational grid with constant water depth of 5 m and irregular boundaries is used to verify the numerical methods. The computational grid has 60 columns and 70 rows and a constant resolution of 500 m. The irregular geometry is intentionally used to check for any discontinuities in processes near the land-water boundaries. The solution should be perfectly symmetric and independent of the geometry of the closed basin. The model is initialized from zero current velocity and water level. The steady state solution is reached by increasing the wind speed over a 3-hr ramp period and allowing the solution to reach the steady state over a 48-hr time period. Table 5.5 summarizes the model setup for this case.

Table 5.5. Flow model settings for the wind setup test case.

Parameter	**Value**
Time step	10 min
Simulation duration	48 hr
Ramp period duration	3 hr
Wind speed	10 m/s
Drag coefficient	0.0016
Advection terms	Off
Mixing terms	Off
Bottom friction	Off
Wall friction	Off
Coriolis force	Off

The calculated wind setup (water surface elevation) is shown in Figure 5.4 for the case of wind from the north and from the west. For both cases, the calculated wind setup is symmetric and has straight contour lines, which is consistent with the analytical solution. Figure 5.5 shows the wind setup along the center line of the domain for the case with wind from the north compared to the analytical solution. The goodness-of-fit statistics along this transect for the calculated vs. analytical water elevation include the Normalized Root Mean Square Error (NRMSE), Mean Absolute Error (MAE), squared correlation coefficient, R^2, and Bias as given in Table 5.6. The calculated water levels are in good agreement with the analytical solution.

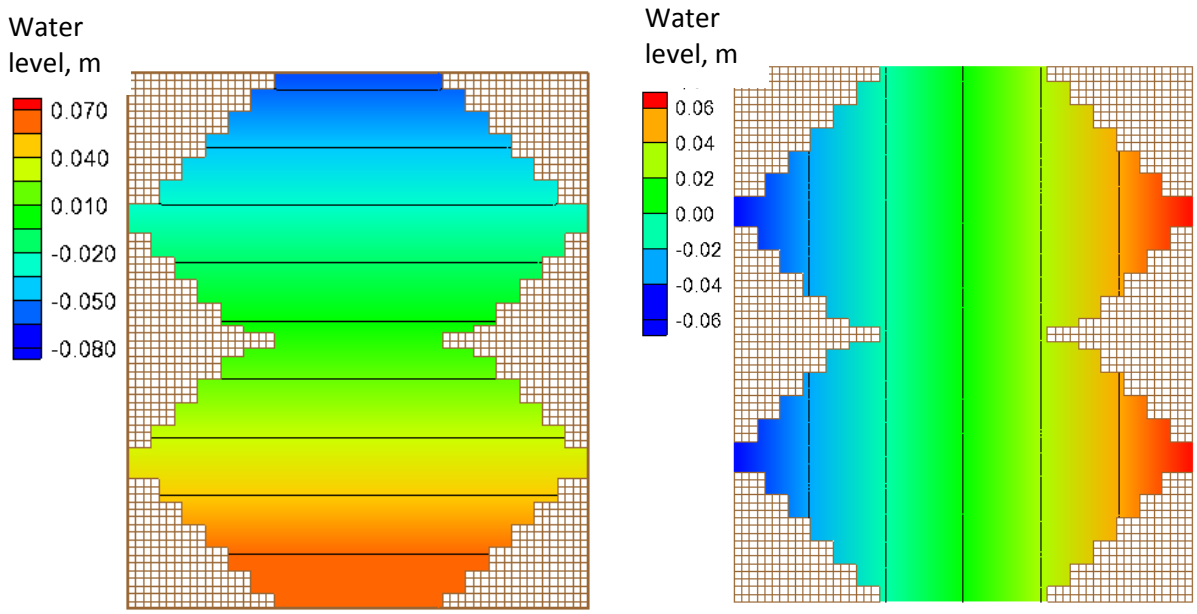

a. Wind from the north

b. Wind from the west

Figure 5.4. Calculated water levels in an irregular domain with a flat bed for the cases of wind from the north (left) and from the west (right).

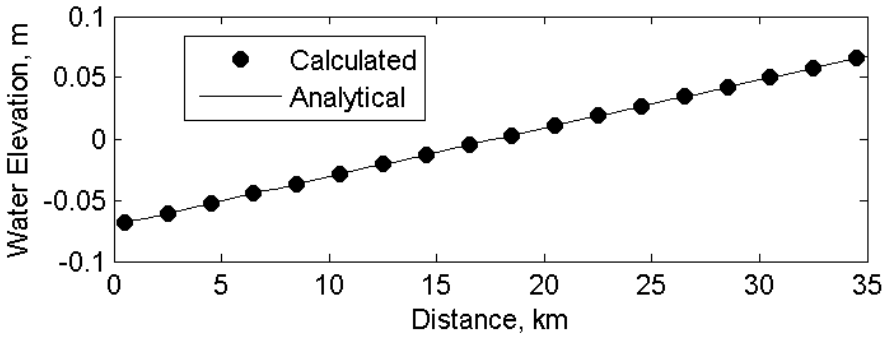

Figure 5.5. Analytical and calculated water levels along the vertical centerline of an irregular basin with flat bed and wind from the north. The calculated results are shown on every 10th grid point for better visualization.

Table 5.6. Water level goodness-of-fit statistics* for the wind setup test case.

	NRMSE, %	**NMAE, %**	**R^2**	**Bias, m**
Value	0.01	0.02	0.999	0.000
*defined in Appendix A				

5.3 Wind-driven Flow in a Circular Basin

DuPont (2001) presented an analytical solution for a closed circular domain on an f-plane with a linear bottom friction. Assuming no advection, diffusion, waves, or atmospheric pressure forcing, the linearized shallow water equations are

$$\frac{\partial U_i}{\partial x_i} = 0 \tag{5.5}$$

$$-\varepsilon_{ij} f_c U_j = -g\frac{\partial \eta}{\partial x_i} - \hat{\kappa} U_i + \varepsilon_{i2}\frac{x_2 W}{RH} \tag{5.6}$$

where

ε_{ij} = permutation operator equal to 1 for i,j, = 1,2; -1 for i,j = 2,1; and 0 for $i = j$

f_c =Coriolis parameter [1/s]

U_i = depth-averaged current velocities in the i direction [m/s]

g = gravitational constant [9.81 m/s^2]

η = water level [m]

$\hat{\kappa}$ =linear bottom friction coefficient [1/s]

R = radius of the circular domain [m]

H = water depth (constant) [m]

W = wind speed gradient [m^2/s^2].

The circular basin has a constant depth and is closed along its perimeter. The analytical solution for the water surface elevation is given by

$$\eta = \begin{cases} \dfrac{Wr^2 \sin 2\theta}{4gHR} & \text{for } f_c = 0 \\ \dfrac{Wf_c}{RgH\kappa}\left[\dfrac{R^2}{8} + \dfrac{r^2}{4}\left(\dfrac{\kappa}{f_c}\sin 2\theta - 1\right)\right] & \text{for } f_c \neq 0 \end{cases} \tag{5.7}$$

where r is the radius. The current velocities are independent of the Coriolis parameter and are given by

$$U_i = \frac{\varepsilon_{ij} x_j W}{2RH\kappa} \tag{5.8}$$

The test case is simulated utilizing unstructured triangular meshes. Two examples of the computational mesh are shown in Figure 5.6.

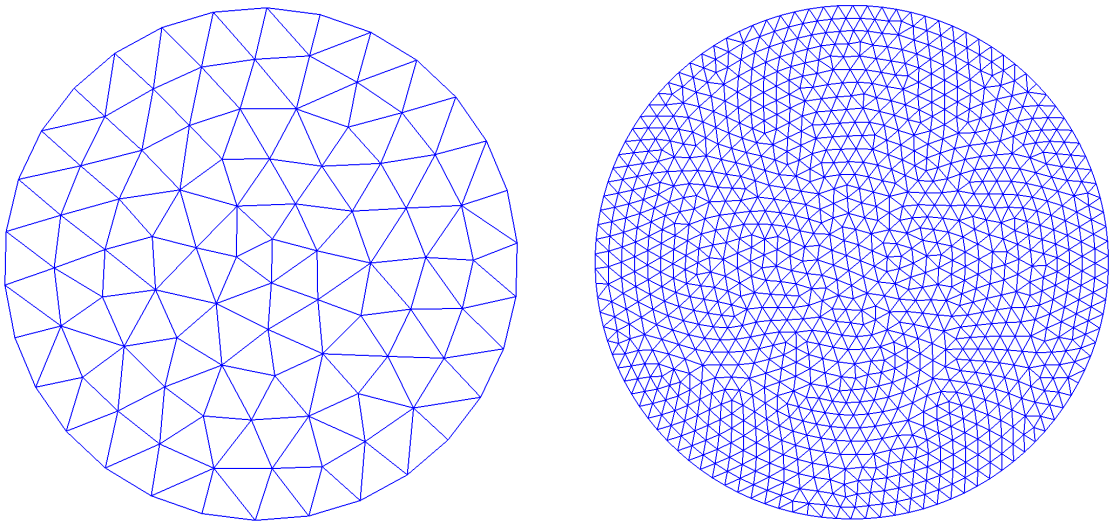

a. Coarse resolution b. Fine resolution

Figure 5.6. Examples of unstructured triangular meshes used to simulate the wind-driven flow in a circular basin.

Table 5.7. Model setup for the circular basin test case.

Parameter	**Value**
Time step	10 min
Simulation duration	10 hrs
Ramp period	6 hrs
Water depth	100 m
Mixing terms	Off
Wall friction	Off
Linear bottom friction coefficient	0.001 1/s
Latitude	0 and 43.43643º (f_c=0.0001 1/s)
Wind gradient	0.0001 m^2/s^2

Following DuPont (2001) the grid convergence is analyzed using the normalized error for the water level defined as

$$E_\eta = \frac{\int |\eta_A - \eta_C| dxdy}{\int dxdy} \sqrt{\frac{\int dxdy}{\int \eta_C^2 dxdy}} \tag{5.9}$$

where η_C and η_A are the calculated and analytical water levels, respectively. The grid convergence for the water levels is presented in Figure 5.7. In the case of the second-order discretizations corrections are included for the grid non-orthogonality. The results indicate that even if the corrections are not applied the model convergence rate is still better than first-order. This is due to the fact that the grid is almost orthogonal.

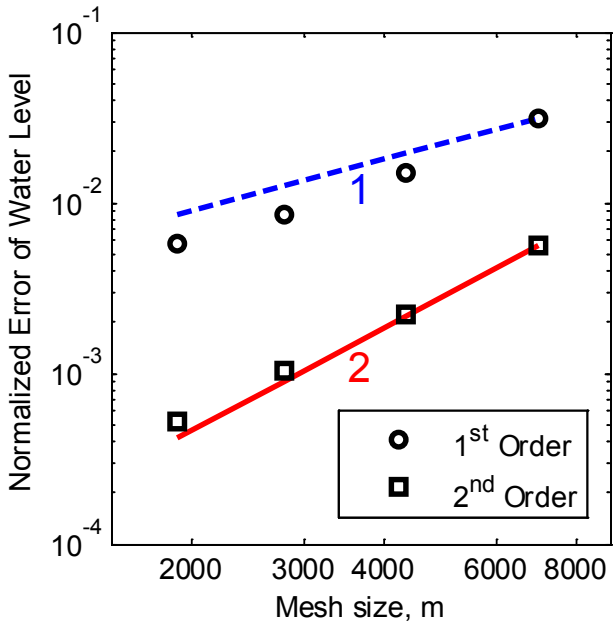

Figure 5.7. Convergence of the normalized error for the water level using the first- and second-order discretizations (for the case without Coriolis). The dashed blue and solid red lines correspond to first- and second-order convergence rates, respectively.

Excellent agreement is obtained with the analytical and computed water levels and current velocities. The computed and analytical water levels and current magnitudes are presented in Figure 5.8 and Figure 5.9 without and with Coriolis, respectively. The calculated water level field is very smooth and insensitive to the mesh. However, the calculated current velocities show relatively minor distortions in some locations due to distortions in the mesh.

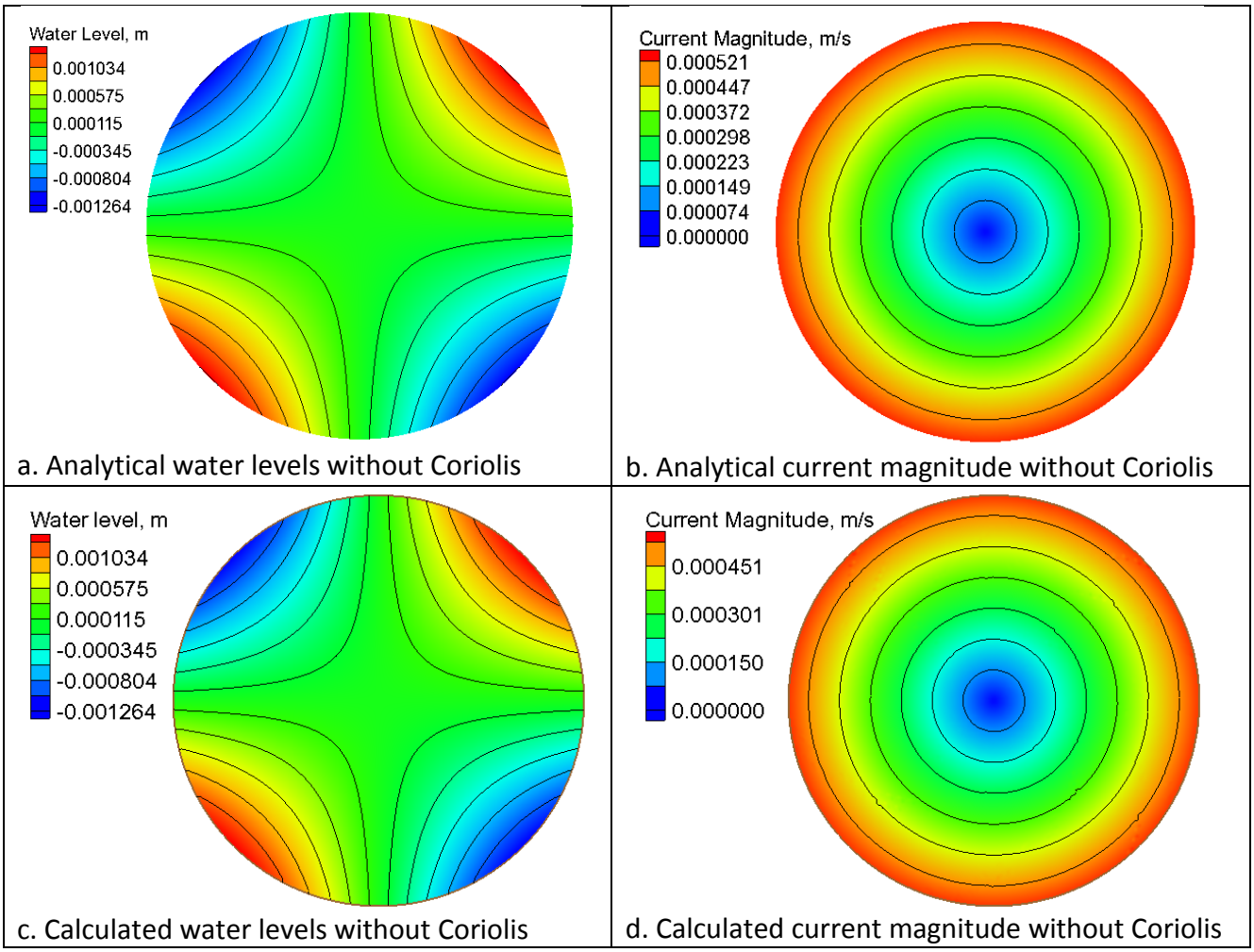

Figure 5.8. Simulated water levels and curent magnitudes without Coriolis.

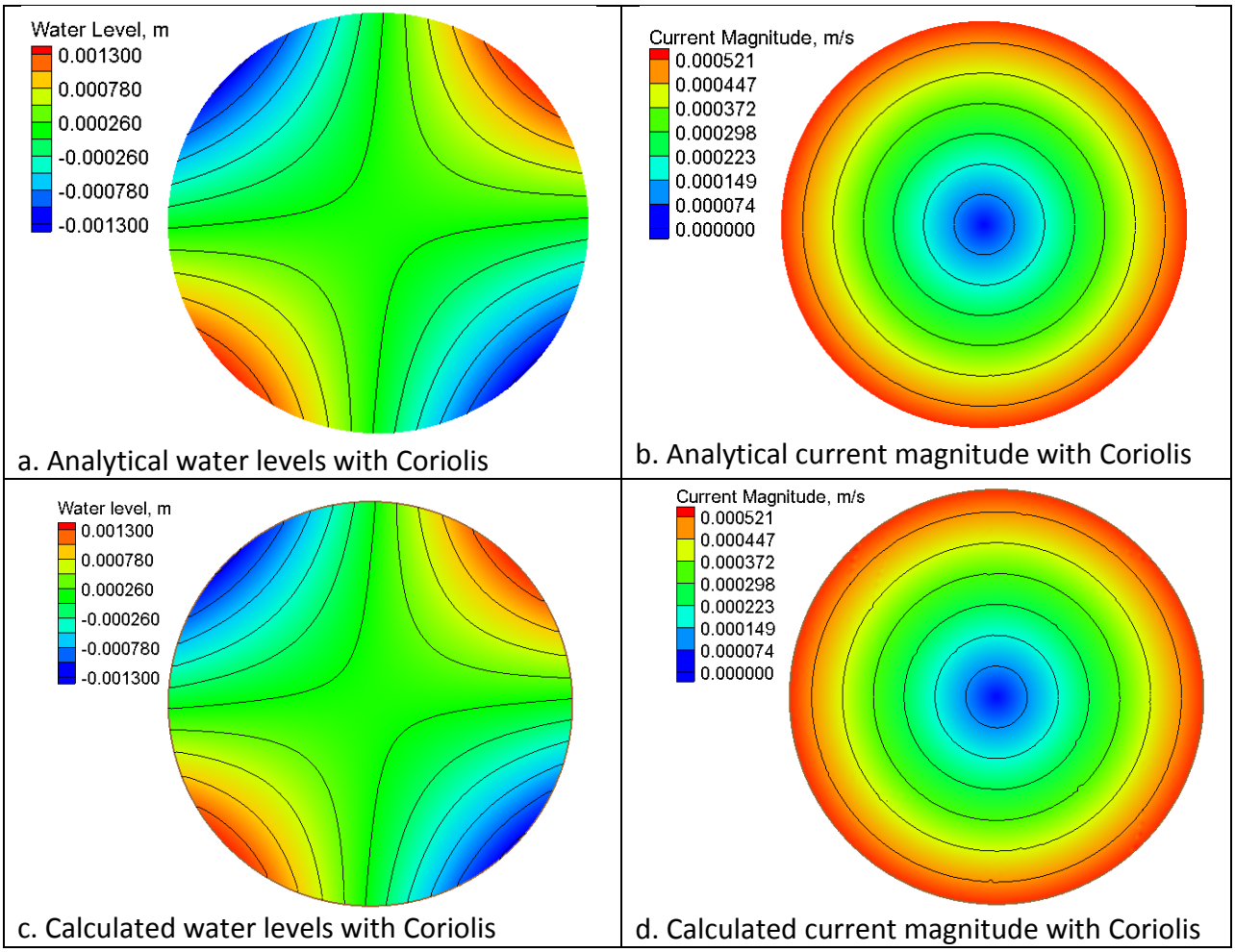

Figure 5.9. Simulated water levels and curent magnitudes with Coriolis.

5.4 Long-wave Propagation in a Rectangular Basin

The sloshing test case is useful for testing the model numerical dissipation for different temporal schemes. Assuming no Coriolis, bottom friction, advection, diffusion, and that the water elevation, is much smaller than the water depth, the governing equations are given by

$$\frac{\partial \eta}{\partial t} + H \frac{\partial U}{\partial x} = 0 \tag{5.10}$$

$$\frac{\partial U}{\partial t} = -g \frac{\partial \eta}{\partial x} \tag{5.11}$$

where

t = time [s]

x = horizontal coordinate [m]

U = current velocity [m/s]

H = water depth (constant) [m]

η = water level with respect to the Still Water Level (SWL) [m]

Eliminating the velocity from both equations leads to the classical wave equation

$$\frac{\partial^2 \eta}{\partial t^2} = gh \frac{\partial^2 \eta}{\partial x^2} \tag{5.12}$$

Given a closed rectangular basin of length L and width W, the following solution can be found for simple harmonic motion (Lamb 1932):

$$\eta(x,t) = A\cos(kx)\exp(i\omega t) \tag{5.13}$$

where $k = m\pi / L$ is the eigenvalue, with $m = 1,2,...$; and $\omega = 2\pi / T$ is the wave frequency, with T being the eigen (wave) period given by

$$T = \frac{2}{\sqrt{gh\left(m / L\right)^2}} \tag{5.14}$$

When $m = 1$, the solution is referred to as the fundamental mode, which is analyzed here. The model domain is 1000-m long and 300-m wide. The computational grid is shown in Figure 5.10. The grid has a constant grid spacing of 100 m. The model setup is summarized in Table 5.8.

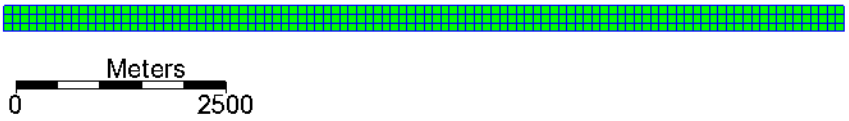

Figure 5.10. Computational grid for the sloshing test case.

Table 5.8. Summary of the model setup for the sloshing test case.

Model Parameter	**Value**
Water depth	10 m
Wave amplitude	1 cm
Time step	18 s
Simulation duration	10 hrs
Ramp period	0 s
Grid resolution	100 m
Advection	Off
Diffusion	Off
Bottom friction	Off
Temporal scheme	1st and 2nd order

Figure 5.11 shows snap shots of the water levels at different times during the simulation

as calculated with the first- and second-order temporal schemes. The first-order scheme shows an appreciable reduction in wave amplitude after only the first wave cycle. The second-order scheme, however, follows closely the analytical solution.

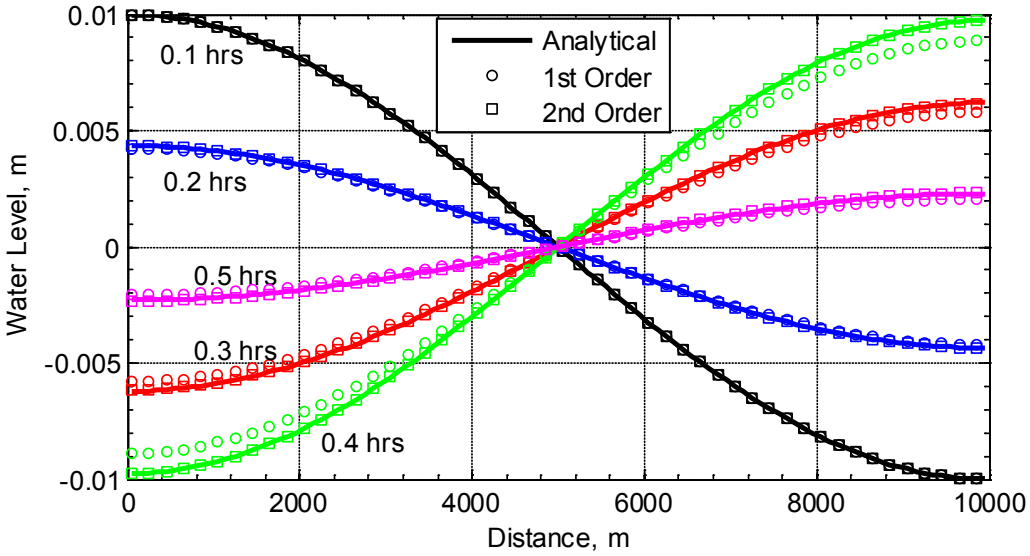

Figure 5.11. Water level profiles at different times for the sloshing test case calculated with the first- and second-order temporal schemes.

In order to demonstrate the low dissipation of the second-order scheme, snap shots of the water levels calculated using the second-order temporal scheme after approximately 16 and 16.5 wave cycles are shown in Figure 5.12.

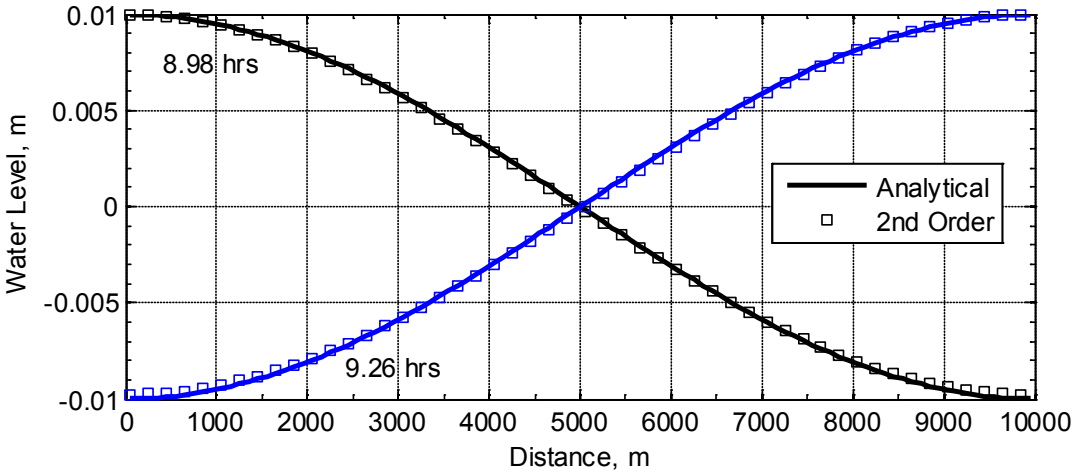

Figure 5.12. Water level profiles at different times for the sloshing test case calculated with the second-order temporal scheme.

The difference in numerical dissipation between 1st and 2nd order temporal schemes can be appreciated in Figure 5.13 which shows the time series of water levels calculated at $x = L$. In the case of the 1st order scheme, the wave amplitude is reduced by approximately half within 4 wave cycles, while the 2nd order schemes maintains the same wave amplitude for the duration of the simulation.

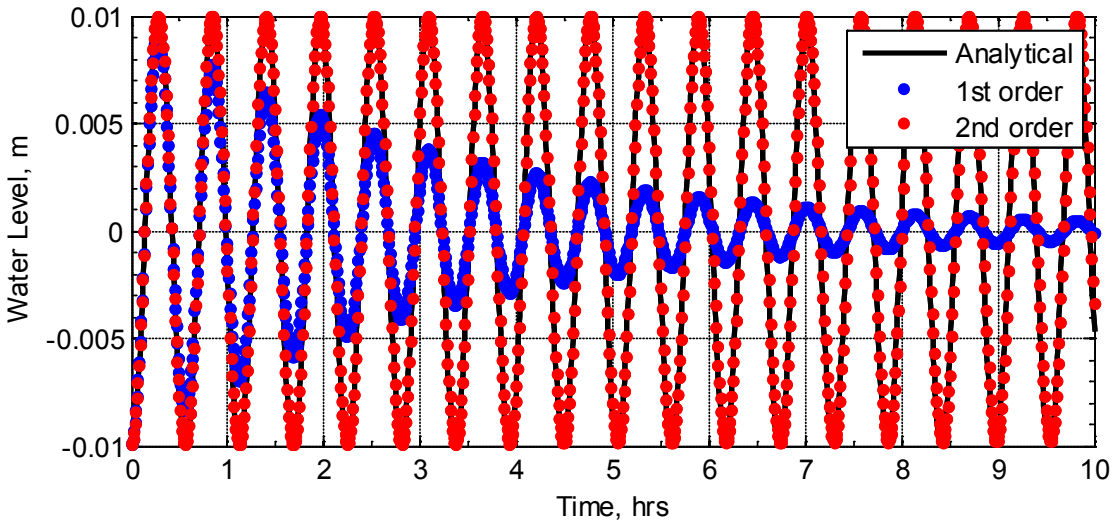

Figure 5.13. Water level time series calculated at $x = L$ using the first- and second-order temporal schemes.

It is noted that there is a small inconsistency between the problem governing equations and the model governing equations. The numerical model solves the shallow water equations in conservative form and does not assume that the wave amplitude is small relative to the water depth. However, as long as the wave amplitude is specified such that it is much small than the water depth, the model governing equations are approximately equivalent to Equations (5.10) and (5.11).

5.5 Tidal Propagation in a Quarter Annulus

The purpose of this verification case is to assess the model performance in simulating long wave propagation. The case is useful for testing the model performance and symmetry with a tidal forcing specified at a curved boundary. Because there is no bottom friction or mixing, the test case is also useful for looking at numerical dissipation.

Lynch and Gray (1978) presented the analytical solution for depth-averaged long-wave propagation in an annular domain. The case is for a linearly sloping bed, and without bottom friction, Coriolis force, or horizontal mixing (see Table 5.9). The offshore boundary consists of a single tidal constituent (see Figure 5.14).

Table 5.9. Quarter annulus setup parameters

Parameter	**Value**
Deepwater tidal amplitude	0.3048 m (1 ft)
Tidal period	12.42 hr (M2 tide)
Inner radius	60.96 km
Outer radius	152.4 km
Inner water depth	10.02 m
Outer water depth	25.05 m
Bathymetry profile	Linear
Bottom friction	None
Mixing terms	Off
Coriolis force	Off

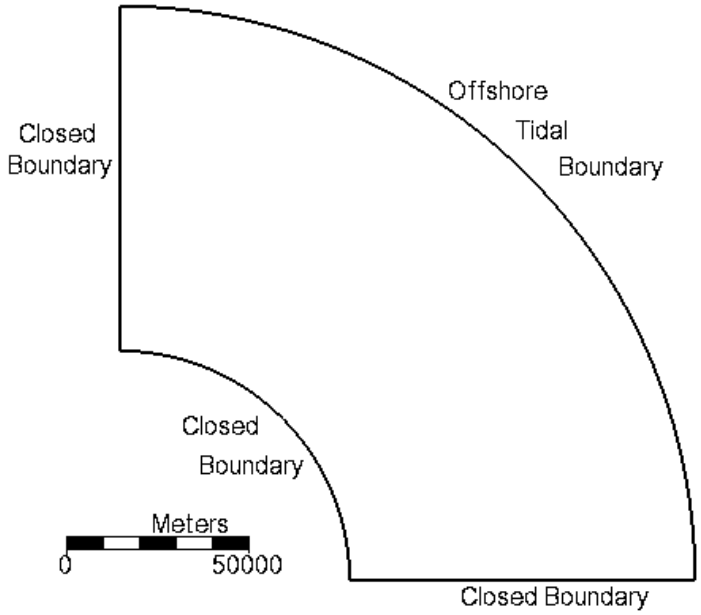

Figure 5.14. Computational domain for tidal propagation in a quarter annulus.

Two computational grids are tested and the results are compared (see Figure 5.15). The first grid is a three-level telescoping Cartesian grid with resolution of 4, 2, and 1 km for each level. Higher resolution is specified near the inner and outer boundaries in order to reduce errors associated with the representation of the curved boundaries with squares. The grid has 1,160 active ocean cells. The second computational grid has 640 quadrilateral cells and a resolution between approximately 3.18 and 6.36 km. A summary of selected model settings for both grids is given in Table 5.10.

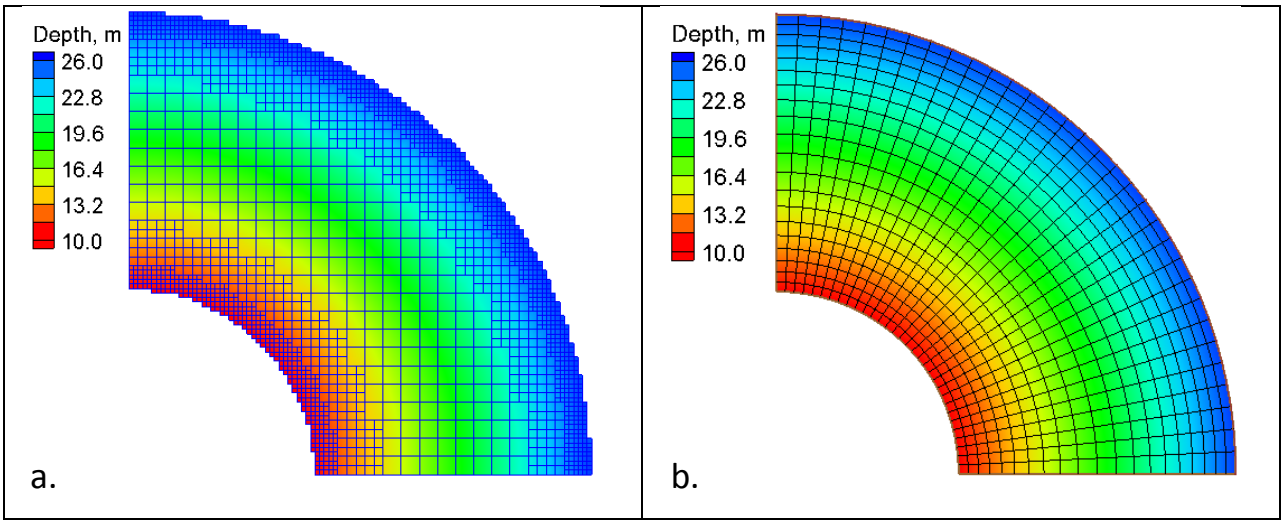

Figure 5.15. Computation grid used for tidal propagation in a quarter annulus: (a) Telescoping grid, (b) Quadrilateral grid.

Table 5.10. Model setup parameters for the quarter annulus test case.

Parameter	**Value**
Time step	10 min
Simulation duration	120 hr
Ramp duration	24 hr
Mixing terms	Off
Advection terms	Off
Wall friction	Off
Coriolis force	Off

A comparison between the analytical and calculated time-series of water levels at the inner edge of the simulation domain is presented in Figure 5.16 for both computational grids. The goodness-of-fit statistics are listed in Table 5.11. The computed water levels agree well with the analytical time series for both computational grids. No significant numerical dissipation is observed, nor numerical instability. The results from the quadrilateral grid are slightly more

accurate due to the better representation of the open boundary despite having approximately half the number of cells.

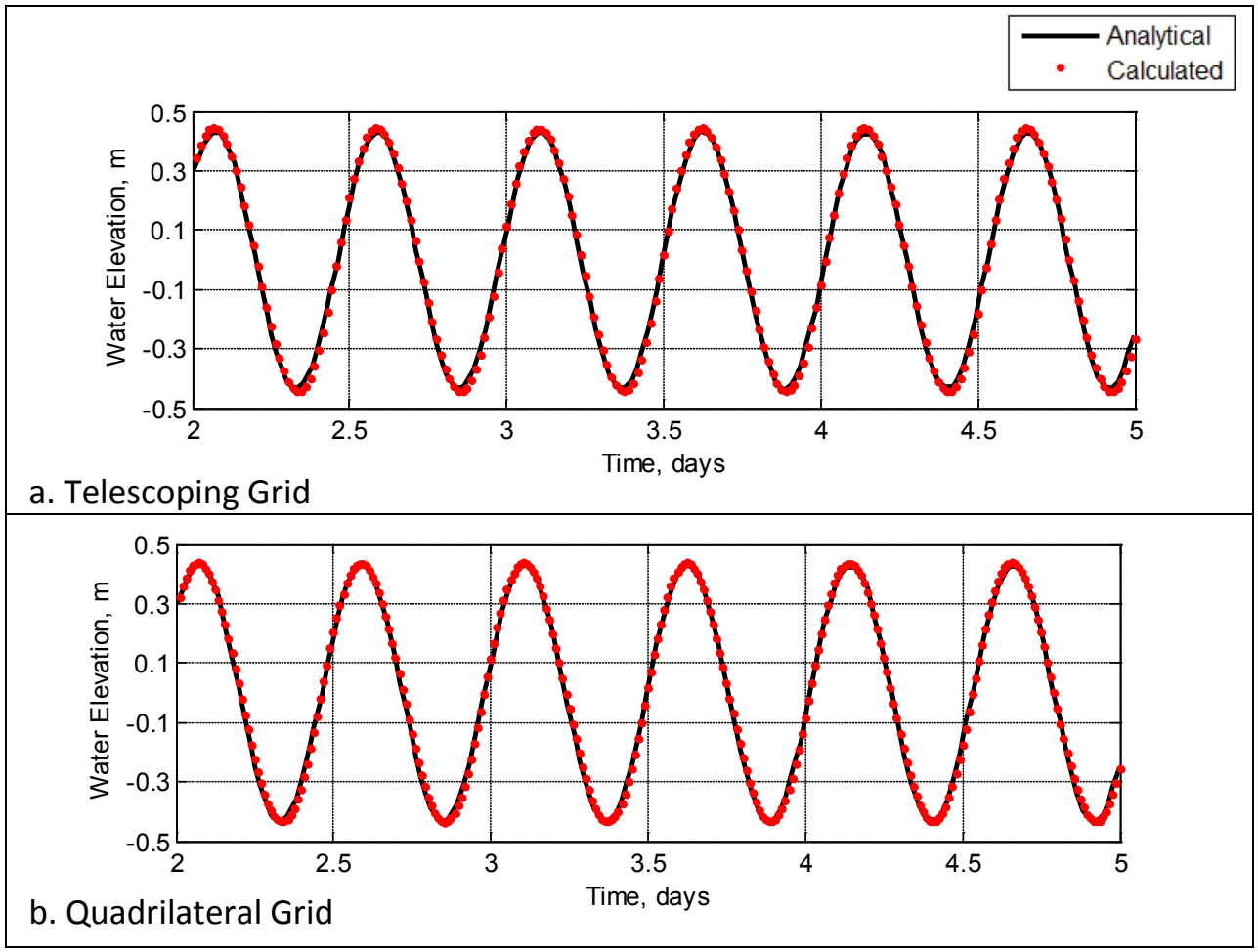

Figure 5.16. Comparison of analytical (solid black) and calculated (red dots) water surface elevations at the center of the inner radius.

Table 5.11. Water level goodness-of-fit statistics for the quarter annulus test case.

Statistic	**NRMSE, %**	**NMAE, %**	**R^2**	**Bias, m**
Cartesian	3.3	2.7	0.999	0.002 m
Quadrilateral	2.5	2.1	0.999	0.002 m

Example water level and current velocity magnitude fields are shown in Figure 5.17 for both computational grids. The water level contours are smooth for both grids and do not show any significant instabilities. The quadrilateral grid shows smooth contours for the current velocity magnitude, whereas the Cartesian grid shows some errors at the offshore boundary. This is due to staircase representation of the curved open boundary. Sensitivity tests showed that the problem persists for smaller time steps. For practical applications all model forcing is specified on straight boundaries and this problem does not occur as demonstrated in subsequent test cases in which telescoping grids are used.

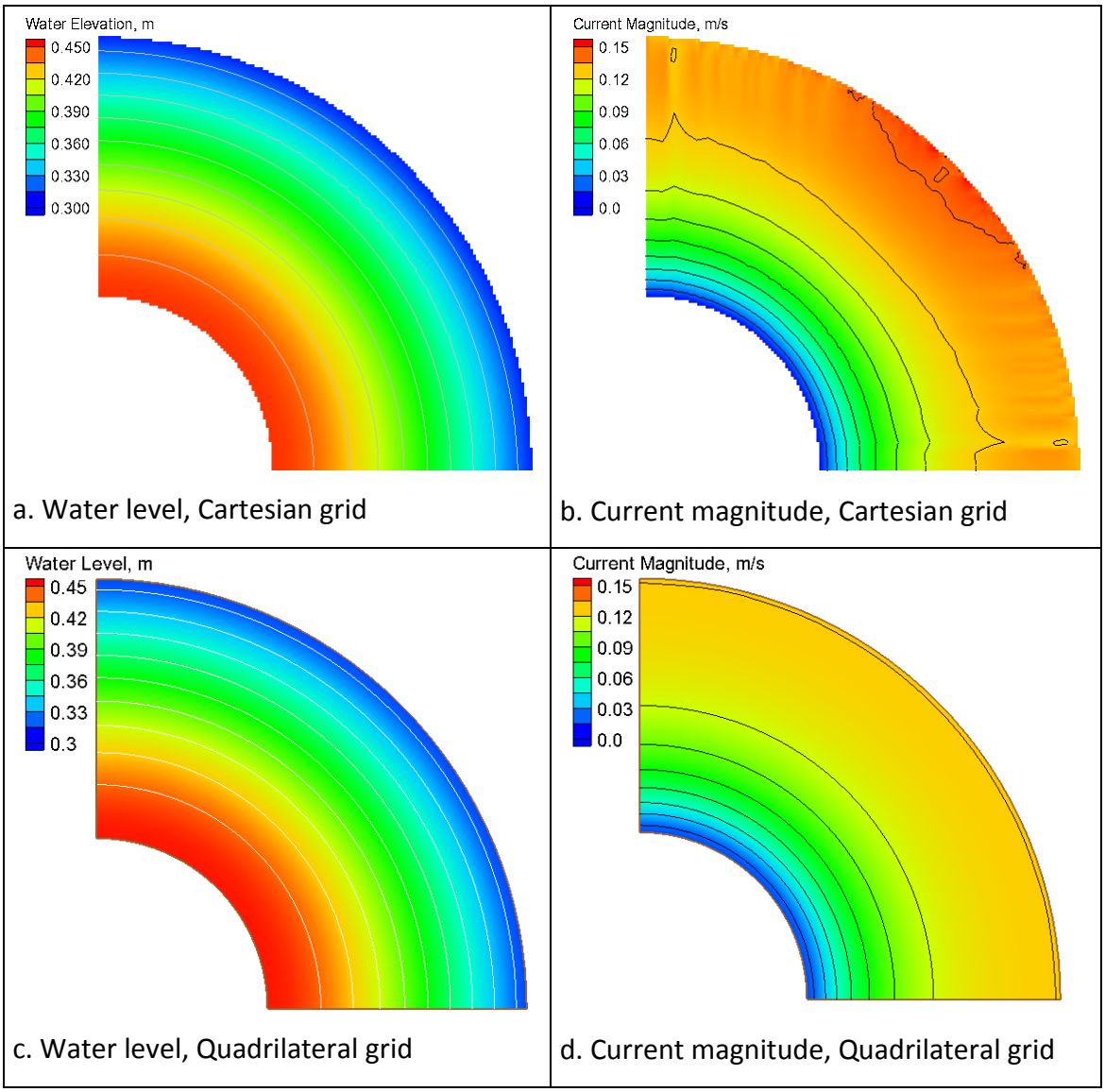

Figure 5.17. Snap shot of water levels at 62 hr (left) and current magnitude at 65.5 hr (right).

5.6 Long-wave Runup Over a Frictionless Slope

The performance of the model in calculation of nonlinear long-wave runup over a frictionless planar slope is assessed by comparing the computed water levels and shoreline position with an analytical solution presented by Carrier et al. (2003). The bed has a constant slope of 1:10 with the initial shoreline located at x = 0 m. Figure 5.18 shows the initial water

level is given by a leading depression N-wave (characteristic of the waves caused by submarine landslides). The initial current velocity is equal to zero everywhere.

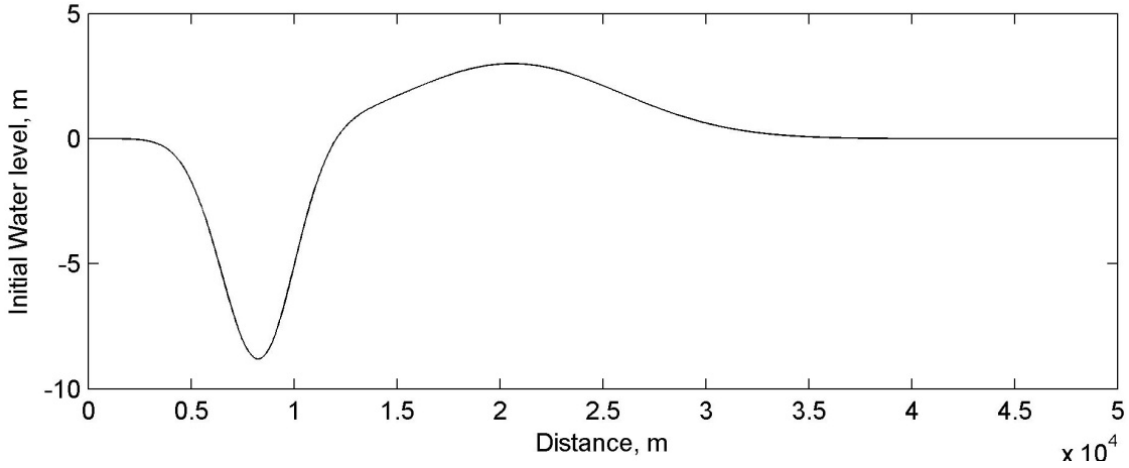

Figure 5.18. Initial water level profile for the long-wave runup test case.

The grid resolution is 3 m for x < 300 m and increases to 10 m offshore with an aspect ratio of 1.05. The general model parameters used in the simulation are shown in Table 5.12. A relatively small time step of 0.1 s is required due to the moving boundary. The computational grid is fixed and the moving wetting and drying boundary is treated as an internal boundary. Cells are judged as wet or dry (no partial wet or dry cells) based on a threshold wetting/drying depth.

Table 5.12. Model parameters for the long-wave runup test case

Parameter	**Value**
Time step	0.1 s
Simulation duration	360 s
Ramp duration	0.0 s
Wetting/drying depth	0.01 m
Wall friction	Off
Mixing terms	Off
Bottom friction	Off

Figure 5.19 shows a comparison of computed and analytical water surface elevations near the shoreline at 4 different elapsed times for the first 1,200 m from the initial shoreline position. The water level variation is characterized by a leading depression wave followed by a runup event. The model performance is generally good as demonstrated by the goodness-of-fit statistics shown in Table 5.13.

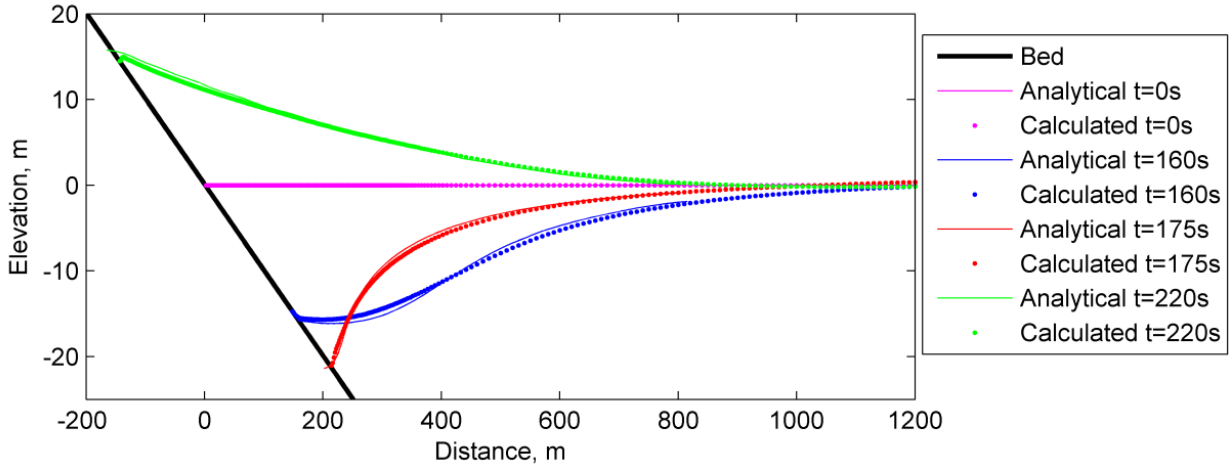

Figure 5.19. Comparison of analytical and calculated water levels at different elapsed times for the long-wave runup test case.

Table 5.13. Water level goodness-of-fit statistics* for the long-wave runup test case.

Time, s	**NRMSE, %**	**NMAE, %**	**R^2**	**Bias, m**
160	3.7	3.8	0.999	-0.012
175	6.5	5.9	0.997	-0.113
220	4.6	5.4	0.999	-0.066
*defined in Appendix A				

A comparison of the numerical and analytical solutions for the shoreline position is shown in Figure 5.20. The water shoreline position of the leading depression wave is well captured including the peak shoreline position. However the shoreline position during the inundation or advancement of the first wave is slightly under predicted. This is due to the small instability which is shown at 220 s near the shoreline position in Figure 5.19. The small instability is formed during the uprush of water but does not grow significantly and does not cause significant error in the computed water levels. Further tests can be done in the future to investigate if the instability can be reduced by reducing the grid spacing or time step. Once the first wave begins to recede, the calculated shoreline position again agrees well with the analytical solution.

It is noted that for practical field applications, the bottom is not frictionless or inviscid, which will improve the model stability. In general, the model's wetting and drying performance is considered satisfactory for the purposes of the model. The implicit solution scheme is designed for practical applications of tidal flow and wind- and wave-induced currents. This verification test provides a good case for testing the nonlinear hydrodynamics and wetting and drying algorithm.

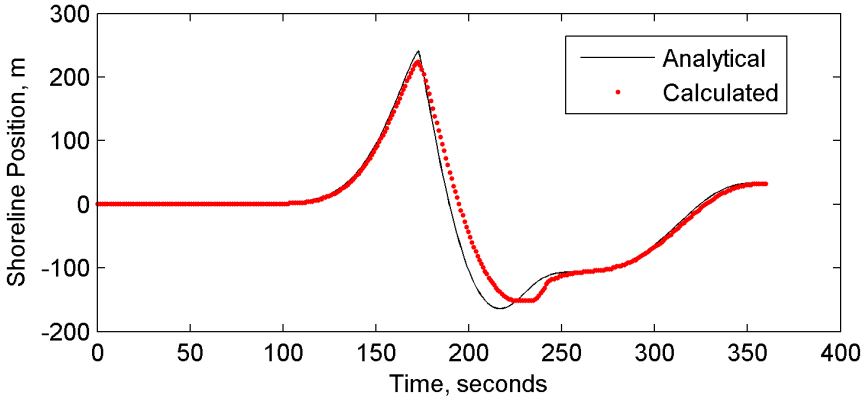

Figure 5.20. Time series comparison of calculated and analytical shoreline positions for the long-wave runup test case.

5.7 Transcritical Flow Over a Bump

This test case is used to assess the model performance in simulation of flow with mixed subcritical and supercritical regimes. Due to a steep change in bed elevation, the flow changes from subcritical to supercritical and back to subcritical. The one-dimensional problem (Caleffi et al. 2003) has a bed elevation given by

$$z_b = \begin{cases} 0, & \text{for } x < 8 \\ 0.2 - 0.05(x-10)^2, & \text{for } 8 \le x < 12 \\ 0, & \text{for } 12 \le x \end{cases} \tag{5.15}$$

where z_b is the bed elevation with respect to the still water level, and x is the horizontal distance. A constant flux boundary is specified at $x = 0$ m and a constant water level boundary is specified at $x = 12$ m. In addition, the bed is frictionless. Table 5.14 shows a summary of the important hydrodynamic parameters for this case.

Table 5.14. Hydrodynamic parameters for the test case of flow over a bump

Parameter	Value
Flow discharge	0.18 m^3/s
Downstream water depth	0.33 m
Bottom Friction	None

The model is applied with a computational domain of 25 ×0.3 m, and a constant grid spacing of 0.1 m (see Figure 5.21). The model is ramped from zero current velocity and a constant water level of 0.33 m over a period of 2.75 hr. A variable time step between 0.0781-20 s is applied. Table 5.15 summarizes the model setup.

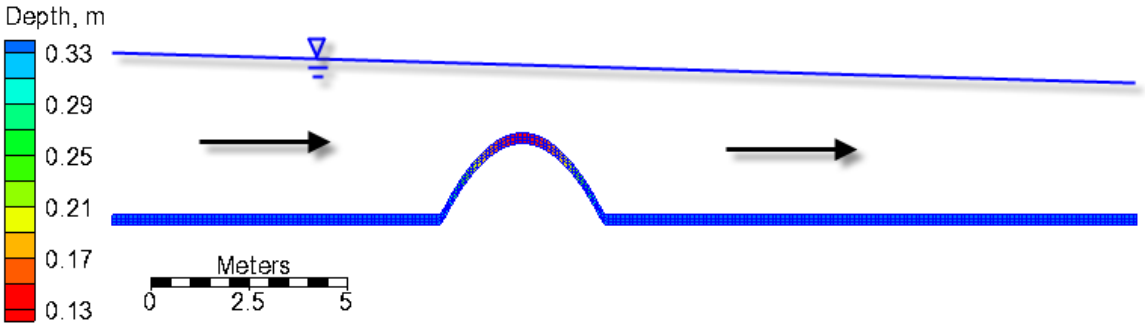

Figure 5.21. Computational grid for the test case of flow over a bump.

Table 5.15. Flow model setup parameters for the test case of flow over a bump.

Parameter	Value
Time step	0.0781-20 s
Simulation duration	3 hr
Ramp duration	2.75 hr
Wall friction	0ff
Manning's coefficient	0.0 $s/m^{1/3}$

A comparison between the analytical and numerical solutions of water level is shown in Figure 5.22. For comparison, the present implicit model is compared to the explicit time stepping scheme of the CMS model. A detailed description of the explicit time stepping scheme is provided in Militello et al. (2004) and Buttolph et al. (2006). The goodness-of-fit statistics summarized in Table 5.16 indicate that the mean calculated error is less than 3% and the squared correlation coefficient R^2 is 0.991. The model produces accurate results with NMAE values equal to 1.28%. The location of the hydraulic jump is captured well. The water level downstream of the bump is slightly under predicted and results in a slight negative bias shown in Table 5.16. It is noted that although the implicit solution scheme is not designed or intended for flows with sharp discontinuities, the model has the ability to produce accurate results.

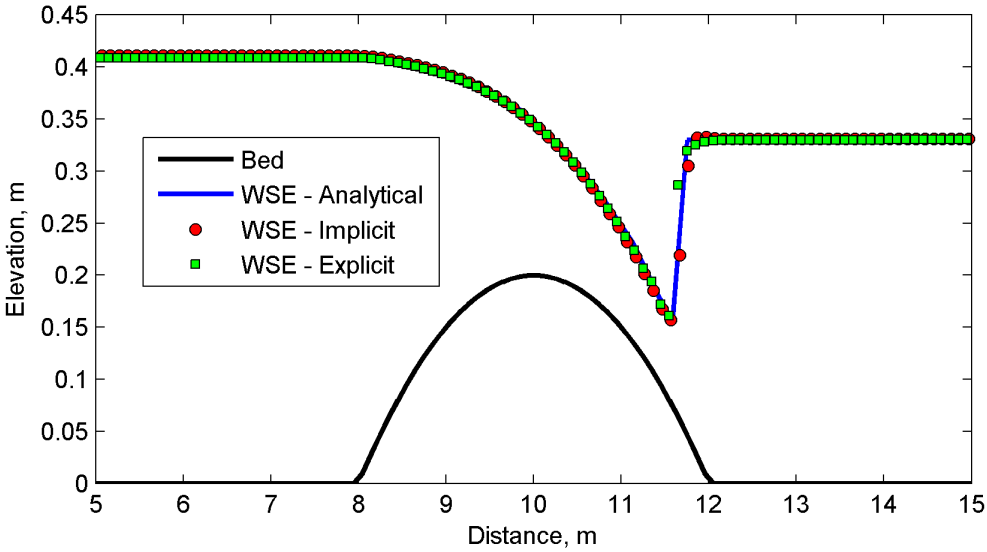

Figure 5.22. Comparison of analytical and calculated water surface elevations for the flow over a bump test case. The bed elevation is also shown for reference.

Table 5.16. Water level goodness-of-fit statistics* for the test case of flow over a bump.

Model	**NRMSE, %**	**NMAE, %**	**R^2**	**Bias, m**
Implicit (present)	2.86	1.28	0.991	0.0003
Explicit (Buttolph et al. 2006)	3.31	1.30	0.991	-0.0017
*defined in Appendix A				

CHAPTER VI

VALIDATION: LABORATORY CASES

The test cases presented in this Chapter are laboratory cases which provide the experiment data from physical models for determining appropriate ranges for calibration parameters as well as validation. The tests cases completed are:

1. Steady flow in a rectangular flume with a spur dike
2. Steady flow in a rectangular flume with a sudden expansion
3. Planar sloping beach with oblique incident regular waves
4. Idealized jettied inlet with equilibrium beach profile and oblique incident regular waves
5. Channel infilling and migration: Steady flow only
6. Channel infilling and migration: Waves parallel to flow
7. Channel infilling and migration: Waves perpendicular to flow
8. Surf-zone hydrodynamics and sediment transport
9. Clear-water erosion over a hard bottom
10. Bed aggradation and sediment sorting

6.1 Steady Flow in a Rectangular Flume with a Spur Dike

The model is applied to an experimental case of steady flow in a flume with a spur dike. The model performance is assessed by comparing the measured and calculated current velocities

behind the spur dike. The specific model features tested are the nonuniform Cartesian grid, inflow flux boundary condition, outflow water level boundary condition, wall boundary condition and subgrid eddy viscosity (turbulence) model (Smagorinsky 1963).

The laboratory flume experiment of Rajaratnam and Nwachukwu (1983) investigated a steady flow in a 37-m long, 0.92-m wide, rectangular flume with a thin plate of 0.1524-m long used to simulate a groin-like structure. Here the numerical model is compared to the experimental run A1 of Rajaratnam and Nwachukwu (1983) in which the flow discharge and water depth were 0.0453 m^3/s and 0.189 m, respectively.

The computational grid consists of 152 x 36 nodes in the longitudinal and lateral directions and has a variable grid resolution of 0.01 to 0.05 m (see Figure 6.1). A nonuniform Cartesian grid allows local refinement near the spur dike. The grid is refined near the structure and near the walls within the recirculation zone behind the structure. A constant flux (flow discharge) is specified at the inflow boundary and a constant water depth at the outflow boundary. A summary of the important model parameters for the flow model is shown in Table 6.1.

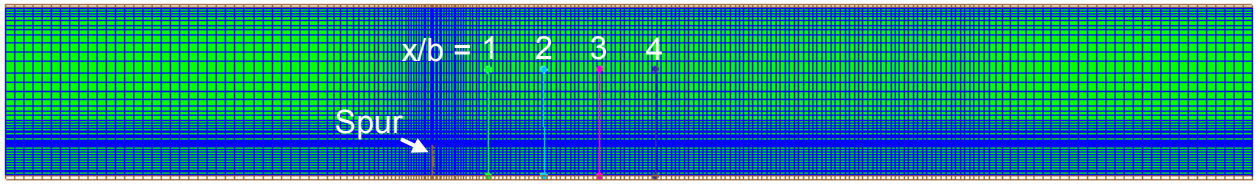

Figure 6.1. Computational grid for the spur-dike case. Colored lines represent the locations where calculated current velocities in the x-direction are extracted and compared to measurements (see Figure 6.2).

Table 6.1. Flow model set-up parameters for the spur dike test case.

Parameter	**Value**
Time step	1 min
Simulation duration	3 hr
Ramp duration	2.5 hr
Manning's coefficient	0.02 $s/m^{1/3}$
Wall friction	On
Turbulence model	Subgrid

Steady-state depth-averaged velocities are interpolated along the four cross-sections located downstream of the spur dike and indicated by vertical colored lines (observation arcs) in Figure 6.1. Velocity measurements were collected at two elevations above the bed. Here, the measured velocities at 0.85 times the water depth are compared with the calculated depth-averaged velocities in Figure 6.2 and the corresponding goodness-of-fit statistics are presented in Table 6.2. The computed steady state water levels and current velocities are shown in Figure 6.2. The flow structure produces an elevated water region directly upstream a depression directly downstream. The flow pattern shows an elongated recirculation zone behind the structure approximately 3-m long and 0.4-m wide. Due to inertial effects, the maximum flow velocity does not occur immediately above the flow structure. Instead, it occurs approximately 0.7 m downstream. The location which the main flow connects or attaches to the southern wall is located approximately 2.6 m from the spur dike.

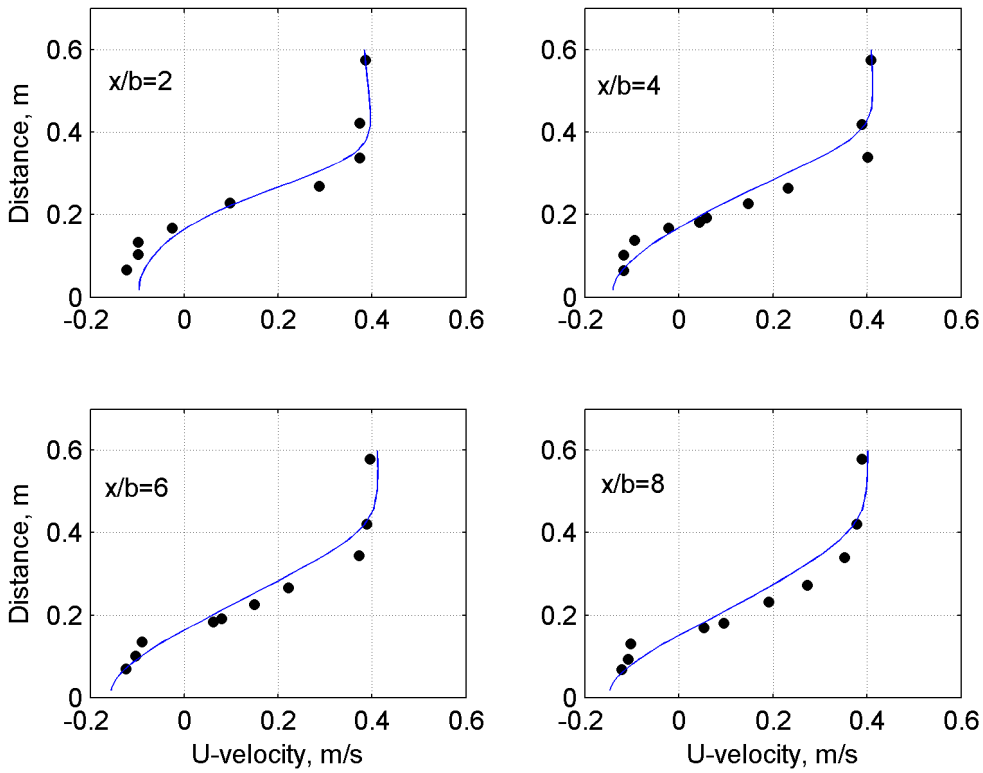

Figure 6.2. Comparison of measured and calculated flow velocities for the spur dike case. The location of transects x/b=2, x/b=4, x/b=6, and x/b=8, are shown in Figure 6.1 as green, blue, pink, and purple, respectively.

Table 6.2. U-velocity goodness-of-fit statistics* for the spur dike test case.

Statistic	**Cross-section location**			
	x/b=2	**x/b=4**	**x/b=6**	**x/b=8**
RMSE, m/s	0.0504	0.0690	0.0557	0.0627
NMAE, %	2.39	7.25	8.84	10.38
R^2	0.978	0.951	0.975	0.993
*defined in Appendix A				

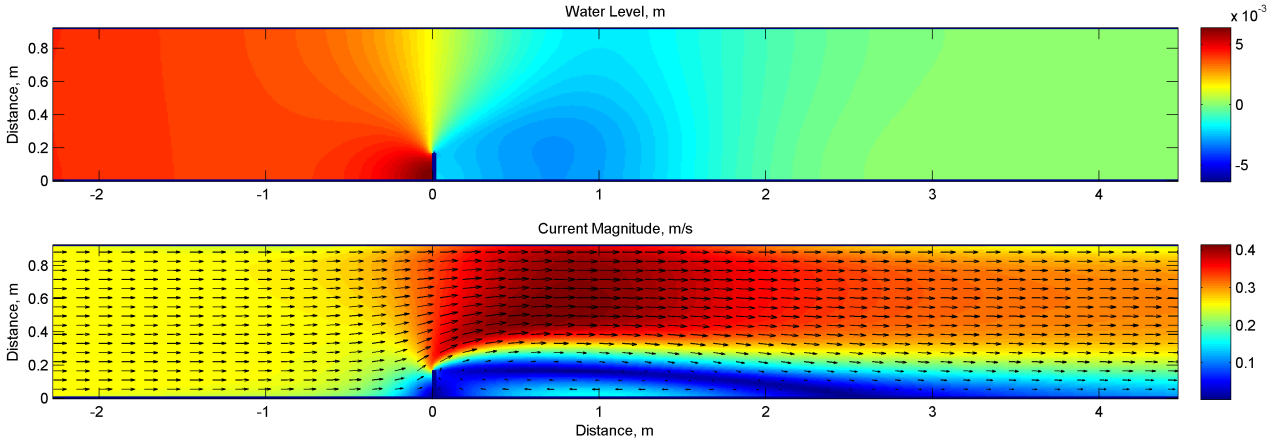

Figure 6.3. Calculated water level (top) and current velocities (bottom) for the spur dike test case.

6.2 Steady Flow in a Rectangular Flume with a Sudden Expansion

The model is applied to an experimental case of steady flow in a flume with a sudden expansion in width. The model performance is assessed by comparing the measured and calculated current velocities behind the sudden expansion. The intended specific model features to be tested are the stretched telescoping grid capability, inflow flux boundary condition, outflow water level boundary condition, wall boundary condition and mixing-length eddy viscosity (turbulence) model (Wu et al. 2011). The flume experiment of Xie (1996) consisted of a rectangular flume 18-m long, with an inflow section 0.6-m wide that abruptly expanded into a section 1.2-m wide. The experiment conditions are shown in Table 6.3.

Table 6.3. Hydrodynamic conditions for the Xie (1996) experiment.

Parameter	**Value**
Inflow	0.03854 m^3/s
Bed slope	1/1000
Downstream water depth	0.115 m

The stretched 3-level telescoping grid is shown in Figure 6.4. The grid has a resolution between 0.03 and 0.45 m with 2,625 active cells. A flux boundary condition is applied at the inflow boundary and a constant water level is specified at the downstream boundary. The initial condition is still water for the entire grid. The model parameters are given in Table 6.4. The mixing-length turbulence model is applied for this case. The bottom friction is estimated to have a Manning's coefficient of 0.015 $s/m^{1/3}$, which is consistent with the concrete bottom used in the flume. The horizontal shear eddy viscosity coefficient, c_h, is estimated to be 0.3 which is very close to the default value of 0.4. The computational time is approximately 1 min on a 2.67 GHz single processor.

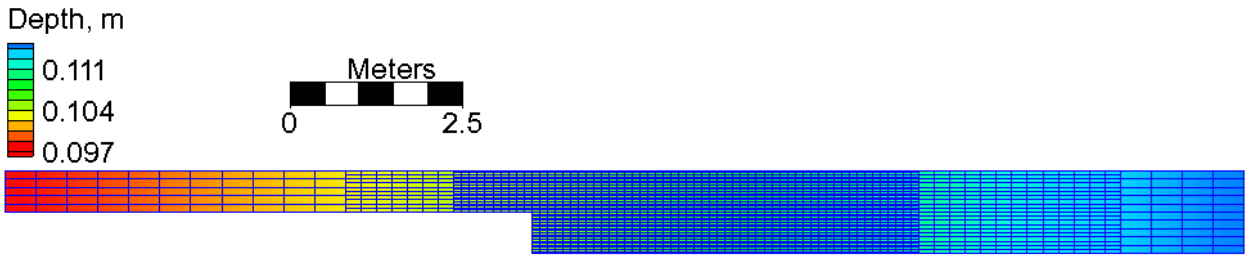

Figure 6.4. Computational grid for the Xie (1996) experiment test case.

Table 6.4. Flow model settings for the Xie (1996) experiment test case.

Parameter	**Value**
Time step	30 s
Simulation duration	1 hr
Ramp duration	0.5 hr
Manning's coefficient	0.015 s/m$^{1/3}$
Turbulence model	Mixing-length
Bottom shear viscosity coefficient (c_v)	0.067 (=default)
Horizontal shear viscosity coefficient (c_h)	0.3 (default =0.4)

Current velocities were measured along transects located every meter from the flume expansion. Figure 6.5 shows a comparison of the measured and computed current velocities in the x-direction. The recirculation zone behind the sudden expansion extends approximately 7 m downstream (see Figure 6.6). In general, the computed current velocities agree well with measurements as demonstrated by the goodness of fit statistics shown in Table 6.5. The NRMSE ranges from 1.60 to 13.98 % for transects 1 to 5, increasing in error away from the expansion area.

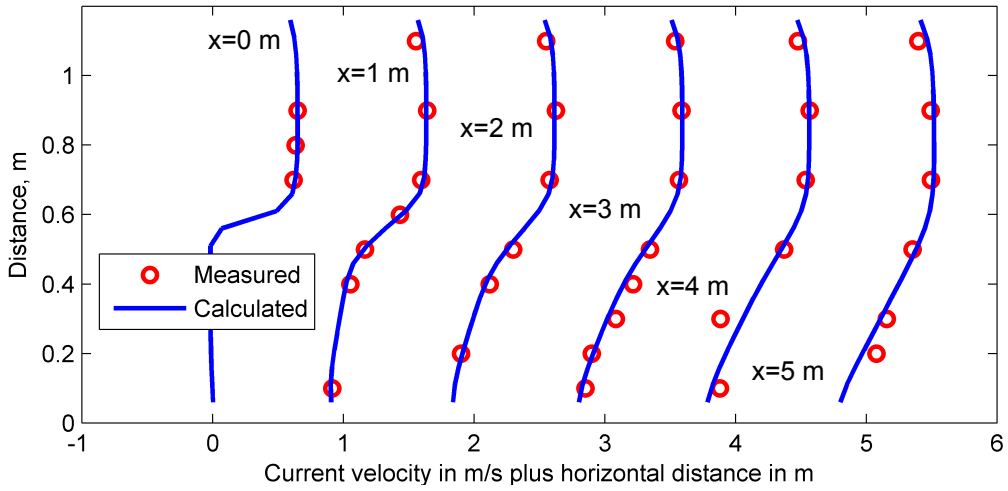

Figure 6.5. Measured and calculated current velocities along 6 cross-sections for the Xie (1996) experiment. For each transect the horizontal distance is added to the current velocity. Transects are spaced 1 m apart starting at 0 m.

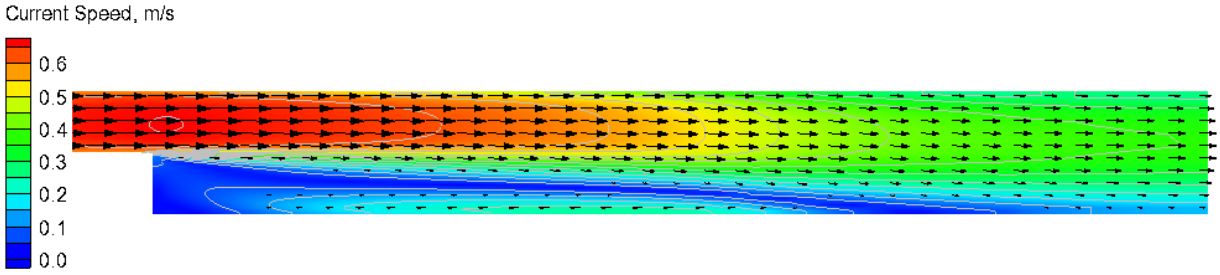

Figure 6.6. Computed current velocity field for the Xie (1996) experiment test case.

Table 6.5. Current velocity goodness-of-fit statistics* for the Xie (1996) experiment test case.

Statistic	**Cross-section location**					
	***x*=0 m**	***x*=1 m**	***x*=2 m**	***x*=3 m**	***x*=4 m**	***x*=5 m**
NRMSE, %	1.60	3.58	4.04	5.26	11.29	13.98
NMAE, %	1.33	2.78	3.61	4.24	7.82	11.80
R^2	0.789	0.995	0.990	0.989	0.936	0.980
Bias, m/s	0.0083	0.0046	-0.0035	-0.0187	0.0246	-0.0022
*defined in Appendix A						

6.3 Planar Sloping Beach with Oblique Incident Regular Waves

The model is applied to a laboratory experiment of wave-induced currents and water levels due to regular waves. The large cross-shore gradient of wave height in the surf zone produces a large forcing useful for testing hydrodynamic model stability and performance under strong wave forcing. The specific model features tested are the surface roller, cross-shore boundary conditions, and combined wave-current bottom shear stress parameterization.

Visser (1991) conducted eight laboratory experiments of monochromatic waves on a planar beach and collected measurements on waves, currents and water levels. In this study, experiments (Cases) 4 and 7 are selected as representative test cases. The bathymetry consisted of a 1:10 slope for the first 1 m from shore, a 1:20 slope for the next 5 m, followed by 5.9-m flat bottom to the wave generator. Cases 4 and 7 had an incident wave height of 0.078 m, peak period of 1.02 s and incident wave angle of 15.4°. Case 4 was run over a concrete bed and Case 7 was run over a thin 0.005-0.01 m layer of gravel grouted onto the concrete floor. A summary of the wave conditions is provided in Table 6.6.

Table 6.6. Wave conditions for the Visser (1991) test cases.

Parameter	**Value**
Wave height (regular)	0.078 m
Wave period	1.02 s
Incident wave angle	15.4º

The computational grid (Figure 6.7) consists of 84 rows and 147 columns with a constant grid resolution in the longshore direction of 0.15 m and a variable grid resolution between 0.04

and 0.15 m in the cross-shore direction. A constant zero water level is forced at the offshore boundary and cross-shore boundaries are applied on each side of the shoreline. The boundary type solves the 1-D cross-shore momentum equations for the longshore current and water level and applies a flux boundary condition for inflow conditions and a water level condition for outflow conditions. The cases are simulated as steady-state solutions with pseudo-time stepping to reach steady-state while coupling waves, currents and water levels. The initial condition is specified as zero current velocity and water level for the whole domain. Waves and hydrodynamics are coupled every 20 min (steering interval) and run until steady-state. The surface roller model (Stive and de Vriend 1994) is run after each wave model run and the roller surface stresses are then added to the wave radiation stresses before running the flow model. A summary of the important flow and wave model settings are given in Table 6.7 and Table 6.8 respectively. The combined wave-current bottom friction is calculated using the formula of Wu et al. (2010). The experiments are simulated in laboratory scale, which is why some of the parameters like the wetting/drying depth are decreased.

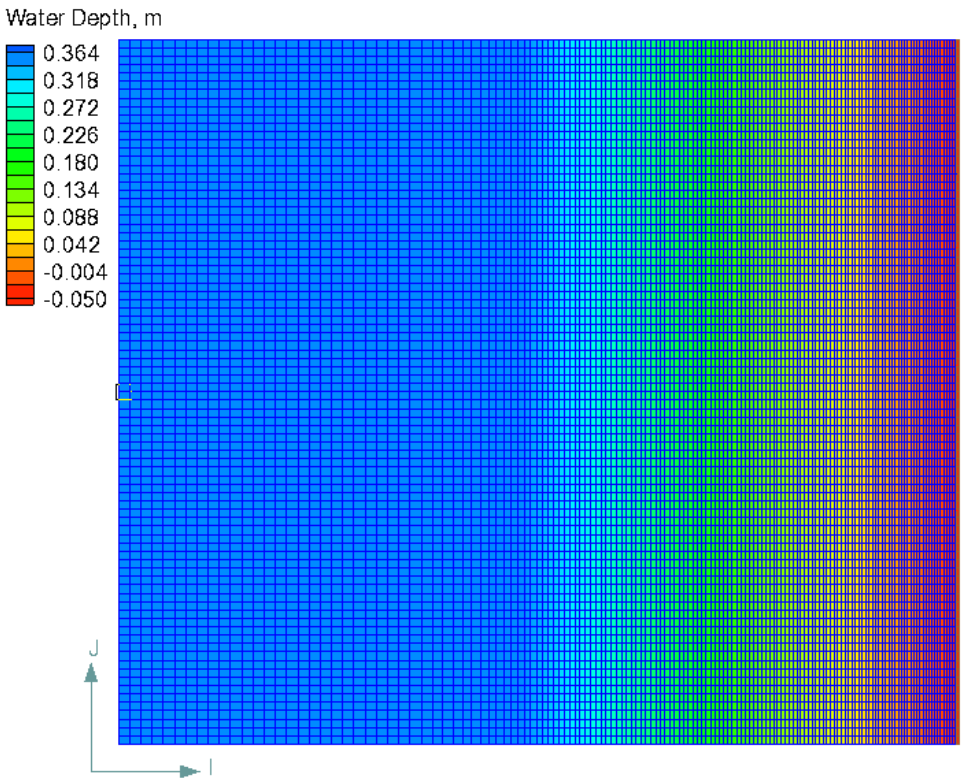

Figure 6.7. Computational grid for the Visser (1991) test cases.

Table 6.7. Flow model settings for the Visser (1991) test cases.

Parameter	**Value**
Time step	1 min
Wetting/drying depth	0.006 m
Simulation duration	3 hr
Ramp duration	2 hr
Wave-current bottom friction	Wu et al. (2010)

Table 6.8. Wave model settings for the Visser (1991) test cases.

Parameter	**Value**
Wave breaking formulation	Battjes and Janssen (1981)
Bottom friction	Off (default)
Steering interval	20 min

All of the wave breaking formulations in the wave model are designed for random waves. However the Visser (1991) laboratory experiments were run with regular (monochromatic) waves which are not useful for validating the wave model. Since the objective of this test case is to assess the performance of the hydrodynamics, it is necessary to calibrate the wave model to obtain the most accurate wave results in order to analyze the performance of the hydrodynamic model. The calibration procedure consists of first calibrating the location of the breaker using the breaker index γ. The flow is then calibrated using the Manning's coefficient and efficiency coefficient (Stive and de Vriend 1994). Additional tests are run for comparison with the same settings except the roller model is turned off. A summary of the calibration parameters is provided in Table 6.9.

Table 6.9. Calibration parameters for the Visser (1991) test cases.

Parameter	**Case 4**	**Case 7**	**Default**
Manning's coefficient, $s/m^{1/3}$ (flow only)	0.0115	0.018	None
Breaker coefficient	0.64	0.9	Automatic (random waves)
Roller dissipation coefficient	0.1	0.1	0.1
Roller efficiency factor	0.8	0.8	1.0

6.3.1 Case 4

The measured and computed wave heights, longshore currents, and water levels for Case 4 are compared in Figure 6.8. Results are shown with and without the surface roller. The results are significantly improved when the surface roller is included as demonstrated by the goodness-of-fit statistics shown in Table 6.10. The NMAE for longshore current is reduced from

approximately 20 to 5%. The roller has the effect of spreading the peak longshore current and moving it closer to the shore. The surface roller also reduces the setup at the breaker and increases it in the surf zone and near the shoreline. Although the water levels and currents are significantly affected by the surface roller the wave height profile shows only minor differences when the roller is included. This is due to the fact that in this case the dominant wave process in the surf zone is the wave breaking and the effect of currents on waves is relatively weak.

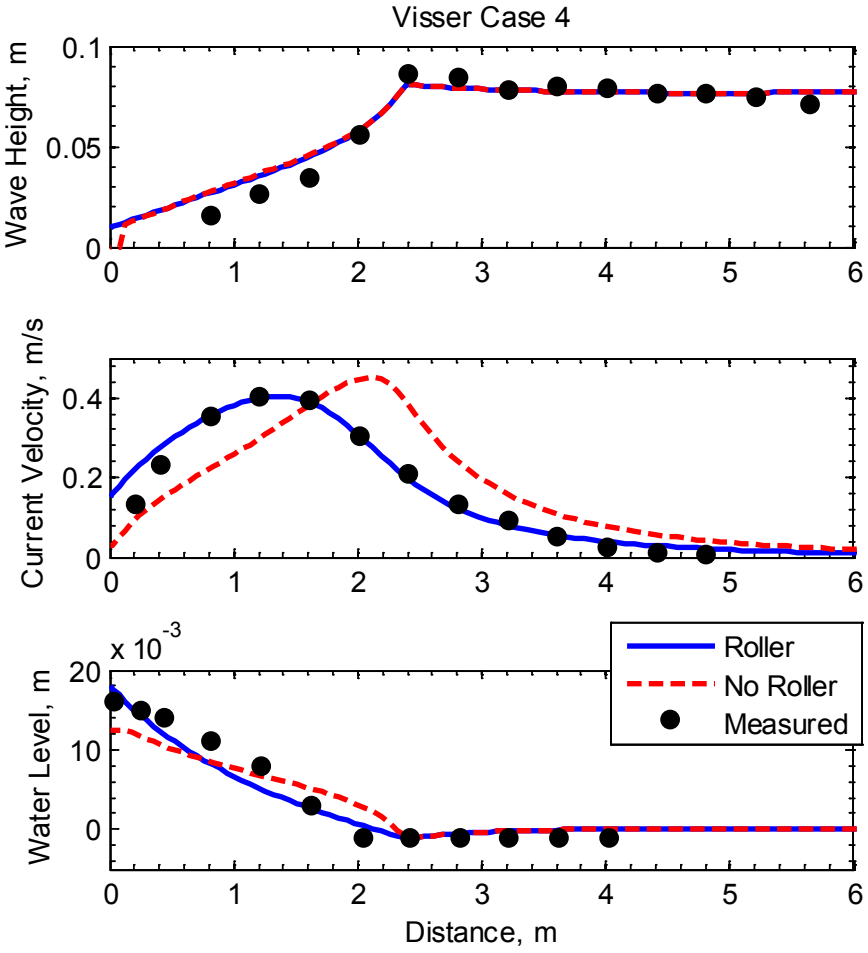

Figure 6.8. Measured and calculated wave height (top), longshore current (middle), and water level (bottom) for Visser (1991) Case 4.

Table 6.10. Goodness-of-fit statistics for the Visser (1991) Case 4.

Roller	**Variable**	**NRMSE, %**	**NMAE, %**	**R^2**	**Bias**
Off	Wave height	7.10	5.35	0.985	0.002 m
	Longshore current	23.06	20.01	0.612	0.024 m/s
	Water level	13.94	11.66	0.954	0.000 m
On	Wave height	6.70	5.11	0.985	0.002 m
	Longshore current	7.28	4.37	0.962	0.011 m/s
	Water level	9.04	7.38	0.957	0.000 m

6.3.2 Case 7

The measured and computed wave heights, longshore currents, and water levels with and without the roller for Case 7 are shown in Figure 6.9. It is interesting to note that although the offshore wave height, period and direction are the same as Case 4, the location of the breaker for Case 7 is significantly further offshore. This may be due to rougher bottom. The results are similar to those of Case 4 in that the longshore current velocities are significantly improved when the roller is included (see Table 6.11). No measurements of water levels are available for Case 7. Similarly to Case 4 the longshore current is well predicted when the roller is included except for the first 1 m from the shoreline where the current velocity is over-predicted.

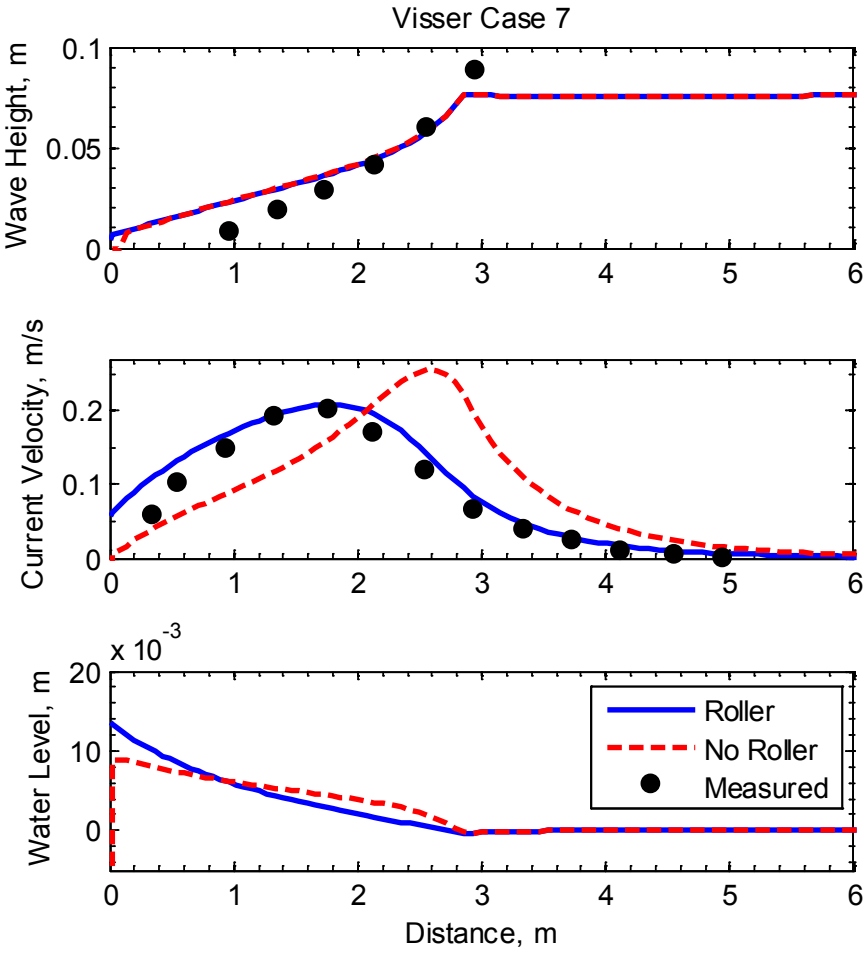

Figure 6.9. Measured and computed longshore currents (top), water levels (middle) and wave heights (bottom) for Visser (1991) Case 7.

Table 6.11. Goodness-of-fit statistics for the Visser (1991) Case 7.

Roller	**Variable**	**NRMSE, %**	**NMAE, %**	**R^2**	**Bias**
Off	Wave height	10.78	9.48	0.99	0.003 m
	Longshore current	33.08	27.26	0.36	0.017 m/s
On	Wave height	10.50	9.17	0.99	0.003 m
	Longshore current	9.92	7.34	0.97	0.015 m/s

6.4 Idealized Jettied Inlet

The purpose of this validation case is to evaluate the model for wave-induced hydrodynamics in the vicinity of an inlet with two absorbing jetties. The specific model features to be tested are the inline flow and wave coupling, wave-adjusted lateral boundary conditions, and Stokes velocities in the continuity and momentum equations.

In 2005 the USACE conducted a physical model study to collect both current and wave measurements in the vicinity of an idealized dual jetty inlet (Seabergh et al. 2005). The idealized inlet experiment was in a 46-m wide by 99-m long concrete basin with 0.6-m high walls. Figure 6.10 shows a map of the facility and basin area. A 1:50 undistorted Froude model scale was used to represent the dimensions of a medium-sized U.S. Atlantic coast inlet. The ocean side parallel contours correspond to an equilibrium profile $h = Ax^{2/3}$, where h is the still water depth, x is the cross-shore coordinate from the shoreline and A is a grain size dependent empirical coefficient (equal to 0.1615 $m^{1/3}$ here). For further details on the physical model and previous modeling results, the reader is referred to Seabergh et al. (2005) and Lin and Demirbilek (2005). Fully reflective and absorbing jetties were constructed for inlet geometries studied in the physical model. However, all of the tests shown here are for the absorbing jetties since they represent those typically found in coastal applications. The incident wave conditions for the test cases used here are shown in Table 6.12. The three cases were chosen to cover a wide range of wave heights.

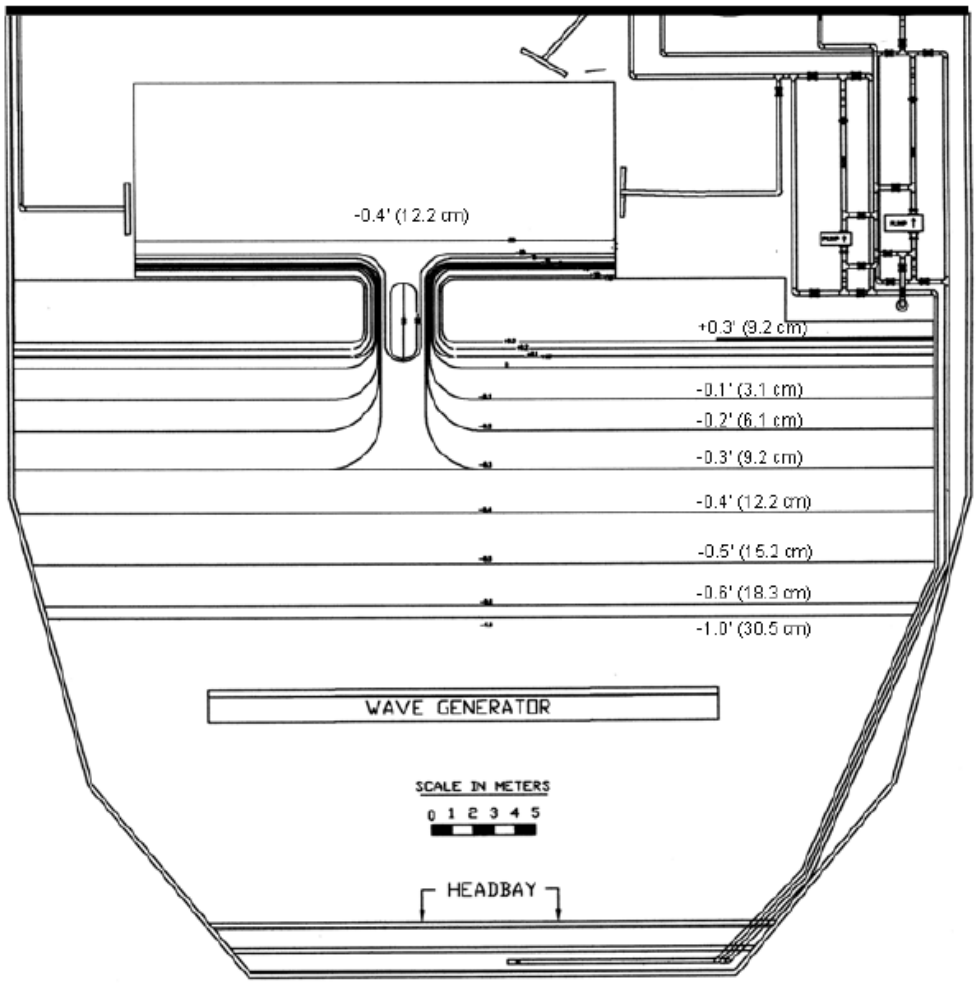

Figure 6.10. Physical model setup for the idealized inlet case (from Seabergh et al. 2005).

Table 6.12. Wave conditions (prototype scale) of three test cases from Seabergh et al. (2005).

Case	Wave height*, m	Wave period, s	Wave Direction**, deg
1	1.65	11.0	-20º
2	2.0	11.0	-20º
3	3.25	8.0	-20º
*Measured at the first offshore station approximately 50 m (prototype) from the jetty tips (see Figure 6.11). **Clockwise from shore normal.			

The computational grid and bathymetry for both the flow and wave models is shown in Figure 6.11. The grid has 31,422 active cells and a constant resolution of 10 m (prototype scale). A list of the basic model setup parameters is given in Table 6.13. A constant zero water level boundary condition is assigned to the offshore boundary. A wall boundary condition is used at all boundaries inside the bay.

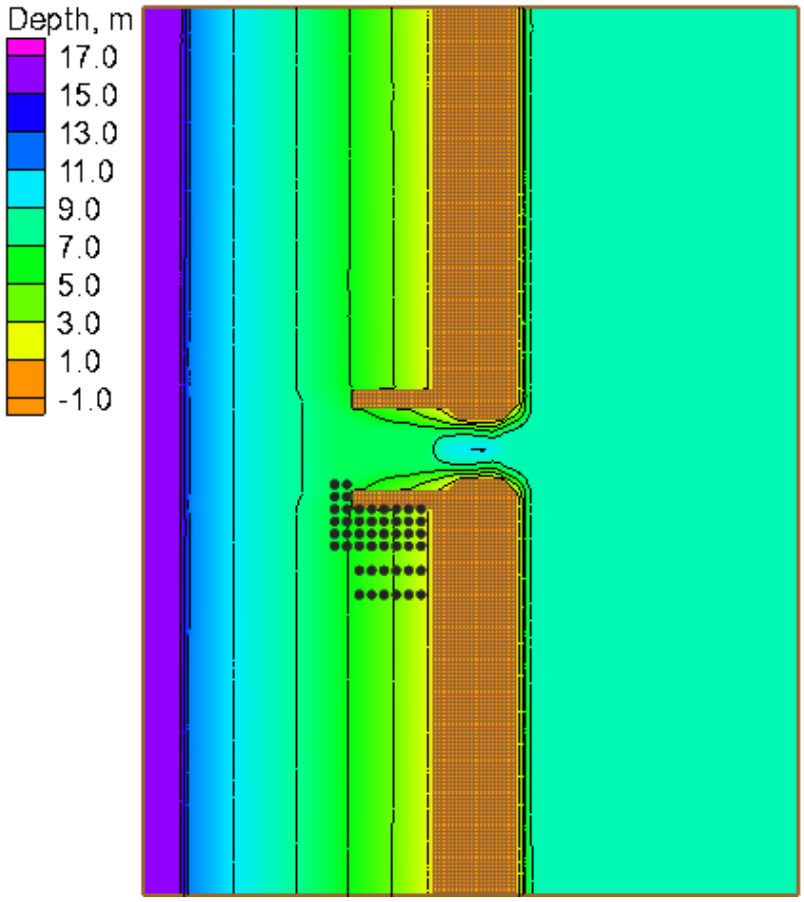

Figure 6.11. Computational grid showing the model bathymetry. Black circles indicate current velocity and wave height measurement stations used in this study.

Table 6.13. Model settings for the Seabergh et al. (2005) experiments.

Parameter	**Value**
Flow time step	6 min
Simulation duration	4 hr
Ramp period duration	3 hr
Manning's *n* (both flow and wave grids)	0.025 s/m$^{1/3}$
Steering interval	1 hr
Wave breaking formula	Battjes and Janssen (1978)
Roller	On
Roller dissipation coefficient	0.05 (default for regular waves)
Roller efficiency factor	1.0
Stokes velocities	On
Wave reflection coefficient	0.0

Default settings are used where possible with the Manning's coefficient being the only calibrated parameter (n = 0.025 s/m$^{1/3}$) for this case study. The roller dissipation coefficient β_D is set to the recommended value for regular waves (β_D = 0.05). Both parameters are held constant for all test cases. Including the roller is very important for regular waves because it improves the prediction of the long-shore current. The wave- and depth-averaged hydrodynamics equations are solved for depth-uniform currents according to Phillips (1977) and Svendsen (2006). The formulation includes Stokes velocities in both the continuity and momentum equations and provides a better prediction of cross-shore currents.

The measured and calculated wave heights and wave-induced nearshore currents are presented in plan view vector plots and also cross-shore transects as discussed below. Note that the wave height and cross-shore profiles are offset by a number indicated to left of each transect which are plotted using different colors. Demirbilek et al. (2009) reported similar results for the

wave height using a previous version of the model. The current velocities reported here are significantly improved with respect to Demirbilek et al. (2009) due to the implementation of the surface roller and Stokes velocities.

6.4.1 Case 1 (H=1.65 m, T=11 s)

The calculated wave height magnitudes and directions agree well with the measurements with a NMAE of 10.62% (see Figure 6.12, Figure 6.13, and Table 6.14). The wave model tends to over-predict wave refraction near the structure and shoreline. The breaker is located at approximately the third cross-shore measurement station from the shoreline and is well predicted by the model (Figure 6.13). Measured and computed current velocities for Case 1 are compared in Figure 6.12 and Figure 6.14. The velocity field is characterized by a narrow longshore current approximately 75-m wide which is deflected seaward by the south jetty. The NRMSE and NMAE values for the longshore current are approximately 24 and 19%, respectively, while for the cross-shore current, they are significantly smaller at 14 and 10%, respectively (see Table 6.14). Most of the longshore current is located within the first 2 measurement stations from the shoreline. The calculated cross-shore currents agree well with the measurements except near the jetty where it is overestimated.

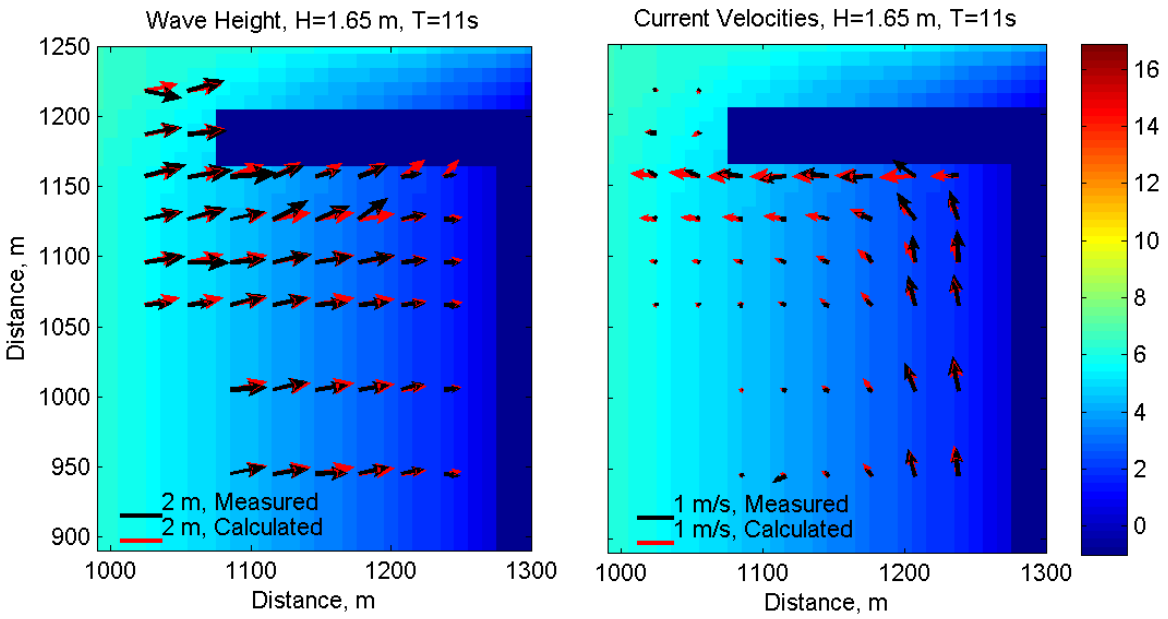

Figure 6.12. Measured and calculated wave height (left) and mean current (right) vectors for Case 1. Background colors indicate the local water depth corresponding to the right color bar.

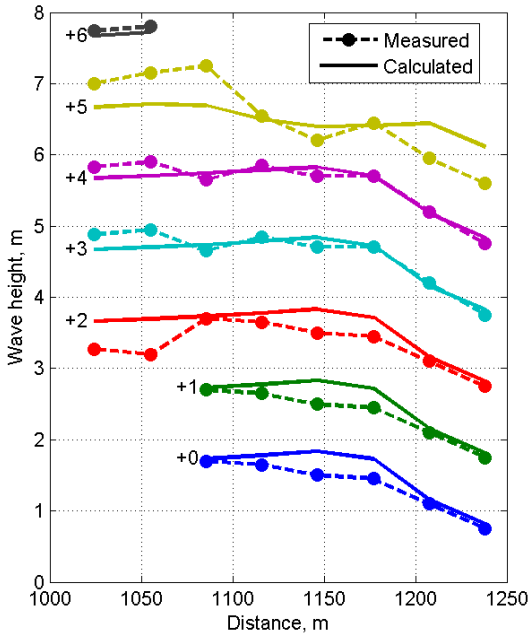

Figure 6.13. Cross-shore transects of measured and calculated wave heights for Case 1 (H = 1.65 m, T = 11 s). For display purposes, wave heights are shifted by the number indicated on the left-hand side of each transect.

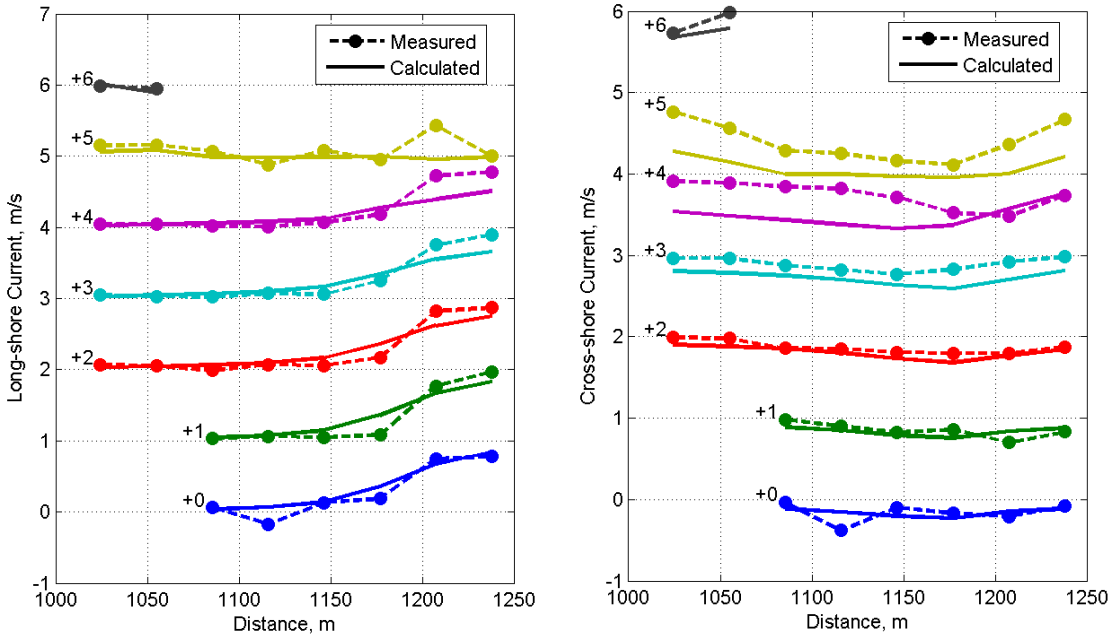

Figure 6.14. Cross-shore transects of measured and calculated longshore (left) and cross-shore (right) currents for Case 1 (H = 1.65 m, T = 11 s). For display purposes, current velocities are shifted by the number indicated on the left-hand side of each transect.

Table 6.14. Goodness-of-fit statistics* for Case 1 (H = 1.65 m, T = 11 s)

Variable	**NRMSE,%**	**NMAE,%**	**R^2**	**Bias**
Longshore current	24.11	18.74	0.836	-0.141 m/s
Cross-shore current	14.27	10.30	0.907	0.017 m/s
Wave Height	13.96	10.62	0.826	0.051 m
*defined in Appendix A				

6.4.2 Case 2 (H=2.0 m, T=11 s)

The calculated wave height magnitudes and directions of Case 2 agree well with the measurements especially far away from the jetty (see Figure 6.15 and Figure 6.16). The wave height NRMSE, NMAE, and R^2 are 12.33%, 8.05 %, and 0.889, respectively (see Table 6.15). Closer to the jetty, the differences are larger possibly due to reflected wave energy from the jetty. Even though the jetties were made of small stones and absorbed most of the wave energy, a

small portion of the wave energy was reflected. The wave model has the capability to simulate reflecting waves. However, for this study it is assumed that the jetty reflectance is negligible. Additional tests will be conducted in the future to test this hypothesis. The breaker is located at approximately the fourth cross-shore measurement station from the shoreline and is well predicted by the model.

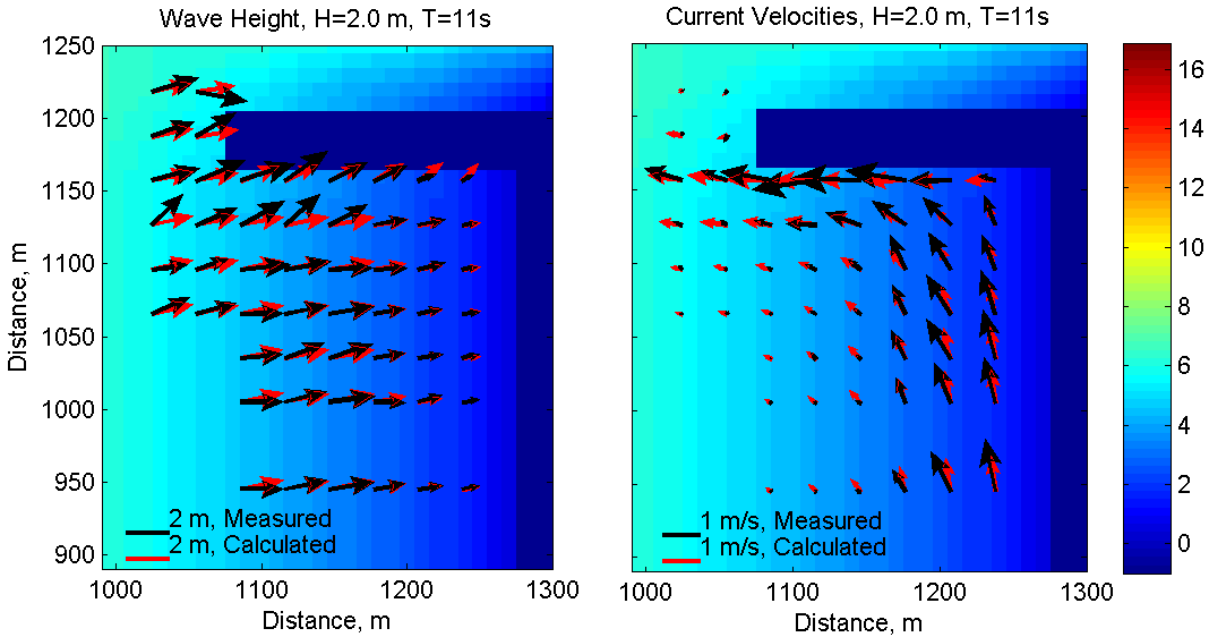

Figure 6.15. Measured and calculate wave height (left) and mean current (right) vectors for Case 2. Background colors indicate the local water depth corresponding the right color bar.

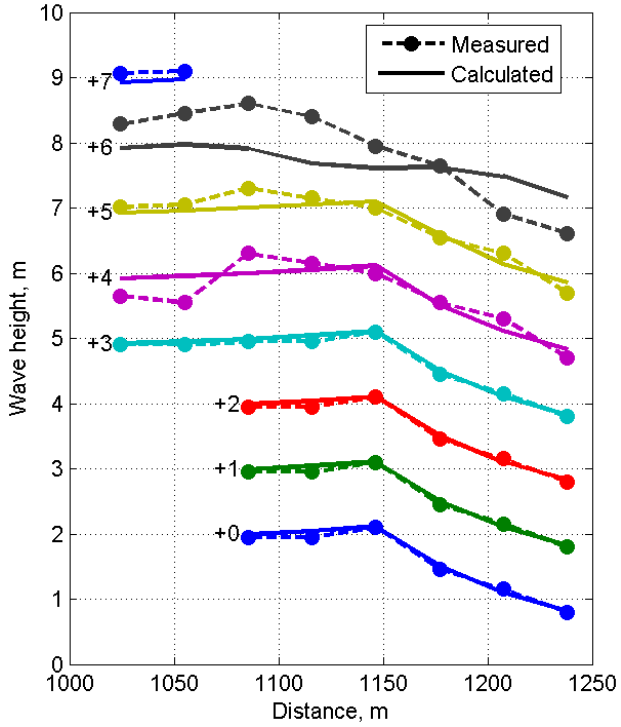

Figure 6.16. Cross-shore transects of measured and calculated wave heights for Case 2 (H = 2.0 m, T = 11 s). For display purposes, wave heights are shifted by the number indicated on the left-hand side of each transect.

Measured and calculated current velocities for Case 2 along cross-sectional transects, shown in Figure 6.17, have NRMSE and NMAE values less than 15 and 13%, respectively (see Table 6.15). Although the breaker zone for Case 2 is wider than in Case 1, most of the long-shore current is still located within the first 3 measurement stations from the shoreline. The calculated cross-shore currents tend to be underestimated near the shoreline and slightly overestimated outside of the breaker for all cross-shore transects except the one adjacent to the jetty.

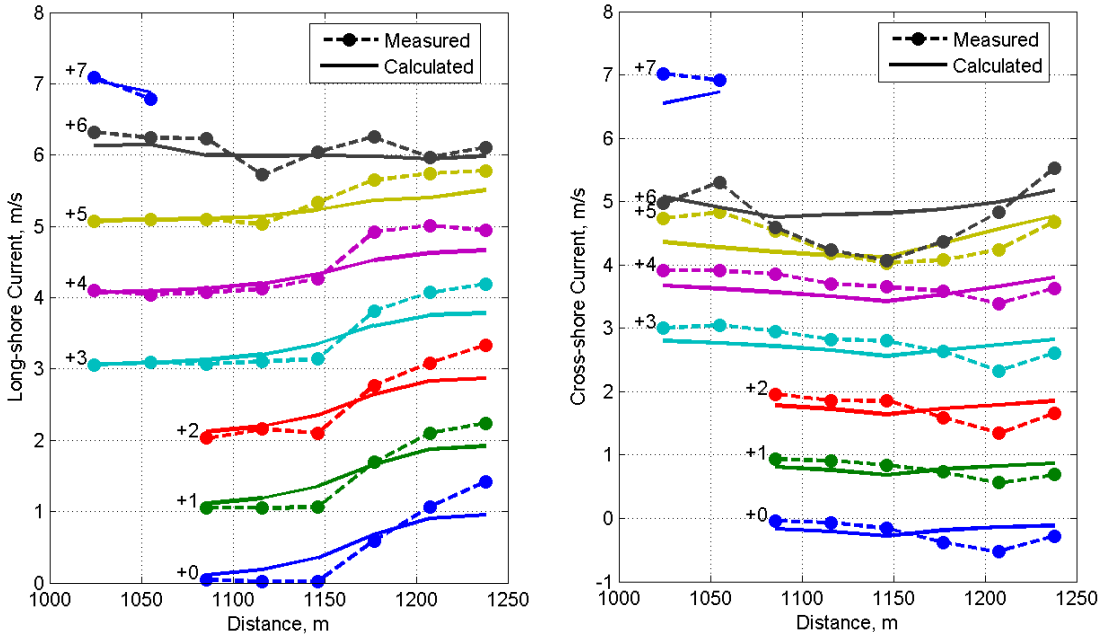

Figure 6.17. Cross-shore transects of measured and calculated long-shore (left) and cross-shore (right) currents for Case 2 (H = 2.0 m, T = 11 s). For display purposes, current velocities are shifted by the number indicated on the left-hand side of each transect.

Table 6.15. Goodness-of-fit statistics* for Case 2 (H = 2.0 m, T = 11s)

Variable	**NRMSE,%**	**NMAE,%**	**R^2**	**Bias**
Longshore current	14.43	12.24	0.797	-0.007 m/s
Cross-shore current	14.69	11.49	0.930	-0.065 m/s
Wave Height	12.33	8.05	0.889	-0.040 m
*defined in Appendix A				

6.4.3 Case 3 (H=3.25 m, T=8 s)

Figure 6.18 shows plan-view vector plots of the measured and computed wave heights and current velocities for Case 3. Cross-shore profiles of measured and computed wave heights and current velocities are plotted in Figure 6.19 and Figure 6.20. For this case, the calculated wave heights are slightly overestimated for most of the measurement locations indicating the wave breaker coefficient is slightly overestimated for this steep wave condition. It is noted that

wave breaker coefficient calculation is intended for irregular waves and has not been calibrated for regular waves. Wave directions agree well with the measurements with the exception of a few measurement stations where significant differences are observed in the incident wave angles. From the measurements it appears that the location of the breaker is outside of the measurement stations. The calculated longshore current velocities show the smallest NRMSE and NMAE of all three cases with values of 14 and 11%, respectively. The cross-shore velocities conversely, show the largest NRMSE and NMAE values of all three cases with values of 28 and 20%, respectively (see Table 6.16). Measured and computed current velocities for Case 3 agree reasonably well. However, the long-shore current speed tends to be overestimated near the breaker.

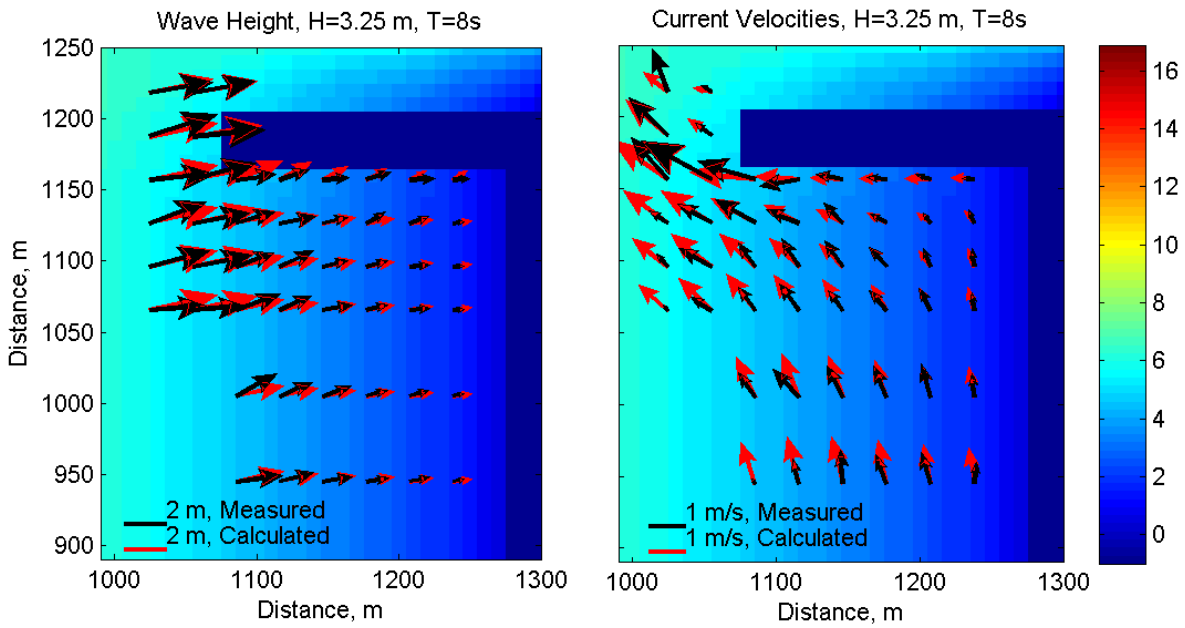

Figure 6.18. Measured and calculated wave height (left) and mean current (right) vectors for Case 3. Background colors indicate the local water depth corresponding the right color bar.

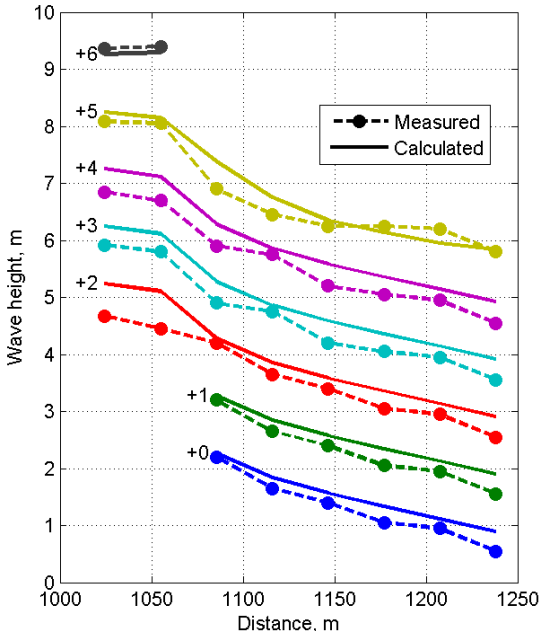

Figure 6.19. Cross-shore transects of measured and calculated wave heights for Case 3 (H = 3.25 m, T = 8 s). For display purposes, wave heights are shifted by the number indicated on the left-hand side of each transect.

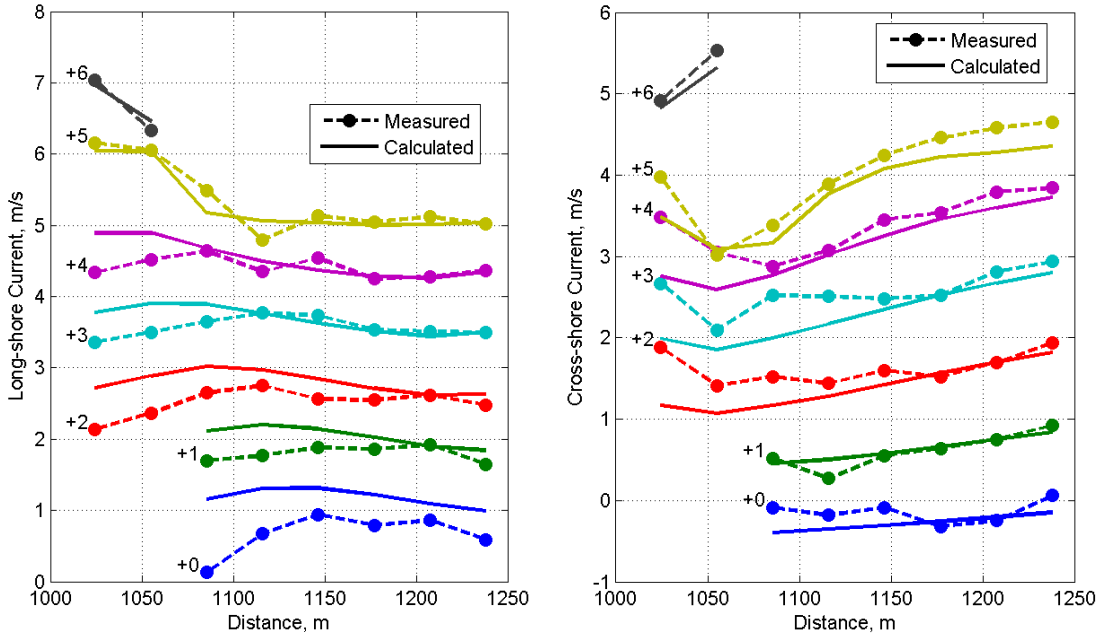

Figure 6.20. Cross-shore transects of measured and calculated long-shore (left) and cross-shore (right) currents for Case 3 (H = 3.25 m, T = 8 s). For display purposes, current velocities are shifted by the number indicated on the left-hand side of each transect.

Table 6.16. Goodness-of-fit statistics* for Case 3 (H = 3.25 m, T = 8 s)

Variable	NRMSE, %	RMAE, %	R^2	Bias
Longshore current	13.86	10.61	0.886	-0.189 m/s
Cross-shore current	27.75	20.48	0.676	0.158 m/s
Wave Height	9.98	8.68	0.978	0.223 m
*defined in Appendix A				

6.5 Channel Infilling and Migration: Steady Flow Only

The model is applied to a laboratory flume study of channel infilling and migration due to a steady flow perpendicular to the channel axis. Model performance is evaluated by comparing measured and computed bed elevations of the channel cross-sections. Three channel cross-sections with slopes from 1:10 to 1:3 are simulated to test the limits of the depth-averaged model. Specific model features tested are: a) single-sized non-equilibrium total-load sediment transport, b) equilibrium inflow concentration boundary condition, and c) zero-gradient outflow boundary condition.

Three laboratory experiments of channel infilling and migration are carried out at the Delft Hydraulics Laboratory (DHL 1980) in a rectangular flume (length = 30 m, depth=0.7 m, and width = 0.5 m) with a medium sand (d_{50} = 0.16 mm, d_{90} = 0.2 mm). In these tests, the mean flow velocity and water depth at the inlet were 0.51 m/s and 0.39 m, respectively. The initial channel cross-sections had side slopes of 1:10, 1:7 and 1:3. Sediment was supplied at a rate of 0.04 kg/m/s at the inlet to avoid erosion. The upstream bed and suspended load transport rates were estimated at 0.01 and 0.03 kg/m/s, respectively.

The laboratory study is simulated as a 1D problem and the flume wall effects are ignored in the simulation for simplicity. The computational grid consists of 3 rows and 220 columns (see Figure 6.21) with constant resolution of 0.1 m. The computational time step is 1 min. A flux boundary is specified for the upstream boundary with an equilibrium sediment concentration. Water level and zero concentration gradient boundary conditions are specified at the downstream boundary. Bed and suspended load scaling factors are adjusted to match the measured inflow transport rates and estimated at 1.2 and 0.5, respectively. The Lund-CIRP transport formula (Camenen and Larson 2005, 2007, 2008) is used for all three cases. The transport grain size is set to median grain size (d_{50} = 0.16 mm), and no hiding and exposure is considered in the present simulations. The bed slope coefficient is set to 1.0. Sensitivity analysis shows that the model results are not sensitive to bed slope coefficients between 0.1 and 2.0. The bed porosity is estimated at 0.35. Representative settling velocity is 0.013 m/s. A summary of selected model parameters is shown in Table 6.17. The total-load adaptation length is calibrated to 0.75 m using the measured bed elevations in the case of side slope 1:10 (Case 1), and then applied in cases of side slopes 1:7 and 1:3 (Cases 2 and 3, respectively) to validate the model.

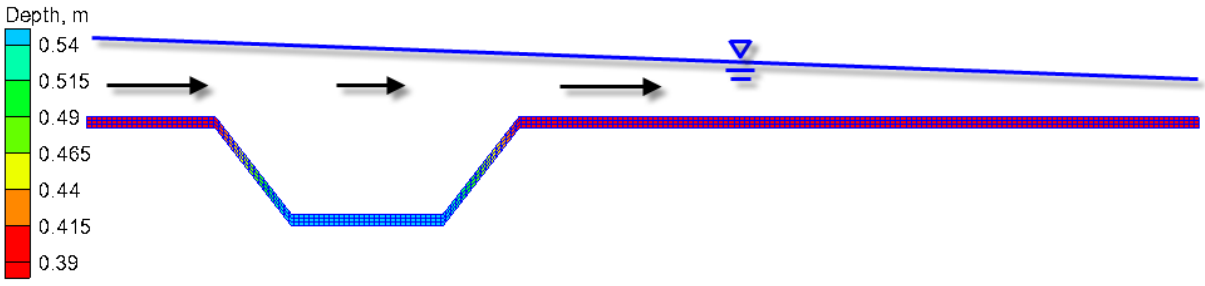

Figure 6.21. Computational grid for the DHL (1980) experiment test case.

Table 6.17. Model parameter settings for DHL (1980) experiment test case.

Parameter	**Value**
Flow time step	1 min
Simulation duration	15 hr
Ramp period duration	0.1 hr
Water density	1,000 kg/m^3
Manning's coefficient	0.025 s/m$^{1/3}$
Wall friction	Off
Transport grain size	0.16 mm
Bed slope coefficient	1.0
Sediment porosity	0.35
Sediment density	2,650 kg/m^3
Suspended load scaling factor	1.2
Bed load scaling factor	0.5
Total load adaptation length	0.75 m
Sediment transport formula	Lund-CIRP

Since the depth-averaged model is expected to perform best for the cases without three-dimensional (3D) flows caused by the steeper side slopes, Case 1 is chosen for calibration. Case 1 also has the most data of the three cases since bed elevations were measured at two time intervals. The only calibration parameter used is the total-load adaptation length which is estimated at 0.75 m. Computed and measured still water depths for Case 1 are compared in Figure 6.22. The goodness-of-fit statistics for calculated water depth in Case 1 are given in Table 6.18. The BSS values indicate excellent model performance; however, it is recognized that these results are calibrated to best represent the measurements.

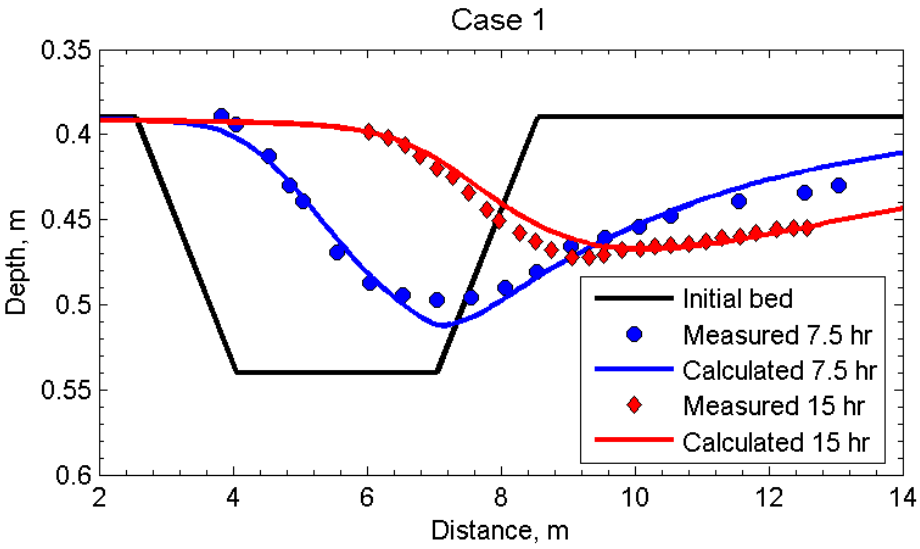

Figure 6.22. Measured and calculated bed elevations for Case 1 of DHL (1980).

Table 6.18. Water depth goodness-of-fit statistics* for Case 1 of DHL (1980).

Case	Time, hr	BSS	NRMSE, %	NMAE, %	R^2	Bias, m
1	7.5	0.905	7.09	5.92	0.956	0.0010
	15	0.932	7.75	5.77	0.955	-0.0031
*defined in Appendix A						

Computed and measured still water depths for Cases 2 and 3 are compared in Figure 6.23 and Figure 6.24. The corresponding goodness-of-fit statistics are given in Table 6.19. The model performance for Cases 2 and 3 is not as good as for Case 1, possibly due to flow separation on the upstream channel side caused by the steeper slopes of Case 3 and perhaps Case 2. When flow separation occurs, it is expected to cause a steepening of the upstream profile by hindering the downstream (downslope) movement of sediment at the upstream channel side. The presence of flow separation for Cases 2 and 3 is supported by the steep measured bathymetry. Since the flow model is depth-averaged in this case, flow separation will cause significant errors in the

computed morphology change. In general, flow separation is greatest at an incident current angle of 90º with respect to the channel axis and reduces as the angle decreases. Since most navigation channels at coastal inlets are approximately aligned with flow, flow separation may not be a major source of error in field applications. In applications with flow separation or other three-dimensional (3D) flow patterns, a corresponding 3D flow and sediment transport model may be necessary.

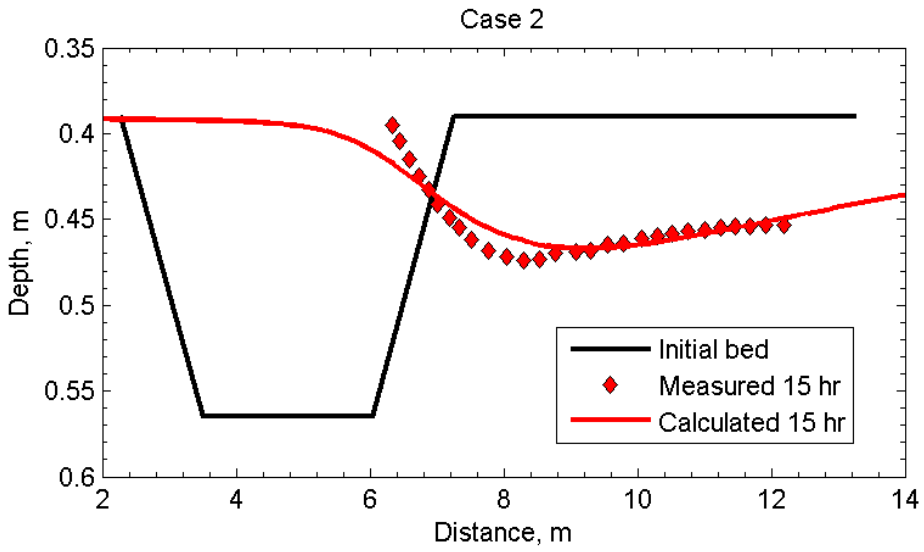

Figure 6.23. Measured and calculated bed elevations for Case 2 of DHL (1980).

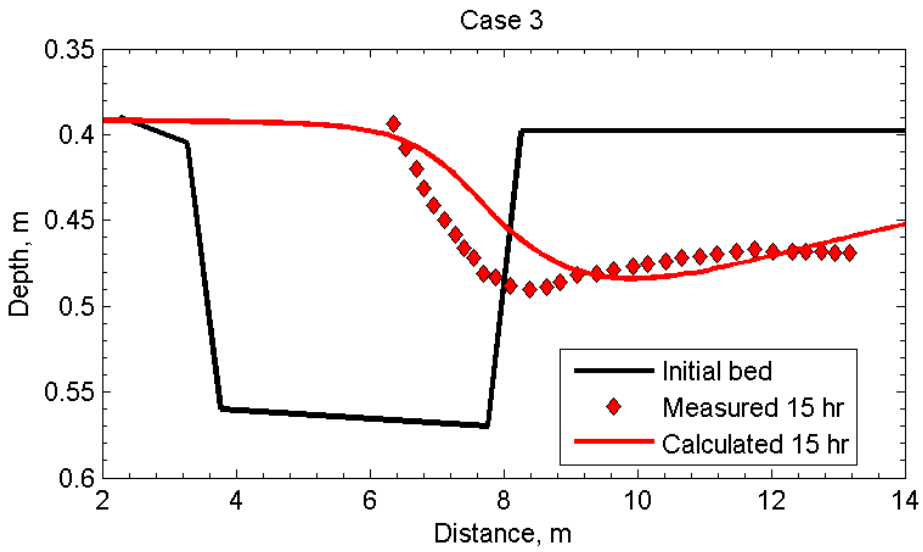

Figure 6.24. Measured and calculated bed elevations for Case 3 of DHL (1980).

Table 6.19. Water depth goodness-of-fit statistics* for Cases 2 and 3 of DHL (1980).

Case	Time, hr	BSS	NRMSE, %	NMAE, %	R^2	Bias, m
2	15	0.888	10.21	7.55	0.880	-0.0005
3	15	0.795	20.19	15.36	0.623	-0.0098
*defined in Appendix A						

6.6 Channel Infilling and Migration: Waves Parallel to Flow

The developed model is applied to a laboratory case to study channel infilling and migration with collinear steady flow and regular waves. Specific model features tested are: a) inline wave-current-sediment coupling, b) the single-sized non-equilibrium total-load sediment transport model, and c) sediment boundary conditions. The model performance is tested using measured water depths and a sensitivity analysis is done for the transport formula, total-load adaptation length, and bed slope coefficient.

Van Rijn (1986) reported results from a laboratory experiment on the evolution of channel morphology in a wave-current flume caused by a cross-channel flow and waves parallel to the flow. The flume was 17-m long, 0.3-m wide and 0.5-m deep. A pumping system was used to generate a steady current in the flume. The inflow depth-averaged velocity and water depth were 0.18 m/s and 0.255 m, respectively. A circular weir was used to control the upstream water depth. Regular waves with a height of 0.08 m and period of 1.5 s were generated by a simple wave paddle. The bed material consisted of fine well sorted sand with d_{50} = 0.1 mm and d_{90} = 0.13 mm. Sand was supplied at a rate of 0.0167 kg/m/s at the upstream end in order to maintain the bed elevation. A summary of the experiment hydrodynamic and wave conditions is presented in Table 6.20.

Table 6.20. Hydrodynamic and wave conditions for the van Rijn (1986) test case.

Variable	**Value**
Upstream water depth	0.255 m
Upstream current velocity	0.18 m/s
Wave height (regular)	0.08 m
Wave period (regular)	1.5 s
Incident wave angle with respect to flow	0 deg
50^{th} percentile (median) grain size, d_{50}	0.1 mm
90^{th} percentile grain size, d_{90}	0.13 mm

For simplicity, the case is simulated as a 1-D problem by neglecting the flume wall effects. The computational grid had a constant resolution of 0.1 m and is 3-cells wide and 140-cells long (see Figure 6.25). The water flux and equilibrium sediment concentration are specified at the upstream boundary, and a water level and zero-concentration-gradient boundary is

specified at the downstream end. Zero current velocity and water levels are specified as the initial condition (cold start). A summary of the relevant flow and wave model settings is provided in Table 6.21 and Table 6.22. The Lund-CIRP (Camenen and Larson 2005, 2007, 2008), Soulsby-van Rijn (Soulsby 1997) (referred to as Soulsby for short), and van Rijn (van Rijn 1984a,b; 2007a,b) transport formulas are tested. Bed and suspended load transport scaling factors are adjusted to match the measured inflow sediment supply rate. Results are presented for a range of adaptation lengths and bed slope coefficients.

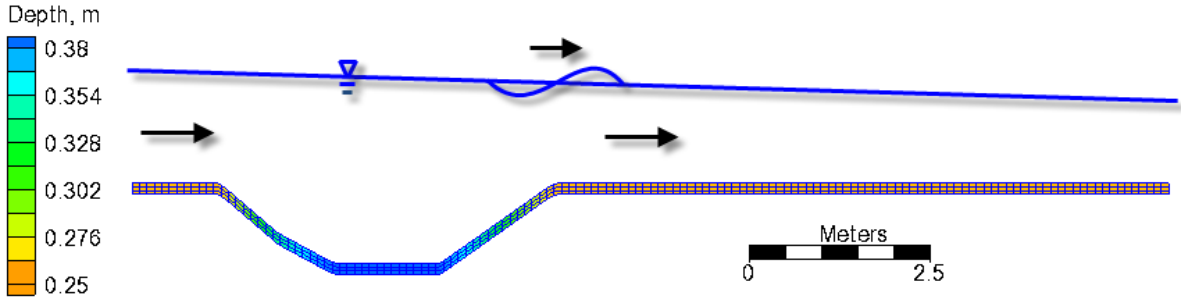

Figure 6.25. Computational grid for the van Rijn (1986) test case.

Table 6.21. Model settings for the van Rijn (1986) test case.

Parameter	**Value**
Time step	2 min
Simulation duration	10 hr
Ramp period duration	0.5 hr
Inflow discharge	0.0138 m^3/s
Outflow water level	-0.002 m
Manning coefficient	0.025 $s/m^{1/3}$
Wall friction	Off
Water density	1,000 kg/m^3
Transport grain size	0.1 mm
Sediment transport formula	Lund-CIRP, Soulsby-van Rijn, and van Rijn
Bed and suspended load scaling factors	0.9 (Lund-CIRP), 2.7 (Soulsby-van Rijn), and 2.0 (van Rijn)
Sediment porosity, p_m	0.3, 0.35, 0.4
Sediment density	2,650 kg/m^3
Bed slope coefficient, D_s	0, 1, 5
Total-load adaptation length, L_t	0.5, 1, 2, 5, and 10 m

Table 6.22. Wave model settings for the van Rijn (1986) test case.

Parameter	**Value**
Wave height (regular)	0.08 m
Wave period (regular)	1.5 s
Incident wave angle with respect to flow	0.0 º
Bottom friction	Off
Steering interval	0.5 hr

The computed bed elevations after 10 hr for different transport formulas, adaptation lengths, bed slope coefficients and porosities are shown in Figure 6.26 to Figure 6.29. The corresponding water depth goodness-of-fit statistics are provided in Table 6.23 to Table 6.26. The current model reproduces the general trends of the morphology change including the upstream bank migration, channel infilling, and downstream bank erosion.

The van Rijn and Soulsby-van Rijn transport formulas produce relatively similar results. Among the three transport formulas, the van Rijn transport formula produces the best agreement as compared with measurements. Both the van Rijn and Soulsby-van Rijn formulas give the best results for total-load adaptation length L_t = 5 m, while the Lund-CIRP formula gives the best results with L_t = 0.5 m and 1 m, consistent with other similar experiments of channel infilling and migration. Of the three formulas tested, the Soulsby-van Rijn formula is the most sensitive to L_t and produces a negative Brier Skill Score (BSS) for L_t =1.0 m and less. The Lund-CIRP formula is the least sensitive to L_t.

The differences in the best fit L_t for different transport formulas are due to differences in the transport capacities over the channel trough. The upstream concentration capacities are equal for all formulas since the bed and suspended load scaling factors are adjusted to match the measured sediment supply rate. These scaling factors are 2.0, 2.7, and 0.9 for the van Rijn, Soulsby-van Rijn, and Lund-CIRP transport formulas, respectively (see Table 6.21). Over the trough, the van Rijn, Soulsby-van Rijn and Lund-CIRP formulas predict concentration capacities equal to 0.051, 0.002, and 0.232 kg/m^3, respectively. The van Rijn and Soulsby-van Rijn formulas estimate much smaller concentration capacities in the channel trough and produced greater channel infilling and migration than the Lund-CIRP formula. The van Rijn and Soulsby-

van Rijn transport formulas also require larger transport scaling factors in order to match sediment supply rate (see Table 6.21). The adaptation length should be independent of the transport formula, yet the results show that errors in the transport formula may lead to different calibrated adaptation lengths. These results emphasize the importance of having an accurate transport formula.

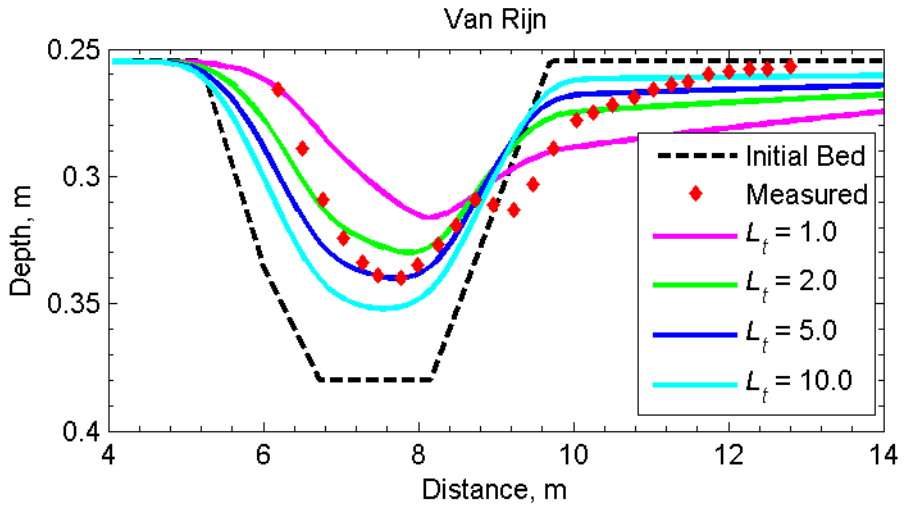

Figure 6.26. Measured and calculated water depths at 10 hr using the van Rijn transport formula and total-load adaptation lengths between 1 and 10 m.

Table 6.23. Water depth goodness-of-fit statistics* using the van Rijn transport formula and varying total-load adaptation length.

Total-load Adaptation Length, m	**BSS**	**NRMSE %**	**NMAE %**	**R^2**	**Bias m**
1.0	0.453	23.50	20.78	0.700	-0.0008
2.0	0.686	13.50	11.15	0.876	0.0002
5.0	0.627	16.05	11.57	0.807	0.0015
10.0	0.471	22.73	17.46	0.766	0.0037
*defined in Appendix A					

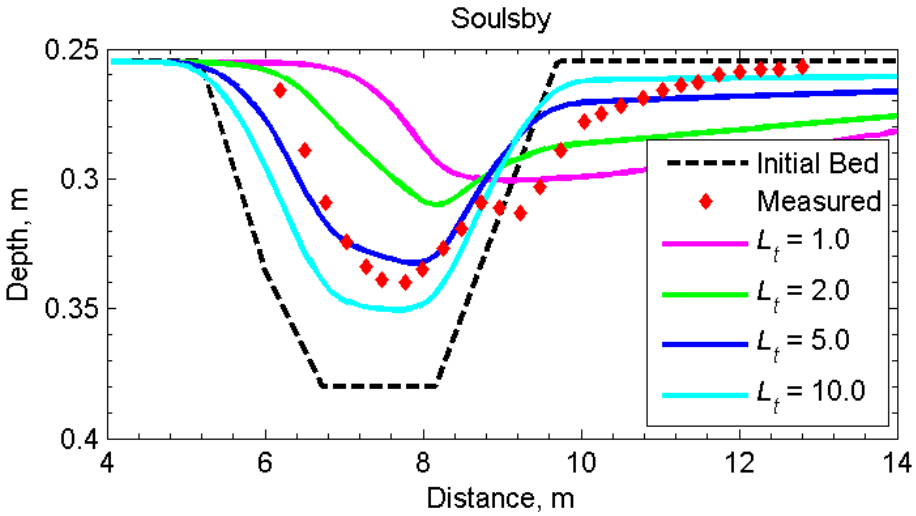

Figure 6.27. Measured and calculated water depths at 10 hr using the Soulsby-van Rijn transport formula and total-load adaptation lengths between 1 and 10 m.

Table 6.24. Water depth goodness-of-fit statistics* using the Soulsby-van Rijn transport formula and varying total-load adaptation length.

Total-load Adaptation Length, m	**BSS**	**NRMSE %**	**NMAE %**	**R^2**	**Bias m**
1.0	-0.025	0.4407	0.3813	0.070	-0.0051
2.0	0.346	0.2812	0.2494	0.461	-0.0048
5.0	0.667	0.1433	0.1111	0.836	-0.0012
10.0	0.486	0.2210	0.1693	0.763	0.0026
*defined in Appendix A					

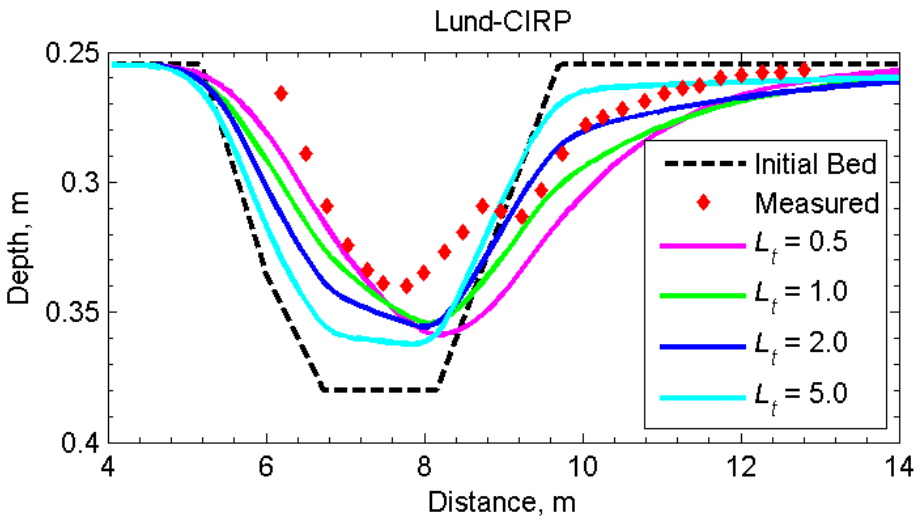

Figure 6.28. Measured and calculated water depths at 10 hr using the Lund-CIRP transport formula and total-load adaptation lengths between 0.5 and 5 m.

Table 6.25. Water depth goodness-of-fit statistics* using the Lund-CIRP transport formula and varying adaptation length.

Total-load Adaptation Length, m	**BSS**	**NRMSE %**	**NMAE %**	**R^2**	**Bias m**
0.5	0.458	0.2396	0.2042	0.909	0.0170
1.0	0.548	0.1998	0.1765	0.938	0.0147
2.0	0.514	0.2147	0.1671	0.866	0.0124
5.0	0.327	0.2973	0.2193	0.744	0.0098
*defined in Appendix A					

The bed slope coefficient D_s is usually not an important calibration parameter for field applications. It has a default value of 1.0. Increasing the bed slope coefficient has the net effect of moving sediment downslope and smoothing the bathymetry. For this laboratory experiment case, the fraction of bed load upstream of the channel is approximately 8-17%. Although the best goodness-of-fit statistics are obtained from D_s = 5.0, it is clear from Figure 6.29 that this

produces excessive smoothing as compared to D_s = 1.0. When the bed slope coefficient is turned off (D_s = 0.0), the calculated bed profile preserves the sharp corners from the initial profile but this is an unrealistic trend.

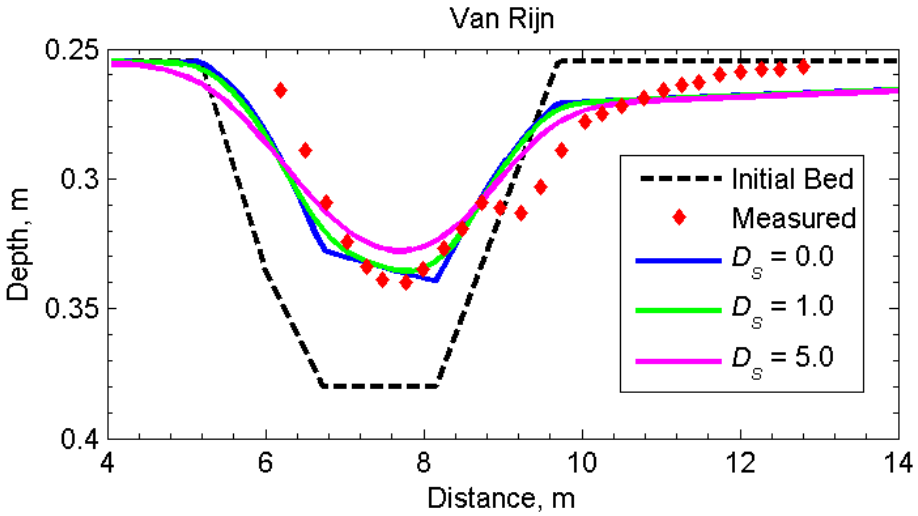

Figure 6.29. Measured and calculated water depths at 10 hr using the van Rijn transport formula and total-load adaptation length of 5.0 m and bed slope coefficient between 0 and 5.

Table 6.26. Water depth goodness-of-fit statistics* using the van Rijn transport formula as a function of varying bed slope coefficient.

Bed slope Coefficient	**BSS**	**NRMSE %**	**NMAE %**	**R^2**	**Bias m**
0.1	0.648	15.13	11.49	0.816	0.0012
1.0	0.669	14.25	10.59	0.834	0.0008
5.0	0.694	13.17	10.70	0.880	-0.0005
*defined in Appendix A					

6.7 Channel Infilling and Migration: Waves Perpendicular to Flow

The sediment transport model is applied to a laboratory case of channel infilling and migration with steady flow and random waves. The case is similar to the previous one except that the waves are parallel to the channel axis (perpendicular to the flow). Specific model features tested in this case are: a) inline wave-current-sediment coupling, b) single-sized non-equilibrium total-load transport model, and c) sediment boundary conditions. The model performance is evaluated using measured water depths and a sensitivity analysis is performed for the total-load adaptation length.

Van Rijn and Havinga (1995) conducted a laboratory experiment on the channel morphology change under steady cross-channel flow with waves perpendicular to the flow. The flume was approximately 4 m wide and had 1:10 side slopes. The depth-averaged current velocity and water depth at the inlet were 0.245 m/s and 0.42 m, respectively. Random waves (JONSWAP form) were generated at a 90º angle to the flow and had a significant wave height of 0.105 m and peak wave period of 2.2 s. The suspended sediment transport rate was measured to be at 0.022 kg/m/s. Table 6.27 summarizes the experimental conditions.

Table 6.27. General conditions for van Rijn and Havinga (1995) experiment.

Parameter	**Value**
Upstream current velocity	0.245 m/s
Upstream water depth	0.42 m
Significant wave height	0.105 m
Peak wave period	2.2 s
Wave direction	90º
Upstream suspended transport rate	0.022 kg/m/s
Median grain size	0.1 mm

For simplicity, the case is simulated as a 1D problem by ignoring the flume wall effects. The same computational grid used for flow and wave models is shown in Figure 6.30 with the colors representing the initial bathymetry. The grid has 390 active computational cells and a constant resolution of 0.1 m. A water flux boundary condition is specified at the upstream boundary (left side) and a water level boundary at the downstream boundary (right side). The initial condition is specified as zero for water level and current velocity over the whole grid. Equilibrium sediment concentration is specified at the inflow boundary and a zero-gradient boundary condition at the outflow boundary.

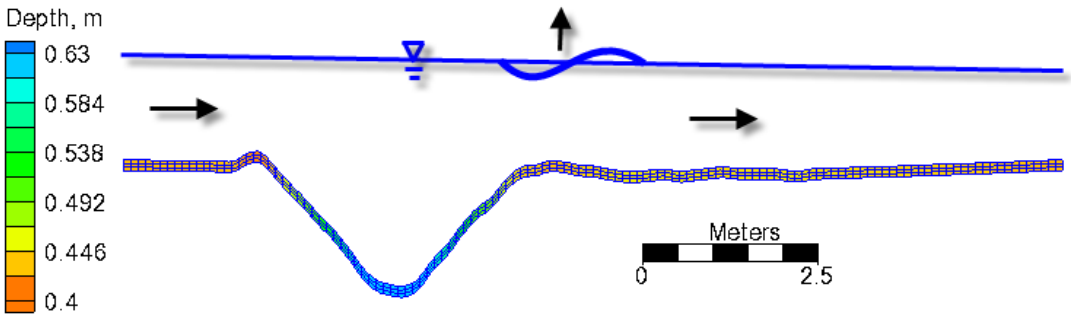

Figure 6.30. Computational grid for the van Rijn and Havinga (1986) test case.

Table 6.28 shows the model setup parameters. Default values are used wherever possible. The Manning's coefficient is estimated as 0.02 $s/m^{1/3}$ by fitting a lognormal distribution to the measured current velocity profile. The Lund-CIRP formula is used to determine the sediment transport capacity. The suspended load scaling factor is adjusted based on the measured inflow transport rate and set to 0.67 which is within the generally accepted range of 0.5-2.0. Since no measurements for bed load are available, the bed-load transport capacity is not modified. The transport grain size is set to median grain size so that no hiding and exposure is considered in the

simulation. Model result sensitivity to the adaptation length L_t is tested for the values of 0.5, 0.7, 1, and 2 m as shown in Table 6.28.

Table 6.28. Model input settings for the van Rijn and Havinga (1995) test case.

Setting	**Value**
Simulation duration	24 hr
Ramp period duration	30 min
Time step	1 min
Manning's coefficient	0.02 $s/m^{1/3}$
Steering interval	3 hr
Transport grain size	0.1 mm
Transport formula	Lund-CIRP
Bed load scaling factor	1.0
Suspended load scaling factor	0.67
Sediment fall velocity	0.6 mm/s
Bed porosity	0.4
Bed slope coefficient	1.0
Total-load adaptation length, L_t	0.5, 0.7, 1, 2 m

Figure 6.31 shows a comparison of the measured and computed bed elevations after 23.5 hr for each adaptation length evaluated. The model reproduces the overall measured trend of the channel migration and infilling. However, the computed bathymetry is much smoother than the measured bathymetry. This is due to the fact that the model does not simulate the small-scale bed forms. Based on the goodness of fit statistics shown in Table 6.29, the model performance is relatively good. For this case, adaptation lengths of 0.5, 0.7, and 1 m give similar results. The results show that the model is somewhat sensitive to the adaptation length. However, once this parameter is calibrated, relatively accurate results can be obtained.

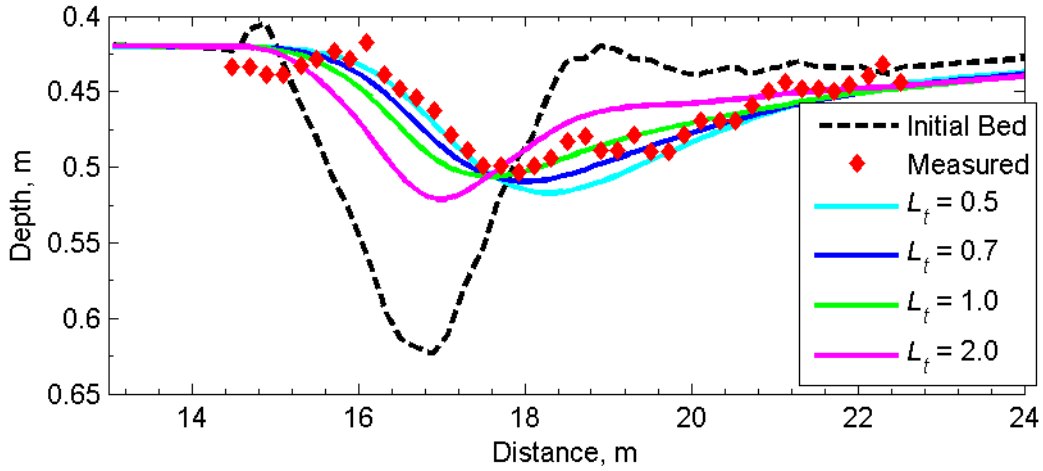

Figure 6.31. Measured and calculated bathymetry at 23.5 hr with varying total-load adaptation lengths between 0.5 and 2.0 m.

Table 6.29. Water depth goodness-of-fit statistics* for the van Rijn and Havinga (1995) experiment.

Total-load Adaptation Length, m	**BSS**	**NRMSE, %**	**NMAE, %**	**R^2**	**Bias, m**
0.5	0.978	15.60	12.55	0.897	0.0071
0.7	0.983	13.85	12.02	0.876	0.0063
1.0	0.976	16.37	12.91	0.754	0.0054
2.0	0.917	30.49	22.91	0.252	0.0039
*defined in Appendix A					

6.8 Surf-zone Hydrodynamics and Sediment Transport

Data from the Large-Scale Sediment Transport Facility provide detailed measurements of wave height, water level, longshore current speed, and sediment transport (bed and suspended load) within a controlled laboratory environment. Application of the model to this test case demonstrates the model capability of calculating the cross-shore distribution of wave height, longshore current, and sediment transport from the wave breaker zone inshore.

The Large-Scale Sediment Transport Facility (LSTF) at the Engineer Research and Development Center of U.S. Army Corps of Engineers (shown in Figure 6.28) is capable of simulating oblique (6.5º incident angle) regular and random waves and a uniform longshore current. The longshore current is recirculated from the downdrift end to the updrift end of the LSTF by adjusting a series of 20 pumps in the cross-shore direction therefore simulating an infinite beach. The test case discussed here represents a natural beach with a uniform longshore current. The experiment was 160 min long and measured the cross-shore distribution of significant wave height, water level, current speed, and suspended sediment transport. All comparisons here are for Case 1, in which a longshore current was induced by oblique random waves and the pumps were adjusted to match the measured longshore current. Table 6.30 summarizes the setup for LSTF Case 1.

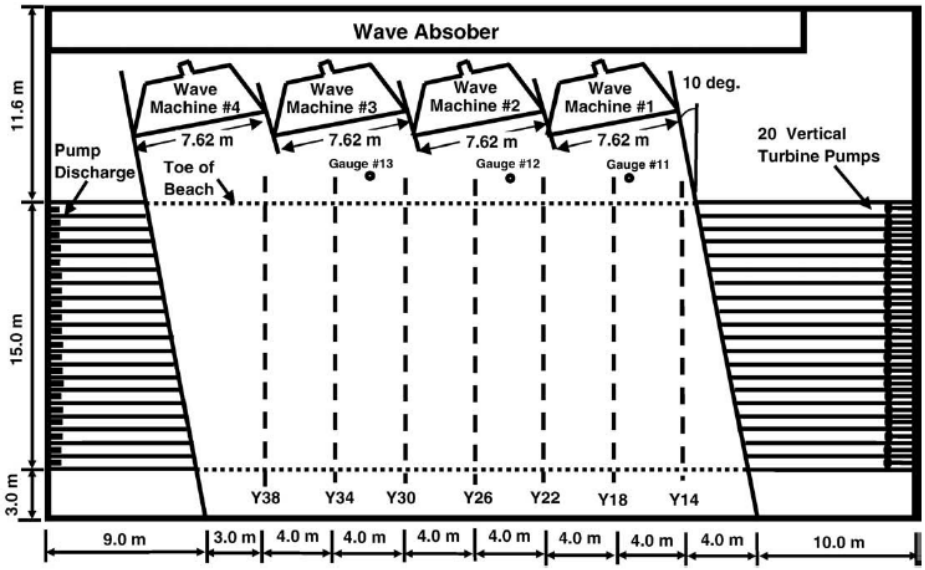

Figure 6.32. LSTF configuration (Gravens and Wang 2007).

Table 6.30. Wave and hydrodynamic conditions for LSTF Test Case 1.

Variable	**Value**
Offshore significant wave height	0.228 m
Peak period	1.465 s
Incident wave angle	6.5^{o}
Water level	-0.001 m

The computational domain is generated based on the interpolation of measured beach profiles from profile Y14 to Y34 (see Figure 6.28). Constant grid resolution of 0.2 and 0.4 m are used in the cross-shore and longshore directions, respectively. A TMA spectrum is assumed at the offshore boundary with the parameter values $\gamma = 3.3$, and $n = 100$ which are related to the spectrum spreading in frequency and direction, respectively (Lin et al. 2008). The offshore water level during the experiment is not equal to the Still Water Level (SWL) because of the wave setup. The offshore water level is approximated for each experiment based on the most offshore water level gauge. Table 6.31 and Table 6.32 summarize the flow and wave model settings, respectively.

Table 6.31. Flow model settings for the LSTF test cases.

Setting	**Value**
Time step	1 min
Wetting and drying depth	0.001 m
Simulation duration	3.0 hr
Ramp duration	2.5 hr
Manning coefficient	0.016 $s/m^{1/3}$
Transport grain size	0.15 mm
Transport formula	Lund-CIRP, van Rijn, and Soulsby-van Rijn
Sediment porosity	0.4
Bed change	Off

Table 6.32. Wave model settings for the LSTF test cases.

Setting	**Value**
Wave breaking	Battjes and Janssen (1978)
Bottom friction	Off
Steering interval	0.25 hr
Roller	On
Roller dissipation coefficient	0.05
Roller efficiency factor	0.5

Calculated wave heights, depth-averaged current velocities, and water levels are compared with the LSTF center line profile measurements in Figure 6.33, Figure 6.34, and Figure 6.35. Table 6.33 summarizes the goodness-of-fit statistics for hydrodynamics in Case 1. Wave heights and water levels have normalized errors of 3-4% and 10-12%, respectively. Similar results were obtained by Nam et al. (2009). Longshore current calculations have larger errors ranging from 18-24%. The calculated peak longshore current is slightly offshore from the

measured peak. Reducing the roller dissipation coefficient may improve these estimates by moving the peak longshore current closer to the shoreline. Another reason is that the location of the second breaker zone, located at approximately 6-7 m from the shoreline, is predicted slightly further offshore, causing the a longshore current peak which is also further offshore.

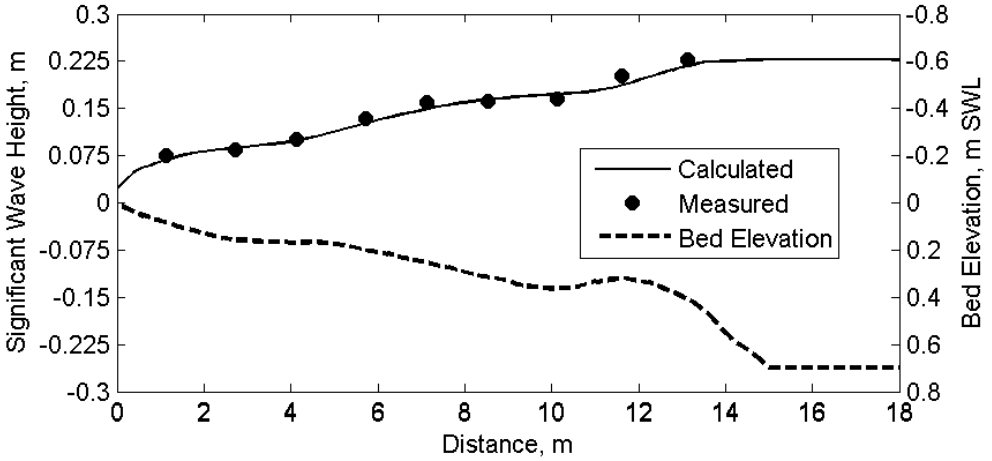

Figure 6.33. Measured and computed significant wave heights for LSTF Case 1.

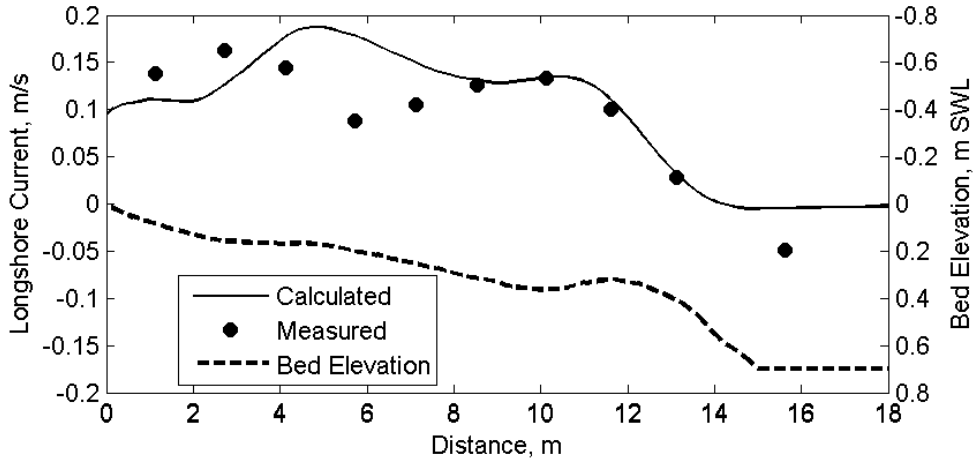

Figure 6.34. Measured and computed longshore currents for the LSTF Case 1.

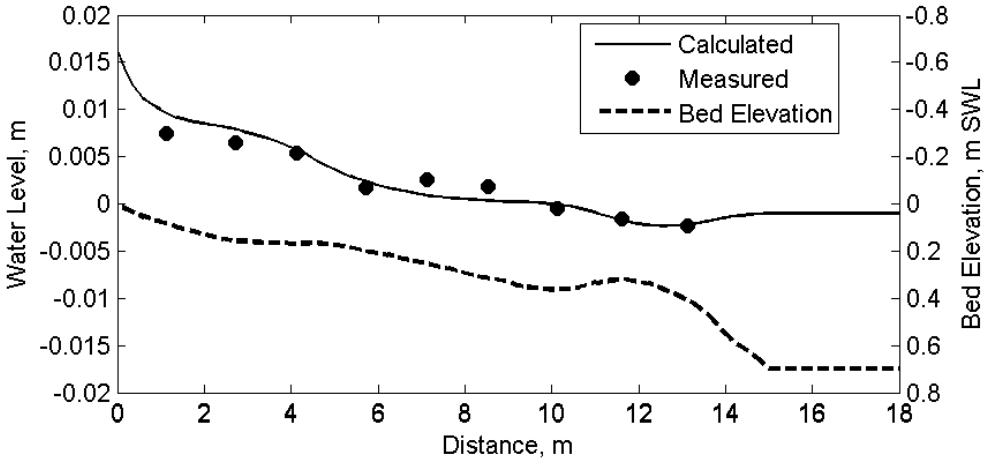

Figure 6.35. Measured and computed mean water levels for the LSTF Case 1.

Table 6.33. Goodness-of-fit statistics* for waves, water levels and longshore currents in the LSTF Case 1

	NRMSE, %	**NMAE, %**	**R^2**	**Bias, m, m/s**
H_s	3.63	3.15	0.982	-0.005
Water Level	12.18	9.86	0.934	0.0001
Longshore Current	24.09	18.09	0.665	0.017
*defined in Appendix A				

Comparisons between the calculated and measured suspended sediment transport in the longshore direction using three sediment transport formulas: Lund-CIRP, Soulsby- van Rijn, and van Rijn are presented in Figures 6.36, 6.37, and 6.38, respectively. The measurements show three peaks in the sediment transport magnitudes, one near the offshore bar, another in the middle of the profile where there is a very slight inshore bar, and the greatest value at the swash zone. All three formulations predict well the locations of the two offshore peaks but underestimate the sediment transport near the shoreline. This is due to the fact that the swash zone is not included. Nam et al. (2009) found similar results without the swash zone transport

and also obtained significantly improved results by including the swash zone sediment transport. The swash zone sediment transport not only increases the transport in the swash zone but also in the surf zone by acting as a concentration boundary condition to the transport equation in the surf zone. In the present model, the wave height and current velocity will always tend to go to zero towards the shoreline, leading to an under prediction of the transport. The Lund-CIRP and Soulsby-van Rijn formulas predict well the magnitude of the transport while the van Rijn formula under-predicts the transport by a factor of about two. It is interesting to note that even though the location of the peak longshore current is not well predicted, the location of the peak longshore sediment transport is well predicted.

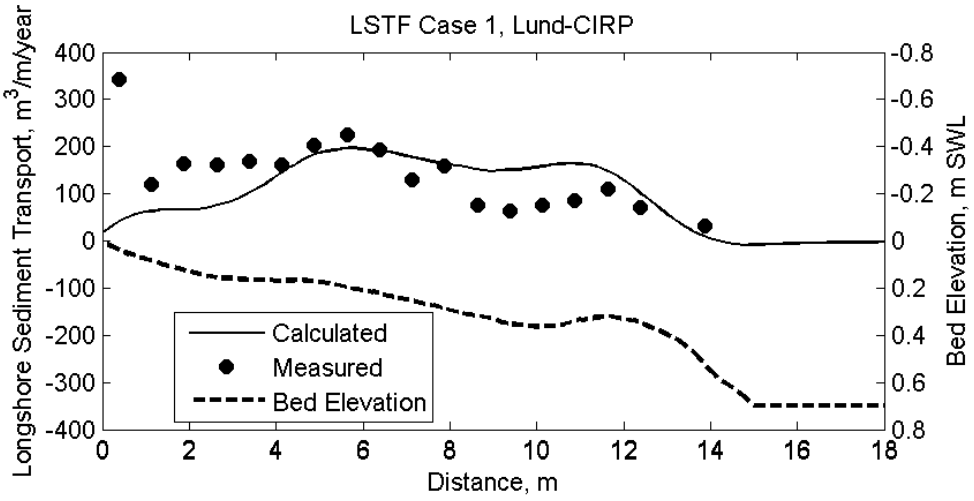

Figure 6.36. Measured and computed longshore sediment transport rates in LSTF Case 1 using the Lund-CIRP formula.

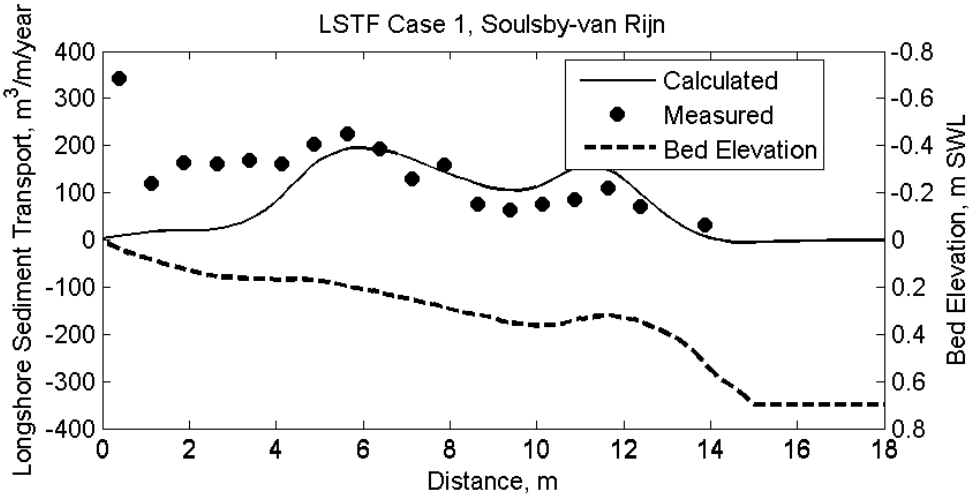

Figure 6.37. Measured and computed longshore sediment transport rates in LSTF Case 1 using the Soulsby-van Rijn formula.

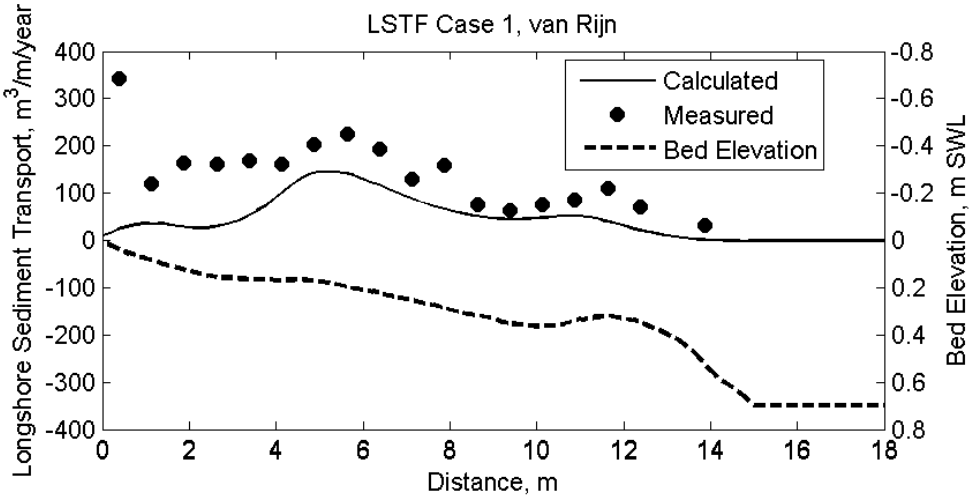

Figure 6.38. Measured and computed longshore sediment transport rates in LSTF Case 1 using the van Rijn formula.

Table 6.34 summarizes the goodness of fit statistics for the sediment transport calculations. All formulas have a negative bias, meaning that they all under-predict the magnitude of the mean sediment transport. Errors range from 22-26%, 26-33%, and 35-40% for the Lund-CIRP, Soulsby-van Rijn, and van Rijn formulations, respectively.

Table 6.34. Sediment transport goodness-of-fit statistics* for LSTF Case 1.

Transport Formula	**NRMSE, %**	**NMAE, %**	**R^2**	**Bias, $m^3/m/year$**
Lund-CIRP	25.88	21.99	0.164	-2.79
Soulsby-van Rijn	32.02	26.01	0.097	-23.38
van Rijn	33.77	29.81	0.567	-66.80
*defined in Appendix A				

6.9 Clear-water Erosion Over a Hard Bottom

The developed model is applied to a laboratory case of a clear water inflow in a rectangular flume with a sandy bed layer over a hard bottom. This experiment is useful for testing the sediment transport model under erosion conditions in the presence of a hard bottom. The case is also used here to compare results for structured and unstructured computational grids.

Thuc (1991) carried out a movable bed laboratory experiment in a rectangular flume 5 m long and 4 m wide, with a narrow 0.2 m-wide inlet and a 3 m-wide outlet. The initial water depth was 0.15 m, with a 0.16-m layer of sand (d_{50} =0.6 mm) over a concrete bottom. The estimated sand settling velocity is 0.013 m/s. Hydrodynamic and sediment parameters for the experiment are summarized in Table 6.35.

Table 6.35. Hydrodynamic and sediment conditions for the Thuc (1991) experiment case.

Parameter	**Value**
Inflow depth-averaged current velocity	0.6 m/s
Initial water depth	0.15 m
Bed median grain size	0.6 mm
Representative sediment fall velocity	0.013 m/s
Bed layer thickness	0.16 m

The transport equation which best fits the measurements is the Soulsby-van Rijn (Soulsby 1997). No measurements of bed or suspended load are available. It is found that the best morphologic results are obtained with bed and suspended load scaling factors of 3.0. The total-load adaptation length is calculated based on a weighted average of the bed and suspended-load adaptation lengths. The suspended-load adaptation length is set to 0.05 m. The bed-load adaptation length is set to the 0.2 times the local water depth. The bed slope coefficient is set to 0.5. Sensitivity analysis shows that the results are not sensitive to the bed slope coefficient. The parameters used are listed in Table 6.36.

Table 6.36. Hydrodynamic and sediment parameters for the Thuc (1991) experiment case.

Parameter	**Value**
Time step	30 s
Simulation duration	4.25 hr
Ramp period duration	0.01 hr
Manning's coefficient	0.03 $s/m^{1/3}$
Transport grain size	0.6 mm
Sediment fall velocity	0.013 m/s
Sediment density	2,650 kg/m^3
Sediment porosity	0.4
Sediment transport formula	Soulsby-van Rijn (Soulsby 1997)
Bed and suspended load scaling factors	3.0
Sediment inflow loading factor	0.0 (clear water)
Total load adaptation coefficient method	Weighted average of bed and suspended load adaptation lengths
Suspended load adaptation length	0.05 m
Bed load adaptation length	0.2 x local water depth
Avalanching	On

As mentioned previously, two computational grids are used for this test. The first is a structured nonuniform Cartesian grid (see Figure 6.39a) with a constant resolution of 0.1 m in the *x*-direction of and a variable resolution between 0.0333 and 0.1333 m in the *y*-direction. The computational mesh consists of 62 rows and 69 columns. The second computational grid used is a hybrid triangular and quadrilateral mesh (see Figure 6.39b). The unstructured mesh has 4533 cells and has a similar resolution to the Cartesian grid. The computational time step is 30 s. A water flux boundary is applied at the upstream end and a water level boundary at the downstream end. The initial water level and current velocities is set to zero for the whole domain (cold start).

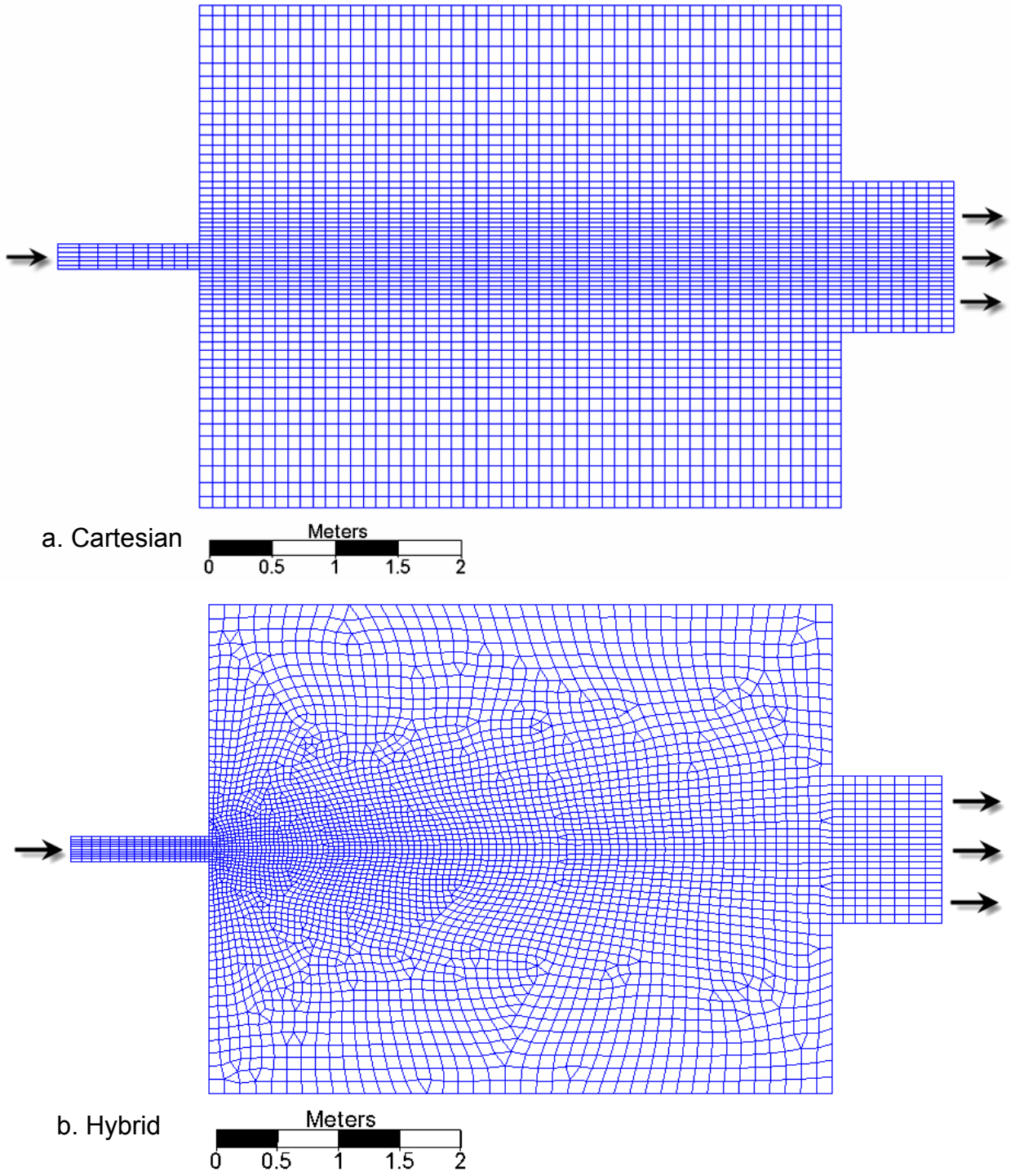

Figure 6.39. Computational grids for the Thuc (1991) experiment case: (a) nonuniform Cartesian grid and (b) unstructured hybrid grid.

The calculated current velocity patterns at 1 hr are presented in Figure 6.40 for both the Cartesian and unstructured grids. Similar results are obtained with both grids. The flow field is characterized by a long and narrow inflow that extends from the inlet across the rectangular domain and through the outlet. There is a small recirculation pattern within the basin but most of the flow from the inlet goes through the basin and out at the downstream end.

The calculated bed change and current velocities after an elapsed time of 4 hr is presented in Figure 6.41 for both the Cartesian and unstructured grids. Similar results are obtained with both computational grids and compared to Min Duc et al. (2004) and Wu (2004). Erosion occurs due to the inflow of clear water, and the eroded sediment moves downstream and deposits forming a dune feature which slowly migrates downstream. Both computational grids show good symmetry about the centerline.

Figure 6.42 compares the measured and calculated bed changes along the longitudinal centerline at 1, 2, and 4 hr for both the structured and unstructured grids. The calculated erosion and deposition depths are in good agreement with the measured data, in particular at times 2 and 4 hr. The computed water depth goodness-of-fit statistics for both computational grids are shown in Table 6.37. The differences in the computed water depths utilizing the structured and unstructured grids is relatively small as demonstrated by the goodness-of-fit statistics Table 6.37.

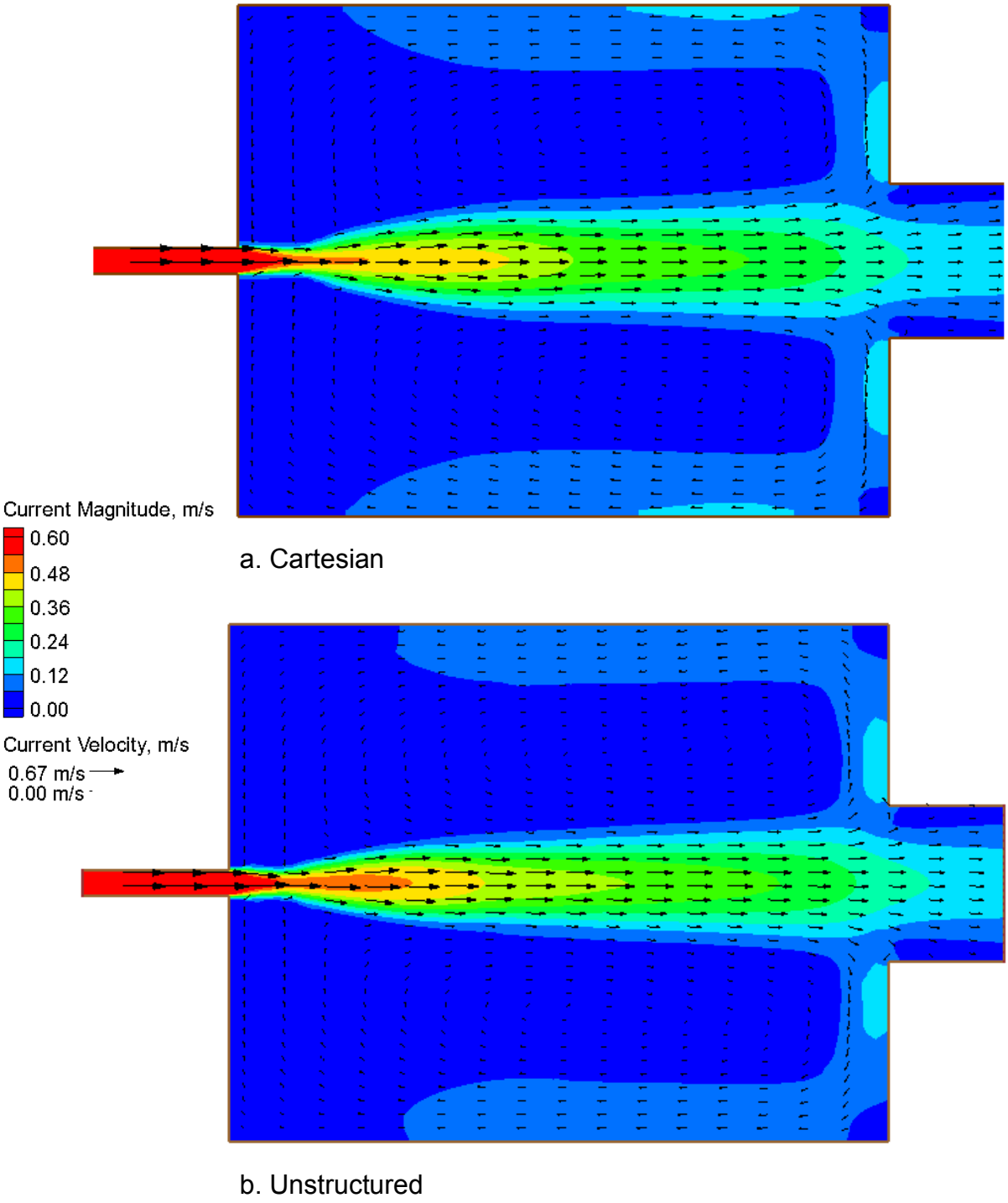

Figure 6.40. Computed current velocities at 1 hr for the Thuc (1991) test case for (a) structured and (b) hybrid grids.

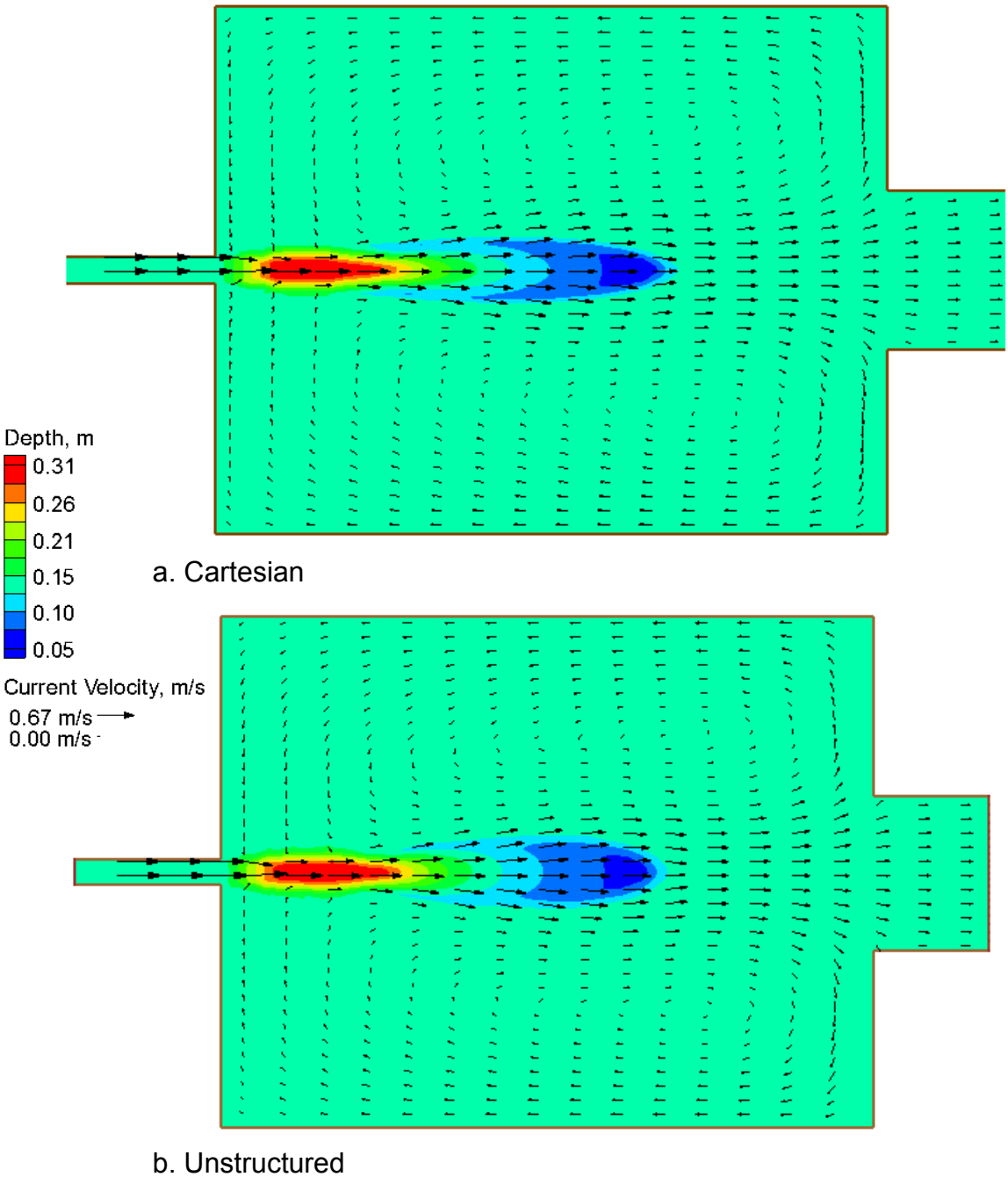

Figure 6.41. Computed bed elevations and current velocities at 4 hr for the Thuc (1991) test case for (a) structured and (b) hybrid grids.

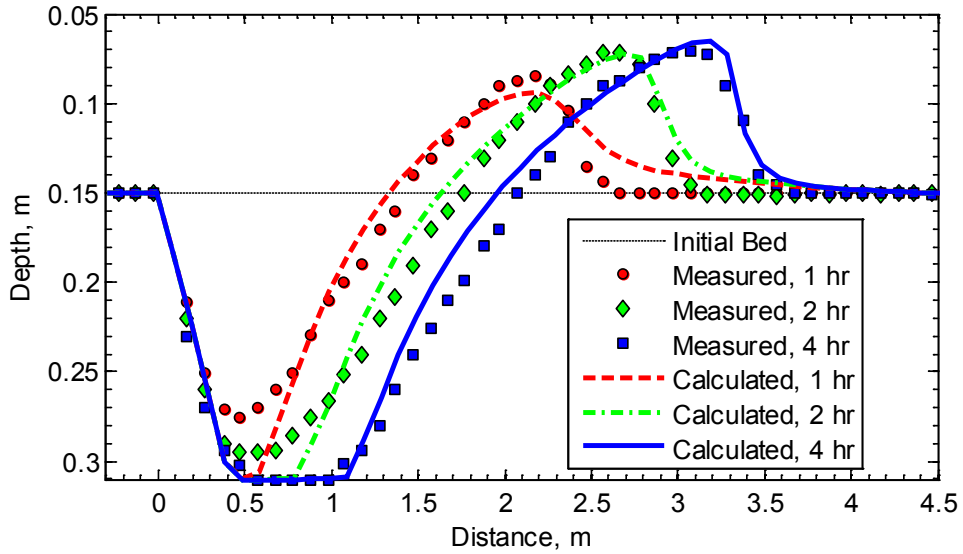

a. Cartesian

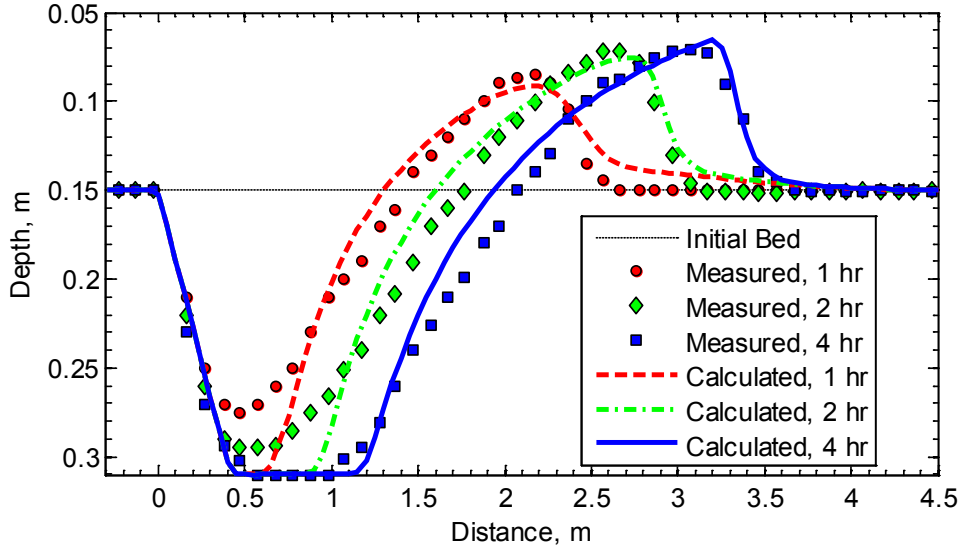

b. Unstructured

Figure 6.42. Comparison of calculated and measured bed elevation profiles at 1, 2, and 4 h along the basin longitudinal centerline for the Thuc (1991) test case: (a) structured and (b) hybrid grid.

Table 6.37. Water depth goodness-of-fit statistics* for the Thuc (1991) test case.

Grid	Time, hr	BSS	NRMSE, %	NMAE, %	R^2	NB, %
Cartesian	1.0	0.943	6.24	4.38	0.96	-0.67
	2.0	0.977	4.55	3.45	0.98	-1.38
	4.0	0.986	4.15	2.81	0.99	-2.25
Unstructured	1.0	0.932	6.80	4.62	0.94	-0.39
	2.0	0.969	5.24	3.88	0.98	-0.89
	4.0	0.986	4.09	2.67	0.99	-1.78
*defined in Appendix A						

6.10 Bed Aggradation and Sediment Sorting

The developed model is applied to three laboratory cases of channel deposition with multiple-sized sediments. These laboratory experiments are useful for testing the nonuniform sediment transport under transcritical flow conditions. The specific model features to be tested are the multiple-sized sediment transport, bed change and bed material sorting algorithms.

Laboratory experiments of bed aggradation and sediment sorting are carried out at the St. Anthony Falls Laboratory (SAFL) by Paola et al. (1992) and Seal et al. (1995). The flume was 45-m long and 0.305-m wide as shown in Figure 6.43. A tailgate was used to keep the downstream end at a constant water level. The inflow water volume flux is 0.049 m^3/s. The initial bed slope is 0.002. A slightly bimodal mixture of sediment ranging in size from 0.125 to 0.64 mm is fed into the flume. A summary of the experimental conditions for the three SAFL cases used here is provided in Table 6.38.

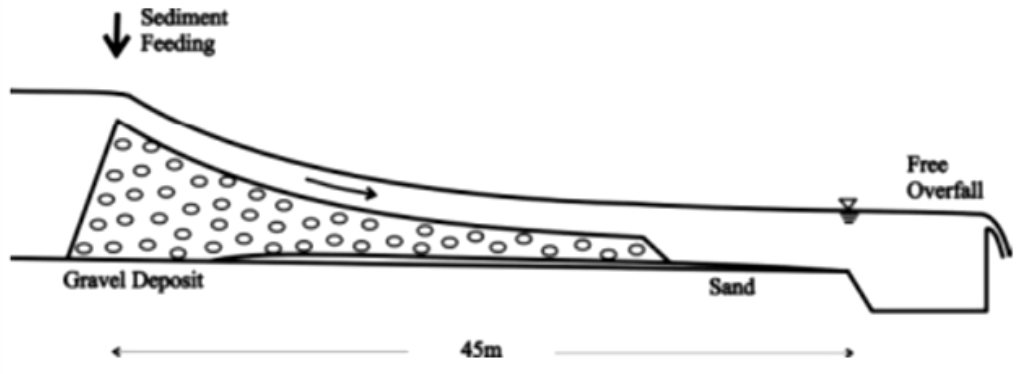

Figure 6.43. Sketch of the SAFL channel aggradation experiments (from Wu 2007).

Table 6.38. Hydrodynamic and sediment conditions for the three simulated SAFL cases.

Variable	**Case 1**	**Case 2**	**Case 3**
Experiment duration, hr	16.83	32.4	64
Inflow discharge, l/s	49	49	49
Initial bed slope	0.002	0.002	0.002
Downstream water level, m (from bed)	0.4	0.45	0.5
Sediment feed rate, kg/min	11.3	5.65	2.83
Initial d_{50}, mm	5.9	5.9	5.9
Initial d_{90}, mm	33.1	33.1	33.1
Geometric standard deviation, mm	5.57	5.57	5.57

The computational grid for the rectangular flume is 3-cells wide and 100-cells long and has a constant resolution of 0.5 by 0.1 m (see Figure 6.44). In the present simulations, a constant flux boundary condition is applied at the upstream end and a constant water level boundary condition is applied at the downstream end of the flume. A 1-hr ramp period is necessary to stabilize the hydrodynamics. During this ramp period, the sediment transport equation is solved but the bed elevation is not updated. In addition, a relatively small time step of 1 s is necessary to stabilize the flow due to the transcritical flow. A summary of the selected hydrodynamic and

sediment transport parameters is presented in Table 6.39. The laboratory study is simulated as a 1-D problem and the flume wall effects are ignored in the simulation for simplicity and therefore wall friction is lumped into the bottom friction. A Manning's roughness coefficient of 0.028 $s/m^{1/3}$ is estimated based on the measured flow depths and bed slopes.

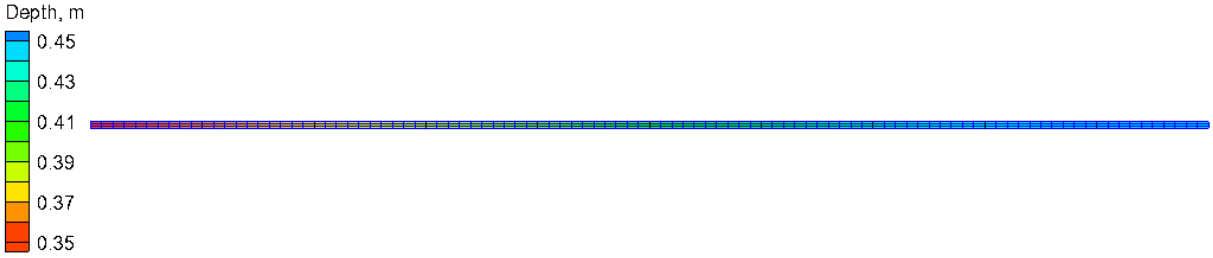

Figure 6.44. Computational grid for the SAFL test cases.

Table 6.39. Model settings for the SAFL test cases.

Parameter	**Value**
Time step	1 s
Simulation duration	Case 1: 18 hr; Case 2 34 hr; Case 3: 65 hr
Ramp period duration	1 hr
Manning's coefficient	0.028 s/m$^{1/3}$
Wall friction	Off
Water density	1,000 kg/m^3
Transport formula	van Rijn
Bed slope coefficient	0.0
Number of sediment size classes	9
Porosity	0.3
Sediment density	2,650 kg/m^3
Suspended load scaling factor	1.0
Bed load scaling factor	1.0
Inflow loading factor	0.9
Morphologic update during ramp period	Off
Total-load adaptation length	0.9 m
Hiding and exposure coefficient	0.45
Minimum bed layer thickness	0.01 m
Maximum bed layer thickness	0.1 m
Number of bed layers	19

Fractional sediment transport rates are applied at the inflow boundary using the sediment feed rate and the grain size distribution shown in Figure 6.45. The grain size distribution consists of 9 sediment size classes from 0.177 to 45.25 mm. A zero-gradient concentration boundary condition is applied at the downstream end. The initial bed material composition is set to the sediment supply distribution. To account for the sediment rolling backwards at the feeding location, an inflow loading factor of 0.9 is applied, meaning 10% of the sediment feed is assumed to role backward. The van Rijn (1986a,b; 2007a,b) transport formula is applied. The

transport formula is modified to account for hiding and exposure by multiplying the critical velocity by a correction factor calculated based on Wu et al. (2000).

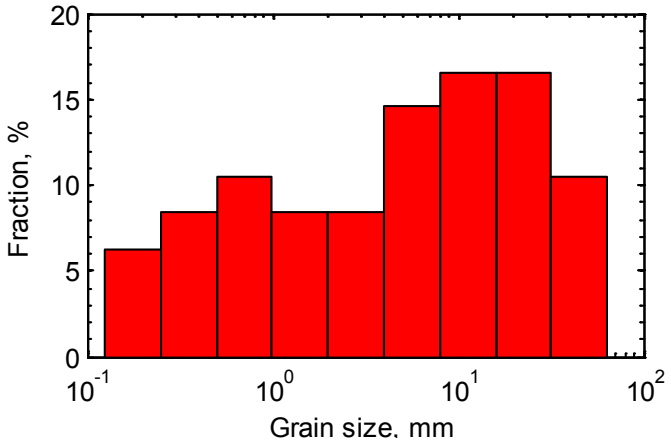

Figure 6.45. Grain size distribution of the sediment supplied at the upstream end of the flume for the SAFL test cases.

Case 2 is chosen for calibration because its hydrodynamic conditions are in between Cases 1 and Case 3 and is therefore the most representative of the group (see Table 6.39). Cases 1 and 3 are run using the same settings and parameters as Case 2 and serve as model validation. Calibration is carried out by first selecting a transport capacity formula and adjusting the bed- and suspended-load transport scaling factors. For simplicity, the same scaling factor is applied to both the bed load and suspended load. The van Rijn (1984a,b; 2007a,b) transport capacity formula with default transport scaling factors of 1.0 is found to provide the best results. Secondly, the total-load adaptation length is adjusted based on the morphology change to 0.9 m, which is very close to other laboratory experiments presented in this dissertation. Lastly, the coefficient used for correcting the critical velocity for hiding and exposure is adjusted to match the measured gain size distribution and is found to be approximately 0.45.

Figure 6.46 shows a comparison of the calculated and measured bed profiles and water levels for Case 2. The rectangles represent bed layers with colors indicating the median grain size (d_{50}). The corresponding goodness-of-fit statistics are given in Table 6.40. Calculated bed elevations have normalized errors less than 5% and BSSs larger than 0.897. The model is able to reproduce the vertical bed aggradation, downstream migration of the depositional fan, the bed slope, and mildly concave bed profile. The final bed material composition is characterized by coarser (finer) sediments upstream (downstream) and upward (downward) due to selective sediment transport and bed sorting. The water level profile is characterized by a hydraulic jump near the tip of the depositional fan. Calculated water levels are accurate with a NMAE of 3%.

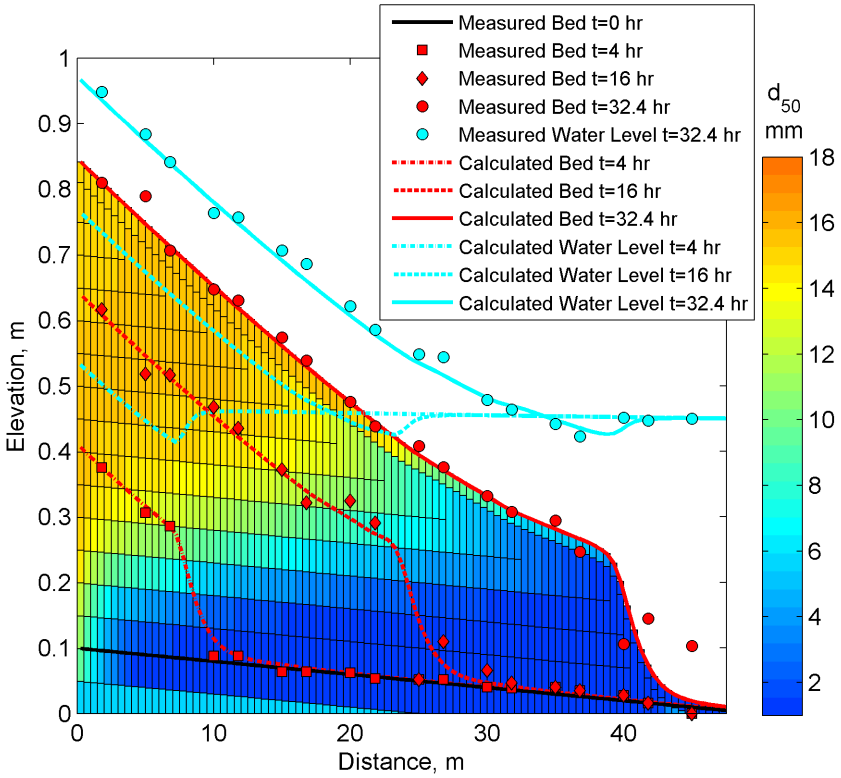

Figure 6.46. Measured and computed bed elevations and water levels at different time steps for the SAFL experiment Case 2. Colored rectangles indicate bed layers with colors corresponding to the median grain size at 32.4 hr.

Interestingly, it is found that the bed profile is not significantly sensitive to the hiding and exposure coefficient and is most sensitive to the bed- and suspended-load transport scaling factors and to lesser extent the total-load adaptation length. The hiding and exposure coefficient does however have a large influence on the bed composition (grain size distribution).

Figure 6.47 compares the calculated and measured bed surface d_{50} and d_{90} at 32.4 hr. There is a noticeable increase in both the d_{50} and d_{90} from the initial bed size. Measured d_{50} grain size shows a downstream fining from approximately 16 to 12 mm, while the d_{90} shows a larger downstream decrease from approximately 55 to 30 mm. The calculated d_{50} grain size has a NMAE, BSS, and R^2 of approximately 53%, 0.78, and 0.55, respectively (see Table 6.40). The d_{50} bias is approximately one third the measure data range. The calculated d_{90} grain size has a lower NMAE of 34% compared to d_{50}, but has a lower BSS and R^2 but a smaller NMAE. The d_{90} bias of 4.7 mm is approximately one fifth the measured data range. Both the calculated d_{50} and d_{90} show a slight increase up to about 14-16 m downstream followed by a relatively steep decrease. The reason for this is not understood and further investigation is needed. However, it is interesting to note that the measured d_{90} grain size also shows a slight increase from 10 to 17 m.

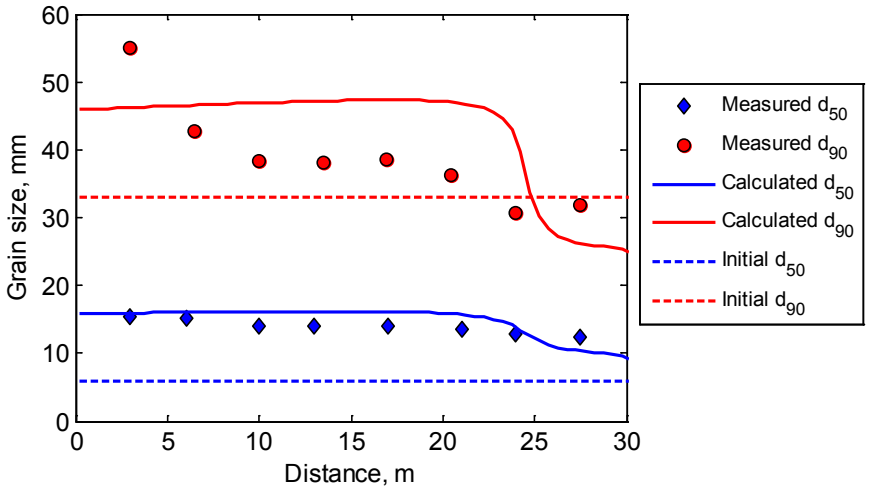

Figure 6.47. Measured and computed d_{50} and d_{90} grain sizes for the SAFL Case 2.

Table 6.40. Goodness-of-fit statistics* for the SAFL experiment Case 2.

	Bed level, m			**Water Level, m**	**d_{50}, mm**	**d_{90}, mm**
Time, hr	**4**	**16**	**32.4**	**32.4**	**32.4**	**32.4**
BSS	0.911	0.897	0.920	0.940	0.782	0.067
NRMSE, %	2.28	4.31	4.88	2.58	57.79	35.28
NMAE, %	1.54	2.86	3.02	2.13	53.48	34.04
R^2	0.994	0.984	0.977	0.995	0.549	0.217
Bias	-0.0020	-0.0011	-0.0088	-0.0061	1.1132	4.6798
*defined in Appendix A						

One possible reason why the bed composition is not sensitive to the bed and suspended transport scaling factors is because the same values are applied to all grain sizes. It is expected that improved grain size distributions can be obtained with grain-size-dependant transport scaling factors. However, since no fractional sediment transport rates are available, it is not possible to estimate these factors. For most practical applications, detailed fractional sediment transport rates are not available and therefore using constant transport scaling factors is sufficient.

The calculated and measured bed profiles and water levels for the validation Case 1 are presented in Figure 6.48. Case 1 corresponds to the experiment case with the largest sediment feed rate and lowest tail gate water level. The corresponding goodness-of-fit statistics are given in Table 6.41. Similar to Case 2, the calculated bed elevations have normalized errors less than 4% and BSSs between 0.87 and 0.924. The model is able to reproduce the bed slope and mildly concave bed profile. The vertical bed aggradation and downstream migration of the depositional fan are slightly over-predicted. Similarly to Case 2, the bed material composition is characterized by coarser (finer) sediments upstream (downstream) and upward (downward) due to selective sediment transport and bed sorting.

The calculated upstream water levels and downstream location of the hydraulic jump are slightly over-predicted due to the over-predicted bed elevation and deposition fan migration, respectively. However, in general, the water level goodness-of-fit statistics indicate good model performance with a BSS of 0.928, a NMAE of 2.36%, and R^2 of 0.995.

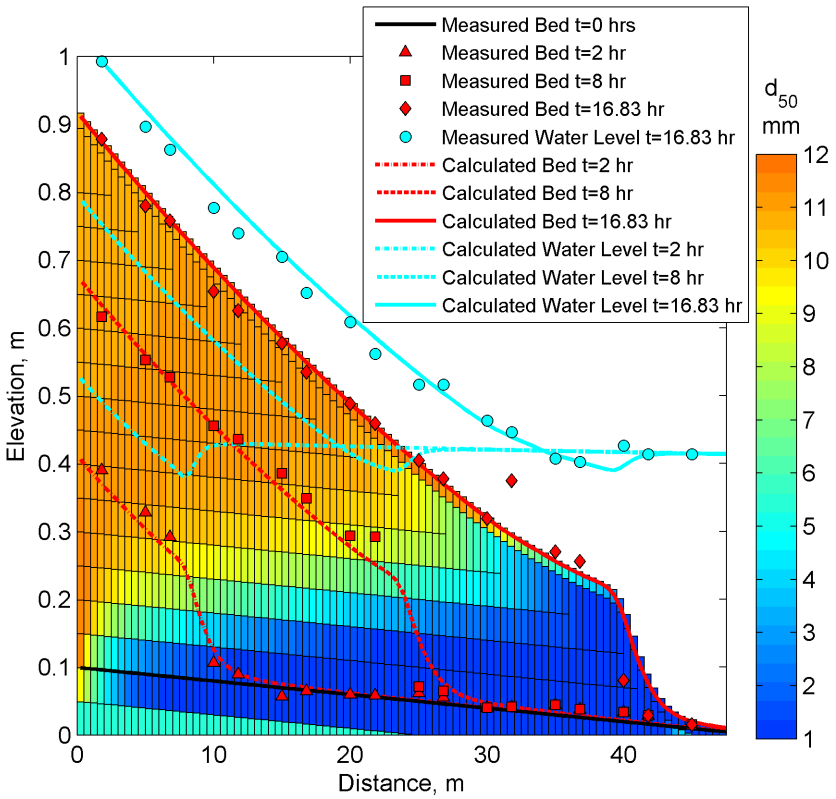

Figure 6.48. Measured and computed bed elevations and water levels at different time steps for the SAFL experiment Case 1. Colored rectangles indicate bed layers with colors corresponding to the median grain size at 16.83 hr.

The calculated and measured bed surface d_{50} and d_{90} for Cases 1 are shown in Figure 6.49. The corresponding goodness-of-fit statistics are given in Table 6.41. Surprisingly, the measured d_{50} is approximately the same as the initial d_{50}. The calculated d_{50} is over-predicted, closer to that of Case 2, at around 11 mm, and has a slight increase before decreasing at a distance of approximately 25 m. The calculated d_{90} is within the measured range upstream (x<5 m) but shows an opposite trend to the measurements by increasing downstream. It is possible that changing the hiding and exposure coefficient may improve the grain size distribution and further tests are needed to test this hypothesis.

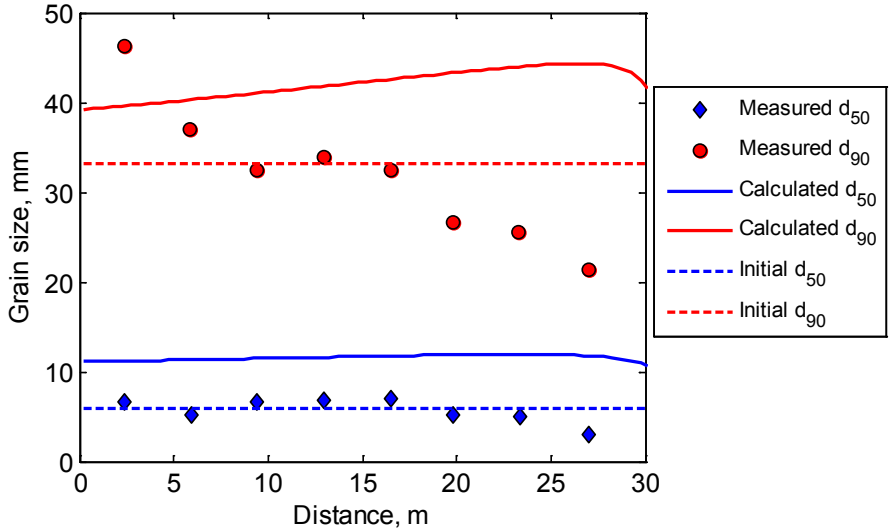

Figure 6.49. Measured and computed d_{50} and d_{90} grain sizes for the SAFL Case 1.

Table 6.41. Goodness-of-fit statistics* for the SAFL experiment Case 1.

	Bed level, m			**Water Level, m**	**d_{50}, mm**	**d_{90}, mm**
Time, hr	**2**	**8**	**16.83**	**16.83**	**16.83**	**16.83**
BSS	0.870	0.914	0.924	0.928	-3.78	-0.838
NRMSE, %	3.54	3.74	3.90	3.07	156.19	53.93
NMAE, %	2.90	2.62	2.44	2.36	152.22	47.50
R^2	0.990	0.989	0.982	0.995	0.129	0.888
Bias	-0.0058	-0.0031	0.0062	0.0077	5.92	10.14
*defined in Appendix A						

The calculated and measured bed profiles and water levels for the validation Case 3 are presented in Figure 6.50. Case 3 corresponds to the experiment case with the smallest sediment feed rate and highest tail gate water level. The corresponding goodness-of-fit statistics are given in Table 6.42. Case 3 has the largest normalized errors of the three cases and range from 1.74 to 7.62%. The BSS range from 0.874 to 0.963 which indicate excellent model performance. The upstream vertical bed aggradation is slightly under-predicted at 64 hr and lead to an under-

prediction of the water elevation. The downstream migration of the depositional fan, bed slope and mildly concave bed profile are well simulated. Similar to the previous cases, the water level profile is characterized by a hydraulic jump near the tip of the depositional fan. The flow model water levels are accurate within approximately 4% of the measurements.

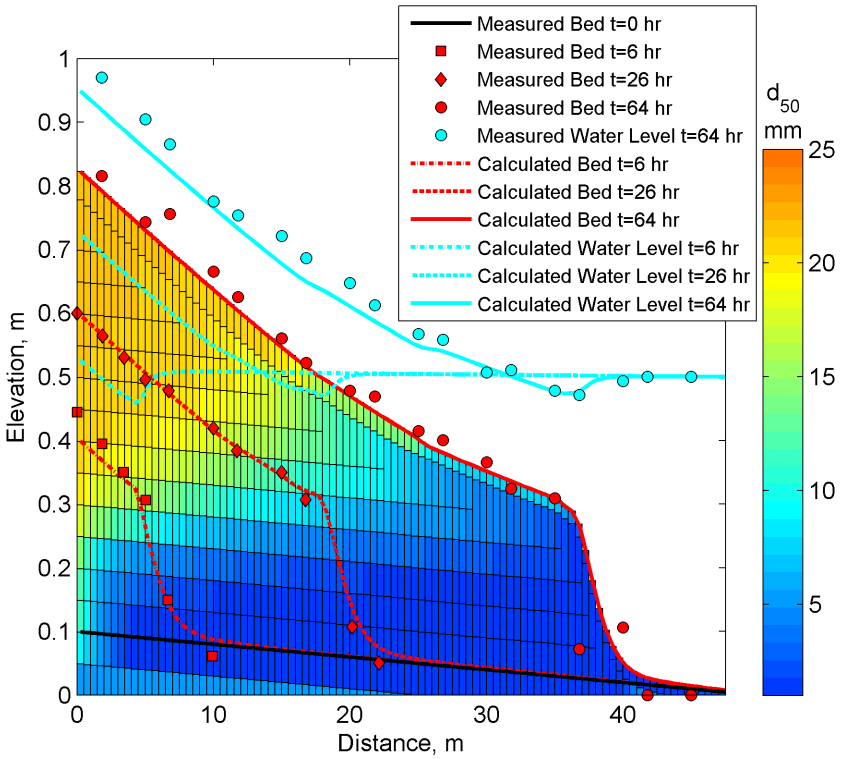

Figure 6.50. Measured and computed bed elevations and water levels at different time steps for the SAFL experiment Case 3. Colored rectangles indicate bed layers with colors corresponding to the median grain size at 64 hr.

The calculated d_{50} for Case 3 on the other hand shows a larger downstream fining while the d_{90} shows a larger downstream decrease from approximately 55 to 30 mm. The calculated d_{50} grain size has a NMAE, BSS, and R^2 of approximately 25%, 0.679, and 0.673, respectively. The calculated d_{90} grain size has a lower NMAE of 34% compared to d_{50}, but has a lower BSS and R^2

but a smaller NMAE. The d_{90} bias of 4.7 mm is approximately one fifth the measured data range. Both the calculated d_{50} and d_{90} show a slight increase up to about 14-16 m downstream followed by a relatively steep decrease. The reason for this is not understood and further investigation is needed. However, it is interesting to note that the measured d_{90} grain size also shows a slight increase from 10 to 17 m.

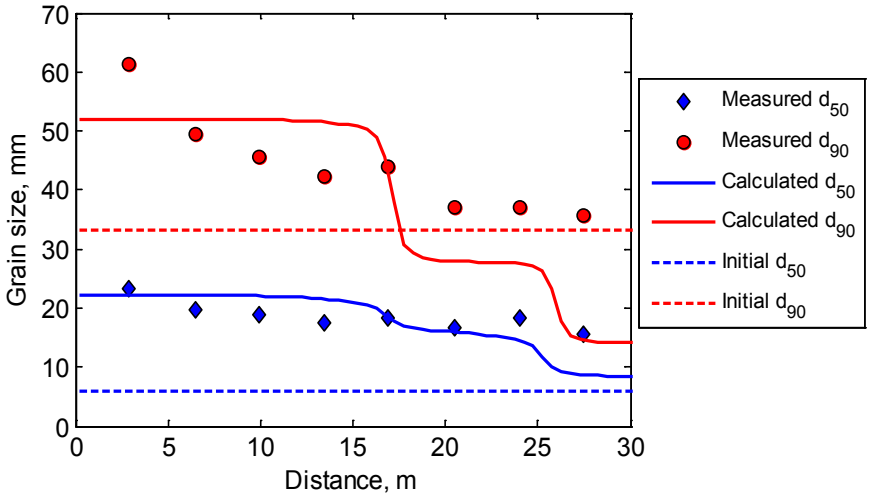

Figure 6.51. Measured and computed d_{50} and d_{90} grain sizes for the SAFL experiment Case 3.

Table 6.42. Goodness-of-fit statistics* for the SAFL experiment Case 3.

	Bed level, m			**Water Level, m**	**d_{50}, mm**	**d_{90}, mm**
Time, hr	**6 hr**	**24 hr**	**64 hr**	**64**	**64**	**64**
BSS	0.874	0.963	0.881	0.867	0.679	0.005
NRMSE, %	7.62	2.35	6.34	5.44	30.41	37.71
NMAE, %	6.67	1.74	3.73	4.26	25.17	31.93
R^2	0.987	0.998	0.961	0.994	0.673	0.699
Bias	-0.0165	0.0071	-0.0033	-0.0188	-1.15	-6.63
*defined in Appendix A						

CHAPTER VII

VALIDATION: FIELD CASES

The field cases described in this chapter are selected for model validation to confirm that the developed model can reproduce the main physical processes of flow and sediment transport under field conditions. The tests cases completed are:

1. Gironde Estuary, France
2. Grays Harbor, WA
3. Hazaki Oceanographic Research Facility, Japan
4. Duck, NC
5. Columbia River, WA/OR

7.1 Gironde Estuary, France

Application of the flow model to the Gironde Estuary demonstrates specification of the flow boundary condition within an estuary, with validation measurements of water level and current speed spaced along the axis of the estuary. The Gironde Estuary is located in southwestern France. It receives runoff from the Garonne and the Dordogne Rivers and opens up to the Atlantic Ocean, as shown in Figure 7.1. The water-surface width varies from 2 to 14 km, and the flow depth in the navigation channel ranges from 6 to 30 m. The estuary is partially mixed and macrotidal, with a 12 hr and 25 min tidal lunar period and a tidal amplitude of 1.5 to

5 m at the mouth (Li et al. 1994).

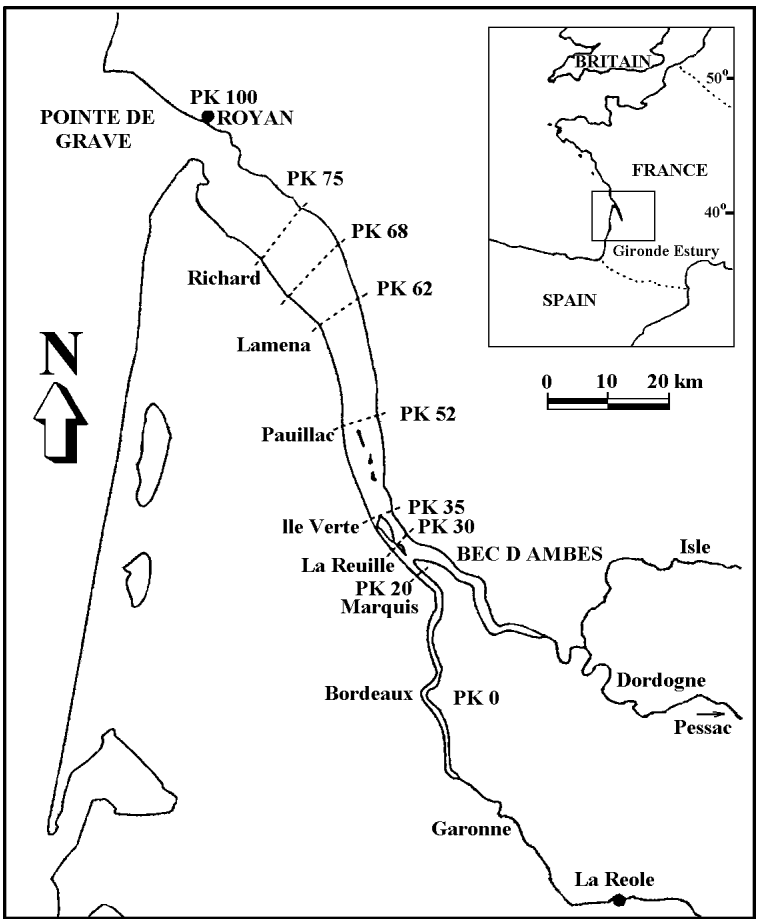

Figure 7.1. Sketch of the Gironde Estuary, France.

The model is applied with a simulation domain extending 80 km from the estuary mouth at the Atlantic Ocean to the Garonne and Dordogne Rivers. The bed topography is provided on a uniform mesh, with a size of 250 × 125 m for each cell. The grid has approximately 16,000 active cells. Because the domain is relatively simple, a uniform mesh is used. The data measured from May 19 to 25, 1975 are used to validate the model for water level and current speed. The computational time step is set to 10 min. At the estuary mouth, the tidal elevation is given by the

recorded time series at the station "Pointe de Grave" (see Figure 7.1). At the two upstream ends, the flow discharges of the Garonne River and the Dordogne River are specified according to the measured data at La Réole and Pessac and the inflow discharges are set to 387 and 846 m^3/s, respectively. The Manning's roughness coefficient is set to 0.018 $s/m^{1/3}$. Figure 7.2 shows the computational grid and observation stations. The Coriolis parameter, f_c, is constant over the whole domain (*f*-plane approximation). Winds are not included in the simulation. The initial condition is specified as still water in the whole domain. A 1-hr ramp period is used at the start of the simulation. Table 7.1 summarizes the model setup parameters. The 100-hr simulation takes approximately 12 min to run on a 2.67 GHz processor.

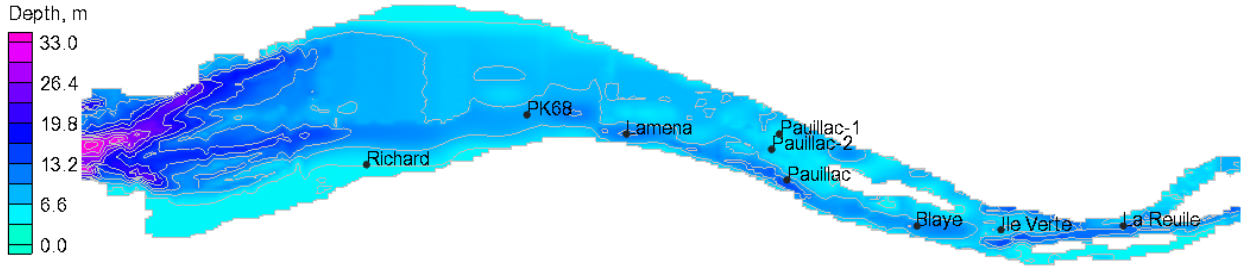

Figure 7.2. Computational grid and observation stations for the Gironde Estuary Test Case.

Table 7.1. Model setup parameters for the Gironde Estuary test case.

Parameter	**Value**
Simulation duration	100 hr
Ramp period duration	1 hr
Time step	10 min
Manning's n coefficient	0.018 $s/m^{1/3}$
Latitude	45.5°

The calculated flow fields in flood and ebb tides are shown in Figure 7.3. The ebb flow is

characterized by a funnel effect at the entrance (mouth or inlet) caused by the narrowing of the estuary in this region. The increase in velocity is likely to be the cause of the channel deepening in this region as shown by the depth contours (see Figure 7.2). The flood tide is also characterized by a funnel effect near Ile Verte which also seems to cause some deepening of the estuary to the south of the island.

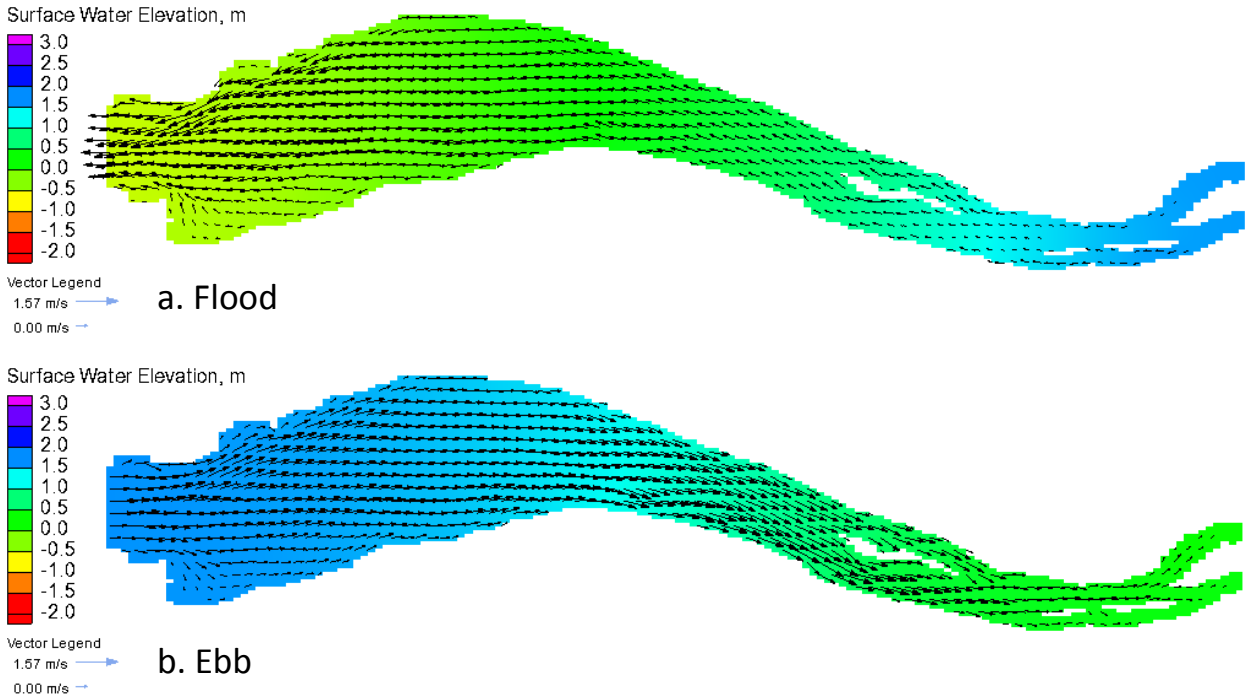

Figure 7.3. Examples of ebb (top) and flood (bottom) tidal currents and water surface elevations in the Gironde Estuary.

Figure 7.4 compares the measured and simulated water levels at five stations within the Gironde Estuary (stations shown in Figure 7.2). In general, the results show good agreement with the measured data in both amplitude and phase. Table 7.2 summarizes the goodness-of-fit statistics for water level. NRMSE and NMAE values for the water levels range from 5 to 7%.

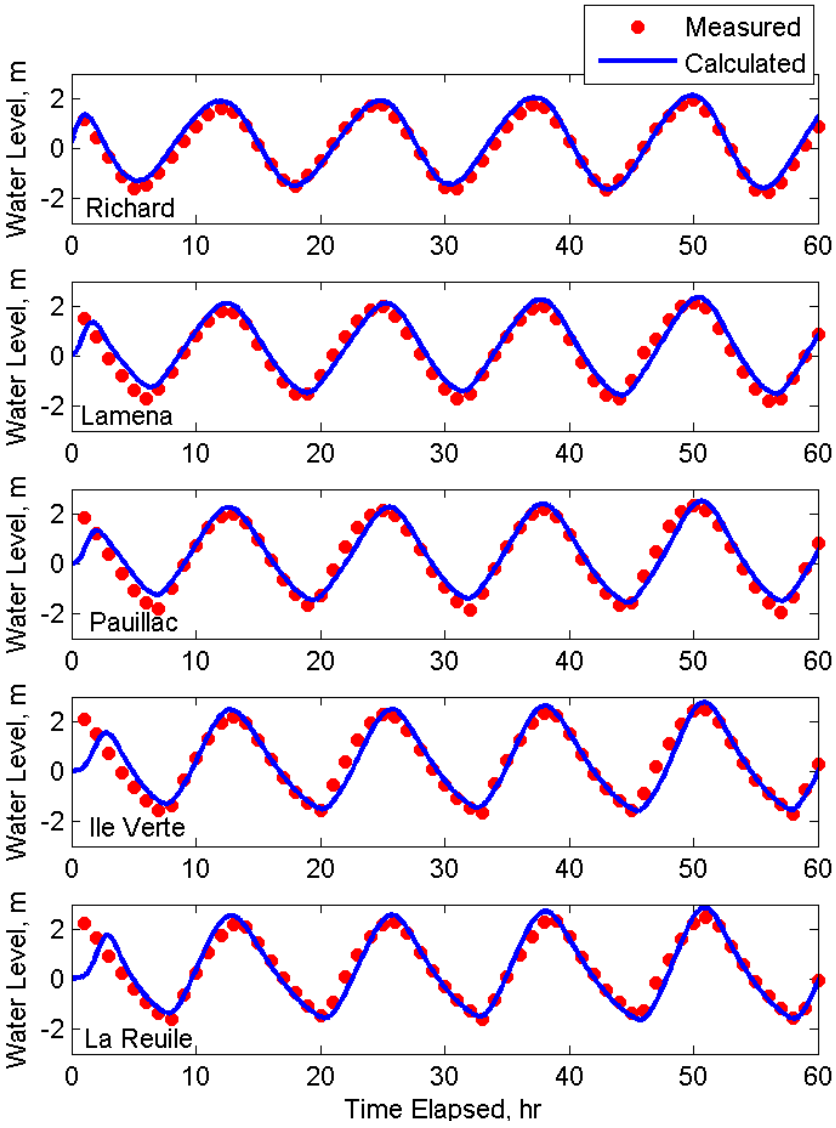

Figure 7.4. Comparison of measured and calculated water levels at five stations in the Gironde Estuary (stations shown in Figure 7.2).

Table 7.2. Water level goodness-of-fit statistics* for the Gironde Estuary test case.

	Station (see Figure 7.2 for location)				
Statistic	**Richard**	**Lamena**	**Pauillac**	**Ile Verte**	**La Reuille**
NRMSE, %	5.10	7.02	6.74	6.40	6.63
NMAE, %	4.33	6.21	5.63	4.34	5.08
R^2	0.982	0.956	0.951	0.962	0.972
Bias, m	0.094	0.128	0.043	-0.060	-0.0252
*defined in Appendix A					

Figure 7.5 shows the comparison of the measured and simulated flow velocities at several stations (stations shown in Figure 7.2). The velocities were measured 1 m below the water surface and 1 m above the river bed, respectively. In this figure, positive current velocities correspond to flood tides and negative velocities to ebb tides. The current measurements at both elevations are relatively similar for all stations except Richard and Lamena. This might be due to baroclinic circulation produced by wind, fresh water intrusion, or other factors near these two stations.

Some of the differences in water surface elevations and current velocities may be due to inaccuracies in the boundary conditions. The boundary conditions at the estuary entrance is obtained from a nearby station and therefore a slight phase lag of about 45 min is subtracted from the calculated water surface elevations in order to match the measured time series. However, since the boundary condition used is not measured exactly at the location of the boundary, some error in phase lag may be expected from this approximation.

Another probable source of error is the bottom roughness coefficient, which is assumed to be constant. Other field experiments show that the bottom roughness in an estuary can vary

significantly due to changes in bed forms and grain sizes within the estuary. Although the model has the capability to use a spatially variable bottom roughness coefficient, there are no data available in this case. The agreement between measured and calculated current speeds is summarized in Table 7.3. NRMSE and NMAE in current speed range from 7-21%. Comparable results were obtained by Wu and Wang (2004) using a similar depth-averaged flow model.

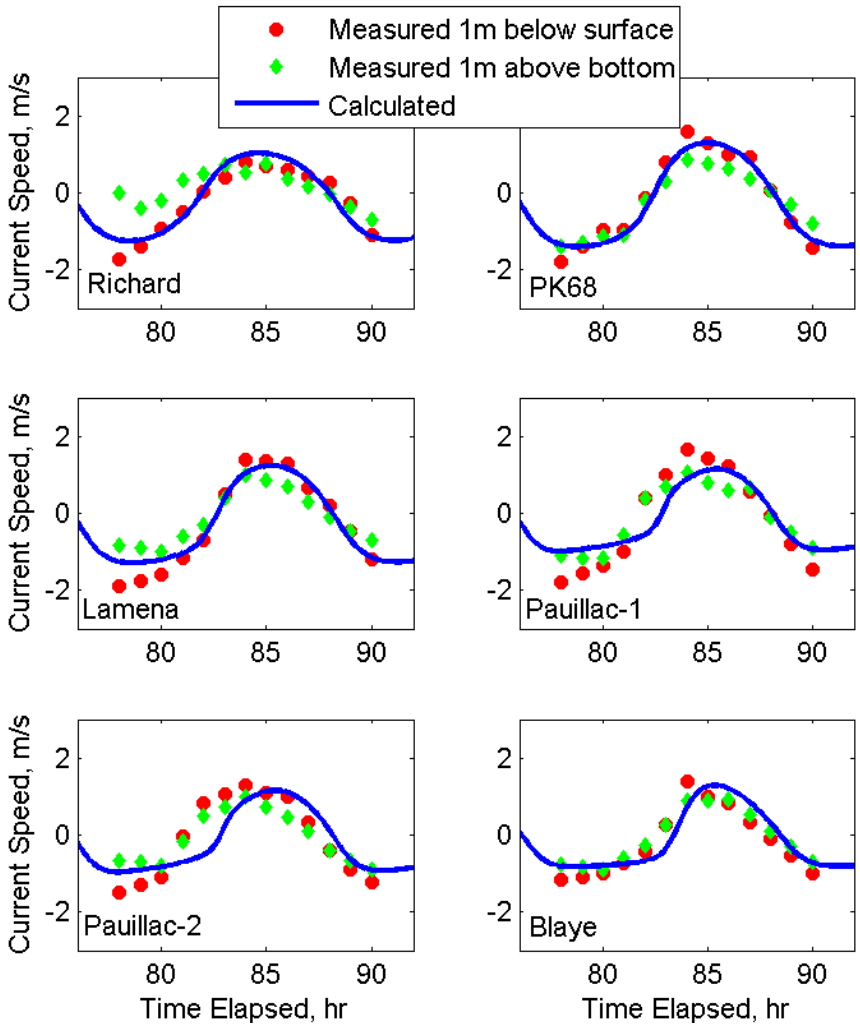

Figure 7.5. Measured and calculated current speeds in the Gironde Estuary (stations shown in Figure 7.2),

Table 7.3. Current speed goodness-of-fit statistics for the Gironde Estuary test case.

	Station (see Figure 7.2 for location)					
Statistic	**Richard**	**PK68**	**Lamena**	**Pauillac-1**	**Pauillac-2**	**Blaye**
NRMSE, %	10.70	7.27	8.81	15.89	20.73	14.98
NMAE, %	9.15	5.71	6.93	13.67	17.05	13.17
R^2	0.911	0.957	0.968	0.856	0.680	0.804
Bias, m/s	0.070	-0.057	0.062	0.022	-0.031	0.095
*defined in Appendix A						

7.2 Grays Harbor, WA

The model performance in simulating the hydrodynamics, wave transformation, and sediment transport at a relatively large and complex inlet and estuary at Grays Harbor, WA is analyzed using field measurements from two different field studies. One field study is used to validate water levels, current velocities, and wave heights, periods and directions, while the other is used to validate nonuniform sediment transport and morphology change.

Grays Harbor is located on the southwest Washington coast about 45 miles north of the Columbia River. The estuary has a wetted surface area of approximately 91 square miles at mean higher high water and 28 squares miles at mean lower low water. The main input of fresh water is from the Chehalis River. The 3-mile wide entrance has two convergent rock jetties which extend from spit points, as shown in Figure 7.6.

7.2.1 USACE Field Study

In 1999 and 2001, the USACE conducted several field experiments at Grays Harbor as part of a navigation study to better understand the sediment transport and functionality of the northern jetty (Osborne et al. 2002). During 1999 measurements of water levels, current velocities, and suspended sediment concentrations were collected at seven locations (black dots in Figure 7.6). The current velocity data used for validation was collected from September to October of 1999. For further details on the field experiment the reader is referred to Osborne et al. (2002). For water levels, NOAA tide gauge stations are used due to their distal location from the inlet entrance (red dots in Figure 7.6).

The computational grid consists of 67,000 cells and has a non-uniform spacing from 28 to 200 m. The model domain is shown in Figure 7.6. Both the wave and flow models use the same grid. The spectral waves from the NOAA buoy 46029 are input at the model boundaries every 3 hr. Wind from the same buoy is included in the wave model. For comparative purposes the explicit time marching scheme of the CMS model described in Militello et al. (2004) and Buttolph et al. (2006) is also run. The implicit and explicit model time steps are set to 15 min and 0.5 s, respectively. A spatially constant Manning's roughness coefficient is calibrated as 0.018 $s/m^{1/3}$ using water level measurements and is the only parameter calibrated. The models are forced with water level measurements taken at Station 0 (see Figure 7.6). The 27-day period from September 14 to October 15 of 1999 is calculated. A summary of selected model settings are presented Table 7.4.

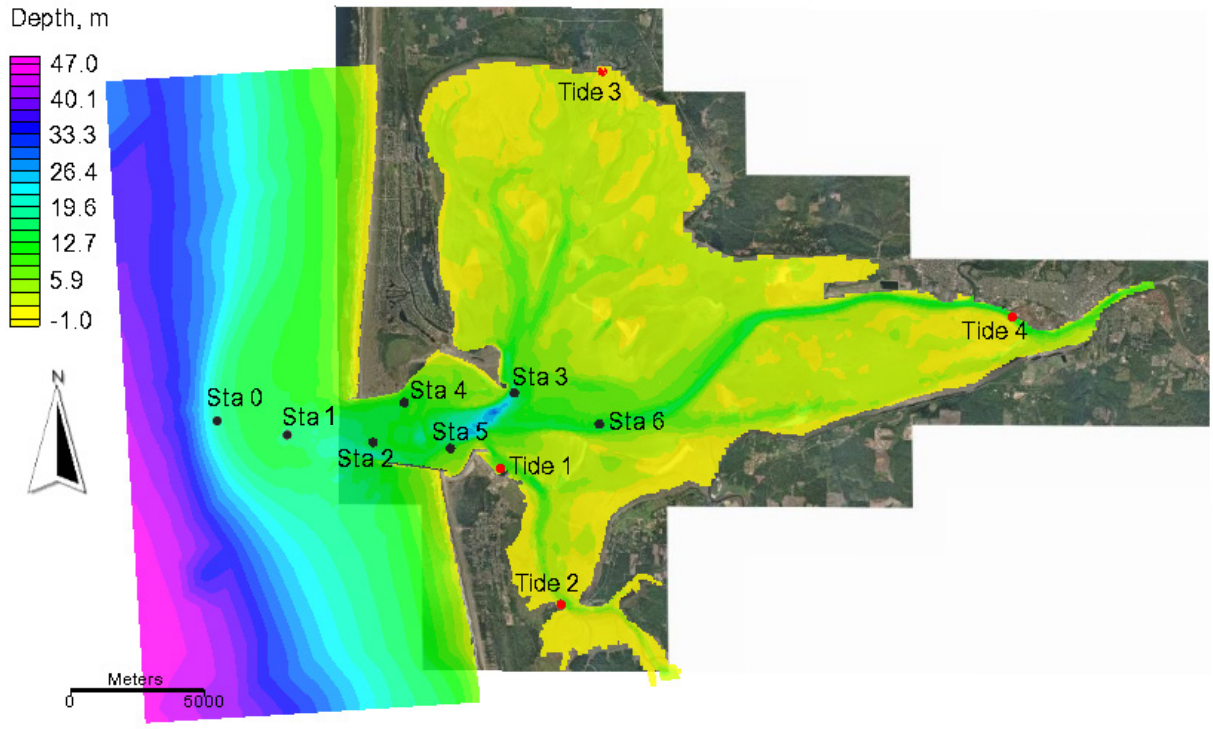

Figure 7.6. Computational domain for the Grays Harbor, WA for the 1999 field study test case.

Table 7.4. Model settings for the Grays Harbor test case.

Parameter	**Value**
Time step	Implicit: 15 min Explicit: 0.5 sec
Simulation duration	27 days
Ramp period	24 hr
Manning's coefficient	0.018 $1/m^{1/3}$
Steering interval	3 hr

A comparison of measured and computed water levels for both temporal schemes is presented in Figure 7.7. The agreement between calculated and measured water levels is generally good as demonstrated by the goodness-of-fit statistics in Table 7.5. Both the explicit and implicit models produce similar results. The goodness-of-statistics indicate that the implicit

model results are slightly better. Sta 3 shows gaps in the computed water levels when the computational cell becomes dry while the measurements indicate a wet condition. This error is likely due to inadequate bathymetry near the tide gauge. In general however the model performance is reasonable with NMAE's for water levels are less than 6%. The implicit model is tested with different time steps between 5-30 min and the differences are found to be negligible. The only areas which show significant differences are those with extensive wetting and drying. However, these areas contain a relatively small tidal prism and do not significantly impact the dynamics near the inlet entrance. It is interesting to note from the water levels (see Figure 7.7) that the hydrodynamics takes approximately 250 hr to eliminate the effect of the initial condition. This suggests that the model needs a spin-up period of approximately 11 days possibly due to the presence of resonance and/or tidal setup in the bay which take time to build up.

The measured and computed current velocities along the principle axis for both temporal schemes is presented in Figure 7.8 and the corresponding goodness-of-fit statistics are presented in Table 7.6. The current velocities are compared along the principle axis because it represents the major component of variance. Flood currents are represented as positive while ebb currents are negative. Peak ebb and flood current velocities range from approximately 1 to 1.5 m/s. Both the explicit and implicit model reproduce well the amplitude and phase of the principle current velocities. As in the case of water levels, the implicit model current velocities agree slightly better with measurements than the explicit model (see Table 7.6). NMAE's for the principle current velocities are less than 10% indicating a good model performance.

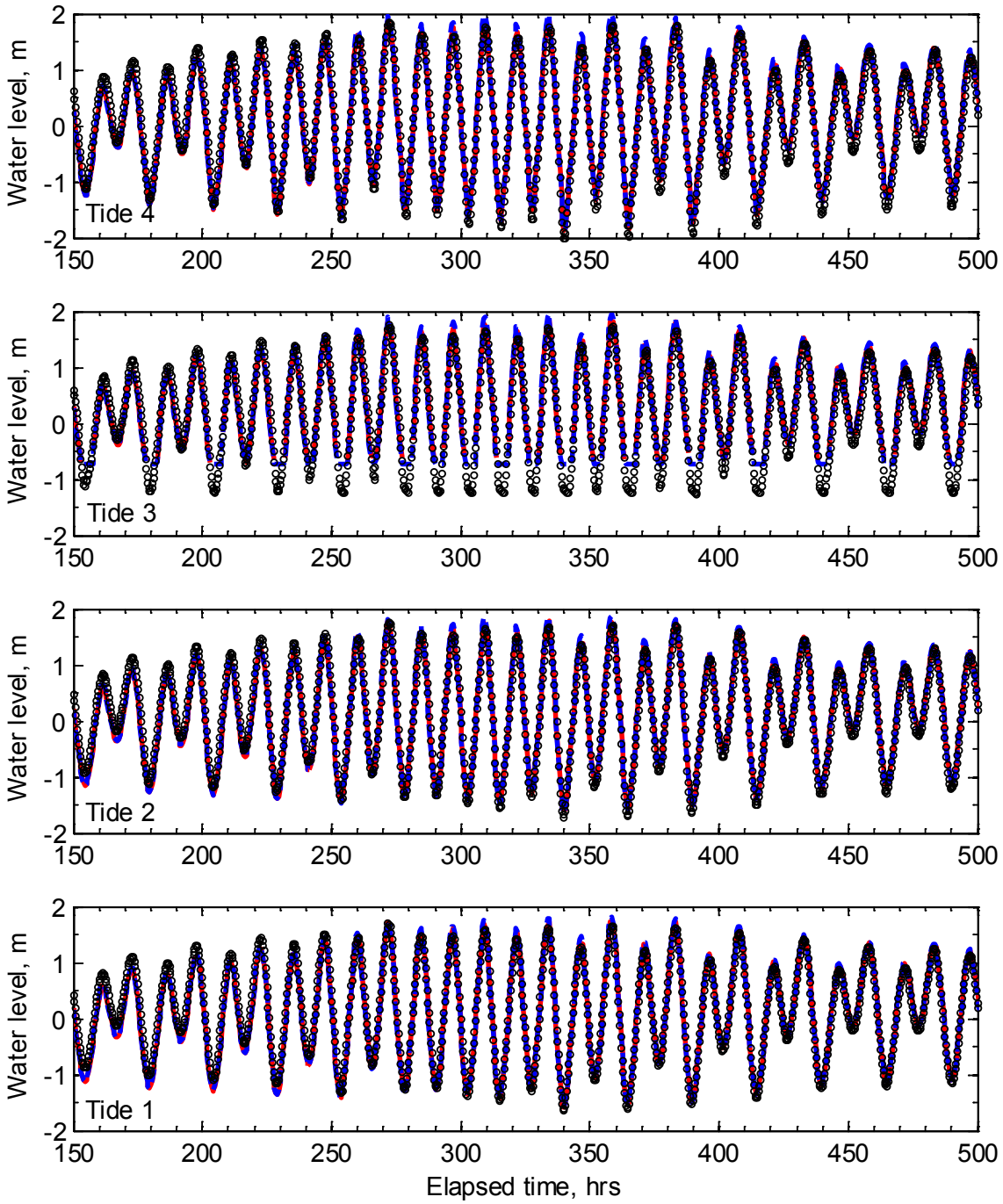

Figure 7.7. Measured and calculated water levels at Grays Harbor, WA. Elapsed times are with respect to September 14, 1999.

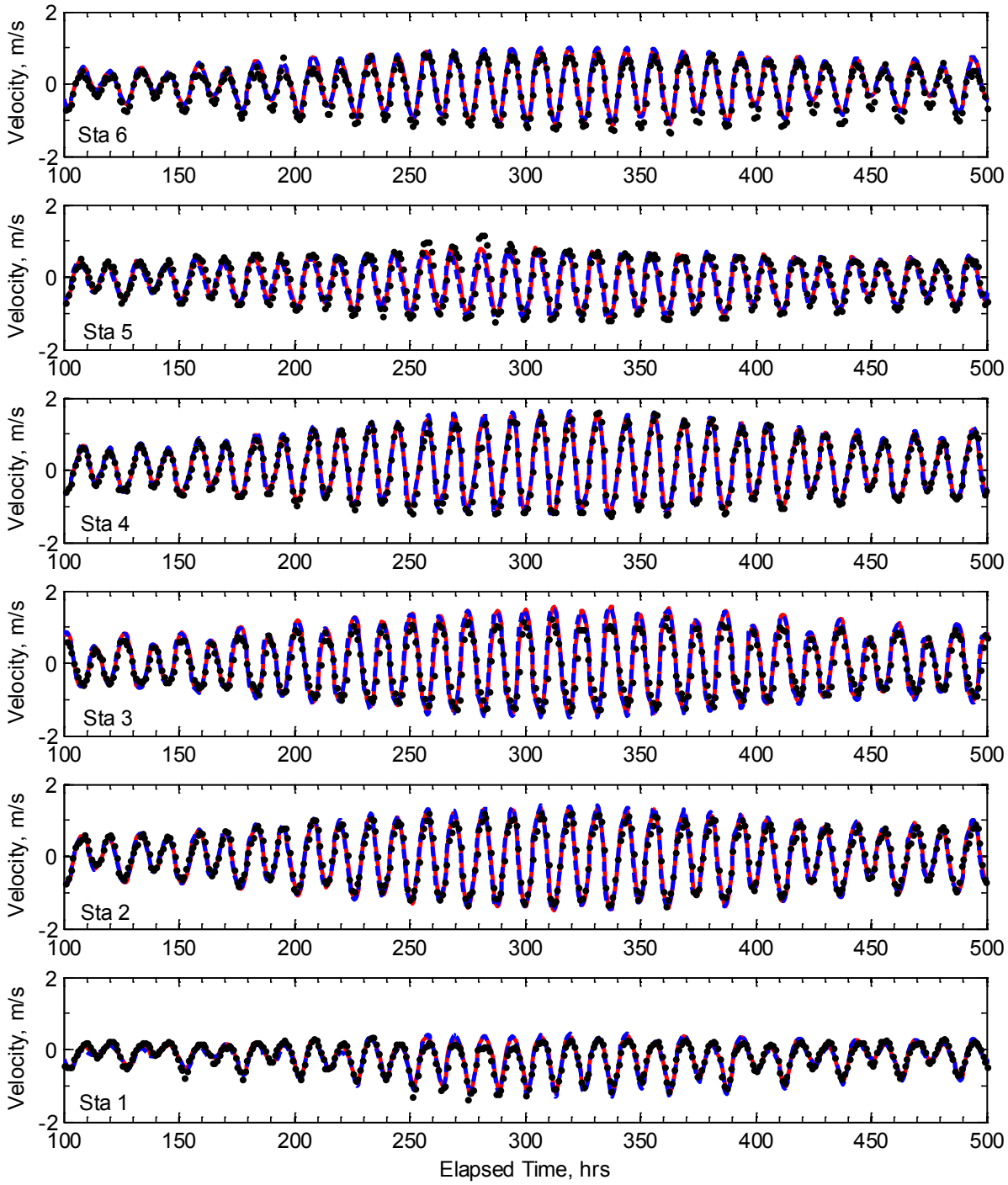

Figure 7.8. Measured and calculated principle current velocities at Grays Harbor, WA. Elapsed times are with respect to September 14, 1999.

Table 7.5. Goodness-of-fit statistics* for the water levels at Grays Harbor, WA.

Scheme	Statistic	Tide 1	Tide 2	Tide 3	Tide 4
Explicit	NRMSE, %	7.72	7.63	8.27	5.78
	NMAE, %	7.31	6.89	7.03	4.85
	R^2	0.991	0.982	0.924	0.98
	Bias, m	0.206	0.204	0.088	0.151
Implicit	NRMSE, %	3.65	4.05	6.51	4.07
	NMAE, %	2.73	3.18	5.45	3.54
	R^2	0.982	0.974	0.939	0.974
	Bias, m	0.031	0.018	-0.015	-0.032
*defined in Appendix A					

Table 7.6. Goodness-of-fit statistics* for principle current velocities at Grays Harbor, WA.

Scheme	Statistic	Sta 1	Sta 2	Sta 3	Sta 4	Sta 5	Sta 6
Explicit	NRMSE, %	8.34	7.49	11.00	4.91	10.18	9.2
	NMAE, %	6.08	5.38	8.55	2.97	7.69	6.91
	R^2	0.892	0.965	0.954	0.980	0.905	0.956
	Bias, m/s	-0.035	-0.026	0.065	0.022	-0.0129	0.1172
Implicit	NRMSE, %	8.46	6.84	10.57	4.38	5.71	7.3
	NMAE, %	6.28	5.33	8.95	3.1	4.06	5.8
	R^2	0.928	0.977	0.971	0.985	0.971	0.979
	Bias, m/s	0.026	-0.01	0.089	0.005	0.0064	0.1148
*defined in Appendix A							

The wave model results discussed here are run with the newly developed implicit flow model. No significant differences are found in the wave model results using the either the explicit or implicit flow models. Figure 7.9 presents the computed and measured significant wave heights at five measurement stations shown in Figure 7.6. The significant goodness-of-fit statistics are presented in Table 7.7. The wave heights are reasonably well simulated at all five stations with NMAE's less than approximately 9%. As expected, the best results are obtained for Sta 1 and 2 and have NMAE's of less than 5.5% which are the closest stations to the offshore buoy, are more directly exposed to offshore waves, and less influences by the jetties. Station 1 is located on the tidal ebb shoal while Sta 2 is located north of the southern jetty tip near the navigation channel. Sta 3 shows a significant amount of scatter during the moderate wave events. However, the general wave height pattern is well simulated. The largest differences occur at Sta 4 near the northern jetty where the wave heights are overestimated for the moderate wave events.

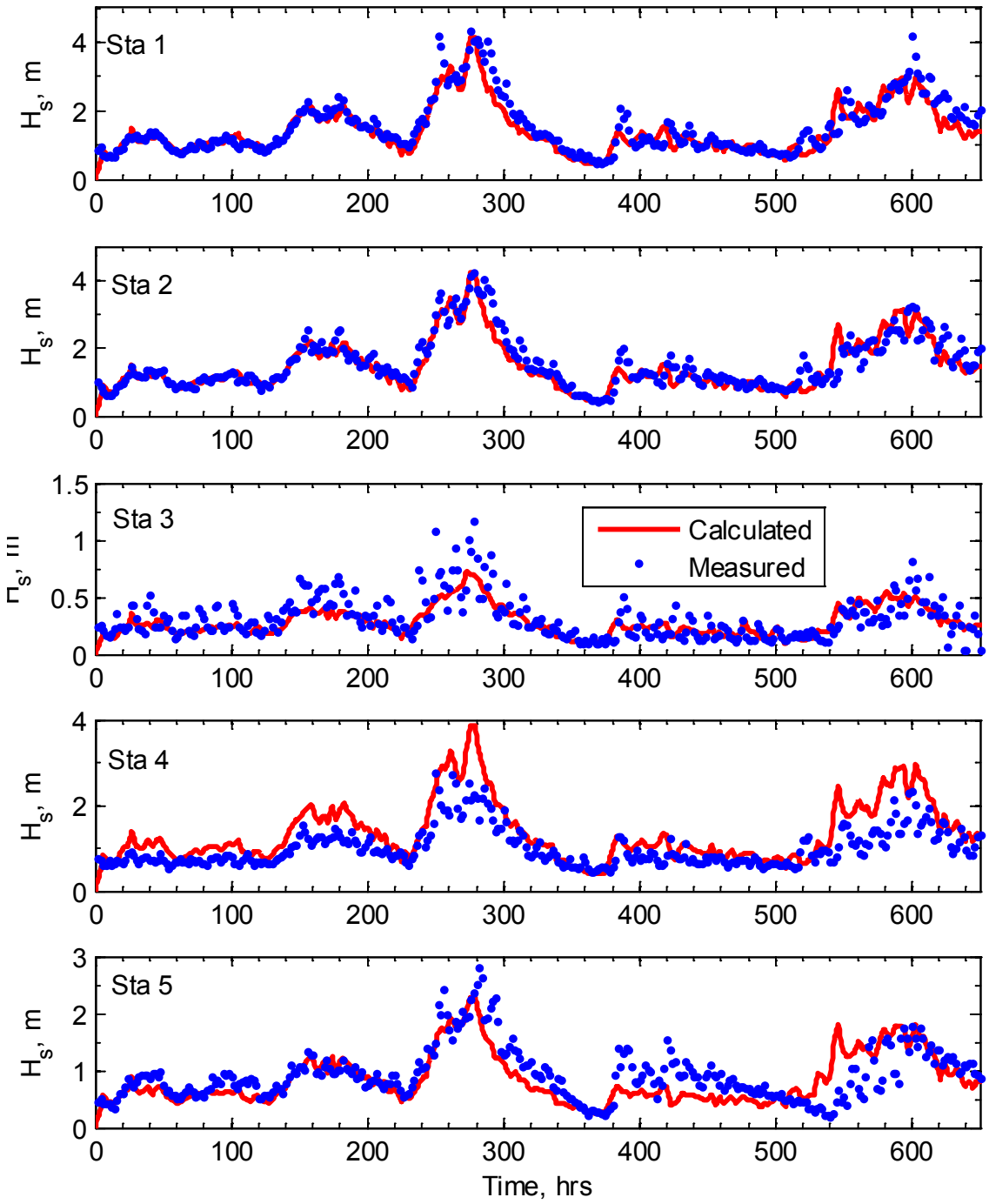

Figure 7.9. Measured and calculated significant wave heights (H_s) at Grays Harbor, WA. Elapsed times are with respect to September 14, 1999.

Table 7.7. Significant wave height goodness-of-fit statistics* at several stations for the Grays Harbor, WA test case.

	Station				
Statistic	**1**	**2**	**3**	**4**	**5**
NRMSE, %	7.94	7.89	11.06	18.34	12.28
NMAE, %	5.45	5.48	8.00	13.6	9.02
R^2	0.841	0.824	0.544	0.749	0.521
Bias	-0.132	-0.097	-0.031	0.338	-0.097
*defined in Appendix A					

Measured and computed peak wave periods are compared in Figure 7.10 and the corresponding goodness-of-fit statistics are presented in Table 7.8. The model captures the general pattern of the peak wave period. The best results are obtained for Sta 1 and 2 which are the more exposed stations to waves. Because the peak wave period is determined as the inverse of the frequency with the largest wave energy, its value is sensitive to the wave spectral shape. This explains the scatter in the measured peak wave periods. From Figure 7.10 it is clear that the peak wave period is better predicted than the correlation coefficient indicates. In fact Sta 3 has the lowest correlation coefficient and the lowest normalized errors. This suggests that the correlation coefficient is not a good statistic for evaluating the peak wave period.

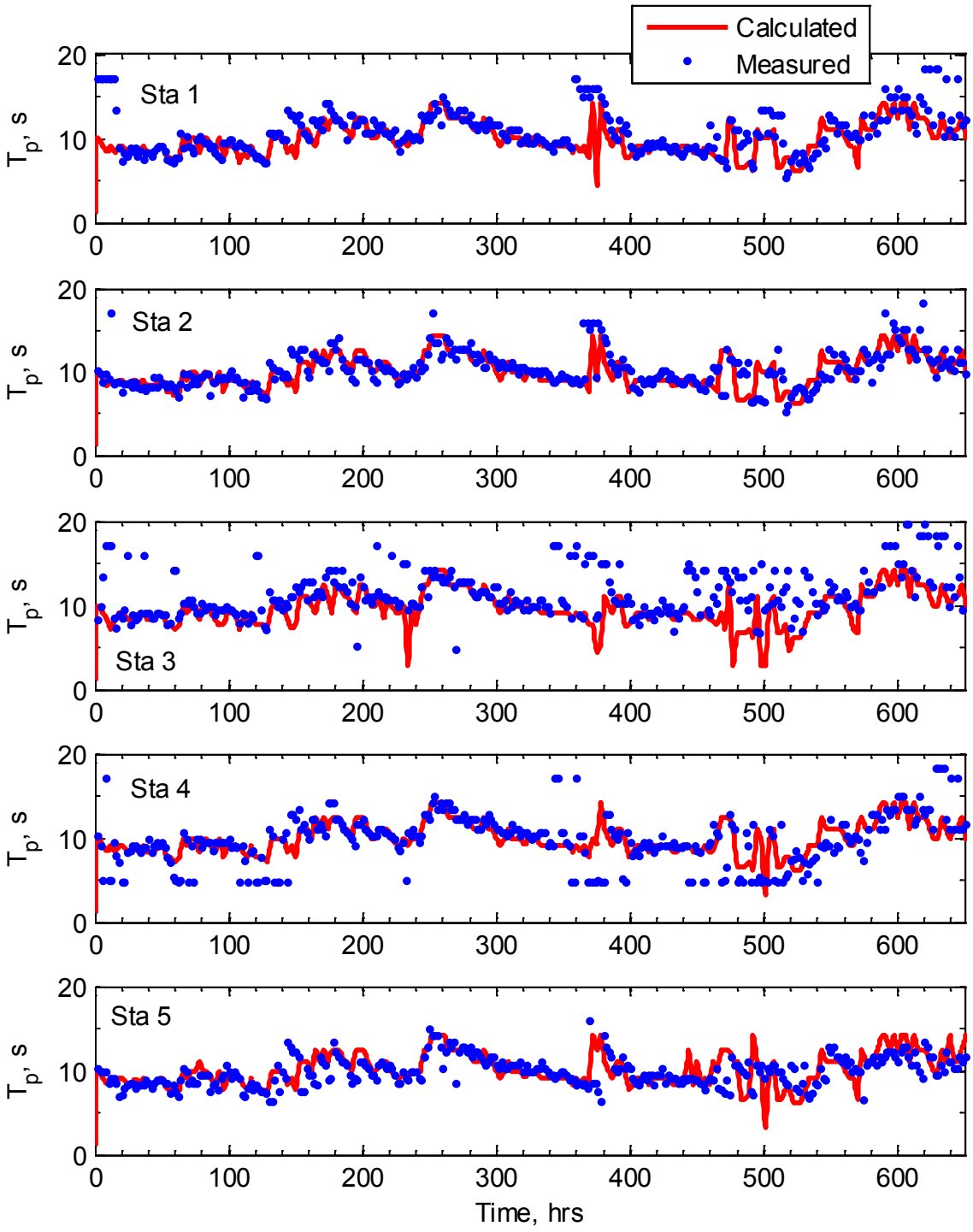

Figure 7.10. Measured and calculated peak wave periods (T_p) at Grays Harbor, WA. Elapsed times are with respect to September 14, 1999.

Table 7.8. Peak wave period goodness-of-fit statistics* at several stations for the Grays Harbor, WA test case.

	Station				
Statistic	**1**	**2**	**3**	**4**	**5**
NRMSE, %	14.25	12.67	7.71	18.57	18.8
NMAE, %	8.7	8.43	1.54	12.21	12.93
R^2	0.276	0.444	0.008	0.296	0.241
Bias, s	-1.042	-0.294	-3.526	0.204	0.258
*defined in Appendix A					

7.2.2 USGS Field Study

The nonuniform sediment transport model is applied to the beaches adjacent to Grays Harbor, WA, USA to test the model skill in predicting nearshore morphology change. The specific model features to be tested are bed material hiding, exposure, sorting, stratification, non-erodible bed surfaces, and transport due to asymmetrical waves, Stokes drift, roller and undertow. The model skill in predicting nearshore morphologic evolution is evaluated with the Brier Skill Score and Correlation Coefficient (see Appendix A).

Between May and July of 2001, the U.S. Geological Survey (USGS) instrumented 6 tripods and collected time series of wave height, water surface elevation, near-bottom current velocity, and sediment concentration proxies (Landerman et al. 2004). Weekly topographic maps and monthly bathymetric surveys along transects spaced 50-200 m apart were collected (see Figure 7.11). In addition, grab samples of surface sediment were collected at several locations.

The first half of the field deployment between May 6-30 of 2001 is simulated. The simulation period is characterized by relatively calm conditions, with a few spring storms with significant wave heights on the order of 3 m. The spectral wave transformation model is run on a ~200,000-cell Cartesian grid with varying grid resolution from 15-120 m (see Figure 7.12). The

waves are forced with spectral wave information from the Coastal Data Information Program (CDIP) buoy No. 03601 located southwest of the inlet at a depth of 42 m. For further details see Sánchez and Wu (2011b).

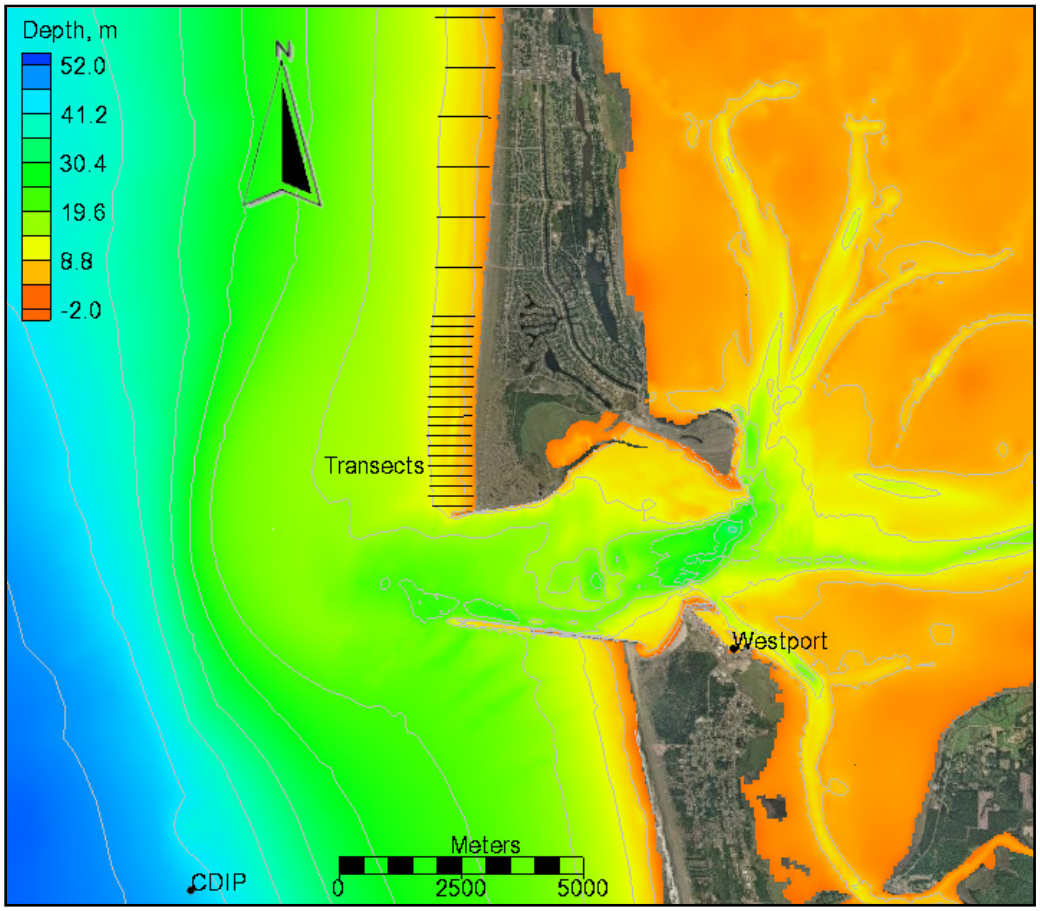

Figure 7.11. Map of Grays Harbor inlet, WA showing the location of the nearshore bathymetric transects during the USGS field study.

The flow model is forced with a water level time series from Westport Harbor with a negative 30 min phase lag correction which is obtained by comparing the measured and computed water levels at West Port Harbor (see Figure 7.11). Winds are interpolated from the

Blended Sea Winds product of the National Climatic Data Center (Zhang et al. 2006). The Manning's coefficient is calibrated in previous studies as 0.018 $s/m^{1/3}$ over the whole domain except on the rock structures where a value of 0.1 $s/m^{1/3}$ is used. A flux boundary condition is applied at the Chehalis River which is obtained from the USGS. The flow model grid has ~55,000-cells and six levels of refinement from 20-640 m (see Figure 7.21). A variable time step is set to a maximum value of 10 min. The sediment transport and bed change are calculated at every hydrodynamic time step.

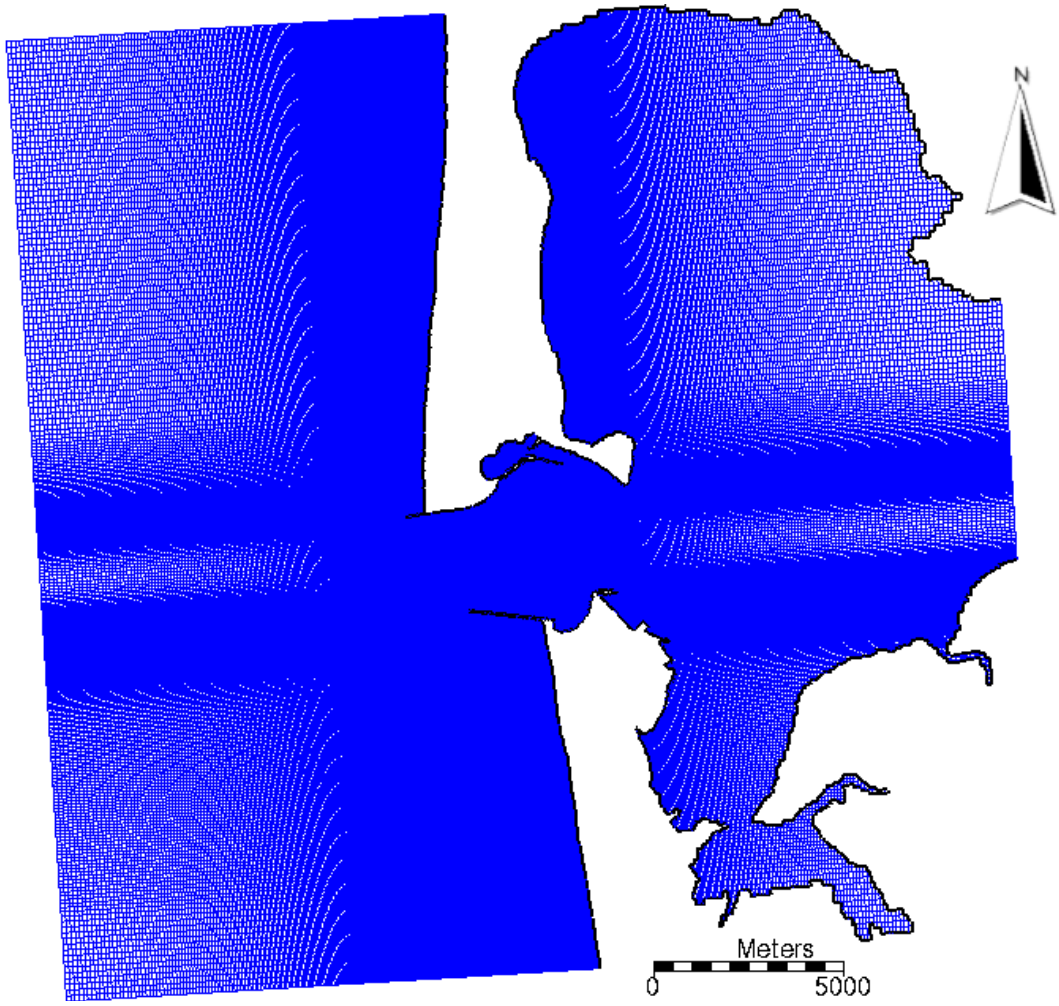

Figure 7.12. Wave model Cartesian grid used for the Grays Harbor, WA field test case.

A ramp of 5 days is implemented based on previous hydrodynamic studies at Grays Harbor, so that the start of the simulation is May 1, 2001. Waves are calculated at a constant 2-hr interval (steering interval). The significant wave height, peak wave period, wave unit vectors, and wave dissipation are linearly interpolated to the flow grid every steering interval and then linearly interpolated in time at every hydrodynamic time step. Wave variables such as wave length and bottom orbital velocities are updated every hydrodynamic time step for wave-current interaction.

When using such a large steering interval, it is important to consider how the water levels, current velocities and bed elevations, which are passed from the flow to the wave model, are estimated. For this application, and for most open coast applications, the nearshore waves are most sensitive to variations in water levels and not currents. Therefore, improved results can be obtained by predicting the water levels at the wave model time step based on a decomposition of the water levels into spatially constant and variable components. The spatially constant component is assumed to be equal to the tidal water surface elevation and the spatially variable component which includes wind and wave setup is estimated based on the last flow time step. The currents and bed elevations which are passed from the flow to wave grid are simply set to the last time step value. Other types of prediction methods could be used; however, the approach described above has been found to be sufficient for most applications and is simple to calculate. After each wave run, a surface roller model is also calculated on the wave grid and the roller stresses are added to the wave stresses before interpolating on to the flow grid. Even though flow and wave models use different grids, the two models are in a single code which facilitates the model coupling and speeds up the computation by avoiding communication files, variable

allocation and model initialization at every steering interval.

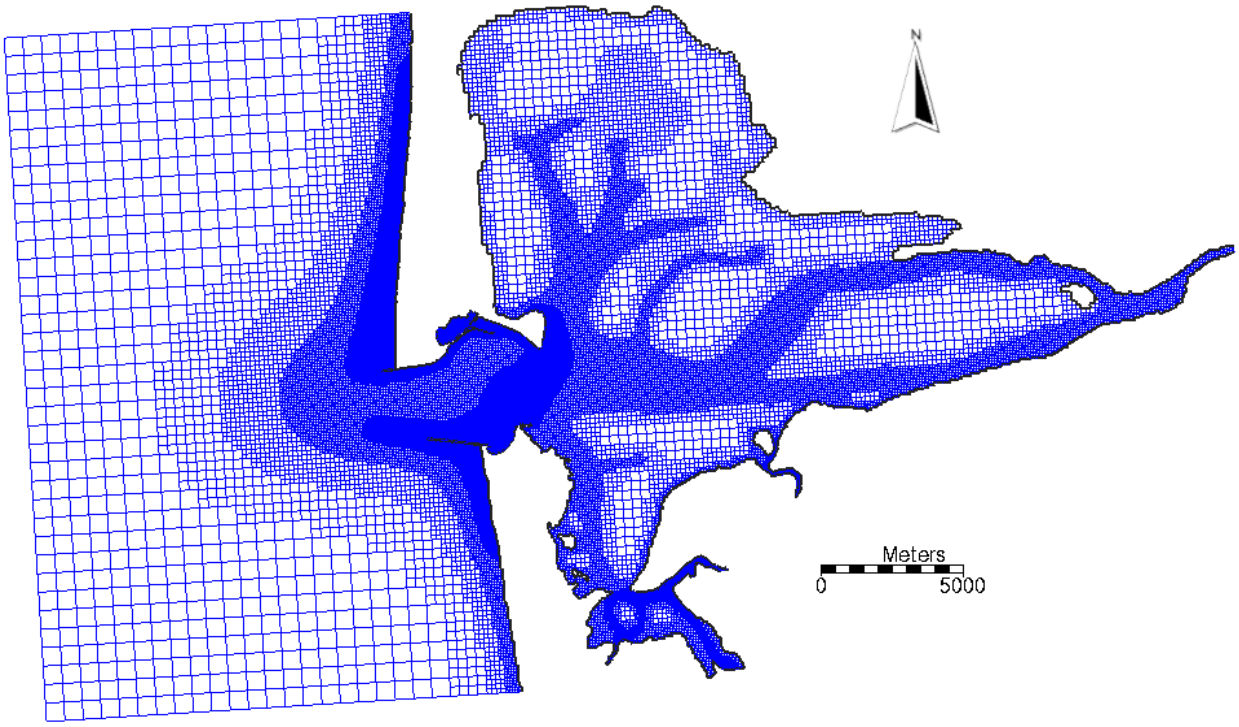

Figure 7.13. Flow model telescoping grid for the Grays Harbor, WA field test case.

The initial bed material composition is specified by a spatially variable median grain size $d_{50}$and constant geometric standard deviation σ_g of 1.3 mm based on field measurements. The initial fractional composition at each cell is assumed to be constant in depth and have a log-normal distribution, and represented by six size classes with characteristic diameters of 0.1, 0.126, 0.16, 0.2, 0.25, and 0.31 mm. An example of the initial grain size distribution is shown in Figure 7.14. Ten bed layers are specified with an initial thickness of 0.5 m each. The Lund-CIRP transport formulas are used to estimate the transport capacity (Camenen and Larson 2007). The total-load adaptation coefficient is calculated as $\alpha_t = Uh/(L_t\omega_s)$ where L_t is the total-load

adaptation length, ω_s is the sediment fall velocity, U is the depth-averaged current speed, and h is the total water dept. Here $L_t = (1 - r_s)L_b + r_s L_s$, where L_b and L_s are the bed- and suspended-load adaptation lengths, respectively. The bed-load adaptation length is set to 10 m, and the suspended-load adaptation length is calculated as $L_s = Uh/(\alpha_s \omega_s)$ where the suspended-load adaptation coefficient α_s is set to 0.5. A constant bed porosity of 0.3 is used in the simulation. The "cross-shore" sediment transport is included as an additional term in the bed change equation. The term is equal to the divergence of the sediment transport due to wave asymmetry and undertow following Larson (2009). For further details the reader is referred to Sánchez and Wu (2011a).

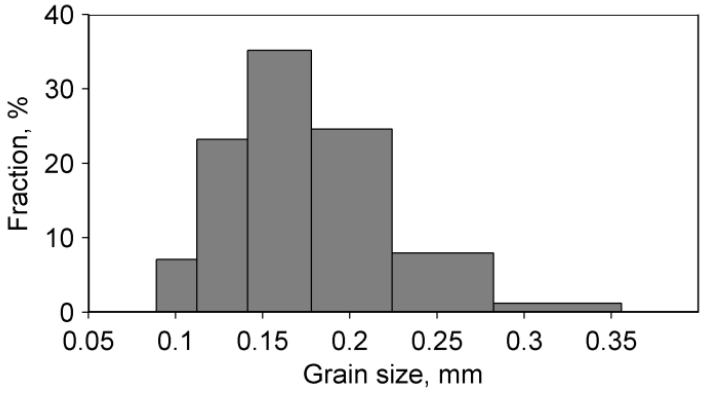

Figure 7.14. Example log-normal grain size distribution (d_{50}= 0.16 mm, σ_g= 1.3 mm).

Calculations are performed on a desktop PC and the 31-day simulation is completed in approximately 10 hr. A comparison of the measured and computed bed changes between May 6 and 30 of 2001 is shown in Figure 7.15. Selected regions of interest are encompassed by black lines in order to help visually compare the bed changes. In general, the results show many common features and similar erosion and deposition patterns. More specifically, the bed change

is characterized by the erosion of the outer bar, deposition in the inner bar face and outer trough, and erosion of the inner trough face. There is a region extending approximately 1 km from the northern jetty, where the bed changes are noticeably different from those further to the north. This region is interpreted as being strongly influenced by the presence of the inlet, ebb shoal and northern jetty. Interestingly, both the measurements and model results show small (200-300 m in length) inner bars form adjacent to the trough, which appear to occur at regular 400-500 m intervals.

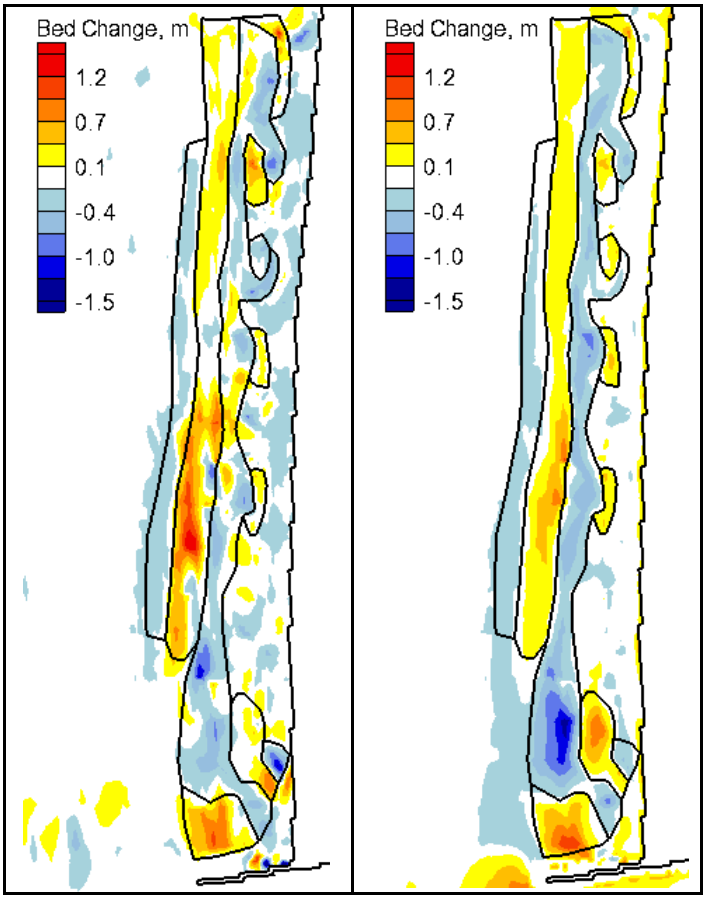

Figure 7.15. Measured (left) and computed (right) bed changes during May 6 and 30, 2001.

The computed bed changes in the foreshore region (beach face) are relatively small compared to the measurements due to the lack of swash zone processes in the present version of the model. Swash zone processes enhance transport in the surf zone by increasing the current velocities, transport rates and mixing at the shoreline. A large portion of the total longshore sediment transport occurs in the swash zone and without these processes, morphodynamic models will tend to underestimate longshore transport rates and bed change in the foreshore region. Walstra et al. (2005) simulated the bed change at transects 9 and 20 using a two-dimensional vertical (2DV) profile evolution model and were able to predict the onshore migration of the bar, but also found that the model performance deteriorates in the foreshore region.

The measured and computed water depths and bed changes for Transects 1 and 9 are shown in and Figure 7.16 and Figure 7.17, respectively. As observed in Figure 7.15, most of bed changes occur from the nearshore bar to the outer beach face. The model is able to accurately predict an onshore bar migration although it underestimates the nearshore bar height which is also observed in Figure 7.15. In order to evaluate the model performance in predicting the nearshore bathymetry, the Brier Skill Score (BSS) is applied to the water depths and the correlation coefficient R^2 to the bed change. Other goodness-of-fit parameters are also calculated and show similar patterns. For simplicity only the aforementioned parameters are shown in Figure 7.18. The goodness-of-fit statistics show a wide range of values.

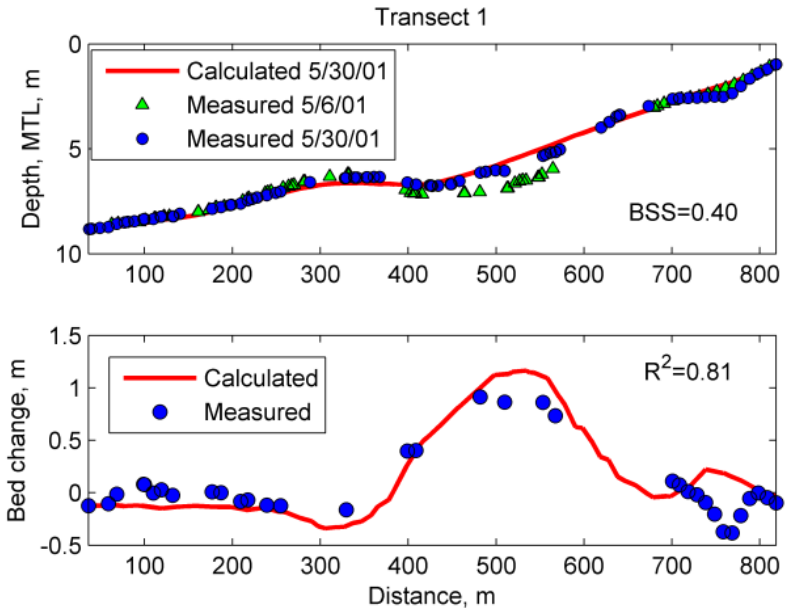

Figure 7.16. Measured and computed water depths (top) and bed changes (bottom) for Transect 1.

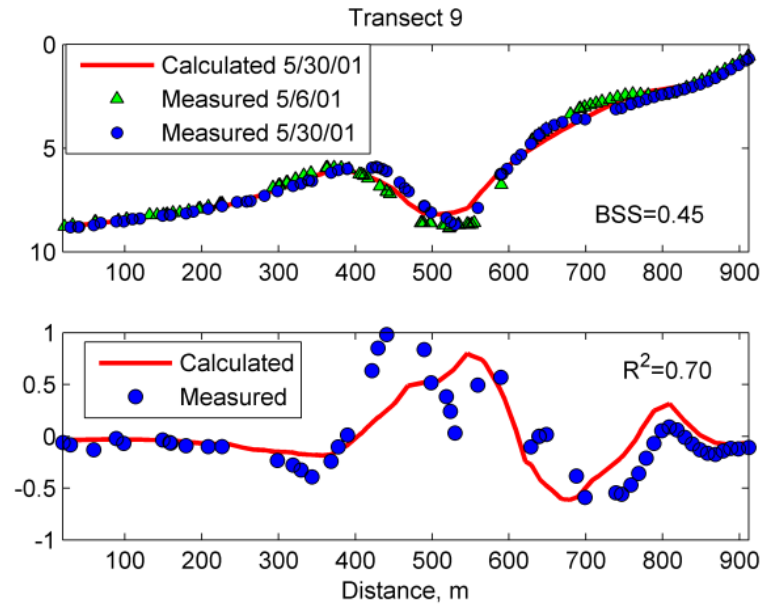

Figure 7.17. Measured and computed water depths (top) and bed changes (bottom) for Transect 9.

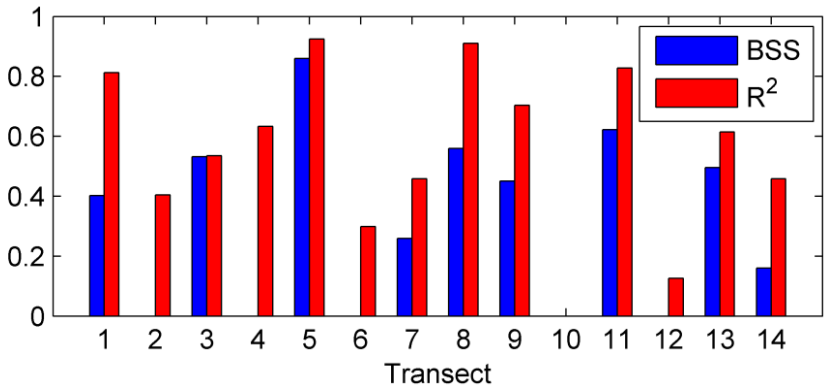

Figure 7.18. Brier Skill Score for water depths and correlation coefficient for computed bed changes at selected Transects.

The measured bed change shows a larger variation than the modeled bed change, indicating that morphology change is sensitive to longshore variations in forcing, initial bathymetry or 3D processes such as rip currents. As discussed by Walstra et al. (2005), the model results indicate that the waves and currents do in fact vary over the spatial scales (10-100 m) of the observed morphological variations.

The computed median grain size on May 30, 2001 is shown in Figure 7.19. Qualitatively, the results agree well with field measurements and typical findings for most inlets and beaches. Coarser sediments are found in the beach face and breaker line (offshore bar) and finer sediments are found in the trough and offshore of the surf zone. In addition, coarser sediments are found in the inlet entrance and finer sediments are found on the periphery of the ebb shoal. In addition, it is noted that the area around the jetties are highly armored due to the strong currents and large waves present, which is also observed in the field.

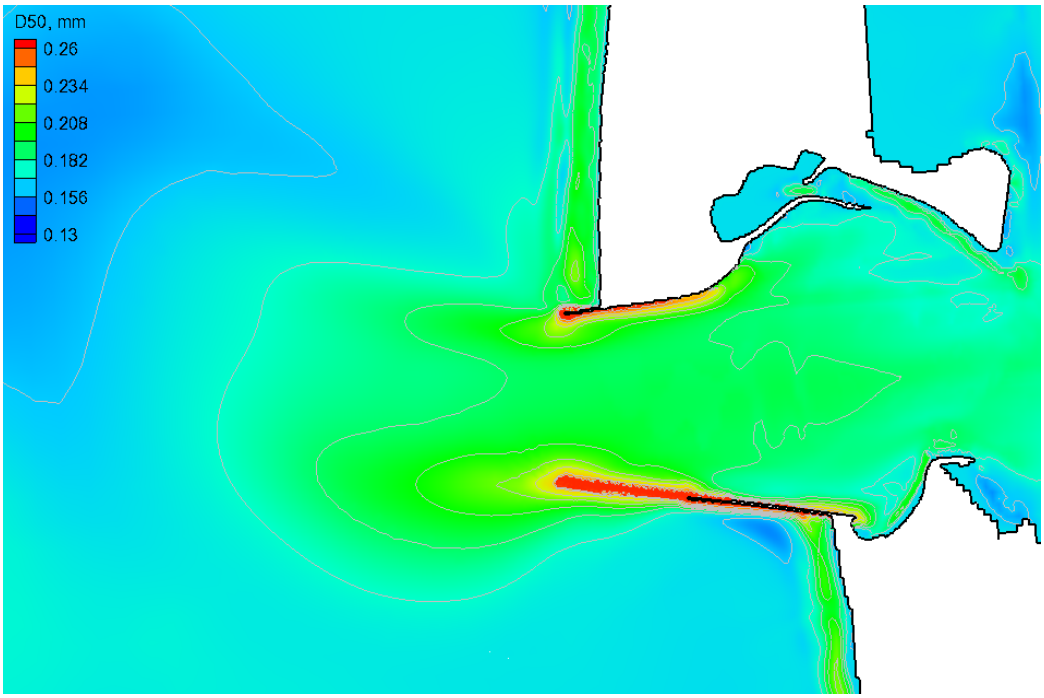

Figure 7.19. Distribution of median grain size calculated after the 25-day simulation for the Grays Harbor, WA test case.

7.3 Hazaki Oceanographic Research Facility, Japan

The developed model is applied to a field case to test the model performance in predicting the cross-shore distribution of the wave height and long-shore current over a double barred beach. Specific model features tested are the nonuniform Cartesian grid, surface roller, and coupling of the flow and wave models.

Kuriyama and Ozaki (1993) measured the cross-shore distribution of longshore current and wave height at the Hazaki Oceanographic Research Facility (HORF) located on the Japan Pacific coast. Longshore current measurements were made from a 427-m long pier using a float. The wave heights were calculated with ultrasonic wave gauges. The data presented here was taken on March 28, 1989. Table 7.9 shows a summary of offshore wave conditions.

Table 7.9. Offshore wave conditions for the HORF test case.

Variable	**Value**
Incident wave angle	27º
Offshore significant wave height	2.14 m
Wave period	8.86 s

A nonuniform Cartesian grid is used with a variable resolution of 3-10 m in the cross-shore direction and a constant resolution of 4-m in the longshore direction (see Figure 7.20). A constant zero water level is specified at the east (offshore) boundary, and cross-shore boundary conditions are used at the north and south boundaries. At the cross-shore boundaries, a longshore flux is given for inflow conditions and a water level that includes wave setup is specified for outflow conditions. This field case is simulated as a steady state condition, for which the model is ramped from still water by using a pseudo-time stepping procedure. The nearshore bathymetry is assumed to be uniform in the longshore direction and the longshore currents and water levels to be well developed. Tide and wind are not included in the simulation. The important settings for flow and wave models are provided in Table 7.10 and Table 7.11, respectively.

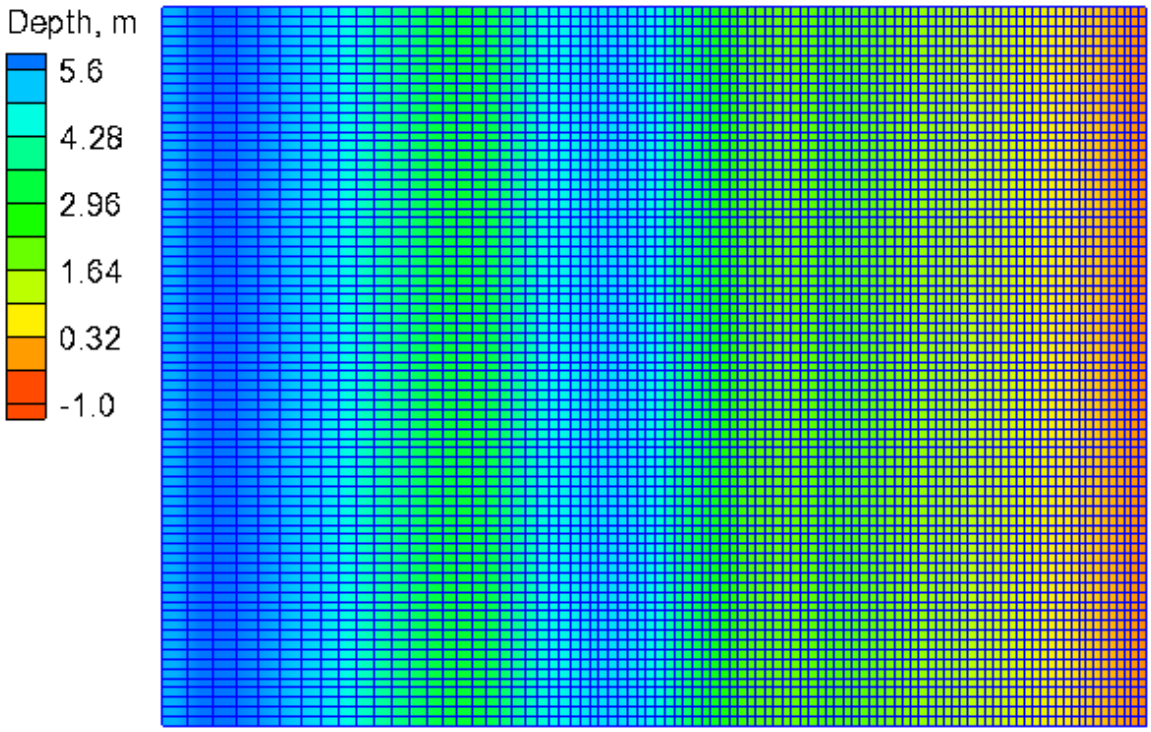

Figure 7.20. Computational grid for the HORF test case.

Table 7.10. Flow model setup parameters for the HORF field test case.

Setting	**Value**
Time step	1 min
Simulation duration	3 hr
Ramp duration	2 hr
Manning's coefficient	0.032 $s/m^{1/3}$

Table 7.11. Wave model setup parameters for the HORF field test case.

Setting	**Value**
Wave breaking	Battjes and Jansen (1978)
Spectrum	TMA
Directional spreading distribution	Cosine Power
Directional spreading parameter γ	3.3
Bottom friction	Off (default)
Steering interval	0.25 hr
Roller	Off, On
Roller efficiency factor	1.0
Roller dissipation coefficient	0.1

The computed significant wave heights are compared to field measurements in Figure 7.21. The wave height profile is characterized by strong wave breaking near the offshore bar and the inner bar and less intense wave breaking on the beach face. In general, good agreement is obtained between the measured and computed wave heights as illustrated by the goodness of fit statistics shown in Table 7.12. The computed longshore currents with and without the surface roller are compared to the measurements in Figure 7.22. The cross-shore distribution of the longshore current is characterized by two peaks due to the double barred beach profile. The magnitude of the longshore current is proportional to the reduction of the wave height squared which explains why the offshore longshore current peak is stronger than the nearshore peak. The location of the longshore current peaks is captured better when the roller is included. The default value for the roller dissipation coefficient of 0.1 is used. It is expected that further improvement of the longshore current could be obtained by calibrating the roller dissipation coefficient.

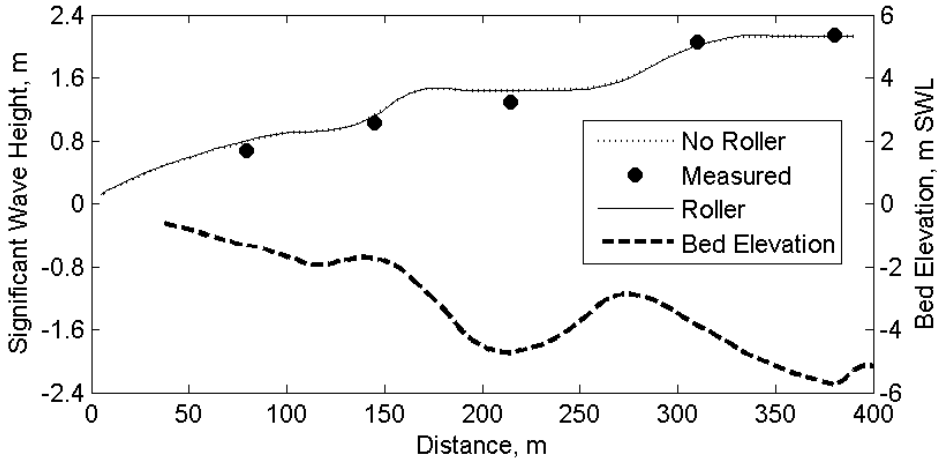

Figure 7.21. Comparison of measured and calculated significant wave heights for the HORF field experiment. The beach profile is also shown for reference.

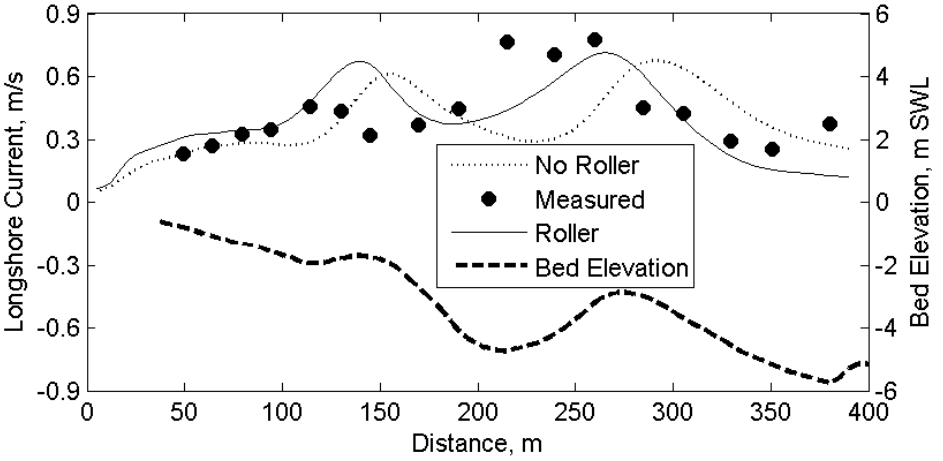

Figure 7.22. Comparison of measured and calculated longshore currents for the HORF field experiment. The beach profile is also shown for reference.

Table 7.12. Significant wave height and longshore current goodness-of-fit statistics* for the HORF field case.

	No Roller		**Roller**	
Statistic	H_s, **m**	V, **m/s**	H_s, **m**	V, **m/s**
NRMSE, %	6.95	38.51	6.65	28.26
NMAE, %	5.89	30.01	5.61	21.44
R^2	0.994	0.0015	0.995	0.3236
Bias	0.066	-0.028	0.062	-0.006
*see Appendix A.				

7.4 Duck, NC DELILAH Field Experiment

The purpose of this case is to test the model performance in predicting nearshore hydrodynamics, specifically the wave height and longshore current on a barred beach profile. The specific model features to be tested are the inline flow and wave coupling and surface roller. Waves and currents were measured at Duck, NC, during the DELILAH field experiment held from October 1-19, 1990. Data presented here were measured along a cross-shore array of instruments with conditions recorded approximately every 3 hr. For additional details on the DELILAH field experiment the reader is referred to Smith et al. (1993). The datasets presented here were collected on October 14 for which the beach profile consisted of a pronounced longshore bar.

A nonuniform Cartesian grid is used with a variable resolution in the cross-shore direction between 2-6 m and a constant resolution in the longshore direction of 6 m (Figure 7.23). Table 7.15 shows the offshore wave conditions at an 8-m water depth.

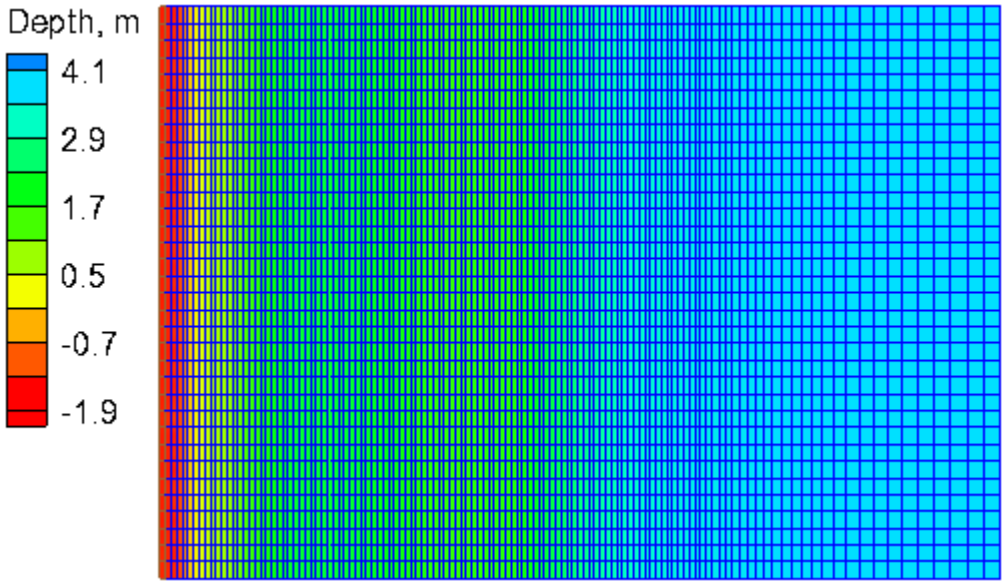

Figure 7.23. Computational grid for the DELILAH test case.

Table 7.13. Offshore wave conditions for the DELILAH test case at 8-m depth.

Variable	**Value**
Incident wave angle	32º
Offshore significant wave height	0.94 m
Wave period	9.7 s

The flow model is run with a time step of 2 min with a 3-hr ramp period and simulation duration of 3.5 hr. The Manning's roughness coefficient is calibrated as 0.018 s/m$^{1/3}$. The simulation requires 1.2 min to execute on a single 2.67GHz processor. A summary of the flow model setup parameters is provided in Table 7.14.

Table 7.14. Flow model setup parameters for the DELILAH test case.

Setting	**Value**
Time step	2 min
Simulation duration	3.5 hr
Ramp duration	3 hr
Manning's coefficient	0.018 $s/m^{1/3}$

The flow and wave models are coupled at a 0.25-hr interval. The wave breaking formula applied is Battjes and Jansen (1978). Two simulations are presented herein with the wave roller terms turned on and off to illustrate significance of the wave roller process. Bottom friction is turned off in the wave model. Sensitivity tests show that the wave bottom friction has a negligible influence on the wave height over such a small distance and that the wave breaking is the dominant form of dissipation. The TMA spectrum is applied with a cosine directional spreading with $\gamma = 3.3$ to represent the wave spectrum in shallow water. A summary of selected wave model settings are shown in Table 7.15.

Table 7.15. Wave model setup parameters for the DELILAH test case.

Setting	**Value**
Wave breaking	Battjes and Janssen (1978)
Spectrum	TMA
Directional spreading distribution	Cosine Power
Directional spreading parameter γ	3.3
Bottom friction	Off
Steering interval	0.25 hr
Roller	Off, On
Roller dissipation coefficient, β_D	0.02,0.05
Roller efficiency factor	1.0

Figure 7.24 shows the cross-shore profile with the measured and calculated significant wave heights, H_s, in the cross-shore array for measurements at 1:00 AM on October 14, 1990. The inclusion of the wave roller effect is nearly insignificant in calculation of the wave height across shore. However, in terms of the calculated longshore current, V, the wave roller effect is important. Figure 7.25 shows the same profile with the measured and calculated longshore currents. Three calculations are shown: no roller, the roller with roller dissipation coefficient, $\beta_D = 0.05$ and $\beta_D = 0.02$. Inclusion of the roller effect more accurately captures the location of the peak in the longshore current further inshore, and also provides a better representation of the magnitude of the current.

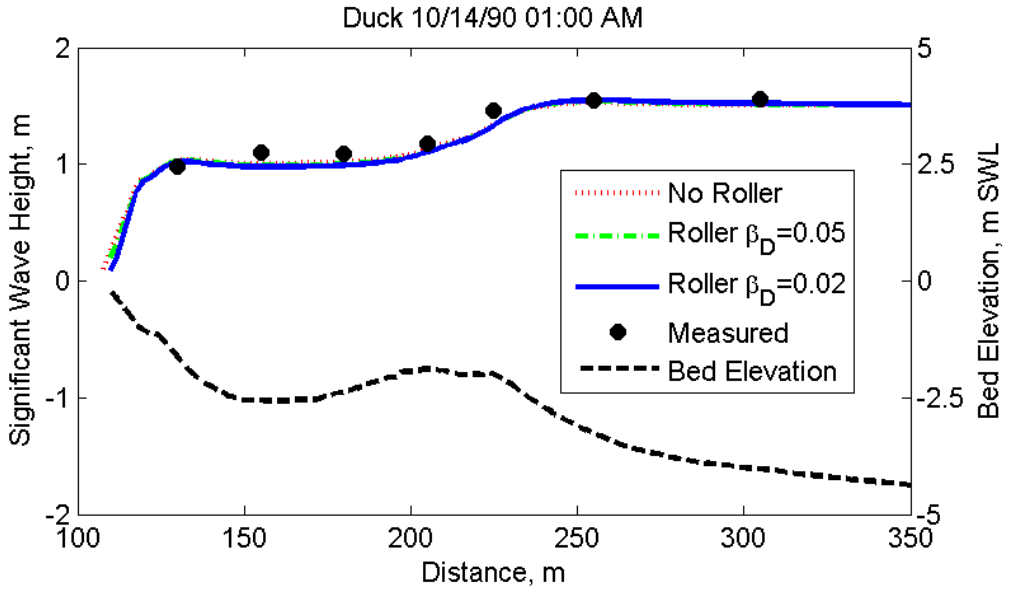

Figure 7.24. Comparison of measured and calculated significant wave heights for the DELILAH field experiment

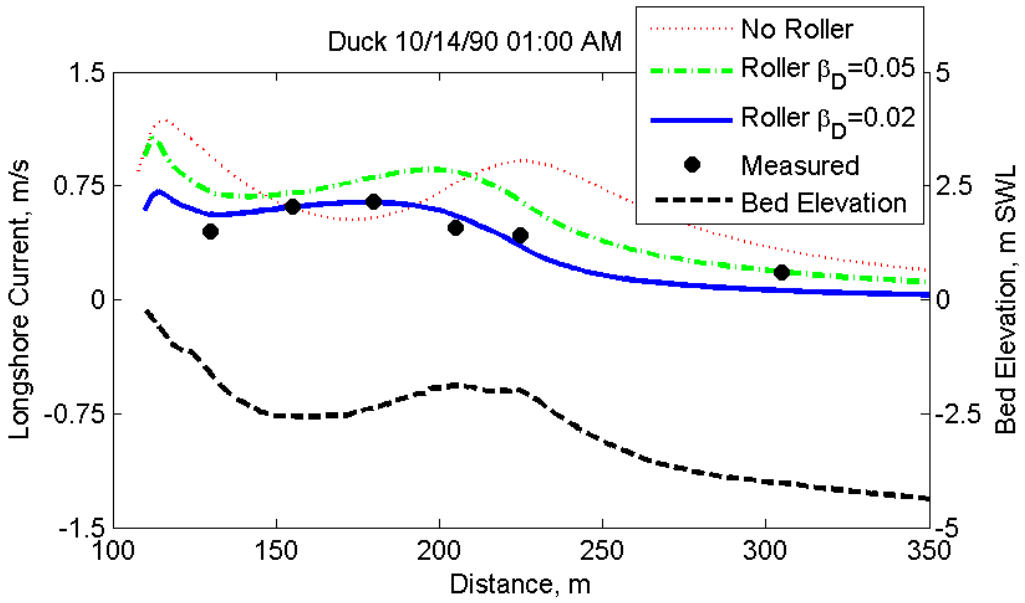

Figure 7.25. Comparison of measured and calculated longshore currents for the DELILAH field experiment

The goodness-of-fit statistics presented in Table 7.16 quantify the model performance with and without the surface roller. Wave height errors actually increase very slightly when the roller is included, although this error is insignificant because it is likely within accuracy of the measurements and numerical calculations. However, error decreases quite significantly for the longshore current when the roller is included, from between 37-46% to 9-12%. The most accurate calculation is obtained with the roller β_D = 0.02, resulting in the squared correlation coefficient R^2 = 0.927 and 0.915 for the significant wave height and longshore current velocity, respectively.

Table 7.16. Goodness-of-fit statistics* for the DELILAH field experiment at 1:00 AM on October 14, 1990.

Roller	**Variable**	**NRMSE, %**	**NMAE, %**	**R^2**	**Bias**
Off	H_s	4.50	4.05	0.933	-0.040 m
	V	46.23	37.11	0.400	0.206 m/s
On β_D=0.05	H_s	4.97	4.37	0.926	-0.046 m
	V	31.81	26.29	0.864	0.169 m/s
On β_D=0.02	H_s	5.18	4.41	0.927	-0.049 m
	V	11.53	8.72	0.915	-0.000 m/s
H_s = Significant wave height [m] V = Longshore current velocity [m/s] *defined in Appendix A					

A second case for data collected during DELILAH at 10:00 AM on October 14, 1990 is run for validation of these parameters. Figure 7.26 shows the cross-shore profile and distribution of significant wave height across the profile. Similar to the previous case, inclusion of the roller does not have a significant effect on the wave height calculation. However, as in the previous case, the simulation including the roller reproduces more accurately the location and magnitude of the longshore current (see Figure 7.27).

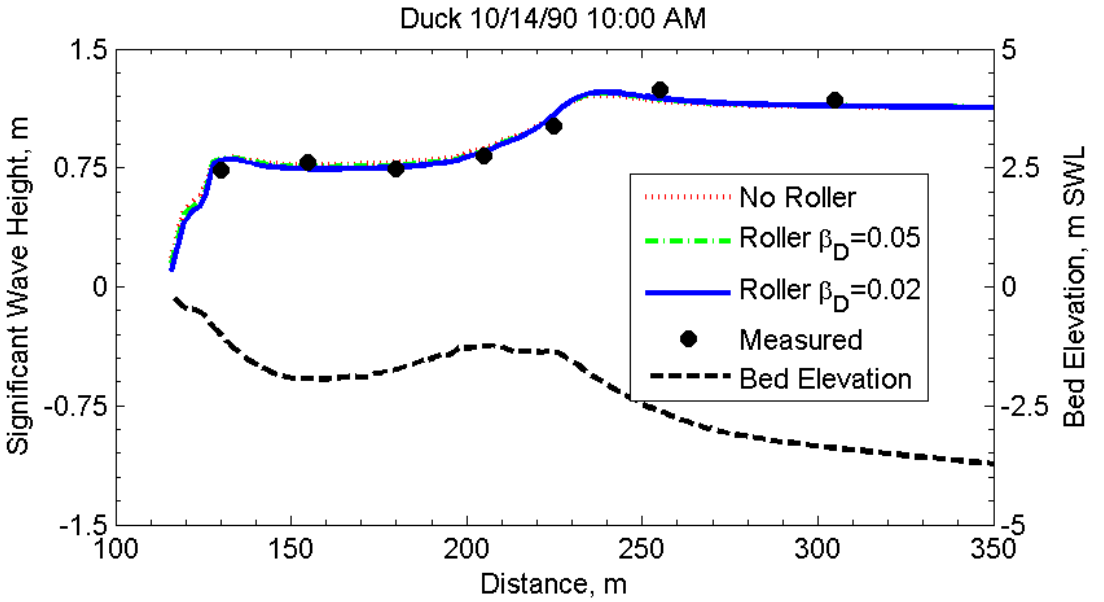

Figure 7.26. Comparison of measured and calculated significant wave heights for the DELILAH field experiment.

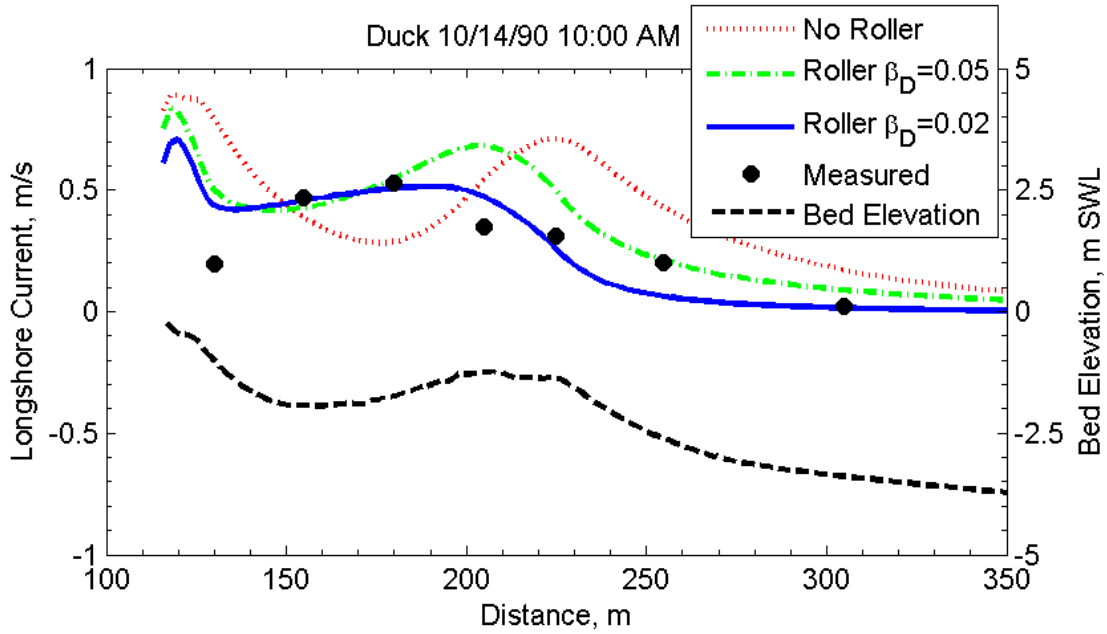

Figure 7.27. Comparison of measured and calculated longshore currents for the DELILAH field experiment.

As opposed to the previous case, the error appears to decrease slightly for the calculated wave height when the roller is included (from 4-4.2% to 3.4-3.7% error), although once again this improvement is likely within the accuracy of the measurements and calculations (see Figure 7.17). Error in longshore current velocity decreases significantly when the roller is included, from 58% for the NRMSE without the roller to 25%. Once again, the best squared correlation coefficient, R^2 occurs with $\beta_D = 0.02$, resulting in $R^2 = 0.945$ and 0.699 for the significant wave height and longshore current velocity, respectively. Typical roller dissipation coefficient values are within 0.05-0.1 and the default value is 0.05. These results indicate that the roller dissipation coefficient may have values smaller than 0.05. More research is needed in better defining the roller dissipation coefficient based on field conditions.

Table 7.17. Goodness-of-fit statistics for the DELILAH field experiment at 10:00 AM on October 14, 1990.

Roller		**NRMSE, %**	**NMAE, %**	**R^2**	**Bias**
Off	H_s	4.23	3.98	0.943	0.019 m
	V	58.53	51.10	0.202	0.189 m/s
On β_D =0.05	H_s	3.84	3.58	0.947	0.014 m
	V	37.16	28.65	0.663	0.141 m/s
On β_D =0.02	H_s	3.70	3.43	0.945	0.010 m
	V	25.21	19.02	0.699	0.044 m/s
H_s = Significant wave height [m] V = Longshore current velocity [m/s] *defined in Appendix A					

7.5 Columbia River Estuary, WA/OR

7.5.1 Site Description

The Columbia River Estuary, WA/OR is located in the northwestern United States and serves as a drainage outlet for an area of 671,000 km^2. The coastal plain-type estuary contains federally maintained deep draft navigation channels which meander through the estuary. The estuary is a major supply of sediment to the littoral cell. The inlet entrance is about 14.5 km wide. The entrance is characterized by three rubble-mound structures which support the federal navigation channel (see Figure 7.28). The south and north jetties constrain the currents in the entrance to help maintain the navigation channel depths and provide wave protection to transiting vessels. Jetty A is primarily a training structure to direct flow away from the foundation of the north jetty.

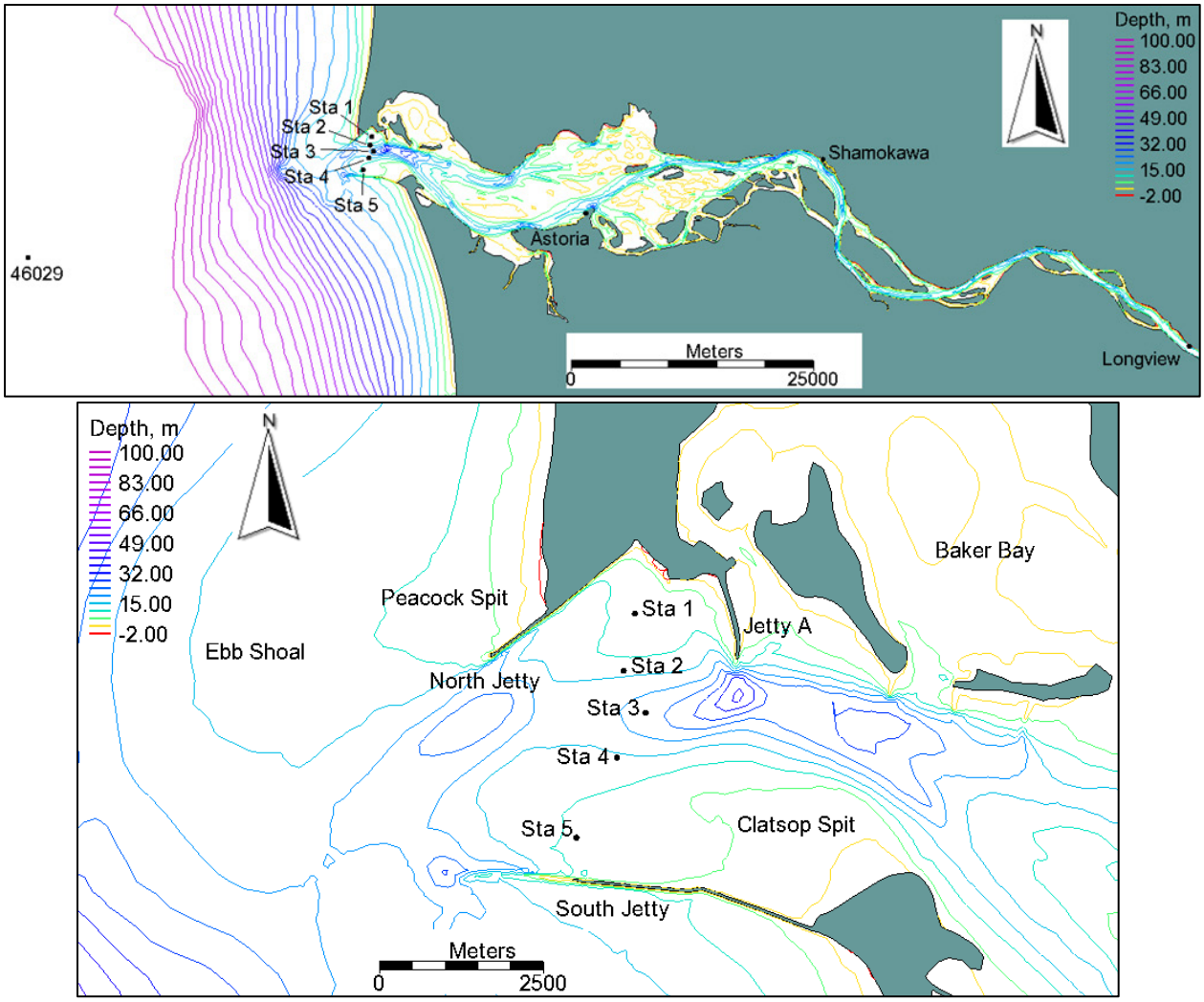

Figure 7.28. Map of the Columbia River Estuary (top) and close view of the entrance (bottom). The locations of observation stations are shown with black dots. Depth contours beyond 100 m are not shown for better visualization.

The tide is mixed semi-diurnal with a mean tidal range of approximately 2.4 m. The mean tidal range increases for the first 24 km due to a decrease in cross-sectional area in the bay (i.e. funneling) and then decreases due to mainly bottom friction (Fox et al. 1984). The river flow has the effect of reducing the tidal range by slowing the tidal wave propagation up river (Fox et al. 1984). The tidal propagation in the estuary is weakly nonlinear with an amplitude to depth

ratio of about 0.1. The entrance is characterized by an asymmetric ebb shoal which extends 7 km offshore.

The entrance of Columbia River is known for its extreme wave conditions and navigation hazards. Waves propagating through the inlet are strongly influenced by strong flood and ebb current velocities. Ebbing current velocities can reach 2.5 m/s and have the effect of increasing the wave heights by 50 to 70% (González 1984, Elias et al. 2012). In addition, the large asymmetric ebb shoal refracts and focuses the wave heights producing large spatial gradients in wave energy and thus generating strong wave-driven currents.

The Columbia River is the fourth largest river in the U.S. and the largest river on the Pacific coast of the U.S. (Kammerer 1990). The river discharge is seasonal and can vary from 2,000 to 4,000 m^3/s in the fall to early spring and with maximum discharges of approximately 11,000 m^3/s in the spring/summer due to snow melt (i.e. freshet) (Bottom et al. 2005). The river produces a buoyant plume which has a significant impact on the estuarine circulation (Jay and Smith 1990, Hamilton 1990).

The estuary is generally classified as a partially mixed although the degree of stratification varies significantly depending on the river discharge and tidal range. Since the present flow model is depth-integrated and barotropic, it is known a priori that some of the processes cannot be simulated. Despite this limitation there is sufficient evidence indicating that a two-dimensional horizontal (2DH) model may capture a sufficient portion of the estuary dynamics to justify using the case for model testing. Firstly, Hamilton (1990) reported that despite the large density gradients, the density-driven horizontal flow is generally weak, especially during spring tides or large river flows. In addition, 1D and 2DH models have used

with some success in simulating the estuarine dynamics. Fread (1976) developed the 1D dynamic wave model DWOPER (Dynamic Wave OPERational) which is used by the National River Forecast Center to forecast hourly water levels from the Vancouver-Portland area to Astoria. Koehler (1988) applied the implicit finite difference model developed by Fread (1976) and analyzed in detail the lower Columbia River. Geise and Jay (1989) utilized a 1D harmonic transport model to study the along channel variations in the tidal propagation in terms of the momentum balance in the lower Columbia River. McAnally et al. (1984) applied the 2DH model RMA-2V to study navigation channel shoaling problems at the entrance of the Columbia River. Gailani et al. (2003) utilized the finite element model ADCIRC (ADvanced CIRCulation) (Luettich et al. 1991) in 2DH mode in dredge material placement study at the entrance of the Columbia River. ADCIRC is used to provide depth-averaged currents and water levels to nested smaller area hydrodynamic and sediment transport models used to simulate the disposal of dredged sediments. Demirbilek et al. (2008) applied ADCIRC (also in 2DH mode) in combination with two wave models in a jetty rehabilitation study. These studies demonstrate that a significant portion of the dynamics of the lower Columbia River can be simulated without a 3D model. In summary, it is understood that the present barotropic model cannot capture all of the processes at the Mouth of the Columbia River (MCR), but it is still useful to apply the model to the MCR and test how well it can reproduce the water levels and the depth-averaged current velocities at several locations within the estuary and lower river.

7.5.2 Field Study Measurements and Conditions

In 2005 the U.S. Army Corps of Engineers (USACE) conducted a field study at the entrance of the Mouth of the Columbia River (MCR) (Moritz 2005). Five bottom-mounted tripods were deployed at the estuary entrance (see Figure 7.28). The tripods were equipped with Acoustic Doppler Profilers (ADCP) to measure current velocity profiles and waves, and Acoustic Doppler Velocimeters (ADV) to measure near-bottom current wave orbital velocities. Salinity measurements were collected using Conductivity Temperature and Depth (CTD) sensors. Sediment concentrations were collected with Optical Backscatter Sensors (OBS). The field data were collected from August 3 to September 9 of 2005, except for Station 3 which ends on August 19 when the tripod was dragged half a mile out to sea by the tow-line of a passing container ship.

Deepwater waves and wind are obtained from the National Oceanic and Atmospheric Administration (NOAA) buoy 46029 location 37 km offshore at the 128-m bathymetric contour (see Figure 7.28) (http://ndbc.noaa.gov). The wave conditions during the study period are relatively moderate with the highest offshore significant wave heights of approximately 2.4 m (see Figure 7.29). The peak wave periods are typically 8 s but varied between 6 and 16 s. The mean wave direction was predominantly from the Northwest. Wind data is also obtained from buoy 46029 and is generally relatively mild (<10 m/s) and from the north-north-west (conducive to upwelling) with short reversals (see Figure 7.30).

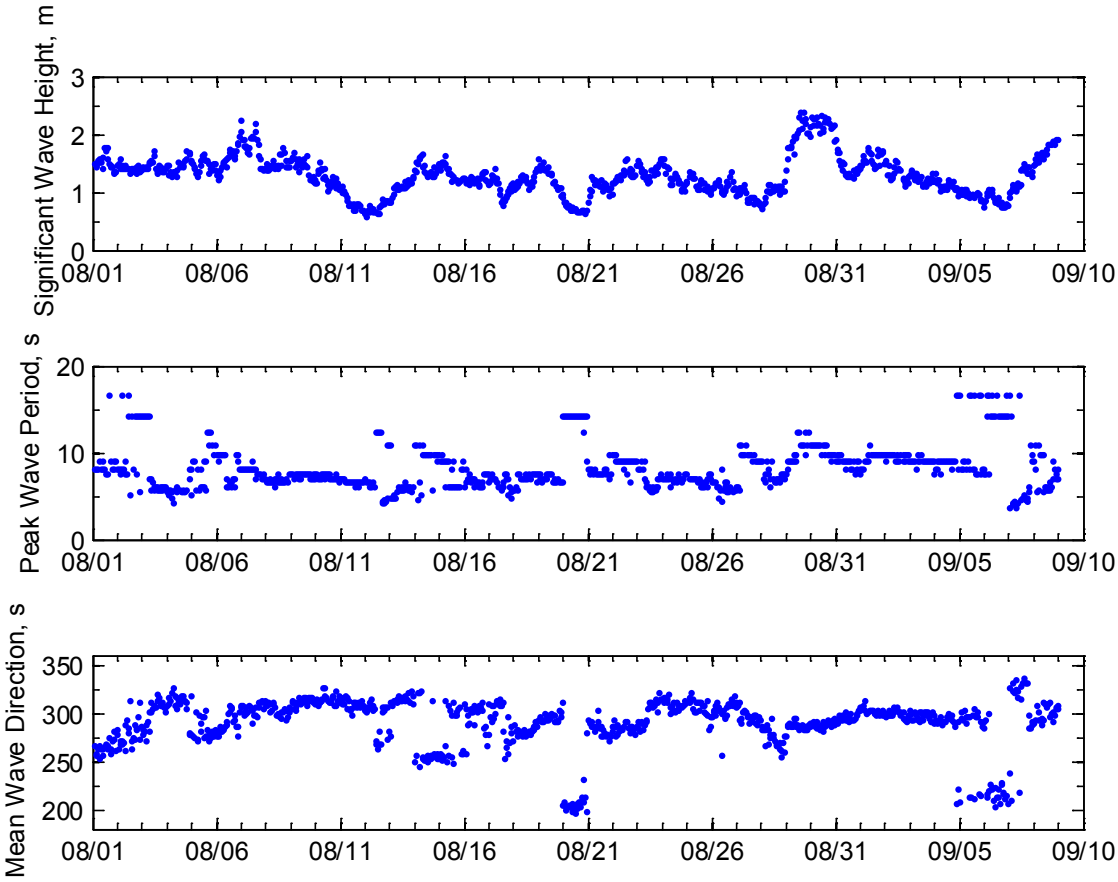

Figure 7.29. Wave data from NOAA buoy 46029.

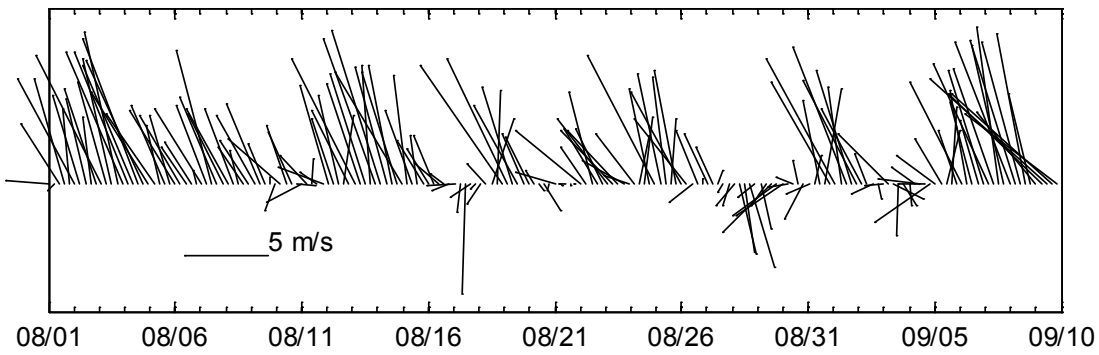

Figure 7.30. Wind from NOAA buoy 46029.

7.5.3 Model Setup

The flow model is run using a hybrid triangular and quadrilateral mesh (see Figure 7.31). The mesh has approximately 16,000 cells. The quadrilateral cells are especially useful in representing the navigation channel and river portion of the domain. The grid resolution is approximately 20 m near the jetties and expands out to approximately 3,500 m at the open ocean boundary. A sensitivity test is done with half the grid size and the results are not significantly different at the observation stations for the field study.

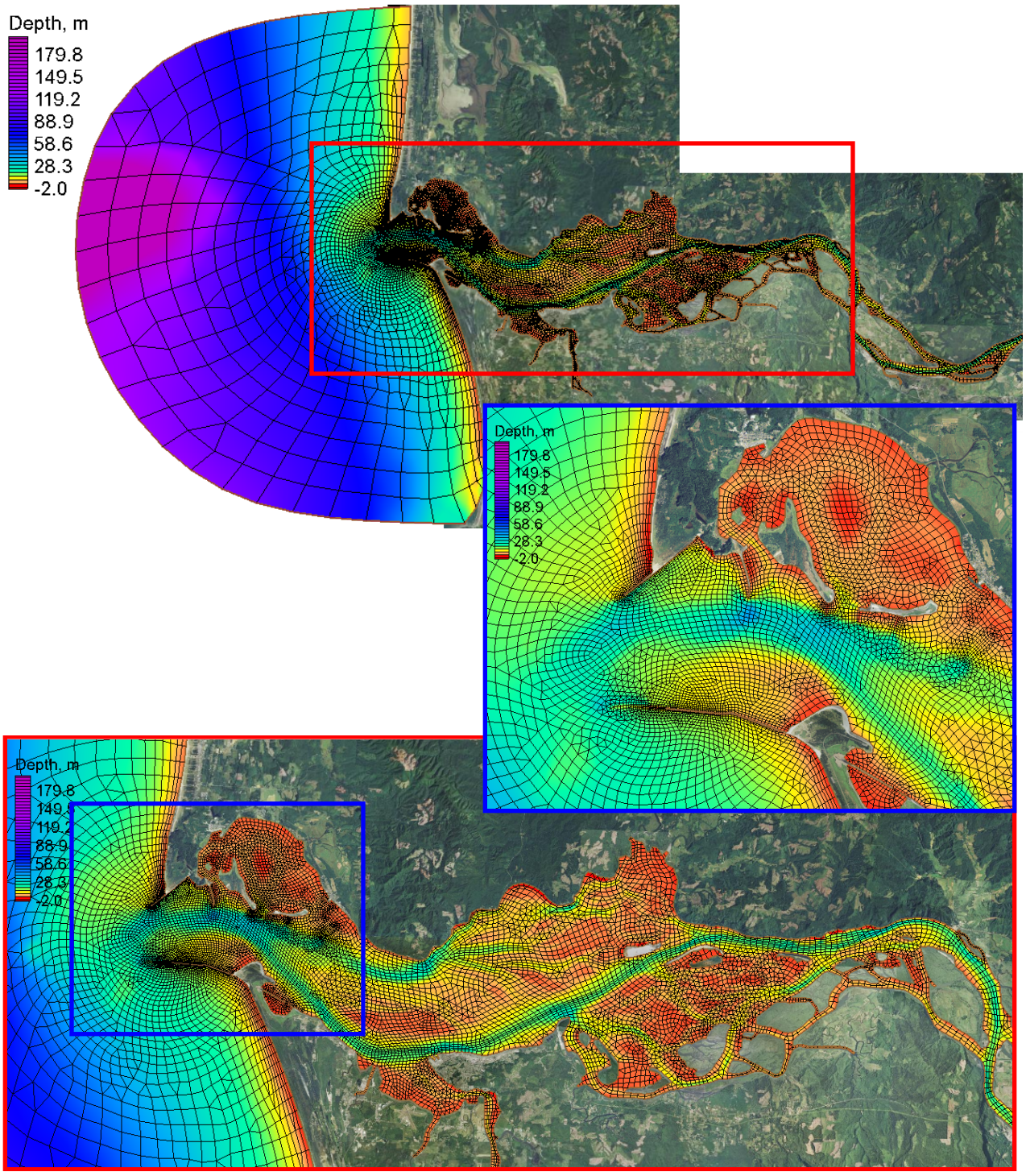

Figure 7.31. Flow model computational mesh for the MCR test case.

A summary of the flow model setup is provided in Table 7.18. The flow model is run using a time step of 5 min. Sensitivity results show that almost identical results are obtained with time steps of 5, 10, and 20 min. The wave mass (or volume) flux is included in the momentum and continuity equations and helps improve slightly the current velocity comparisons. The offshore boundary is forced with the calibrated tidal constituents obtained by Elias et al. (2012) shown in Table 7.19. The daily average river discharge is approximately constant during the study time period and is set to 4,000 m^3/s. The Manning's roughness coefficient is calibrated based on measured water levels and increased from 0.018 $s/m^{1/3}$ at the entrance, 0.025 $s/m^{1/3}$ near Astoria, to 0.03 $s/m^{1/3}$ near Shamakowa. These values are similar to those reported by Elias et al. (2012), who also calibrated the bottom roughness and found similar results where the roughness increases from the entrance. Preliminary simulations in which the mesh domain ends near the Beaver U.S Army Station produce excessive tidal amplitudes at Shamakowa, and it is found that extending the computational domain eliminates the problem suggesting that the tidal wave is being reflected from the upstream river boundary. Calibration of tide gauge Longview (65 km from the entrance) requires an increased Manning's roughness coefficient from 0.03 $s/m^{1/3}$ at Shamakowa to 0.038 $s/m^{1/3}$ near Longview. This value is relatively large and may be due to unresolved bathymetry or the reflection from the upstream river boundary. Since the computational mesh of Elias et al. (2012) did not extend that far upstream it is not possible to compare.

Table 7.18. Flow model setup for the MCR test case.

Variable	**Value**
Time step	5 min
Simulation duration	40 days
Wave mass flux	On
Ocean water level forcing	Tidal constituents
River discharge	4,000 m^3/s
Wind forcing	Buoy 46029
Wind reference frame	Lagrangian
Manning's' coefficient	0.018-0.038 $s/m^{1/3}$

Table 7.19. Tidal constituent amplitudes and phases used to force the flow model at the open ocean boundary (from Elias et al. 2012).

Constituent	**Amplitude, m**	**Phase, deg**
M2	0.920	224
K1	0.425	233
S2	0.266	247
O1	0.266	218
N2	0.190	199
P1	0.129	230
K2	0.070	239
NO1	0.056	194
Q1	0.055	210

The wave model grid has approximately 59,000 cells and a variable grid resolution between 50 and 600 m (see Figure 7.32). The wave model only covers the area near the entrance. A larger wave grid with the same offshore coverage as the flow model is also tested but no difference in observed in the results at the mega-transect stations.

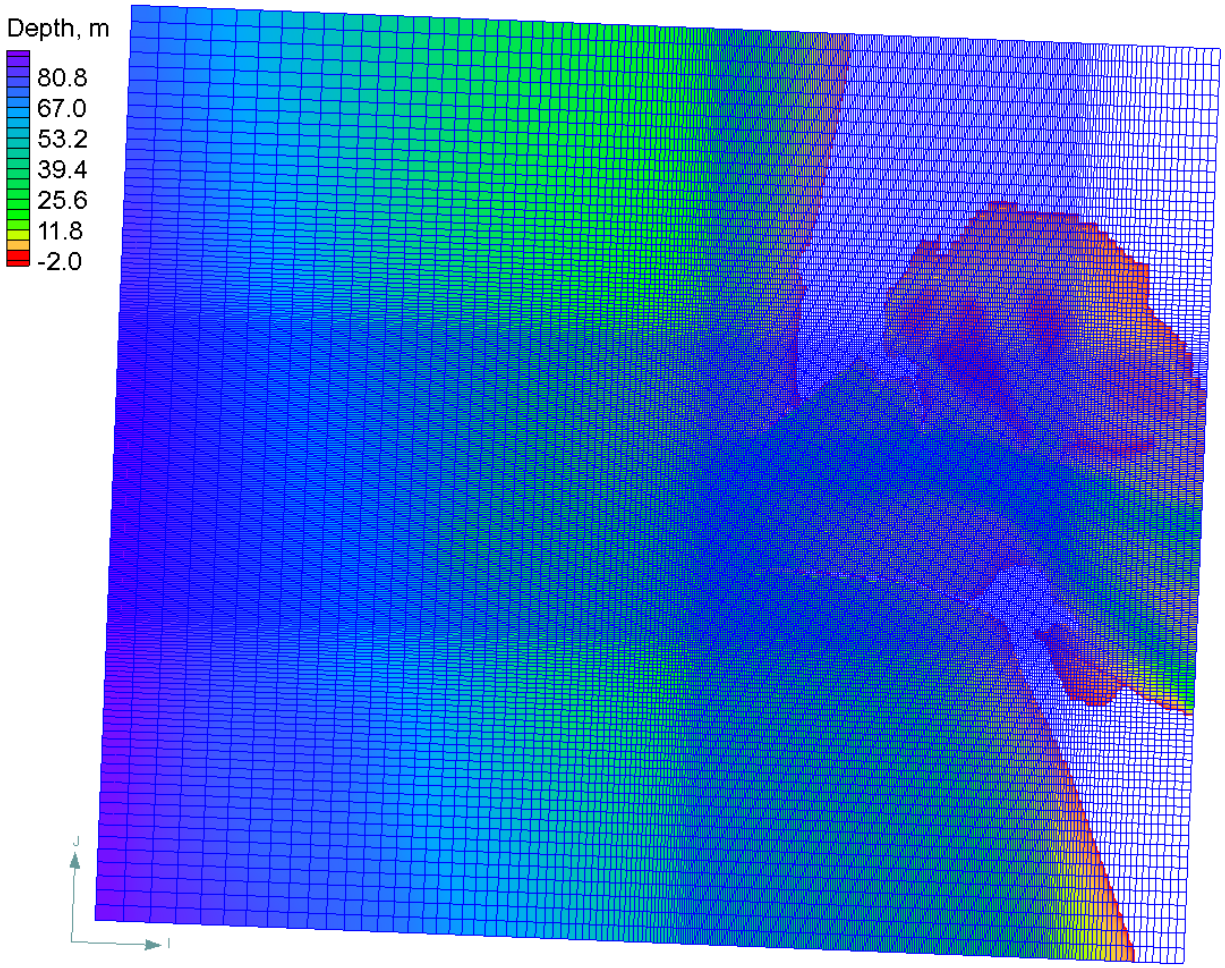

Figure 7.32. Wave model computational mesh for the MCR test case.

Wave model is run using mostly default settings (see Table 7.20). The bottom friction is set to zero and is known to insignificantly impact the results. The wave model time step or steering interval is set to 1 hr. Sensitivity tests using a steering interval of 30 min show no significant difference at the mega-transect observation stations, partly due to the wave spectra being linearly interpolated in time from the observed spectra which are at 3-hr intervals.

Table 7.20. Wave model setup parameters for the MCR test case.

Setting	**Value**
Wave breaking	Battjes and Janssen (1978)
Spectrum	Buoy 46029
Bottom friction	Off
Steering interval	1.0 hr
Roller	Off

7.5.4 Results and Discussion

The computed wave heights at Stations (Sta) 4 and 5 are shown in Figure 7.27. The model performance is quantified with several goodness-of-fit statistics presented in Table 7.21. The model reproduces the general wave height variation but tends to underestimate the wave heights during ebb tides. When the waves encounter the opposing current, the wavelength is reduced, so that the wave is compressed and the wave height increases. In addition, opposing currents also refract the waves towards areas with stronger currents. In some cases, it is observed from the field data that the wave height can increase by 50-70% during ebb tide. Elias et al. (2012) used the SWAN spectral wave model to simulate the same time period and obtained good agreement with measurements. Demirbilek et al. (2008) tested a similar spectral wave model STWAVE (Smith et al. 2001) for the same time period but for selected times at slack tide (low current velocities), so it is unclear if similar results would be obtained with STWAVE. Further research is needed to determine the cause for the wave height under-prediction for strong opposing currents.

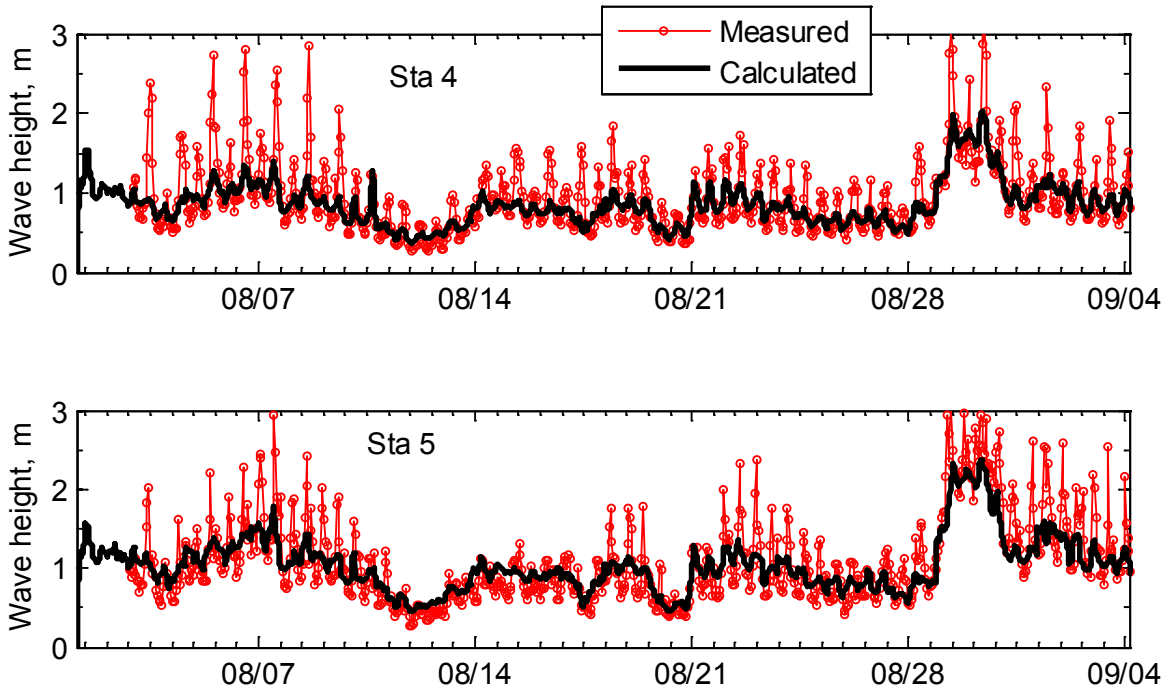

Figure 7.33. Comparison of measured and calculated significant wave heights at Stations 4 (top) and 5 (bottom). Horizontal axis indicates the month/day of 2005.

Table 7.21. Goodness-of-fit statistics* for the wave height for two stations in the entrance of the Columbia River.

Station	**NRMSE, %**	**NMAE, %**	**NB, %**	**R^2**
4	10.3	7.2	-1.63	0.44
5	11.4	8.3	-0.5	0.46
*defined in Appendix A				

A comparison of the computed and measured peak wave periods is presented in Figure 7.34. In general the model results agree reasonably well with the measurements. The goodness-of-fit statistics are presented in Table 7.22. From viewing the time-series comparison it is clear that the model performance is better than indicated from the goodness-of-statistics. The reason for the apparent poor performance in the statistics is because the peak wave period is sensitive to the spectral shape for random wave fields which may have several peaks.

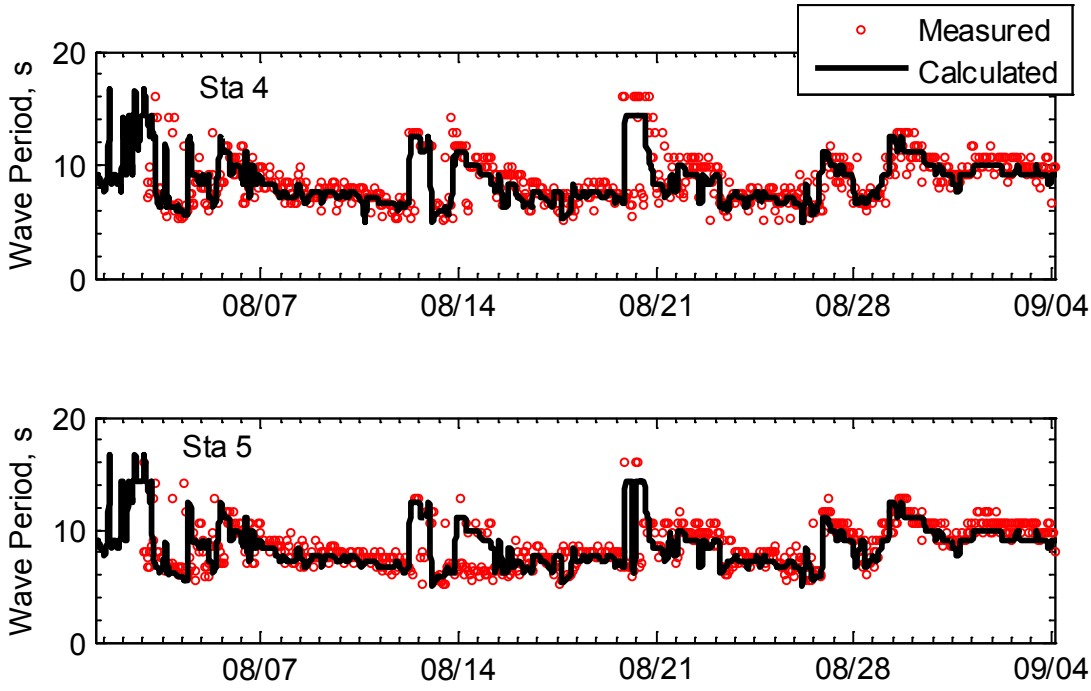

Figure 7.34. Comparison of measured and calculated peak wave periods at Stations 4 (top) and 5 (bottom). Horizontal axis indicates the month/day of 2005.

Table 7.22. Goodness-of-fit statistics* for the wave period for two stations in the entrance of the Columbia River.

Station	**NRMSE, %**	**NMAE, %**	**NB, %**	**R^2**
4	21.4	13.9	-3.7	0.09
5	17.9	12.4	-1.7	0.12
*defined in Appendix A				

The calculated and measured mean wave directions are compared in Figure 7.35. The measured mean wave direction is very noisy, with some values being unrealistic such those near 200 deg. For this reason, the goodness-of-statistics are not presented for the mean wave direction.

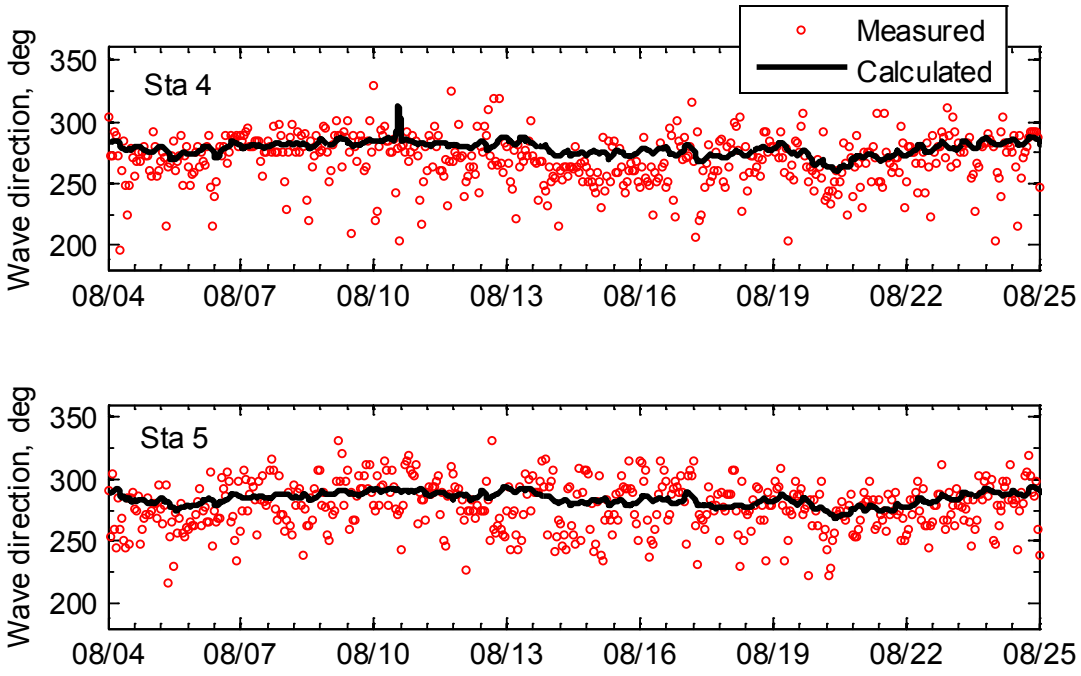

Figure 7.35. Comparison of measured and calculated mean wave directions at Stations 4 (top) and 5 (bottom). Horizontal axis indicates the month/day of 2005.

Example snap shots of the peak ebb and flood velocities are shown in Figure 7.36. One can see the model can simulate the tidal currents in the estuary, as well as the longshore currents along the coastal lines. A comparison of the measured and computed depth-averaged (principal component) current velocities is presented in Figure 7.37 and the model performance is quantified by several goodness-of-fit statistics presented in Table 7.23. Positive velocities indicate flood and negative velocities indicate ebb. In general the current velocities are better simulated in the central part of the entrance at Sta 2, 3, and 4. The flood velocities are generally well captured except for Sta 4, which are slightly under-predicted, while the peak ebb velocities are somewhat underestimated except for Sta 1, especially during spring tides. The under-prediction of ebb currents may be due to several reasons. One reason is that the river flow discharge increases the ebb current and reduces the flood current.

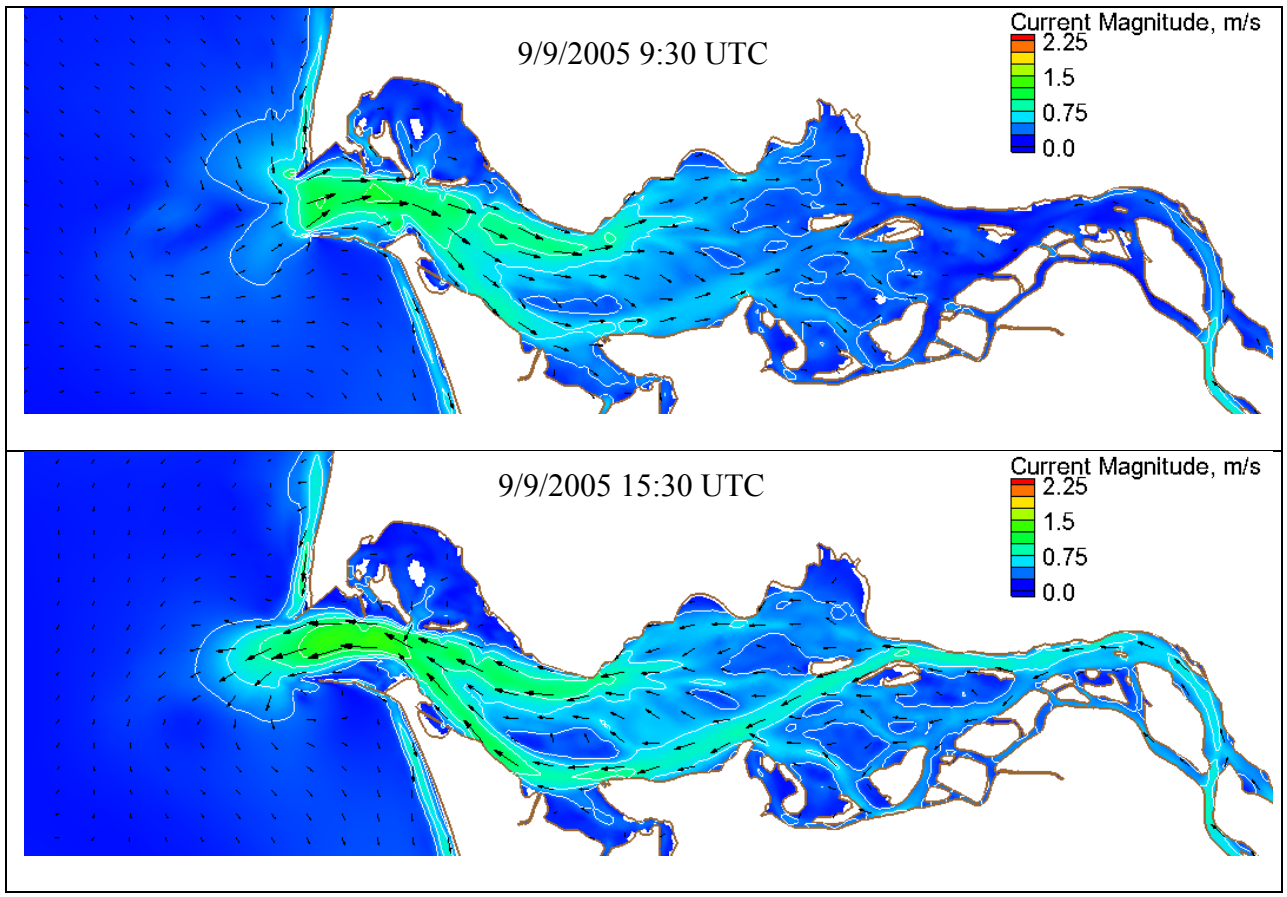

Figure 7.36. Example peak flood (top) and ebb (bottom) current velocities for the MCR test case.

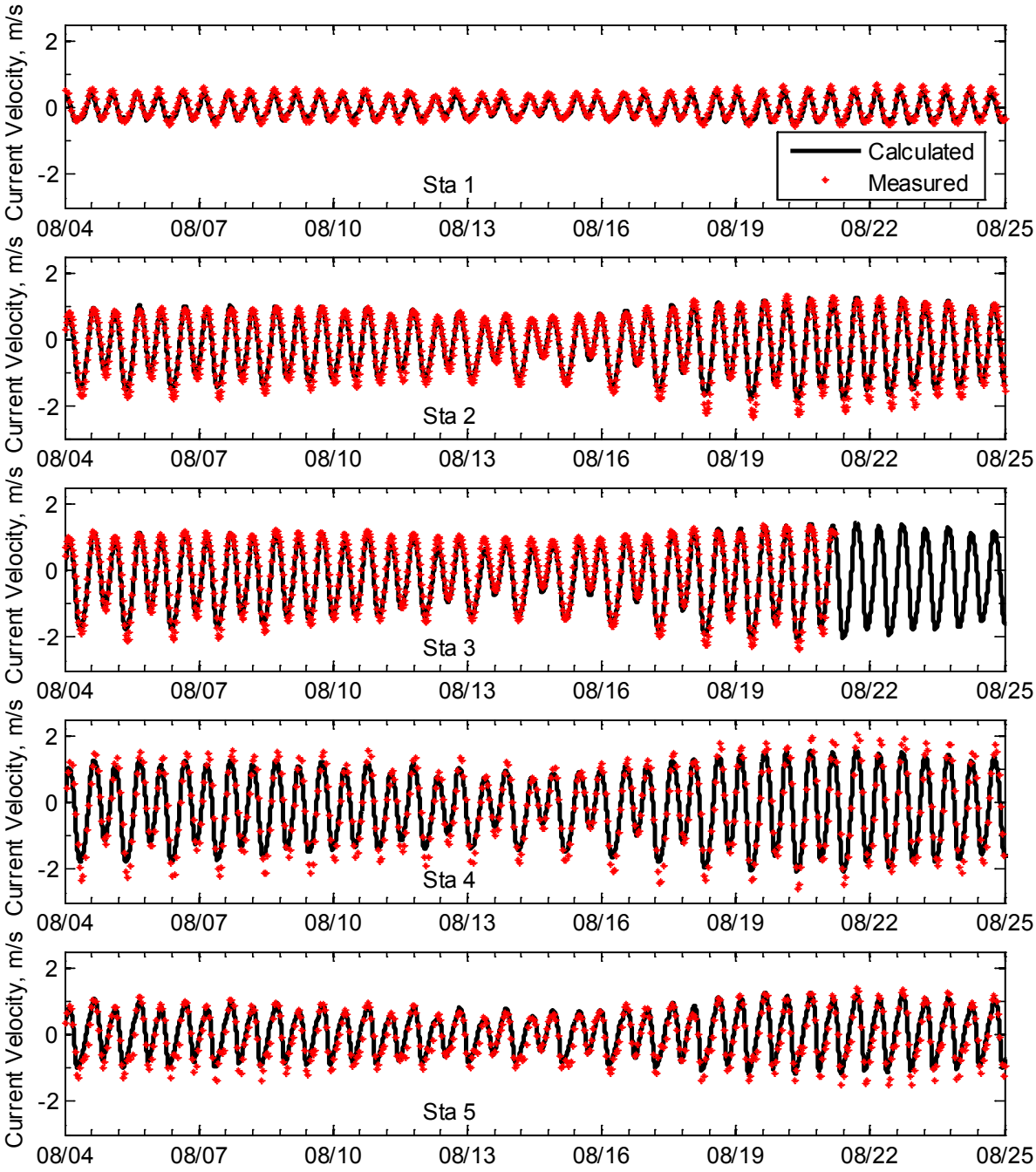

Figure 7.37. Comparison of measured and calculated depth-averaged current velocities (principle component) at Sta 1 through 5 for the MCR test case. Horizontal axis indicates the month/day of 2005.

Table 7.23. Goodness-of-fit statistics* for the depth-averaged current velocity (principle component) at Sta 1 through 5 for the MCR test case.

Sta	NRMSE, %	NMAE, %	NB, %	R^2
1	9.4	7.7	-3.7	0.91
2	5.2	4.1	2.4	0.96
3	6.1	4.9	-2.5	0.95
4	5.5	4.6	-1.7	0.96
5	8.5	6.2	3.2	0.92
*defined in Appendix A				

Ebb currents are stronger due flow stratification with a discharge of lower salinity water in the upper portion of the water column while the saltier and denser ocean water is drawn into the bay in the lower part of the water column. During ebb tide, the vertical stratification reduces the internal vertical shear and allows the surface flow to 'slide' over the denser flow below producing the effect of decreasing the net 2DH bottom friction (Giese and Jay 1989, Elias et al. 2012). Elias et al. (2012) showed that the average peak flood velocities are not significantly influenced by density gradients (salinity) while the peak ebb velocities have a larger magnitude when density gradients are included. This agrees with the results of this study. If the vertical stratification occurred during the whole tidal cycle, then it could be lumped into the bottom roughness and calibrated using field measurements. However, in the MCR the degree of stratification varies significantly during the tidal cycle, being strongest during ebb tide and weakest during flood tide.

In addition, mass conservation requires that the total ebb flow be equal to the flood flow plus the river discharge and Stokes drift. Therefore, another possible contributing factor in the under-prediction of the ebb velocities is the under-prediction of the wave heights during ebb tide. The largest differences between computed and measured current velocities occur at Sta 4 and 4.

This may be partly due to errors in the local bathymetry as indicated by the differences between the observed water depths in the field and the model bathymetry grid.

The measured and computed water levels at four stations are compared in Figure 7.38 and the corresponding goodness-of-fit statistics are presented in Table 7.24. The water levels are well simulated at all four stations, but the model performance decreases with distance from the entrance with the worst being at Longview which is about 65 km from the entrance. The water levels demonstrate the decreasing tidal amplitude with distance from the entrance due to bottom friction. If the water level time series at Sta 5 is considered representative of the ocean water levels due to its position, then the model performance at Sta 5 is indicative of the error associated with the boundary tidal constituent forcing and missing atmospheric effect. It is noted that the model is able to simulate the tidal wave setup produced during the spring tide which is observed as subtidal oscillation in the water levels.

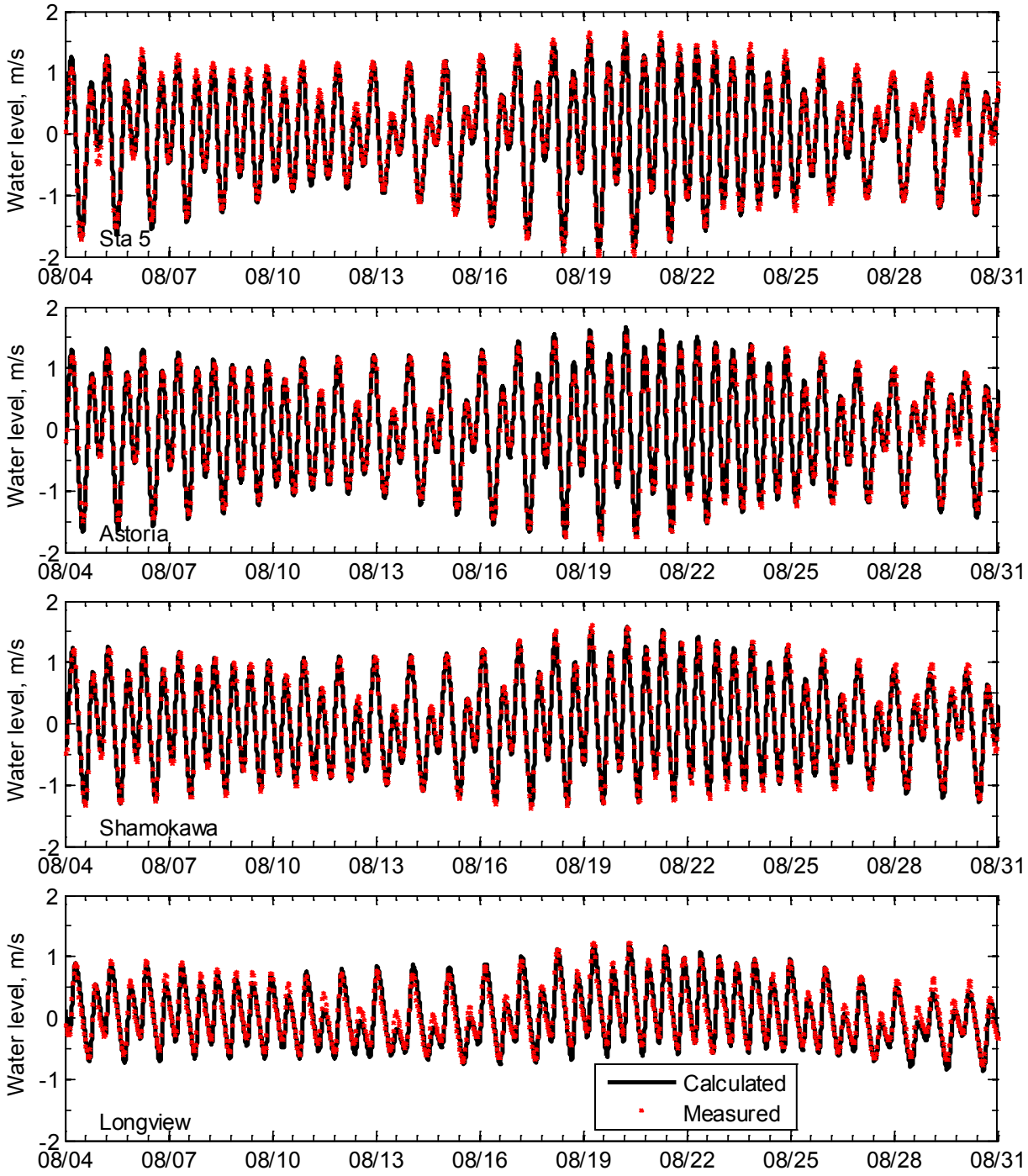

Figure 7.38. Comparison of measured and calculated water levels at several tide gauge stations. Horizontal axis indicates the month/day of 2005.

Table 7.24. Goodness-of-fit statistics* at four water level observation stations.

Station	**NRMSE, %**	**NMAE, %**	**NB, %**	**R^2**
5	3.8	3.0	0.0	0.97
Astoria	4.5	3.6	-0.5	0.97
Shamokawa	4.2	3.2	-0.2	0.97
Longview	9.6	7.5	-0.8	0.79
*defined in Appendix A				

CHAPTER IX

CONCLUSIONS AND RECOMMENDATIONS

A coastal morphodynamic modeling system has been developed and tested for a wide variety of cases. The modeling system includes models for: (1) hydrodynamics, (2) sediment transport and morphology change, (3) spectral wave transformation, and (4) surface roller. Models (1), (2), and (4) have been developed or enhanced in this study.

The hydrodynamic model includes the major physical coastal processes such as advection, turbulent mixing, combined wave-current bottom friction; wave volume flux; wind, atmospheric pressure, wave, river, and tidal forcing; and Coriolis-Stokes force. The model solves the depth-integrated and wave-averaged continuity and momentum equations using a fully implicit finite-volume method. The model is developed for general polygonal grids and has been tested using uniform and nonuniform Cartesian, telescoping Cartesian, triangular, quadrilateral, and hybrid triangular/quadrilateral grids. The grid cells are numbered by means of a general unstructured index system, so that all types of grids are supported under the same framework. Primary variables are collocated at cell centroids. The coupling of velocity and water level on a collocated grid is achieved using the SIMPLEC (van Doormaal and Raithby 1984) algorithm and a Rhie and Chow (1983) type momentum interpolation for inter-cell fluxes. A second-order three-level time stepping scheme is added and found to significantly reduce the numerical diffusion. First- and second-order spatial discretizations are employed with simplifications

utilizing the underlying grid geometry wherever possible. Several iterative solvers, such as GMRES, BiCGStab, SIP, ICCG, and Gauss-Seidel with and without SOR, are used to solve the discretized governing equations.

A multiple-sized sediment transport model has been established with emphasis on practical engineering applications at coastal inlets and navigation channels. The governing equations consist of total-load transport, bed change, and bed sorting equations. The model combines bed load and suspended load into a single total-load transport equation for each sediment size class, so that one less differential equation is needed for each size class. This is particularly economical for multiple-sized sediment transport modeling. The model includes bed-material hiding and exposure, sorting, layering, bed slope effects, avalanching, and sediment transport over non-erodible bottoms. The adaptation length in the nonequilibrium sediment transport model is calibrated for each case and found to be between 0.5 to 2.0 m for laboratory cases. For the Grays Harbor, WA field case the total-load adaptation length is calculated as a weighted average of the bed- and suspended-load adaptation lengths. The bed-load adaptation length is set to 10 m, and the suspended-load adaptation is calculated using a constant adaptation coefficient of 0.5. Sediment transport is calculated on the same computational grid using the same fully implicit finite volume scheme as the hydrodynamics. The sediment transport and bed change are computed in the same time step as the hydrodynamics, so that the sediment mass balance is satisfied conveniently. The sediment transport model is decoupled from the hydrodynamic model, but the nonuniform sediment transport, bed change and bed material sorting equations are solved in a coupled form. This semi-coupling algorithm is computationally efficient.

The spectral wave model originally developed by Mase (2005) (see also Lin et al. 2008, 2011a,b) has been coupled to the hydrodynamic and sediment transport models. A coupling procedure has been developed specifically for coastal inlets and open coast applications, which allows for larger wave model time steps (steering intervals). The surface roller model of Stive and de Vriend (1994) has been modified to include an efficiency factor controlling how much energy is transferred to the roller from wave breaking. The efficiency factor is found to vary between 0.5 and 1.0, while the dissipation coefficient varies between 0.02 and 0.1 for the test cases used in this study. The surface roller is implemented on the same nonuniform Cartesian grid as the spectral wave model using finite-difference methods.

The developed model has been verified using seven analytical cases and validated using ten laboratory experiments and five field studies. The test cases cover a wide range of conditions, time and spatial scales. The model performance and behavior varies case by case but in general is found to be satisfactory, and the calculated results are in good agreement with analytical solutions and measurements, as demonstrated by several goodness-of-fit statistics. Verifications using analytical solutions show that the governing equations are correctly discretized numerically and implemented in the computer code. The grid convergence test demonstrates the numerical discretizations can reach second-order accuracy. Validations using the laboratory and field measurements indicate that the developed model is able to simulate the major physical processes in coastal hydro- and morphodynamic systems under study.

The flow model can simulate reasonably well the recirculation flows near a spur dike and behind a sudden expansion in channels, long wave propagations and tidal currents in estuaries and bays, as well as nearshore currents and water levels due to wind and waves. The wetting and

drying algorithm is found to be robust and lead to an accurate prediction of the shoreline position as demonstrated using the long-wave runup case of Carrier et al. (2003). The wetting and drying algorithm works well for field cases even with relatively large time steps of 15 min (for Grays Harbor, WA). Wave-induced currents are well simulated for both monochromatic and random waves. The longshore currents are improved when including the surface roller, whereas the water levels are only slightly improved and the wave heights are not significantly influenced by the surface roller. These results indicate that once the flow model is calibrated for a specific site, using mainly the bottom roughness, the model can be applied at the same site for different wave conditions without having to recalibrate the model.

The sediment transport model works well for the cases of erosion due to clear inflow in a basin, channel aggradation due to over-loaded nonuniform sediments, and morphology change in a beach with nonuniform sediments. It is noted that the model can predict reasonably well the longshore sediment transport in the surf zone, but may under-predict in the area near the swash zone due to that the model does not consider the swash zone processes. As the LSTF experiment test case shows, the longshore sediment transport in the swash zone can be significant and even larger than that in the surf zone. The non-equilibrium total-load sediment transport model is able to reproduce the overall morphologic behavior of channel infilling with and without waves. The model provides better results for the mild (1:10) channel slope test case than the steeper slope (1:7 and 1:3) cases. This may be due to that flow separation is not accounted for in the present depth-averaged model. Therefore, caution is required when applying the model to steep bed slopes.

The results show the importance of having an accurate sediment transport formula and how

errors in the transport formula may lead to differences in calibration parameters such as the total-load adaptation length. For practical applications it is recommended to run multiple simulations using different transport formulas and other model settings to assess sensitivity of model results. The model calibration should begin with the sediment transport scaling factors and then the total-load adaptation length, as in the case of single-size sediment transport. If measurements of grain size distributions are available, then the hiding and exposure coefficient should be calibrated next. The bed slope coefficient is shown to be of secondary importance compared to the transport formula and adaptation length. When developing a new model setup and grid for engineering applications, it is useful to start with a simple grid and model forcing, and then slow increase the model grid setup complexity, only as needed, until satisfactory results are obtained for the purpose of the project. This iterative process has the added benefit of providing insights to the importance of physical processes and model sensitivity to parameters and grid geometry.

In the future, the developed model will be enhanced to consider a quasi-3D formulation for hydrodynamics and sediment transport. Analytical expressions were developed for momentum and sediment dispersion, and preliminary results have been obtained. However, due to time constraints and limited testing it is decided not to include these in the dissertation.

The bottom roughness in the hydrodynamics is specified as an input parameter and is held constant throughout the simulation. In the case of sediment transport, the bottom roughness is estimated based on the bed composition and ripple dimensions for the case of the Lund-CIRP (Camenen and Larson 2005, 2007, 2008) equations, while the roughness from the hydrodynamics is used in the other transport formulas. In the future, the option will be added to estimate the bed roughness for both the hydrodynamics and sediment transport based on the local

bed composition and bed forms. Although there is a still a large uncertainty in estimating bed forms under combined waves and currents, this approach is more physically correct.

LIST OF REFERENCES

REFERENCES

Abbott, M.B. 1979. Computational Hydraulics: Elements of the Theory of Free Surface Flows Pitman Publishing, London, 326 pp.

Anderson, J.D. 1995. Computational Fluid Dynamics – The Basics with Applications, McGraw-Hill, Incorporate., 206. New York.

Andrews, D.G., and McIntyre, M.E. 1978a. An exact theory of nonlinear waves on a Lagrangian mean flow. Journal of Fluid Mechanics, 89, 609–646.

Arakawa, A., and Lamb, V.R. 1977. Computational design of the basic dynamical processes of the UCLA general circulation model, Methods of Computational Physics, 17, 174–265.

Ariathurai, C.R., and Arulanandan, K., 1978. Erosion rates of cohesive soils. Journal of Hydraulics Division, 104 (2), 279–282.

Armanini, A., and di Silvio, G. 1986. Discussion on the paper 'A depth-averaged model for suspended sediment transport', by Gallappatti, G., and Vreugdenhil, C. B. Journal of Hydraulic Research, 24(5), 437–441

Ashida, K., and Michiue, M. 1972. Study on hydraulic resistance and bed load transport rate in alluvial streams, Transactions, Japan Society of Civil Engineering, 206, 59–69.

Bailard, J.A. 1981. An energetics total load sediment transport model for a plane sloping beach. Journal of Geophysical Research, 86(C11), 10938–10954.

Batten, B.K., and Kraus, N.C. 2006. Evaluation of downdrift shore erosion, Mattituck Inlet, New York: Section 111 Study, Technical Report ERDC/CHL-TR-06-1, U.S. Army Engineer Research and Development Center, Coastal and Hydraulics Laboratory, Vicksburg, Mississippi.

Barth, T.J. 1992. Aspects of unstructured grids and finite-volume solvers for the Euler and Navier–Stokes equations, AGARD Report 787, Nevilly, sur Seine, France.

Beck, T.M., and N.C. Kraus. 2010. Shark River Inlet, New Jersey, entrance shoaling: Report 2,

Analysis with Coastal Modeling System. Technical Report ERDC/CHL-TR-10-4, U.S. Army Engineer Research and Development Center, Coastal and Hydraulics Laboratory, Vicksburg, Mississippi.

Beck, T.M., and Legault, K. 2012. St. Augustine Inlet, Florida: Application of the coastal modeling system. Technical Report ERDC/CHL-TR-12-14, U.S. Army Engineer Research and Development Center, Coastal and Hydraulics Laboratory, Vicksburg, Mississippi.

Bijker, E.W., 1971. Longshore transport computations. Journal of the Waterways, Harbors and Coastal Engineering Division, 97(4), 687–703.

Booij, N., Holthuijsen, L.H., and Ris, R.C., 1996. The 'SWAN' wave model for shallow water. Proceedings 25th International Conference on Coastal Engineering, ASCE, Orlando, 668–676.

Booij, N., Holthuijsen, L.H., Doorn, N., and Kieftenburg, A.T.M.M. 1997. Diffraction in a spectral wave model. Proceedings of the Third International Symposium Waves'97, ASCE, New York, pp 243–255.

Bosboom, J., Aarninkhof, S.G.J., Reniers, A.J.H.M., Roelvink, J.A. and Walstra, D.J.R. 1997. UNIBEST-TC 2.0. Overview of model formulations. Delft Hydraulics Report H2305.42.

Bottom, D.L., Simenstad, C.A., Burke, J., Baptista, A.M., Jay, D.A., Jones, K.K., Casillas, E., and Schiewe, M.H. 2005. Salmon at river's end: The role of the estuary in the decline and recovery of Columbia River salmon. NOAA Technical Memorandum. NMFS-NWFSC-68, U.S. Department of Commerce.

Buttolph, A.M., Reed, C.W., Kraus, N.C., Ono, N., Larson, M., Camenen, B., Hanson, H.,Wamsley, T., and Zundel, A. K. 2006. Two-dimensional depth-averaged circulation model CMS-M2D: Version 3.0, Report 2: Sediment transport and morphology change. Tech. Rep. ERDC/CHL TR-06-9, U.S. Army Engineer Research and Development Center, Coastal and Hydraulic Engineering, Vicksburg, Mississippi.

Bye, J.A.T. 1985. Large-scale momentum exchange in the coupled atmosphere–ocean, coupled ocean–atmosphere models. Elsevier Science Publishers, Amsterdam, pp. 51–61.

Byrnes, M.R., Griffee, S.F., and Osler, M.S. 2010. Channel dredging and geomorphic response at and Adjacent to Mobile Pass, Alabama. Technical Report ERDC/CHL-TR-10-8, U.S.

Army Engineer Research and Development Center, Coastal and Hydraulics Laboratory, Vicksburg, Mississippi.

Caleffi, V., Valiani, A., and Zanni, A. 2003. Finite volume method for simulating extreme flood events in natural channels. Journal of Hydraulic Research, 41(2), 167–177.

Camenen, B., and Larson, M. 2005. A general formula for non-cohesive bed load sediment transport. Estuarine, Coastal and Shelf Science, 63, 249–260.

Camenen, B., and Larson, M. 2007. A unified sediment transport formulation for coastal inlet application. Technical report ERDC/CHL CR-07-1, US Army Engineer Research and Development Center, Vicksburg, Mississippi.

Camenen, B., and Larson, M. 2008. A general formula for noncohesive suspended sediment transport. Journal of Coastal Research, 24 (3), 615–627.

Carrier, G., Wu, T.T., and Yeh, H. 2003. Tsunami runup and draw-down on a plane beach. Journal of Fluid Mechanics, 475, 79–99.

Cayocca, F. 2001. Long-term morphological modeling of a tidal inlet: The Arcachon Basin, France. Coastal Engineering, 42, 115–142.

CEM 2002. Coastal Engineering Manual. Engineer Manual 1110-2-1100, U.S. Army Corps of Engineers, Washington, D.C. (in 6 volumes).

Chesher, T.J., Wallace, H.M., Meadowcroft, I.C., and Southgate, H.N. 1993. A Morphodynamic Coastal Area Model. First Annual Report, HR Wallingford Report SR 337.

Choi, S.K., Nam, H.Y., and Cho, M. 1995. A comparison of higher-order bounded convection schemes. Computational Methods in Applied Mechanics and Engineering, 121, 281–301.

Chawla, A., and Kirby, J.T. 2002. Monochromatic and random wave breaking at blocking points. Journal of Geophysical Research, 107(C7), 4-1–4-19.

Dabees, M., and Moore, B.D. 2011. Inlet evolution modeling of multiple inlet systems in Southwest and Central Florida. Journal of Coastal Research, Special Issue, 59, 130–137.

Dawe, J.T., and Thompson, L. 2006. Effect of ocean surface currents on wind stress, heat flux, and wind power input to the ocean. Geophysical Research Letters, 33, L09604.

de Vriend, H.J., Bakker, W.T., Bilse, D.P., 1994. A morphological behavior model for the outer delta of mixed-energy tidal inlets. Coastal Engineering, 23, 305–327.

de Vriend, H.J., and Stive, M.J.F. 1987. Quasi-3D modeling of nearshore currents, Coastal

Engineering, 11, 565–601.

Dean, R.G., and Dalrymple, R.A. 1991. Water wave mechanics for engineers and scientist. World Scientific Publishing Company Incorporated, pp 353.

Delft 1999a. Unibest-CL+ V5.0 for Windows User Manual (Draft Version 5.0). Delft Hydraulics.

Delft 1999b. Unibest-TC: A generic tool to investigate the morphodynamic behavior of crossshore profiles, User manual V2.02. Delft Hydraulics report 8.6520.00.

Deigaard, R., Fredsøe, J., and Brøker Hedegaard, I. 1986. Suspended sediment in the surf zone. Journal of Waterway, Port, Coastal and Ocean Engineering, 112(1), ASCE, 115–128.

Demirbilek, Z., Lin, L., and Nwogu, O.G. 2008. Wave modeling for jetty rehabilitation at the Mouth of the Columbia River, WA/OR, USA. Technical Report ERDC/CHL-TR-08-03, U.S. Army Engineer Research and Development Center, Coastal and Hydraulics Laboratory, Vicksburg, Mississippi.

Demirbilek, Z., Lin, L., and Seabergh, W.C. 2009. Laboratory and numerical modeling studies of hydrodynamics near jetties. Coastal Engineering Journal, 51(2), 143–175.

Ding, Y., Wang, S.S.Y., and Jia, Y., 2006. Development and validation of a quasi-three dimensional coastal area morphological model. Journal of Waterway, Port, Coastal and Ocean Engineering, 132(6), 462–476.

Ding, Y., and Wang, S.S.Y., 2008. Development and application of coastal and estuarine morphological process modeling system. Journal of Coastal Research, Special Issue 52, 127–140.

Dingemans, M.W., Radder, A.C., and de Vriend, H.J. 1987. Computation of the driving forces of wave-induced currents. Coastal Engineering, 11, 539–563.

Einstein, H.A., 1950. The bed load function for sediment transportation in open channels, Technical Bulletin 1026, U.S. Department of Agriculture, Soil Conservation Service, Washington, D.C.

Elfrink, B., Brøker, I., Deigaard, R., Hansen, E.A. and Justesen, P. 1996. Modelling of 3D sediment transport in the surf zone, Proceedings of the 25th International Conference on Coastal Engineering, ASCE, 3805–3817.

Elfrink, B., Brøker, I., and Deigaard, R. 2000. Beach profile evolution due to oblique wave

Attack. Proceedings of the 27th International Conference on Coastal Engineering, ASCE, 3021-3034.

Elias, E.P.L., Gelfenbaum, G., Van der Westhuysen, A.J. 2012. Validation of a coupled wave-flow model in a high energy setting: The mouth of the Columbia River. Journal of Geophysical Research, 117, 1–21.

Engelund, F., and Fredsøe, J. 1976. A sediment transport model for straight alluvial channels. Nordic Hydrology, 7, 293–306.

Engelund, F., and Hansen, E. 1967. A monograph on Sediment Transport in Alluvial Streams. Teknisk Forlag, Copenhagen. 556

Exner, F.M. 1925. Über die wechselwirkung zwischen wasser und geschiebe in flüssen, Akad. Wiss. Wien Math. Naturwiss. Klasse, 134(2a), 165–204.

Feddersen, F., Guza, R.T., Elgar, S., and Herbers, T.H.C. 2000. Velocity moments in alongshore bottom stress parameterizations, Journal of Geophysical Research, 105(C4), 8673-8686.

Ferziger, J. H., and Peric, M. 1997. Computational Methods for Fluid Dynamics, Springer-Verlag, Berlin/New York, 226 p.

Fortunato, A.B., and Oliviera, A. 2004. A modeling system for tidally driven long-term morphodynamics, Journal of Hydraulic Research, 42(4), 426–434.

Fortunato, A.B., Oliviera, A. 2007. Improving the stability of a morphodynamic modeling system. Journal of Coastal Research, Special Issue 50, 486–490.

Foster, T.M., Skou, A.J. 1992. LITPACK an integrated modelling system for littoral processes and coastline kinetics, 3rd International Software Exhibition for Environmental Science and Engineering, Como, Italy.

Fox, D.S., Bell, S., Nehlsen, W., and Damron, J. 1984. The Columbia River estuary: Atlas of physical and biological characteristics. Columbia River estuary Data Development Program, Astoria, Oregon.

Fread, D.L. 1976. Theoretical development of implicit dynamic routing model, paper presented at the Dynamic Routing Seminar, Lower Mississippi River Forecast Center, Slidell, Louisiana.

Fredsøe, J. 1984. Turbulent boundary layer in wave-current motion. Journal of Hydraulic Engineering, ASCE, 110, 1103–1120.

Fredsøe, J., Andersen, O.H., and Silberg, S. 1985. Distribution of suspended sediment in large waves. Journal of Waterways, Port, Coastal and Ocean Engineering, ASCE, 111(6), l041–1059.

Gailani, J.Z., Smith, J.W., Kraus, N.C., McGee, D.D., Hands, E.B., Mayers, C.J., Moritz, H.R., Moritz, H.P., Siipola, M.D., Slocum, D.B., Byrnes, M.R., Li, F., Dibble, T.L., Hollings, W.H., Lund, C.R., Sollitt, C.K., and Standley, D.R. 2003. Monitoring dredged material disposal at the Mouth of the Columbia River, WA/OR, USA. Technical Report ERDC/CHL-TR-03-5, U.S. Army Engineer Research and Development Center, Coastal and Hydraulics Laboratory, Vicksburg, Mississippi.

Gallappatti, G., and Vreugdenhil, C.B. 1985. A depth-integrated model for suspended sediment transport. Journal of Hydraulic Research, 23(4), 359-377.

Graf, W.H., and Altinakar, M. 1998. Fluvial Hydraulics. Wiley & Sons Ltd., 681 pp.

González, F.I. 1984. A case study of wave-current-bathymetry interactions at the Columbia River entrance. Journal of Physical Oceanography, 14(6), 1065-1078.

Gravens, M.B., 1996. Approach to modeling inlet and beach evolution. Proceedings 25th International Conference on Coastal Engineering. ASCE, Orlando, 4477–4490.

Gravens, M.B. and Wang, P., 2007. Data report: Laboratory testing of longshore sand transport by waves and currents; morphology change behind headland structures. Technical Report ERDC/CHL TR-07-8, U.S. Army Engineer Research and Development Center, Coastal and Hydraulics Laboratory, Vicksburg, Mississippi.

Groeneweg, J., 1999. Wave-current interaction in a generalized Lagrangian mean formulation. PhD thesis, Delft University of Technology, Delft, The Netherlands.

Ham, F.E., Lien, F.S., and Strong, A.B. 2002. A Cartesian grid method with transient anisotropic adaptation. Journal of Computational Physics, 179. 469–494.

Hanson, H., Aarninkhof, S, Capobianco, M., Jimenez, J.A., Larson, M., Nicholls, R.J., Plant, N.G., Southgate, H.N., Steetzel, H.J., Stive, M.J.F., and de Vriend, H.J. 2003. Modelling of Coastal Evolution on Yearly to Decadal Time Scales. Journal of Coastal Research, 19(4), 790–811.

Hanson, H., and Kraus, N.C. 1989. GENESIS: Generalized model for simulating shoreline change, Report 1: Technical Reference. Technical Report CERC-89-19, U.S. Army

Engineer Waterways Experiment Station, Coastal Engineering Research Center, Vicksburg, Mississippi.

Hanson, H., and Kraus, N.C. 1991. Numerical simulation of shoreline change at Lorain, Ohio. Journal of Waterway, Port, Coastal and Ocean Engineering, 117(1), 1–18.

Hamilton, P. 1990. Numerical modelling of circulation and density structure in the Columbia River Estuary. Progress in Oceanography, 25, 113–156.

Harlow, F.H. and Welch, J.E. 1965. Numerical calculation of time-dependent viscous incompressible flow of fluid with free surface. Physics of Fluids. 8, 2182.

Hedegaard, I.B., and Deigaard, R. 1988. A model for cross-shore sediment transport and coastal profile development. Proceedings IAHR, 2nd International Symposium on Wave Research and Coastal Engineering, Hannover.

Hirano, M. 1971. River bed degradation with armoring, Transactions of Japanese Society of Civil Engineering, 3(2), 194–195.

Holland, K.T., and Elmore, P.A. 2008. A review of heterogeneous sediments in coastal environments. Earth-Science Reviews, 89, 116–134.

Holthuijsen, L.H., Booij, N., and Herbers, T.H.C. 1989. A Prediction Model for Stationary, Short-Crested Waves in Shallow Water with Ambient Currents, Coastal Engineering, 13, 23–54.

Hsu, S.A. 1988. Coastal meteorology. Academic Press, San Diego, California.

Hubbard, M.E. 1999. Multidimensional slope limiters for MUSCL-type finite volume schemes on unstructured grids. Journal of Computational Physics, 155, 54–74.

Jasak, H., Weller, H.G., and Gosman, A.D. 1999. High Resolution NVD differencing scheme for arbitrarily unstructured meshes. International Journal of Numerical Methods for Fluids, 31, 431–449.

Jay, D.A., and Smith, J.D. 1990. Circulation, density distribution and spring-neap transitions in the Columbia River estuary, Progress in Oceanography, 25, 81–112.

Jia, Y., and Wang, S.S.Y. 1999. Numerical model for channel flow and morphological change studies, Journal of Hydrologic Engineering, ASCE, 125(9), 924–933.

Jia, Y., Wang, S.S.Y., and Xu, Y.C. 2002. Validation and application of a 2D model to channel with complex geometry. International Journal of Computational Engineering Science,

3(1), 57-71.

Johnson, I.G., 1966. Wave Boundary Layer and Function Factors. Proceedings 10th Coastal Engineering Conference. ASCE, 127–148.

Johnson, H.K., and Zyserman, J.A. 2002. Controlling spatial oscillations in bed level update schemes. Coastal Engineering, 46(2), 109–126.

Johnson, B.D., Kobayashi, N., and Gravens, M.B. 2012. Cross-shore numerical model CSHORE for waves, currents, sediment transport, and beach profile evolution. Technical Report ERDC/CHL TR-12-22, U.S. Army Engineer Research and Development Center, Coastal and Hydraulics Laboratory, Vicksburg, Mississippi.

Jonsson, I.G. 1990. Wave-current interactions. Chapter 7, The Sea. B. Le Mehaute and D. Hanes (ed.). New York, NY: John Wiley and Sons, 65–120.

Kana, T.W., Hayter, E.J., and Work, P.A., 1999. Mesoscale sediment transport at southeastern US tidal inlets: Conceptual model applicable to mixed energy settings. Journal of Coastal Research, 15(2), 303–313.

Karim, M.F., and Kennedy, J.F. 1982. IALLUVIAL: A Computer-Based Flow- and Sediment-Routing for Alluvial Stream and Its Application to the Missouri River. Iowa Institute of Hydraulic Research Report No. 250, University of Iowa; Iowa City, Iowa.

Kammerer, J.C. 1990. Largest rivers in the United States. Water fact sheet, United States Geological Survey, Open-File Report, 87–242.

Kernkamp, H.W.J., van Dam, A., Stelling, G.S., and de Goede, E.D. 2011. Efficient scheme for shallow water equations on unstructured grids with application to the Continental Shelf, Ocean Dynamics, 61, 1175–1188.

Koehler, R.B. 1988. An analysis of a numerical tidal model applied to the Columbia River, Master's Thesis, Naval Postgraduate School, Monterrey, California.

Komar, P.D., and Miller, M.C. 1975. On the comparison between the threshold of sediment motion under waves and unidirectional currents with a discussion of the practical evaluation of the threshold. Journal of Sedimentary Petrology, 45, 362–367.

Komen, G.J., Cavaleri, L., Doneland, M., Hasselmann, K., Hassselmann, S., and Janssen, P.A.E.M. 1994. Dynamics and modeling of ocean waves, Cambridge University Press, UK. 560 pp.

Kraus, N.C., 2000. Reservoir model of ebb-tidal shoal evolution and sand bypassing. Journal of Waterway, Port, Coastal, and Ocean Engineering, 126(6), 305–313.

Kraus, N.C., and Larson, M. 1991. NMLONG – Numerical model for simulating the longshore current. Report 1: Model development and tests. Technical Report DRP-91-1, U.S. Army Engineer Waterways Experiment Station, Vicksburg, Mississippi.

Kubatko, E.J., Westerlink, J.J., and Dawson, C. 2006. An unstructured grid morphodynamic model with a discontinuous Galerkin method for bed evolution. Ocean Modelling, 15(1–2), 71–89.

Kuriyama, Y., and Y. Ozaki. 1993. Longshore current distribution on a bar-trough beach, Field measurements at HORF and numerical model. Report of Port and Harbour Research Institute 32(3), Ministry of Transport, Japan, 3–37.

Lai, Y.G. 2010. Two-dimensional depth-averaged flow modeling with an un-structured hybrid mesh. Journal of Hydraulic Engineering, 136, 12–23.

Lamb, H. 1932. Hydrodynamics. 6th ed. New York: Dover Publications. 738 pp.

Landerman, L., Sherwood, C. R., Gelfenbaum, G., Lacy, J., Ruggiero, P., Wilson, D., Chrisholm, T., and Kurrus, K. 2004. Grays Harbor Sediment Transport Experiment: Spring 2001 – Data Report. U.S. Geological Survey Data Series.

Larson, M. 2009. Cross-shore sediment transport from undertow and asymmetry. Report to the Coastal Inlets Research Program, December 2009. Unpublished.

Larson, M., and Kraus, N.C. 1989. SBEACH: Numerical model for simulating storm-induced beach change. Technical Report CERC-89-9, Waterways Experiment Station, Coastal Engineering Research Center, Vicksburg, Mississippi.

Larson, M., and Kraus, N.C. 1991. Numerical model of longshore current for bar and trough beaches, Journal of Waterways, Port, Coastal, and Ocean Engineering, 11(4), 326–347.

Leliavsky, S, 1966. An introduction to fluvial hydraulics, Dover, New York, 257 pp.

Lesser, G., Roelvink, J., van Kester, J., and Stelling, G. 2004. Development and validation of a three-dimensional morphological model. Coastal Engineering, 51(8–9), 883–915.

Li, H., Brown, M.E., Smith, T.D., and Podoski, J.H. 2009. Evaluation of proposed channel on circulation and morphology change at Kawaihae Harbor and Pelekane Bay, Island of Hawaii, HI. Technical Report ERDC/CHL TR-09-19, U.S. Army Engineer Research and

Development Center, Coastal and Hydraulics Laboratory, Vicksburg, Mississippi.

Lin, B.N. 1984. Current study of unsteady transport of sediment in China. Proceedings Japan-China Bilateral Seminar on River Hydraulics and Engineering Experience, July, Tokyo-Kyoto-Sapporo, Japan, 337–342.

Lin, L., and Demirbilek, Z. 2005. Evaluation of two numerical wave models with inlet physical model. Journal of Waterway, Port, Coastal, and Ocean Engineering, 131(4),149–161.

Lin, L., Demirbilek, Z., Mase, H., Zheng, J., and Yamada, F. 2008. CMS-Wave: a nearshore spectral wave processes model for coastal inlets and navigation projects. Technical Report ERDC/CHL TR-08-13. U.S. Army Engineer Research and Development Center, Coastal and Hydraulics Laboratory, Vicksburg, Mississippi.

Lin, L., Demirbilek, Z., and Mase, H. 2011a. Recent capabilities of CMS-Wave: A coastal wave model for inlets and navigation projects. Journal of Coastal Research, Special Issue 59, 7–14.

Lin, L., Demirbilek, Z., Thomas, R., and Rosati III, J. 2011b. Verification and validation of the Coastal Modeling System, Report 2: CMS-Wave, Technical Report ERDC/CHL-TR-11-10, U.S. Army Engineer Research and Development Center, Coastal and Hydraulics Laboratory, Vicksburg, Mississippi.

Longuet-Higgins, M.S., and Stewart, R.W. 1961. The changes in amplitude of short gravity waves on steady non-uniform currents, Journal of Fluid Mechanics, 10(4), 529–549.

Luijendijk, A.P., Henrotte, J., Walstra, D.J.R., van Ormodt, M. 2010. Quasi-3D modeling of surf zone dynamics, Coastal Engineering, 2, 1–12.

Lynch, D.R., and Gray, W.G. 1978. Analytical solutions for computer flow model testing. Journal of the Hydraulics Division, 104, 1409–28.

Lumborg, U., and Windelin, A. 2003. Hydrography and cohesive sediment modelling: application to the Rømø Dyb tidal area, Journal of Marine Systems, 38(3–4), 287–303.

MacDonald, N.J., Davies, M.H., Zundel, A.K., Howlett, J.D., Lackey, T. C., Demirbilek, Z., and Gailani, J.Z. 2006. PTM: Particle Tracking Model; Report 1: Model theory, implementation, and example applications. Technical Report ERDC/CHL-TR-06-20. U.S. Army Engineer Research and Development Center, Coastal and Hydraulics Laboratory, Vicksburg, MS.

Madsen, O.S. 1994. Spectral wave–current bottom boundary layer flows. Proceedings of the 24th Conference on Coastal Engineering, ASCE, Kobe, Japan, 1, 384–398.

Majumdar, S. 1988. Role of underrelaxation in employing momentum interpolation practice for calculation of flow with non-staggered grids. Num. Heat Transfer, 13, 125–132.

Mase, H., 2001. Multidirectional random wave transformation model based on energy balance equation. Coastal Engineering Journal. 43(4), 317–337.

Mase, H., Oki, K., Hedges, T.S., and Li, H.J. 2005. Extended energy-balance-equation wave model for multidirectional random wave transformation. Ocean Engineering, 32(8–9), 961–985.

Mason, C.C., and Folk. R.L. 1958. Differentiation of beach, dune and eolian flat environments by size analysis: Mustang Island, Texas, Journal of Sedimentary Petrology, 28(2), 211–226.

McAnally, W.H., Letter, J.V., Stewart, J.P., Thomas, A., and Brogdon, N.J. 1984. Application of the Columbia Hybrid Modeling System. Journal of Hydraulic Engineering, 110, 627–642.

Mei, C.C. 1989. The Applied Dynamics of Ocean Surface Waves, Advanced Series on Ocean Engineering, World Scientific, New York.

Meyer-Peter, E, and Müller, R. 1948. Formulas for bed-load transport. Proceedings of the 2nd Meeting of the International Association for Hydraulic Structures Research. 39–64.

Militello, A., Reed, C.W., Zundel, A.K., and Kraus, N.C. 2004. Two-dimensional depth-averaged circulation model CMS-M2D: Version 2.0, Report 1, Technical documentation and user's guide. Technical Report ERDC/CHL TR-04-02, U.S. Army Engineer Research and Development Center, Coastal and Hydraulics Laboratory, Vicksburg, Mississippi.

Min Duc, B., Wenka, T., and Rodi, W. 2004. Numerical modeling of bed deformation in laboratory channels. Journal of Hydraulic Engineering, ASCE, 130(9), 894–904.

Moritz, H.R. 2005. Mouth of the Columbia River mega-transect instrument deployment. Internal document. U.S. Army Engineer District, Portland, Oregon.

Myrhaug, D., Holmedal, L.E., Simons, R.R., and MacIver, R.D. 2001. Bottom friction in random waves plus current flow. Coastal Engineering, 43, 75–92.

Nairn, R.B., and Southgate, H.N. 1993. Deterministic profile modelling of nearshore processes. Part 2. Sediment transport and beach profile development. Coastal Engineering, 19(1–2),

57–96.

Nam, P.T., Larson, M., Hanson, H., Hoan, L.X. 2009. A numerical model of nearshore waves, currents, and sediment transport. Coastal Engineering, 56, 1084–1096.

Nicholson J., Broker, I., Roelvink, J.A., Price, D., Tanguy, J.M., and Moreno, L. 1997. Intercomparison of coastal morphodynamic models. Coastal Engineering, 31(1), 97–123.

Nishimura, H. 1988. Computation of nearshore current. In Nearshore dynamics and coastal processes, K. Horikawa, ed., University of Tokyo Press, Tokyo, Japan, 271–291.

Nielsen, P. 1992. Coastal bottom boundary layers and sediment transport. World Scientific, Singapore, 324 pp.

Pacanowski, R.C. 1987. Effect of equatorial currents on surface wind stress. Journal of Physical Oceanography. 17, 833–838.

Paola, C., Parker, G., Sinha, S.K., Southard, J.B., and Wilcock, P.R. 1992. Downstream fining by selective deposition in a laboratory flume. Science, 258, 1757–1760.

Parker, G., Kilingeman, P.C., and McLean, D.G. 1982. Bed load and size distribution in paved gravel-bed streams, Journal of the Hydraulics Division, ASCE, 108(4), 544–571.

Partheniades, E. 1965. Erosion and deposition of cohesive soils. Journal of the Hydraulics Division, ASCE 91(1), 105–139.

Patankar, S.V. 1980. Numerical heat transfer and fluid flow, Hemisphere, New York.

Pelnard-Considere, R. 1956. Essai de theorie de l'Evolution des forms de rivages en plage de sable et de galets, Fourth Journees de l'Hydrolique, les energies de la Mer, Question III, Rapport No. 1, 289–298.

Phillips, O.M. 1977. The dynamics of the upper ocean. (2nd ed.). Cambridge University Press.

Phillips, B.C. and Sutherland, A.J., 1989. Spatial lag effects in bed load sediment transport. Journal of Hydraulic Research, 27(1), 115–133.

Ping, W., Davis, R.A., and Kraus, N.C. 1998. Cross-shore distribution of sediment texture under breaking waves along low-wave-energy coasts, Journal of Sedimentary Research, 68(3), 497–506.

Popinet, S., and Rickard, G. 2006. A tree-based solver for adaptive ocean modelling, Ocean Modelling. 16(3-4), 224-249.

Powell, M.D., Vickery, P.J., and Reinhold, T.A. 2003. Reduced drag coefficient for high wind

speeds in tropical cyclones, Nature, 422, 279–283.

Reed, C.W., and Lin, L. 2011. Analysis of Packery Channel Public Access Boat Ramp Shoreline Failure, Journal of Coastal Research Special Edition, Coastal Education and Research Foundation, Inc., Special Issue, 59, 150–155.

Reniers, A.J.H.M., Thornton, E.B., Stanton, T.P., and Roelvink. J.A. 2004. Vertical flow structure during Sandy Duck: observations and modeling. Coastal Engineering, 51, 237–260.

Resio, D.T. 1988. A steady-state wave model for coastal applications. Proceedings of the 21st Coastal Engineering Conference. ASCE, 929–940.

Rhie, T.M. and Chow, A. 1983. Numerical study of the turbulent flow past an isolated airfoil with trailing-edge separation. AIAA J., 21, 1525–1532.

Richardson, J.F., and Zaki, W.N. 1954. Sedimentation and fluidization, Transactions of the Institution of Chemical Engineering, 32, 35–53.

Roelvink, J.A. 2003. Implementation of roller model, draft Delft3D manual, Delft Hydraulics Institute.

Roelvink, J.A., and Banning, G.K.F.M. van. 1994. Design and development of Delft3D and application to coastal morphodynamics. Hydrodynamics '94. Verwey, Minns, Babovic & Maksimovic (eds), Balkema, Rotterdam, 451–455.

Roelvink, D., Reniers, A., Dongeren, A.V., de Vries, J.V.T, Lescinski, J. and McCall, R. 2010. XBeach Model Description and Manual (Version 6), UNESCO-IHE Institute for Water Education.

Roelvink, D., and Reniers, A. 2012. A guide to modeling coastal morphology. World Scientific, Advances in coastal and ocean engineering – Vol. 12, pp 274.

Rosati, J.R., Frey, A.E., Brown, M.E., and Lin, L. 2011. Analysis of Dredged Material Placement Alternatives for Bottleneck Removal, Matagorda Ship Channel, Texas, Technical Report ERDC/CHL-TR-11-2, U.S. Army Engineer Research and Development Center, Coastal and Hydraulics Laboratory, Vicksburg, Mississippi.

Ruessink, B.G., Miles, J.R., Feddersen, F., Guza, R.T. and Elgar, S. 2001. Modeling the alongshore current on barred beaches. Journal of Geophysical Research, 106(C10), 22451–22464.

Ruessink, B.G., Kuriyama, Y., Reniers, A.J.H.M., Roelvink, J.A., and Walstra, D.J.R. 2007. Modeling cross-shore sandbar behavior on the time scale of weeks. Journal of Geophysical Research, 112(F3), 2156–2202.

Ruessink, B.G., Terwindt, J.H.J. 2000. The behavior of nearshore bars on the time scale of years: a conceptual model. Marine Geology, 163, 289–302.

Saad, Y. 1993. A flexible inner-outer preconditioned GMRES algorithm. SIAM Journal Scientific Computing, 14, 461–469.

Saad, Y. 1994. ILUT: a dual threshold incomplete ILU factorization, Numerical Linear Algebra with Applications, 1, 387–402.

Saad, Y. and Schultz, M.H. 1986. GMRES: A generalized minimal residual algorithm for solving nonsymmetric linear systems. SIAM Journal of Scientific and Statistical, Computing, 7, 856–869.

Saad, Y. 1996. Iterative methods for sparse linear systems. PWS Publishing Company, 528 pp.

Sánchez-Arcilla, A., Collado, F. and Rodriguez, A. 1990. Another quasi-3D model for surf-zone flows, Proc. 22nd International Conference on Coastal Engineering, 316–329.

Sánchez, A., and Wu, W. 2011a. A non-equilibrium sediment transport model for coastal inlets and navigation channels. Journal of Coastal Research, Special Issue 59, 39–48.

Sánchez, A., and Wu, W. 2011b. Nonuniform sediment transport modeling and Grays Harbor, WA. Proceedings Coastal Sediments ’11.

Schoonees, J.S., and Theron, A.K. 1995. Evaluation of 10 cross-shore sediment transport/morphological models. Coastal Engineering, 25, 1–41.

Seabergh, W.C., Lin, L., and Demirbilek. Z. 2005. Laboratory study of hydrodynamics near absorbing and fully reflecting jetties. Technical Report ERDC/CHL-TR-05-8, U.S. Army Engineer Research and Development Center, Coastal and Hydraulics Laboratory,Vicksburg, Mississippi.

Seal, R., Parker, G., Paola, C., and Mullenbach, B. 1995. Laboratory experiments on downstream fining of gravel, narrow channel runs 1 through 3: supplemental methods and data. External Memorandum M-239, St. Anthony Falls Hydraulic Laboratory, University of Minnesota, Minneapolis.

Shin, J.K., and Choi, Y.D. 1992. Study on the improvement of the convective differencing

scheme for the high-accuracy and stable resolution of the numerical solution, Transactions KSME, 16(6),1179-1194 (in Korean).

SPM 1984. Shore Protection Manual, 4th ed., 2 Vol., U.S. Army Engineer Waterways Experiment Station, U.S. Government Printing Office.

Smagorinsky, J. 1963. General circulation experiments with the primitive equations, Monthly Weather Review, 93(3), 99–164.

Smith, J.M., Larson, M., and Kraus, N.C. 1993. Longshore current on a barred beach: Field measurements and calculation. Journal of Geophysical Research, 98(C12), 22717-22731.

Smith, J.M., Sherlock, A.R., Resio, D.T. 2001. STWAVE: Steady-state spectral wave model, Tech. Report ERDC/CHL-SR-01-01, US Army Engineer Research and Development Center, Coastal and Hydraulics Laboratory, Vicksburg, MS.

Soulsby, R.L. 1987. Calculating bottom orbital velocity beneath waves. Coastal Engineering 11, 371–380.

Soulsby, R.L., Hamm, L., Klopman, G., Myrhaug, D., Simons, R.R., and Thomas, G.P., 1993. Wave–current interactions within and outside the bottom boundary layer. Coastal Engineering, 21, 41–69.

Soulsby, R.L. 1995. Bed shear-stresses due to combined waves and currents, in Advanced in Coastal Morphodynamics, eds. M.J.F Stive, H.J. de Vriend, J. Fredsoe, L. Hamm, R.L. Soulsby, C. Teisson, and J.C. Winterwerp, Delft Hydraulics, The Netherlands. 4–20 to 4–23 pp.

Soulsby, R.L. 1997. Dynamics of marine sands, Thomas Telford, London. 249 pp.

Soulsby, R.L., and Damgaard, J.S., 2005. Bedload sediment transport in coastal waters. Coastal Engineering, 52 (8), 673–689.

Spalding, D.B. 1972. A novel finite-difference formulation for differential expressions involving both first and second derivatives. International Journal for Numerical Methods in Engineering, 4(4), 551–559.

Stelling, G.S., and Duinmeijer, S.P.A. 2003. A staggered conservative scheme for every Froude number in rapidly varied shallow water flows. International Journal for Numerical Methods in Fluids, 43, 1329–1354.

Stive, M.J.F., and de Vriend, H.J. 1994. Shear stresses and mean flow in shoaling and breaking

waves. Proceedings of the 24th Coastal Engineering International Conference 1994, Kobe, Japan. American Society of Civil Engineers, New York, 594–608 pp.

Stone, H.L. 1968. Iterative solution of implicit approximations of multidimensional partial differential equations. SIAM Journal of Numerical Analysis, 5(3), 530–538.

Struiksma, N., Olewensen, K.W., Flokstra, C., and de Vriend, H.J., 1985. Bed deformation in curved alluvial channels. Journal of Hydraulic Research, 23(1), 57–79.

Styles, R., and Glenn, S.M. 2000. Modeling stratified wave and current bottom boundary layers on the continental shelf. Journal of Geophysical Research, 105 (C10), 24119–24139.

Svendsen, I.A. 1984. Mass flux and undertow in a surf zone. Coastal Engineering, 8, 347–365.

Svendsen, I.A. 2006. Introduction to nearshore hydrodynamics. World Scientific. 722 pp.

Svendsen, I. A., Haas, K., and Zhao, Q. 2002. Quasi-3D nearshore circulation model, SHORECIRC, Version 2.0, Report, Center for Applied Coastal Research, University of Delaware, Newark.

Swart, D.H. 1974. Offshore sediment transport and equilibrium beach profiles. Technical Report. Delft, The Netherlands: Delft Hydraulics Laboratory. Publication 131.

Szmytkiewicz, M., Biegowski, J., Kaczmarek, L.M., Okrój, T., Ostrowski, R., Pruszak, Z., Rózynsky, G., and Skaja, M. 2000. Coastline changes nearby harbour structures: Comparative analysis of one-line models versus field data, Coastal Engineering, 40, 199–139.

Tajima, Y., and Madsen, O.S. 2006. Modeling near-shore waves, surface rollers, and undertow velocity profiles. Journal of Waterway, Port and Coastal Ocean Engineering. 132, 429–438.

Tanaka, H., and Thu, A. 1994. Full-range equation of friction coefficient and phrase difference in a wave-current boundary layer. Coastal Engineering, 22, 237–254.

Theisel, H. 1995. Vector field curvature and applications. Ph.D. Dissertation, Rostock University, Germany.

Thuc, T. 1991. Two-dimensional morphological computations near hydraulic structures. Doctoral Dissertation, Asian Institute of Technology, Bangkok, Thailand.

van Albada, G.D., Van Leer, B., and Roberts, W.W. 1982. A comparative study of computational methods in cosmic gas dynamics. Astronomy and Astrophysics, 108, 76–

84.

van der Salm, G.L.S. 2013. Coastline modelling with UNIBEST: Areas close to structures. M.S. Thesis. Delft University of Technology, The Netherlands.

van Doormal, J.P., and Raithby, G.D. 1984. Enhancements of the SIMPLE method for predicting incompressible fluid flows, Numerical Heat Transfer, 7, 147–163.

van Dongeren, A.R., A.J.H.M. Reniers, J.A. Battjes and I.A. Svendsen 2003. Numerical modeling of infragravity wave response during Delilah. Journal of Geophysical Research, (108:C9), 3288.

van Leer, B. 1979. Toward the ultimate conservative difference scheme. V. A second order sequel to Godunov method. Journal of Compuational Physics, 32, 101–136.

van Rijn, L.C. 1984a. Sediment transport, Part I: bed load transport. Journal of Hydraulic Engineering, ASCE, 110(10), 1431–1456.

van Rijn, L. C. 1984b. Sediment transport. Part II: Suspended load transport. Journal of Hydraulic Engineering, ASCE, 110(11), 1613–1641.

van Rijn, L. C. 1984c. Sediment transport. Part III: Bed forms and and alluvial roughness. Journal of Hydraulic Engineering, ASCE, 110(11), 1733–1754.

van Rijn, L.C. 1985. Two-dimensional vertical mathematical model for suspended sediment transport by currents and waves. Report S488-IV, Delft Hydraulics, Delft, The Netherlands.

van Rijn, L.C. 1993. Principles of Sediment Transport in Rivers, Estuaries and Coastal Seas. Aqua Publications, The Netherlands.

van Rijn, L.C. 2007a. Unified view of sediment transport by currents and waves. Part I: Initiation of motion, bed roughness, and bed-load transport. Journal of Hydraulic Engineering, 133(6), 649–667.

van Rijn, L.C. 2007b. Unified view of sediment transport by currents and waves. Part II: Suspended Transport, Journal of Hydraulic Engineering, 133(6), 668–689.

Walstra, D.J.R., Roelvink, J.A., and Groeneweg, J. 2000. Calculation of wave-driven currents in a 3D mean flow model, 27th International Conference on Coastal Engineering, Sydney, 1050–1063.

Walstra, D.J.R, Ruggiero, P., Lesser, G., and Gelfenbaum, G. 2005. Modeling nearshore

morphological evolution at seasonal scale. Proceedings of the 5th International Conference on Coastal Dynamics, Barcelona, Spain.

Wang, P., Beck, T.M., and Roberts T.M. 2011. Modeling regional-scale sediment transport and medium-term morphology change at a dual inlet system examined with the Coastal Modeling System (CMS): A case study at Johns Pass and Blind Pass, West-central Florida. Journal of Coastal Research, Special Issue 59, pp. 49-60.

Wang, S.S.Y., and Hu, K.K., 1992. Improved methodology for formulating finite-element hydrodynamic models, In T,J, Chung, (ed) Finite Element in Fluids, Hemisphere Publication Cooperation, 8, 457–478.

Wang, L., and Wu, C. 2010. An adaptive version of ghost-cell immersed boundary method for incompressible flows with complex stationary and moving boundaries. Physics, Mechanics, and Astronomy, 53, 923–932.

Warner, J.C., Sherwood, C.R., Signell, R.P., Harris, C.K. and Arango, H.G. 2008. Development of a three-dimensional, regional, coupled ,wave, current and sediment transport model, Computers and Geosciences, 34, 1284–1306.

Watanabe, A., 1985. Three-dimensional predictive model of beach evolution around a structure. Proceedings of the International Symposium of Water Wave Research. University of Hannover, Germany, 121-142.

Watanabe, A. 1987. 3-dimensional numerical model of beach evolution. Proceedings Coastal Sediments ’87, 802–817.

Watanabe, A., 1988. Numerical model of beach topography change. In: Horikawa, K. (ed), Nearshore dynamics and coastal processes. University of Tokyo Press, Tokyo, Japan, 241–243.

Whitham, G.B. 1974. Linear and nonlinear waves. John Wiley, New York, New York.

Wiberg, P.L., Sherwood, C.R. 2008. Calculating wave-generated bottom orbital velocities from surface-wave parameters, Computers and Geosciences, 34(10), 1243-1262.

Wright, D.G., and Thompson, K.R. 1983. Time-averaged forms of the nonlinear stress law, Journal of Physical Oceanography, 13, 341–346.

Wu, W., Wang, S.S.Y., and Jia, Y. 2000. Nonuniform sediment transport in alluvial rivers. Journal of Hydraulic Research, IAHR, 38(6), 427–434.

Wu, W. 1991. The study and application of 1-D, horizontal 2-D and their nesting mathematical models for sediment transport. PhD dissertation, Wuhan University of Hydraulic and Electric Engineering, Wuhan, China.

Wu, W. 2004. Depth-averaged 2-D numerical modeling of unsteady flow and nonuniform sediment transport in open channels. Journal of Hydraulic Engineering, ASCE, 135(10) 1013–1024.

Wu, W., Wang, P., and Chiba, N. 2004. Comparison of five depth-averaged 2-D turbulence models for river flows. Archives of Hydro-Engineering and Environmental Mechanics, Polish Academy of Science, 51(2), 183–200.

Wu, W. 2007. Computational River Dynamics. Taylor & Francis, 494 p.

Wu, W., Altinakar, M., and Wang, S.S.Y. 2006. Depth-averaged analysis of hysteresis between flow and sediment transport under unsteady conditions. International Journal of Sediment Research, 21(2), 101–112.

Wu, W., and Lin, Q. 2011. Extension of the Lund-CIRP formula for multiple-sized sediment transport under currents and waves, Report to the Coastal Inlets Research Program, October 2011, Internal Document.

Wu, W., Sánchez, A., and Mingliang, Z. 2010. An implicit 2-D depth-averaged finite volume model of flow and sediment transport in coastal waters. Proceeding of the 32nd International Conference on Coastal Engineering. Shanghai, China.

Wu, W., Sánchez, A., and Mingliang, Z. 2011. An implicit 2-D shallow water flow model on an unstructured quadtree rectangular grid, Journal of Coastal Research, Special Issue 59, 15–26.

Wu, W., and Vieira, D.A. 2002. One-dimensional channel network model CCHE1D 3.0 -- Technical manual, Technical Report No. NCCHE-TR-2002-1, National Center for Computational Hydroscience and Engineering, The University of Mississippi, Mississippi.

Wu, W., Wang, S.S.Y., and Jia, Y. 2000. Nonuniform sediment transport in alluvial rivers. Journal of Hydraulic Research, IAHR, 38(6), 427-434.

Wu, W., and Wang, S.S.Y., 2004. Depth-averaged 2-D calculation of flow and sediment transport in curved channels, International Journal of Sediment Research, 19(3), 172–

190.

Zarillo, G.A., and Brehin F.G.A. 2007. Hydrodynamic and Morphologic Modeling at Sebastian Inlet, FL. Proceedings of Coastal Sediments ’07, New Orleans, LA, ASCE Press, 1297–1311.

Zhang, H.-M., Reynolds, R.W., and Bates, J.J. 2006. Blended and Gridded High Resolution Global Sea Surface Wind Speed and Climatology from Multiple Satellites: 1987 – Present” American Meteorological Society 2006 Annual Meeting, Paper #P2.23, Atlanta, Georgia.

Zhu, J. 1991. A low-diffusive and oscillation-free convection scheme. Communications in Applied Numerical Methods, 7, 225–232.

Zwart, P.J., Raithby, G.D., and Raw, M.J. 1998. An integrated space-time finite volume method for moving boundary problems. Numerical Heat Transfer, B34, 257.

Zundel, A.K., 2006. Surface-water Modeling System reference manual – Version 9.0. Brigham Young University Environmental Modeling Research Laboratory, Provo, Utah.

Zyserman, J.A., and Ronberg, J.K. 2001. Model intercomparison - MORWIN project: 2d morphological modelling and 3D modelling of flow in the area of Bock Inlet, Technical Report. 50848-01, DHI.

APPENDIX

APPENDIX A: GOODNESS-OF-FIT STATISTICS

10.1 Brier Skill Score

The Bier Skill Score (BSS) is defined as

$$\mathrm{BSS} = 1 - \frac{\left\langle (x_m - x_c)^2 \right\rangle}{\left\langle (x_m - x_0)^2 \right\rangle} \tag{A1}$$

where the angled brackets indicate averaging, subscripts m, c, and 0 indicate measured, calculated, and initial values, respectively. The BSS ranges between negative infinity and one. A BSS value of 1 indicates a perfect agreement between measured and calculated values. Scores equal to or less than 0 indicates that the mean observed value is as or more accurate than the calculated values. The following quantifications are used for describing the BSS values: 0.8<BSS<1.0 = excellent, 0.6<BSS<0.8 = good, 0.3<BSS<0.6 = reasonable, 0<BSS<0.3 = poor, BSS<0 = bad.

10.2 Root-Mean-Squared Error

The Root Mean-Squared-Error (RMSE) is defined as

$$\mathrm{RMSE} = \sqrt{\left\langle (x_c - x_m)^2 \right\rangle} \tag{A2}$$

The RMSE has the same units as the measured data. Lower values of RMSE indicate a better match between measured and computed values.

The Normalized Root-Mean-Squared Error (NRMSE) is

$$\mathrm{NRMSE} = \frac{\mathrm{RMSE}}{\mathrm{range}(x_m)} \tag{A3}$$

The NRMSE is often expressed in units of percent. The measured data range $\text{range}(x_m)$ can be estimated as $\max(x_m) - \min(x_m)$. Lower values of NRMSE indicate a better agreement between measured and computed values.

10.3 Mean Absolute Error

The Mean Absolute Error (MAE) is defined as

$$\text{MAE} = \left\langle \left| x_c - x_m \right| \right\rangle \tag{A4}$$

Similarly, the Normalized Mean Absolute Error (NMAE) is given by

$$\text{NMAE} = \frac{\text{MAE}}{\text{range}(x_m)} \tag{A5}$$

The NRMSE is often expressed in units of percent. Smaller values of NMAE indicate a better agreement between measured and calculated values.

10.4 Bias

The Bias is defined as

$$\text{Bias} = \left\langle x_c - x_m \right\rangle \tag{A6}$$

in which positive values indicate over-prediction and negative values indicate under-prediction.

The normalized bias is defined as

$$\text{NB} = \frac{B}{\text{range}(x_m)} \tag{A6}$$

Positive values indicate over prediction and negative values indicate under prediction. The NB is often expressed in units of percent.

10.5 Correlation Coefficient

Correlation is a measure of the strength and direction of a linear relationship between two variables. The correlation coefficient R is defined as

$$R = \frac{\langle x_m x_c \rangle - \langle x_m \rangle \langle x_c \rangle}{\sqrt{\langle x_m^2 \rangle - \langle x_m \rangle^2} \sqrt{\langle x_c^2 \rangle - \langle x_c \rangle^2}} \tag{A5}$$

A correlation of 1 indicates a perfect one-to-one linear relationship and -1 indicates a negative relationship. The square of the correlation coefficient describes how much of the variance between two variables is described by a linear fit. The interpretation of the correlation coefficient depends on the context and purposes. For the present work, the following qualifications are used: $0.7<R^2<1$ = strong, $0.4<R^2<0.7$ = medium, $0.2<R^2<0.4$ = small, and $R^2<0.2$ = none.

VITA

Alejandro Sánchez was born in Zapopan Mexico, on January 7, 1981. He earned a Bachelor of Science in Oceanography from the Autonomous University of Baja California in 2004 and Master's in Engineering from the University of Hawai'i at Manoa in Ocean and Resources Engineering in 2007.